SELECTIVE OXIDATION AND REACTIVE WETTING OF 2MN-SI STEELS DURING CONTINUOUS HOT-DIP GALVANIZING

SELECTIVE OXIDATION AND REACTIVE WETTING OF 2MN-SI STEELS DURING
CONTINUOUS HOT-DIP GALVANIZING

By GHAZAL SEYED MOUSAVI, B.Sc., M.Sc.

A Thesis Submitted to the School of Graduate Studies in Partial Fulfilment of the Requirements

for the Degree Doctor of Philosophy

McMaster University

DOCTOR OF PHILOSOPHY (2018) McMaster University, Department of Materials Science and Engineering, Hamilton, Ontario

TITLE: Selective Oxidation and Reactive Wetting of 2Mn-Si Steels During Continuous Hot-Dip Galvanizing

AUTHOR: Ghazal Seyed Mousavi, B.Sc (Imam Khomeini International University), M.Sc. (University of Tehran)

SUPERVISOR: Dr. Joseph R. McDermid

NUMBER OF PAGES: xviii, 191

ABSTRACT

The influence of annealing process parameters i.e. oxygen partial pressure and annealing time, on the selective oxidation and reactive wetting of Fe-0.1C-2Mn-1.3Si (wt.%) and Fe-0.1C-2Mn-1.7Si (wt.%) advanced high strength steels during continuous galvanizing was investigated. The effect of the addition of 0.05 wt.% Sn on the selective oxidation and reactive wetting of the Fe-0.1C-2Mn-1.7Si (wt.%) steel was also determined. The experimental steels were annealed at intercritical annealing temperatures at which an intercritical microstructure of 50 ferrite -50 austenite (vol.%) was obtained, calculated for each grade of steel using THERMO-CALC software considering the local equilibrium-non partitioning (LE-NP) formalism, for annealing times of 60 to 600 s in a N_2-5 vol.% H_2 gas atmosphere, where the oxygen potential was controlled by varying the dew point (dp) at 223 K (–50 °C), 243 K (–30 °C) and 278 K (+5 °C). For reactive wetting studies, samples were immersed in a 0.2 wt.% dissolved Al continuous galvanizing bath. The oxide chemistry, spatial distribution and morphology were found to be affected by the annealing process parameters. As a consequence, the reactive wetting of the steels by the continuous galvanizing bath could be controlled via controlling these parameters

For the Fe-0.1C-2Mn-1.3Si (wt.%) alloy, annealing under the lowest pO_2 223 K (–50 °C) dp process atmosphere led to the formation of a thick, compact, multi-layer oxide comprised of film-like SiO_2 and $MnSiO_3$ with granular MnO on top. Insignificant internal oxidation was observed in this case. Increasing the process atmosphere pO_2 using the 243 K (–30 °C) dew point resulted in a considerable increase in the depth of internal oxidation and decrease in the thickness of external oxides, which is indicative of the occurrence of the transition from external to internal oxidation. Under this annealing condition, surface oxides were composed of thinner film-like $MnSiO_3$, Mn_2SiO_4 and SiO_2 oxides, compared to the 243 K (–50 °C) dp process atmosphere, as well as MnO oxides. Further increasing the process atmosphere pO_2 via raising the dew point to

iii

278 K (+5 °C) dp resulted in modification of the surface oxides from film-like to nodule-like MnO, $MnSiO_3$ and Mn_2SiO_4 particles. Prolonged annealing times were also found to increase either the thickness of external oxides or depth of internal oxidation.

For the Fe-0.1C-2Mn-1.7Si (wt.%) alloy, similar modifications in the morphology of the external oxides were observed after increasing the process atmosphere dew point from 223 K (–50 °C) to 278 K (+5 °C) dp, due to the transition from external to internal oxidation. Although steel surface was covered with thick, compact film-like SiO_2, $MnSiO_3$ and MnO under the 223 K (–50 °C) dp process atmosphere, thinner and less compact film-like and plate-like SiO_2, $MnSiO_3$ oxides and $MnSiO_3$ nodule-like particles were identified on the surface under the 243 K (–30 °C) and 278 K (+5 °C) dp process atmospheres, respectively. $MnSiO_3$ and Mn_2SiO_4 oxide particles as well as network of $MnSiO_3$ embracing SiO_2 core were found, respectively, in the bulk microstructure and along the grain boundaries in the steel subsurface. Detailed investigations into the growth kinetics of the external and internal oxides revealed that both thickness of the external oxides and depth to which internal oxides formed increased parabollically with increasing annealing time.

Poor reactive wetting was obtained for both alloys when using the lowest pO_2 273 K (–50 °C) dp process atmosphere due to the formation of thick, compact oxide layer on the steel surface, which formed a barrier between the substrate and Zn bath, preventing the required Fe dissolution from the substrate surface for the formation of the desired η-$Fe_2Al_5Zn_X$ interfacial phase. This is while a well-developed interfacial Fe-Al intermetallic layer, indicative of a good reactive wetting, was observed for both alloys when using the two higher pO_2 process atmospheres (i.e. 243 K (–30 °C) dp and 278 K (+5 °C dp)), due to the presence of either thinner film-like or plate/nodule-like oxides on the steel surface after annealing. This external oxide morphology

facilitated contact between the Zn-alloy bath and the substrate via a variety of mechanisms, including interfacial infiltration through cracks due to thermal coefficient of expansion mismatch between the external oxide and substrate as well as aluminothermic reduction, which resulted in Fe dissolution from the substrate and consequent formation of the Fe-Al intermetallics.

Moreover, the addition of 0.05 wt.% Sn to the Fe-0.1C-2Mn-1.7Si (wt.%) steel significantly improved the reactive wetting by the continuous galvanizing bath, which was found to be due to its beneficial effect on reducing the oxidation growth rate by segregating to the steel surface to about 150 times greater than its bulk concentration, occupying the potential sites for oxide nucleation, therefore altering the morphology of surface oxides. Under the lowest pO_2 273 K (−50 °C) dp process atmosphere, the addition of Sn reduced the compactness of the external granular MnO oxides and increased their size. Under the intermediate pO_2 243 K (−30 °C) dp process atmosphere, the addition of Sn altered the morphology of the surface oxides from large, thick and compact $MnSiO_3$ and SiO_2 particles to small, thin and less compact ones. Sn had its most significant effect on external oxide alteration under the highest pO_2 278 K (+5 °C) dp process atmosphere, which was exemplified by changing their morphology from film-like and fine, closely spaced nodule-like $MnSiO_3$ particles to big, widely spaced ones. The modified oxide morphology obtained due to the addition of Sn to the steel chemistry facilitated contact between the Zn-alloy bath and the substrate, thus resulted in the formation of smaller and more compact interfacial Fe-Al crystals and lower bare areas compared to the reference steel, therefore improved the reactive wetting during continuous galvanizing.

ACKNOWLEDGEMENTS

Table of Contents

Table of Figures

xii

List of Tables

Declaration of Academic Achievements

This dissertation was used to fulfill the requirement of Ph.D. degree. The major research for the dissertation was undertaken from January 2015 to December 2018. Over the course of this thesis study, I fulfilled theoretical and experimental research on selective oxidation and reactive wetting of two grades of advanced high strength steels during continuous hot-dip galvanizing. The major results of the research have been published in two accepted peer-review journal papers, one submitted manuscript peer-review journal and a draft manuscript for submission to an ISI journal, as listed below. I carried out the experiments, analyzed the results and wrote all four articles under the supervision of Dr. J.R. McDermid. It should be mentioned that the permission to reprint the published journal articles has been obtained from the owners of the copyright.

1. G. Seyed Mousavi, J.R. McDermid, Selective oxidation of a C-2Mn-1.3Si (Wt Pct) advanced high strength steel during continuous galvanizing heat treatments, Metall. Mater. Trans. A 49 A (2018) 5546-5560. https://doi.org/10.1007/s11661-018-4854-2.

2. G. Seyed Mousavi, J.R. McDermid, Effect of dew point on the reactive wetting of a C-2Mn-1.3Si (wt.%) advanced high strength steel during continuous galvanizing, Surf. Coat. Technol. 351 (2018) 11-20. https://doi.org/10.1016/j.surfcoat.2018.06.060.

3. G. Seyed Mousavi, B. Langelier, J.R. McDermid, Effect of Sn addition, process atmosphere pO_2 and annealing time on the selective oxidation of a C-2Mn-1.7Si (wt.%) advanced high strength steel during continuous galvanizing, Metall. Mater. Trans. A, Submitted (2018).

4. G. Seyed Mousavi, J.R. McDermid, Effect of annealing atmosphere pO_2 and Sn on the reactive wetting of a C-2Mn-1.7Si (wt.%) advanced high strength steel during continuous galvanizing, Draft Manuscript.

1. INTRODUCTION

1.1. Overall Context

Since the 1990s, there has been legislative demands on the car companies to improve fuel efficiency. As one of the main approaches to this end, steel industry has continuously developed new steel products in order to be able to reduce car weight via using thinner cross-sections of material. The observed increase in the use of advanced high strength steels (AHSS) in modern vehicles is the result of this challenge, which, due to possessing high strength and ductility, have satisfied this requirement [1,2]. Dual phase (DP) and low alloy Transformation Induced Plasticity (TRIP) steels are considered as being in the first generation (1G) AHSS with unique combination of high strength, good formability and high energy absorption capacity, deriving from their multi-phase microstructure. In order to achieve these properties, steel containing specific alloying elements such as carbon, manganese and silicon is subjected to well-designed heat treatments [3-8]. Carbon is responsible for stabilizing austenite and is a potent solid solution strengthener [9]. Manganese is an austenite stabilizer and a moderate solid solution strengthener [10]. Silicon, on the other hand, is a potent solid solution strengthener and plays a critical role in delaying carbide formation in TRIP alloys [8,11-13]

However, one of the most important challenges comes into play when protecting the integrity of these AHSSs from corrosion via continuous hot-dip galvanizing [14,15]. This challenge occurs due to the fact that oxides of alloying elements such as Si and Mn are thermodynamically stable under the commonly used industrial annealing atmosphere of N_2-(5-20 vol.%) H_2-H_2O and form on the surface and in the subsurface of the substrate, respectively known as external and internal oxidation. External oxides, depending on their morphology and chemistry, can make the

galvanizing process of DP and TRIP steels challenging due to their possible adverse effect on reactive wetting of the steel strip by the molten Zn-Al-Fe alloy during the continuous hot dip galvanizing process [16-25]. From the morphological point of view, a thick, compact oxide layer or small, closely-spaced oxide particles have been reported to act as a barrier between the substrate and Zn bath and subsequently avert the formation of the desired η-$Fe_2Al_5Zn_X$ interfacial layer, indicative of a good reactive wetting during continuous galvanizing. This is while steel surfaces covered with either thinner oxide layers or large, widely-spaced oxide particles have shown good reactive wetting [16-19,21,26]. Regarding oxide chemistry; on the other hand, Mn-rich oxides are shown to cause less severe wetting problems due to the beneficial kinetics of aluminothermic reaction by the bath dissolved Al [24,27,28]. Besides, it was proved thermodynamically that Mn-Si oxides could be reduced by the bath dissolved Al during continuous galvanizing [29]. On the other hand, Si containing oxides have been shown to result in poor reactive wetting during continuous galvanizing and are suggested to be avoided [30-34]. Both morphology and chemistry of the external oxides have proven to be altered by carefully manipulating the dissolved oxygen concentration on the steel surface using various techniques such as increasing the annealing atmosphere dew point at a given annealing temperature [16,18,21-23,35,36] and/or the addition of surface active elements to the steel composition [37-39].

1.2. Research Objectives

The majority of the studies to date have considered the effects of either annealing process atmosphere pO_2 [16,18,19,40-43] or steel chemistry [33,34,38,38,39,44,45] on the selective oxidation and reactive wetting of AHSSs by the continuous galvanizing bath. In addition, while understanding the kinetics of oxide formation during annealing prior to continuous galvanizing is

very important, as it leads to better management of the galvanizing process and higher quality products, there are few studies taking into account the role of annealing time on the surface oxide characteristics [46-48]. Thus, the objective of the present research is to conduct a comprehensive examination on the mutual effects of steel chemistry (e.g. Si/Mn ratio), annealing process atmosphere pO_2 (by varying the dew point) and annealing time on the selective oxidation and reactive wetting of two 0.1C-2Mn-Si (wt.%) advanced high strength steels with silicon contents of 1.3 and 1.7 wt.%. In particular, the effect of selective oxide chemistry, morphology and spatial distribution of the surface oxides on the reactive wetting and development of the desired η-$Fe_2Al_5Zn_X$ interfacial microstructure will be determined.

In order to assess the effect of surface active elements on oxide surface chemistry and morphology and the consequent reactive wetting during continuous galvanizing, a minor addition (0.05 wt.%) of Sn was made to the 0.1C-2Mn-1.7Si (wt.%) experimental steel and its effect was analyzed as a function of annealing atmosphere pO_2 and annealing time.

From the practical viewpoint, the project provided compositional and process information which will aid in process design of these industrially important alloys.

1.3. Thesis Layout

The remainder of this thesis consists of seven chapters as follows:

- Chapter 2 presents a comprehensive literature review on the current state of knowledge of the microstructure and mechanical properties of dual phase and transformation induced plasticity steels and their application in the automotive industry. The thermodynamics and kinetics of selective oxidation and the transition from internal to external oxidation are discussed. Reactive wetting during continuous hot-dip galvanizing and its relationship with the oxidation occurring during annealing has also been included.

- Chapter 3 reproduces the first accepted journal article entitled "Selective oxidation of a C-2Mn-1.3Si (wt.%) advanced high strength steel during continuous galvanizing heat treatments" published in Metallurgical and Materials Transaction A. The main contribution of this article is to address the effect of annealing process parameters, i.e. oxygen partial pressure and annealing time, on the selective oxidation of a Fe-0.1 C-2Mn-1.3Si (wt.%) AHSS. A comparison between the experimental observations and the Wagner model used to predict the selective oxidation mode was also made.

- Chapter 4 reproduces the second accepted journal article entitled "Effect of dew point on the reactive wetting of a C-2Mn-1.3Si (wt.%) advanced high strength steel during continuous galvanizing" published in Surface Coatings and Technology. This article links the reactive wetting of a Fe-0.1 C-2Mn-1.3Si (wt.%) AHSS and steel surface chemistry, external oxide morphology and annealing process atmosphere oxygen partial pressure, as previously discussed in Chapter 3.

- Chapter 5 reproduces a submitted journal manuscript entitled "Effect of Sn addition, process atmosphere pO_2 and annealing time on the selective oxidation of a C-2Mn-1.7Si (wt.%) advanced high strength steel during continuous galvanizing" submitted to Metallurgical and Materials Transaction A in 2018, in which a comprehensive investigation was performed on the combined effect of annealing parameters and the addition of 0.05 wt.% Sn on the thermodynamics and kinetics of oxide formation and growth during continuous galvanizing heat treatments for the subject 0.1C-2Mn-1.7Si (wt.%) alloy.

- Chapter 6 represents a draft manuscript of a journal article entitled "Effect of annealing atmosphere pO_2 and Sn on the reactive wetting of a C-2Mn-1.7Si (wt.%) advanced high strength steel during continuous galvanizing". The reactive wetting of the experimental steel

during continuous galvanizing in a Zn-(0.2 wt.% dissolved Al, Fe) bath was examined as a function of annealing atmosphere pO_2 and the addition of 0.05 wt.% Sn by determining a relationship between the external oxide characteristics and the coating microstructure and properties.

- Chapter 7 synthesizes the results reported in the previous chapters to highlight the significance of this Ph.D. research compared to the current state of knowledge and proposes ideas for future research.

- Chapter 8 summarizes the key findings of the research.

1.4. References

[1] C.M. Tamarelli, The evolving use of advanced high-strength steels for automotive applications, Steel Market Development Institute (2011).

[2] J. Galan, L. Samek, P. Verleysen, K. Verbeken, Y. Houbaert, Rev. Met. 48 (2012) 118-131.

[3] V.F. Zackay, E.R. Parker, D. Fahr, R. Busch, ASM Trans. Q.60 (1967) 252-259.

[4] P. Tsipouridis, "Mechanical properties of dual-phase steels", Ph.D. thesis, Technischen Universitat Munchen (2006).

[5] S. Oliver, T.B. Jones, G. Fourlaris, Mater. Sci. Technol. 23 (2007) 423-431.

[6] M.S. Rashid, Ann. Rev. Mater. Sci. 11 (1981) 245-266.

[7] H. Liu, F. Li, W. Shi, S. Swaminathan, Y. He, M. Rohwerder, L. Li, Surf. Coatings Technol. 206 (2012) 3428-3436.

[8] R. Kuziak, R. Kawalls, S. Waengler, Arch. Civ. Mech. Eng. 8 (2008) 103-117.

[9] P.J. Jacques, E. Girault, Ph. Harlet, F. Delannay, Iron Steel Inst. Japan Int. 41 (2001) 1061-1067.

[10] B.C. De Cooman, Curr. Opin. Solid State Mater. Sci. 8 (2004) 285-303.

[11] W. Bleck, S. papaefthymiou, A. Frehn, Steel Research Int. 75 (2004) 704-710.

[12] R.G. Davies, Metall. Trans. A. 10 (1979) 113-118.

[13] P. Jacques, E. Girault, T. Catlin, N. Geerlofs, T. Kop, S. van der Zwaag, F. Delannay, Mater. Sci. Eng. A 273-275 (1999) 475-479.

[14] S.M.A. Shibli, B.N. Meena, R. Remya, Surf. Coatings Technol. 262 (2015) 210-215.

[15] M. Guttmann: Mater. Sci. Forum 155-156 (1994) 527-548.

[16] L. Cho, S-J. Lee, M-S. Kim, Y-H. Kim, B.C. De Cooman, Metal. Mater. Trans. A 44A (2013) 362-371.

[17] S. Alibeigi, R. Kavitha, R.J. Meguerian, J.R. McDermid, Acta Mater. 59 (2011) 3537-3549.

[18] E.M. Bellhouse, "Galvanizing of Al-Si TRIP-assisted steels", Ph.D. thesis, McMaster University (2010).

[19] S. Alibeigi, "Short-term formation kinetics of the continuous galvanizing interfacial layer on Mn-containing steels", Ph.D. thesis, McMaster University (2014).

[20] S. Prabhudev, S. Swaminathan, M. Rohwerder, Corros. Sci. 53 (2011) 2413-2418.

[21] E.M. Bellhouse, J.R. McDermid, Metal. Mater. Trans. A 41A (2010) 1539-1553.

[22] E.M. Bellhouse, J.R. McDermid, Metal. Mater. Trans. A 42A (2011) 2753-2768.

[23] E.M. Bellhouse, J.R. McDermid, Metal. Mater. Trans. A 43A (2012) 2426-2441.

[24] M. Pourmajidian, J.R. McDermid, Metal. Mater. Trans. A 49A (2018) 1795-1808.

[25] M. Pourmajidian, J.R. McDermid, Iron Steel Inst. Japan Int. 58 (2018) 1635-1643.

[26] M. Blumenau, M. Norden, F. Friedel, K. Peters, Surf. Coat. Technol. 205 (2011) 3319–3327.

[27] R. Khondker, A. Mertens, and J.R. McDermid, Mater. Sci. Eng. A 463 (2007) 157–165.

[28] R. Kavitha, J.R. McDermid, Surf. Coatings Technol. 212 (2012) 152–158.

[29] Y.F. Gong, T.J. Song, H.S. Kim, J.H. Kwak, B.C. De Cooman, in Asia-Pacific Galvaniz. Conf., Seoul (2009).

[30] J. Mahieu, S. Claessens, B.C. De Cooman, Metall. Mater. Trans. A 32A (2001) 2905–2908.

[31] J. Maki, J. Mahieu, B.C. De Cooman, S. Claessens, Mater. Sci. Technol. 19 (2003) 125–131.

[32] M.S. Kim, J.H. Kwak, J.S. Kim, Y.H. Liu, N. Gao, N.Y. Tang, Metall. Mater. Trans. A 40A (2009) 1903–1910.

[33] Y. Kim, J. Lee, J. Park, S.-H. Jeon, Met. Mater. Int. 17 (2011) 607–611.

[34] K.-Ch. Lin Ch.-S. Lin, Iron Steel Inst. Japan Int. 54 (2014) 2380–2384.

[35] R. Sagl, A. Jarosik, D. Stifter, G. Angeli, Corr. Sci. 70 (2013) 268-275.

[36] G. Seyed Mousavi, J.R. McDermid, Surf. Coat. Technol. 351 (2018) 11-20.

[37] M. Pourmajidian, B. Langelier, J.R, McDermid, Metal. Mater. Trans A 49A (2018) 5561-5573.

[38] L. Cho, E.-J. Seo, G.-S. Jung, D.-W. Suh, B.C. De Cooman, Metall. Mat. Trans. A 47A (2016) 1705-1719.

[39] J. Oh, L. Cho, M. Kim, K. Kang, B.C. De Cooman, Metal. Mater. Trans. A 47A (2016) 5474-5486.

[40] L. Cho, G-S. Jung, B.C. De Cooman, Metal. Mater. Trans. A 45A (2014) 5158-5172.

[41] H. Liu, Y. He, S. Swaminathan, M. Rohwerder, L. Li, Surf. Coat. Technol. 206 (2011) 1237-1243.

[42] S.-K. Lee, J.-S. Kim, J.-W. Choi, N. Kang, K.-M. Cho, Met. Mater. Int. 17 (2011) 251-257.

[43] X.-S. Li, S.-I. Baek, C.-S. Oh, S.-J. Kim, Y.-W. Kim, Scr. Mater. 57 (2007) 113-116.

[44] Y. Takada, S. Shimada, J. Lee, M. Kurosaki, T. Tanaka, Iron Steel Inst. Japan Int. 49 (2009) 100-104.

[45] L. Cho, M-S. Kim, Y-H. Kim, B.C. De Cooman, Metal. Mater. Trans. A 45A (2014) 4484-4498.

[46] V.A. Lashgari, G. Zimbitas, C. Kwakernaak, W.G. Sloof, Oxid. Met. 82 (2014) 249-269.

[47] T.L. Baum, R.J. Fruehan, S. Sridhar, Metal. Mater. Trans. B 38B (2007) 287-297.

[48] R.M. Hudson, H.E. Biber, E.J. Oles, Jr., C.J. Warning, Metall. Trans. A 8A (1997) 1713-1719.

2   LITERATURE REVIEW

In order to select appropriate materials for automotive applications, several factors including safety, fuel efficiency, environmental friendliness, manufacturability and cost must be considered [1-3]. Among these factors, until recently, safety has been the most important concern for automotive companies due to the strict vehicle safety standards regulated by the Ministry of Transport (MOT) in Canada [4]. In this regard, automotive manufacturers initially used components, such as air bags and anti-lock braking systems (ABS) to enhance passenger safety. However, the addition of these components significantly increased the curb-side mass of vehicles. This resulted in higher fuel consumption, which had adverse impacts from both the economic and environmental points of view [1,3]. Thus, in 1994, a consortium of 35 steel sheet producers from 18 countries gathered to design a lightweight all-steel automotive body-in-white structure [5] by replacing conventional low-C steels with advanced high strength steels (AHSSs). This was the beginning of the large-scale use of the first generation of AHSSs (1G AHSSs), which have a better balance between strength and ductility versus conventional low carbon steels in automotive parts [3,6,7] (Figure 2.1). 1G AHSSs can be roughly divided into the following types:

- Dual Phase (DP)
- Complex Phase (CP)
- Martensitic Steel (MS)
- TRansformation- Induced Plasticity (TRIP) and
- Press Hardening Steel (PHS)
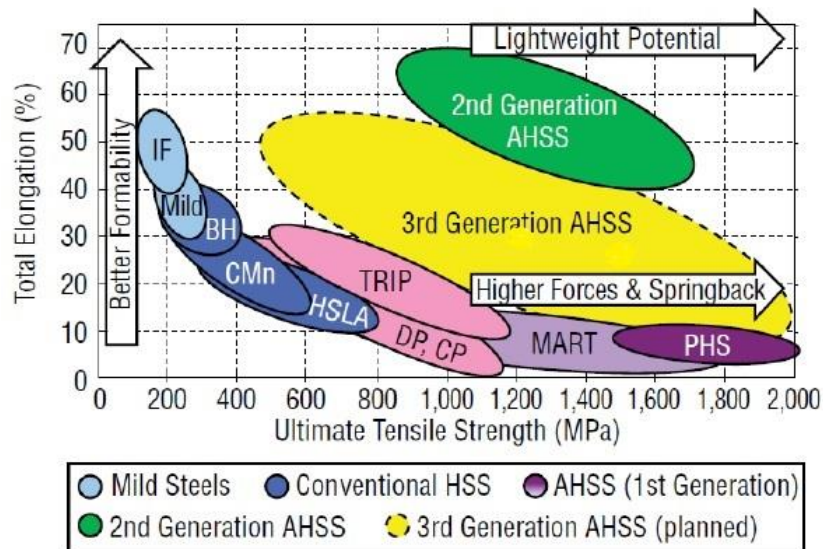
Figure 2.1: Comparison of conventional and the first generation of advanced high strength steels with regard to their ultimate tensile strength and total elongation [from 7].

1G AHSS mechanical properties, which are the result of their multi-phase microstructures, including a ferrite matrix with varying volume fractions of martensite, bainite, carbide free bainitic ferrite and/or retained austenite, allow automotive manufacturers to use thinner steel sheets while maintaining or enhancing vehicle mechanical and safety performance. Furthermore, due to AHSSs having a good combination of strength and ductility, in the competitive market of automotive materials, they keep pace with "light-weight" materials such as aluminium and magnesium alloys, plastics and composites in terms of specific strength [1-3].

Each of the aforementioned types of AHSS is used in specific automotive structural applications based on various considerations. One of the most important criteria is the ability of the material to carry the imposed dynamic and static loads, especially in crash events [1,3]. As shown in Figure 2.2 [8], there are two major structural zones in cars with completely different

safety requirements: i.e. the safety cage and crumple zones. The safety cage, which is the passenger compartment, has to meet the requirements of protecting the passengers by preventing any deformation or intrusions in the case of a low- to high-speed crash events. On the contrary, the crumple zones, which are located at the front and rear of the vehicle, need to be able to absorb energy during collisions. Thus, AHSSs with high work hardening rates, high strength and high ductility with a large area under their stress-strain curves are selected for this purpose [1,9].

Figure 2.2: Schematic of the two major crash zones of a vehicle [8].

2.1 DP and TRIP steel microstructure and mechanical properties

Dual Phase (DP) and TRansformation Induced Plasticity (TRIP) steels are amongst the first generation (1G) AHSS and offer an excellent combination of high ultimate tensile strength, superior formability and high energy absorption potential. This makes DP and TRIP steels the most widely used AHSS in the automotive industry due to providing significant mass reduction, increased fuel efficiency and enhanced vehicle safety [2,3,10,11]. The desired microstructure of both types of steels can be achieved by applying an appropriate heat treatment and a combination of alloying elements in the steel composition. The main alloying elements used in these steels are C, Mn and Si (0.06-0.5 wt.% C, 1.5-3 wt.% Mn), where DP and TRIP compositions are, respectively confined to the lower and higher ends of the ranges [12-14].

DP steels have a low yield to ultimate tensile strength ratio, high energy absorption capacity, a high early-stage strain hardening rate and homogeneous plastic flow. The DP steel microstructure, which is responsible for their unique properties, consists of a softer ferrite matrix embedded with martensite islands and (sometimes) a small amount of retained austenite and bainitic ferrite. The most common way of obtaining the desired DP steel microstructure of well-dispersed martensite islands in a recrystallized ferrite matrix is to intercritically anneal the ferrite-pearlite cold rolled steel sheet and then quench it at a sufficient minimum cooling rate to a temperature below the martensite finish temperature [12,15-18].

TRIP steels; on the other hand, usually contain ferrite, carbide-free bainitic ferrite, retained austenite and a small amount of athermal martensite [19-21]. They exhibit a better combination of strength and ductility than typically found in dual phase steels. This is because, in contrast to DP steels, they maintain their high work hardening rate at high strains [13,19-21]. This is brought about by applying the annealing heat treatment and selecting the steel composition in a way to provoke the so-called TRIP effect, in which high carbon retained austenite gradually transforms to martensite during deformation. The gradual transformation of retained austenite to martensite maintains the instantaneous work hardening rate at high values of stress and strain, thereby retarding the onset of necking. The appropriate heat treatment for this purpose includes heating the steel to the intercritical annealing (IA) temperature, rapidly cooling it to the isothermal bainitic transformation (IBT) temperature, holding for tens of seconds at the IBT and cooling to room temperature below a critical rate. The process is designed to stabilize the retained austenite by enriching it with carbon through the formation of bainitic ferrite in the microstructure during the IBT [20]. In order to stabilize the austenite, higher amounts of manganese and carbon are required than those typically used in DP steels. Also, the silicon

content has to be high enough (>1 wt.%) to delay cementite precipitation during the IBT [21]. However, as will be discussed in detail later, high levels of silicon can lead to poor coating quality during continuous galvanizing. In order to overcome this problem, it has been suggested to partially or totally replace silicon by aluminium which has a similar capability of delaying cementite formation [22,23] during the IBT but has only a mild solid solution strengthening effect.

2.2   Continuous Galvanizing

2.2.1   *Overview of the industrial continuous hot-dip galvanizing process*

Steels readily corrode when exposed to ambient environments, particularly humid or aqueous enviroments with significant chloride concentrations, as commonly encountered in Canadian winter road environments. Protecting steels from corrosion can be done via barrier protection and/or galvanic protection.

Zinc coatings are of great interest to the automotive industry for steel corrosion protection due to their two-fold barrier and galvanic protection nature. Applying zinc coatings to steel sheet can be done by continuous hot- dip galvanizing which compared to other possible techniques, has been reported to offer the most cost effective light, strong and formable coating [24,25]. Figure 2.3 shows a schematic of the continuous galvanizing line (CGL). Prior to entering the annealing furnace, the steel sheet is cleaned and made free of metallic debris (primarily Fe fines from previous processing) and organic contaminants (primarily oils). After being subjected to an appropriate annealing heat treatment to control the steel microstructure and mechanical properties, it is cooled to the zinc bath temperature (typically 733 K (460 °C)) and is finally immersed into the zinc bath for a few seconds, during which the reaction between the substrate and the liquid bath results in the formation of the coating layer via a reactive wetting mechanism

(to be discussed below). High pressure air or nitrogen is blown onto the steel sheet via slot jets upon exiting the zinc bath in order to control the coating thickness. The coating is then cooled and subjected to finishing operations such as temper rolling, tension leveling, the application of dry lubricants, oiling and finally recoiling and packaging for shipment [26,27].
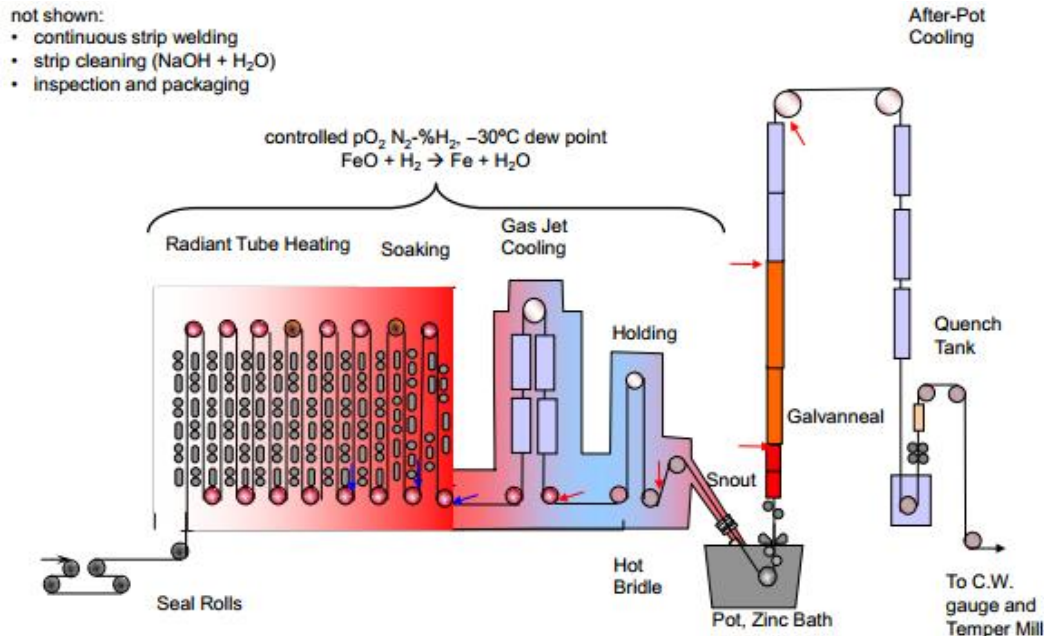
Figure 2.3: Schematic showing CGL line [Courtesy of Mr. E.A. Silva (2005)].

2.3 Selective Oxidation

2.3.1 Thermodynamics of selective oxidation

Annealing DP and TRIP steels in the continuous galvanizing process is performed in a N_2-(5-20 vol.%) H_2 atmosphere with a controlled dew point (i.e. fixed water vapour content) in which the native iron oxides, i.e. iron oxides formed during previous processing steps, are reduced. However, the oxygen potential in these atmospheres are sufficient for the oxidation of alloying

elements with more stable oxides. Oxidation of the general alloying element M occurs in these process atmospheres according to the reaction:

$$\frac{x}{y}M(s)+H_2O(g)=\frac{1}{y}M_xO_y(s)+H_2(g) \tag{2.1}$$
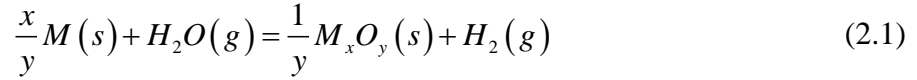
which is the sum of two chemical reactions:

$$H_2O(g)=H_2(g)+\frac{1}{2}O_2(g) \tag{2.2}$$

$$\frac{x}{y}M(s)+\frac{1}{2}O_2(g)=\frac{1}{y}M_xO_y(s) \tag{2.3}$$
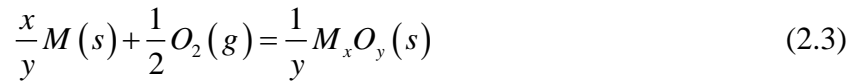
where the free energy change for the general reaction i is given by:

$$\Delta G_i = \Delta G_i^o + RT\ln K_i \tag{2.4}$$

and where ΔG_i is the Gibbs free energy of formation for reaction i at the reaction temperature T, ΔG_i^o is the standard Gibbs free energy of formation at temperature T, R is the universal gas constant and K_i is the reaction i equilibrium constant at T. Assuming that the oxide formed in reaction (2.3) is a pure condensed species, $K_{2.3}$ can be written as:

$$K_{2.3}=\frac{a_{M_xO_y}^{1/y}}{a_M^{x/y}\,p_{O_2}^{1/2}}=\frac{1}{a_M^{x/y}\,p_{O_2}^{1/2}} \tag{2.5}$$

At equilibrium (i.e. $\Delta G_{2.3}=0$), it is possible to write the free energy change for reaction (2.3) as:

$$\Delta G_{2.3}^o=-RT\ln\frac{1}{a_M^{x/y}P_{O_2}^{1/2}} \tag{2.6}$$

Per reactions (2.1) and (2.2), the oxygen to form the metallic oxide M_xO_y during CGL annealing (reaction (2.3)) is provided by the dissociation of H_2O vapour in contact with the

metallic species M in the annealing atmosphere where, for 1 mole of water vapour in reaction (2.2):

$$K_{2.2} = \frac{P_{H_{2(g)}} P_{O_{2(g)}}^{1/2}}{P_{H_2O_{(g)}}} \tag{2.7}$$

The partial pressure of H_2O (g) is often described using the dew point temperature (T_{dp} in °C), defined as the temperature (T_{dp}) at which the following reaction is at equilibrium:

$$H_2O(l) = H_2O(g) \tag{2.8}$$

for which:

$$\Delta G_{2.8}^{o} = -RT_{dp} \ln K_{2.8} \tag{2.9}$$

and, if it is assumed that H_2O (l) in equation (2.10) is a pure condensed species and its activity equals unity:

$$K_{2.8} = \frac{P_{H_2O_{(g)}}}{a_{H_2O_{(l)}}} = P_{H_2O_{(g)}} \tag{2.10}$$

As in an experimental atmosphere, pH_2 and pH_2O are fixed, pO_2 is the only temperature variant thermodynamic descriptor of the process atmosphere (reaction (2.3)).

The process atmosphere oxygen partial pressure as a function of annealing temperature and dew point for a N_2-5 vol.% H_2 atmosphere is shown in Figure 2.4. The effect of activity of the alloying element in the steel solution is also shown for Mn. The Mn activity of 0.012 was chosen as it is approximately the activity of Mn in one of the experimental alloys (Fe-0.1C-2Mn-1.3Si (wt.%)) at the intercritical annealing temperature of 1093 K (820 °C), as calculated using THERMO-CALC software and the TCFE2 database (Thermo- Calc database for Fe-alloys, version 2.0) using the local equilibrium-non partitioning (LE-NP) formalism. Figure 2.4 indicates that, although a typical annealing atmosphere of N_2-5 vol.% H_2 with dew points in the

range of 223 K (–50 °C) to 278 K (+5 °C) is reducing for iron oxides, its oxygen partial pressure

with respect to the major alloying elements Mn and Si in 1G AHSSs is sufficient to form stable

oxides. The phenomenon of the formation of alloying element oxides in a process atmosphere

reducing to iron oxides is commonly referred to as selective oxidation [28]. Depending on

whether the inward flux of oxygen is higher than the outward flux of the alloying element or vice

versa, selective oxidation can be divided into two types: external selective oxidation and internal

selective oxidation [29].
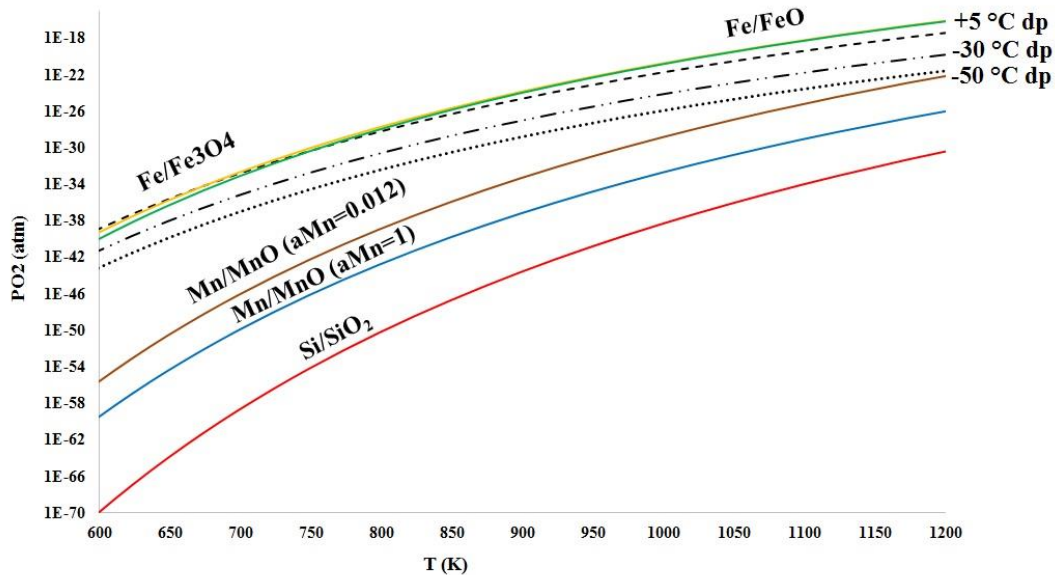
Figure 2.4: Thermodynamic stability of Si, Mn and Fe oxides with respect to annealing temperature and oxygen partial pressure.

2.3.2   Kinetics of Oxidation

In simple reactions, oxidation kinetics follow logarithmic, linear or parabolic models [30].

Logarithmic model is representative of oxidations which occur at temperatures below 673 K

(400 °C) and in the case of the formation of oxide film with a thickness of 100 nm or less, and is

shown by either of the following equations, which are used for direct and inverse logarithmic models, respectively [30]:

$$X = k_{\log} \log(t)$$
$$\frac{1}{X} = -k_{inv} \log(t)$$

(2.11)

Here, X can be the oxide's thickness or mass, or the amount of oxygen consumed per surface area, etc, k_{log} and k_{inv} are the direct and inverse logarithmic rate constant, respectively and t is time.

Linear kinetics confines to the oxidations occur at the metal surface or phase boundaries, where the oxide is either porous and non-protective, highly volatile, or cracked and spalled off, or when it melts and forms eutectic phases with the substrate [31].

In the linear model, the rate (k_l) is constant with time (equation (2.12)) [30],

$$X = k_l t$$

(2.12)

Parabolic kinetics, on the other hand, model the oxidations occur at high temperatures, where the rate determining factor during the process is the diffusion of cations and/or anions, as well as the electrons through a compact oxide film [32]. Assuming that the growth of an oxide layer is controlled by the transport of cations, the following equity is satisfied between the the outward diffusion flux of cations ($J_{M^{+2}}$) and the inward flux of vacancies (J_{V_M}) [30]:

$$J_{M^{+2}} = -J_{V_M} = D_{V_M} \frac{C''_{V_M} - C'_{V_M}}{X}$$

(2.13)

where D_{V_M} is the diffusion coefficient of the cation vacancies and C''_{V_M} and C'_{V_M} are their concentrations at the oxide/substrate and oxide/gas interfaces, respectively. Having equilibrium at each interface and a constant value for $C''_{V_M} - C'_{V_M}$, equation (2.13) can be written as [30]:

$$J_{M^{+2}} = \frac{1}{V_{ox}} \frac{dX}{dt} = D_{V_M} \frac{C''_{V_M} - C'_{V_M}}{X} \qquad (2.14)$$

where V_{ox} is the molar volume of the oxide. By naming $D_{V_M} V_{ox} (C''_{V_M} - C'_{V_M})$ as k_P (rate

constant) and integrating equation (2.14) and considering $X=0$ at $t=0$, parabolic kinetics can be

modelled by the following equation [30]:

$$X^2 = k_p t + C \qquad (2.15)$$

It is worth to mention that the aforementioned models represent ideal cases and usually

oxidation behaviour can be explained by the combination of the aforementioned models [31,33].

2.3.3   Wagner Model and its Modifications

The first model to predict the transition from internal to external selective oxidation was

proposed by Wagner [29]. He suggested that, for a single crystal metallic binary *M-X* alloy in

which M is the noble matrix and X the selectively oxidized solute element, the following

relationship for transition from internal to external oxidation is established:

$$N^0_{x,crit} = \left[\frac{\pi g^* V_m N^S_O D_O}{2n V_{XO_n} D_X} \right]^{1/2} \qquad (2.16)$$

where:

- $N^0_{x,crit}$ is the critical mole fraction of the alloying element *X* that, if the bulk concentration of

  X exceeds this, will result in the transition from internal to external oxidation;

- g^* is the critical volume fraction of the oxide in the matrix which blocks the inward flux of

  oxygen and results in the transition from internal to external oxidation, initially determined

  to be 0.3 by Rapp [34] for a Ag-In alloy and later determined experimentally as 0.2 by

  Lashgari et al. [35] for austenitic Fe-Mn alloys;

- N_O^S is the oxygen molar concentration at the external surface;

- V_M, V_{XO_n} are molar volumes of the alloy and the metallic oxide, respectively;

- n is the stoichiometric ratio between oxygen and X atoms in the oxide;

- and D_O and D_X are the bulk diffusion coefficients for oxygen and selectively oxidized alloying element X, which can be computed using the following equations, respectively:

$$D_O = D_O' \exp\left(\frac{-Q_O}{RT}\right) \tag{2.17}$$

$$D_X = D_X' \exp\left(\frac{-Q_X}{RT}\right) \tag{2.18}$$

Here, Q_O, Q_X are the activation energies for the diffusion of oxygen and the alloying element X, respectively, D_O', D_X' are their pre-exponential factors, T is the absolute temperature and R is the universal gas constant.

Internal selective oxidation occurs if the following conditions are satisfied [30]:

- the inward flux of oxygen is greater than the outward flux of the oxide-forming solute X;

- $N_X^0 < N_{X,crit}^0$;

- the formation of XO_n is thermodynamically favourable;

- no film or layer at the surface of the alloy blocks the inward flow of oxygen at the start of oxidation and;

- the solubility of oxygen in the matrix must be high enough in order to provide negative values for the Gibbs energy of the reaction $\underline{X} + n\underline{O} = XO_n$, in which $\underline{O}$ is dissolved oxygen in the alloy matrix.

External selective oxidation, on the other hand, occurs when the outward flux of the alloying element is greater than the inward flux of oxygen and $N_X^0 \geq N_{X,crit}^0$.

However, Wagner's model has several assumptions which makes it inappropriate to be used as a general model for all alloy systems. These include the following: (i) the selective oxidation behaviour was modelled for a single crystal binary alloy, (ii) the formed oxide was assumed to have a zero solubility product (K_{sp}) in the matrix and (iii) the internal oxide was assumed to have a spherical morphology [36].

Several modifications have been proposed to the classic Wagner model to make it more applicable to practical alloy systems. One of these modifications was proposed by Mataigne et al. [37], who considered the fact that oxygen and alloying elements can diffuse much faster through short circuit diffusion paths such as grain boundaries and dislocation pipes than in the lattice. In their proposed model, grain boundary oxidation was considered by assuming that the activation energy for grain boundary diffusion was half the value of that for bulk diffusion, as given by:

$$N_{X,crit,GB}^{O} = \left[\frac{\pi g^* V N_O^S D_O' \exp(\frac{-Q_O}{2RT})}{2 n V_{XO_n} D_X' \exp(\frac{-Q_X}{2RT})} \right]^{1/2} \quad (2.19)$$

Second, due to the fact that Wagner's model was proposed for binary alloys, it was assumed that a single oxide formed. Mataigne et al. [37] further modified the model by assuming that the effect of alloying elements on the inward diffusion of O was additive, resulting in the following criterion for the internal-external oxidation transition:

$$\sum_N N_X^0 (n D_X V_{XO_n})^{1/2} \geq (\frac{0.3 \pi V N_O^S D_O}{2})^{1/2} \quad (2.20)$$

where, if the inequality is satisfied, external selective oxidation will occur.

Third, Wagner neglected to consider the effect of different phases in the alloy microstructure on the internal to external oxide transition. Shastry et al. [38] proposed a model to address this issue in ferrous alloys by taking into account the differing diffusion rates of oxygen and the alloying elements in austenite (γ) and ferrite (α). Their modification to the Wagner model dictated that external selective oxidation will occur when the following inequality is satisfied:

$$f\left[\sum N_X^0 (nD_X V_{XO_n})^{1/2}\right]_\gamma + (1-f)\left[\sum N_X^0 (nD_X V_{XO_n})^{1/2}\right]_\alpha \geq \left[\frac{0.3\pi V}{2}\right]^{1/2}\left\{\left[f\left[N_O^S D_O\right]^{1/2}\right]_\gamma + \left[(1-f)\left[N_O^S D_O\right]^{1/2}\right]_\alpha\right\} \quad (2.21)$$

where f is the volume fraction of austenite. Using the above equations and inequalities, it is possible to predict the selective oxidation behaviour of individual alloying elements in α-Fe and γ-Fe for a specific annealing atmosphere and temperature considering both bulk and grain boundary diffusion.

2.4   Reactive wetting

As will be discussed in the following sections of this chapter, after immersing the steel into the continuous galvanizing bath, whether any reaction product was formed at the zinc/substrate interface and their composition, size and distribution (if formed) indicate the quality of the coating. Thus, it is worth to briefly explain different thermodynamic conditions that might occur during this process.

In a solid (*s*)-liquid (*l*)-vapor (*v*) system, when the gravitational force is neglected, equation (2.22), suggested by Young [39], shows the relationship between the horizontal components of the interfacial tensions (γ) of each two phases:

$$\gamma_{sv} - \gamma_{sl} = \gamma_{lv}\cos\theta \quad (2.22)$$

where θ is the equilibrium contact angle, as shown in Figure 2.5.
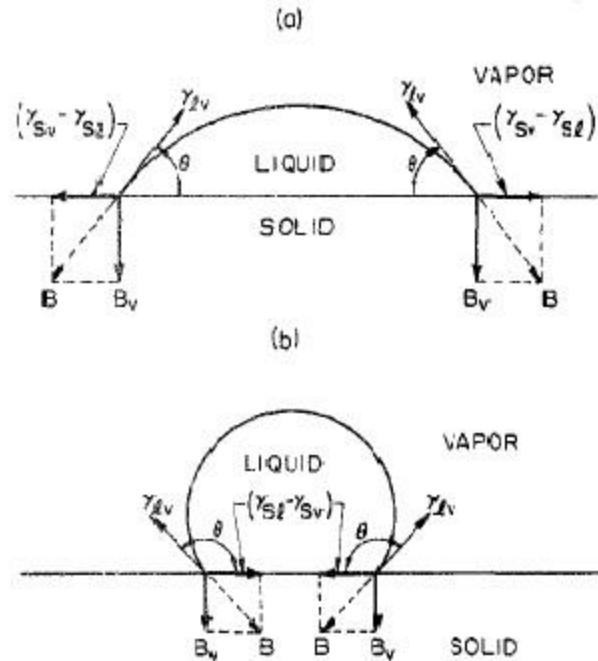
Figure 2.5: Components of forces present in a solid-liquid-vapor system with an (a) acute and (b) obtuse contact angle. B is the balancing force equal and of opposite direction to Υ_{lv} [40].

The degree of wetting of the solid by the liquid phase, in such a system can be defined based on the conditions of thermodynamic equilibrium (i.e. minimum free energy). Two types of conditions can be considered. Chemical equilibrium condition and chemical non-equilibrium condition.

Under chemical equilibrium conditions, the free energy changes in the system is directly related to the changes in the interfacial areas. In this case, the equilibrium contact angle can be determined by the values of the interfacial tensions between the phases in the system, using the Young's equation (equation (2.22)).

Under chemical non-equilibrium conditions, on the other hand, free energy changes depend on both changes in mass and changes in the interfacial areas. First stage of the chemical reaction is confined to the mass transfer through the interface, which results in a reduction in the

interfacial free energy and thus, the free energy of the system by $-\Delta G/A$ (ΔG is the change in the free energy and A is the interfacial area). When the chemical reaction completes at the interface, it proceeds into the bulk region by diffusion, during which the values of interfacial tension and the specific interfacial free energy change, till they reach their static values when the reaction completes.

2.5   The Zn(Al,Fe) bath

In order to prevent the formation of brittle Fe-Zn intermetallics and improve the formability of zinc-based metallic coatings, small amounts of aluminium are added to the zinc bath [41]. Table 2.1 shows the thermodynamic characteristics of intermetallic phases which can form during continuous galvanizing of a steel substrate in a Zn (Al, Fe) bath. As can be seen, the Gibbs free energy of the Fe-Al intermetallic phases is signficantly more negative than that of Fe-Zn intermetallic phases. Thus, formation of brittle Fe-Zn intermetallics is temporarily inhibited by the formation of the η-$Fe_2Al_5Zn_X$ interfacial layer. This interfacial layer is known industrially as the inhibition layer, since it "inhibits" the reaction of Fe with Zn, thereby retarding the formation of undesirable Fe-Zn intermetallics [25]. It is noteworthy that aluminium exists in two forms in the zinc bath. Some Al is dissolved in the liquid zinc (dissolved Al, known industrially as the effective Al), and the remaining Al is partitioned to the intermetallic particles commonly referred to dross and is removed as a waste product of the CGL process. Only the dissolved Al takes part in interfacial layer formation [42]. It should be pointed out that, although the formation of Fe-Zn intermetallics can be delayed by the addition of aluminium to the continuous galvanizing bath, it cannot be completely prevented. Given sufficient reaction time with the liquid Zn (Al, Fe) bath, inhibition breakdown occurs, resulting in the destruction of the Fe-Al interfacial layer and growth of Fe-Zn intermetallics. In this process, zinc atoms diffuse into the

steel substrate through the η-Fe$_2$Al$_5$Zn$_X$ interfacial layer, saturate the steel with Zn (first along triple points and grain boundaries in the steel due to the higher diffusion rates through these paths), followed by the nucleation of ζ-FeZn$_{13}$ at the grain boundaries and lateral growth of the Fe-Zn phases based on their Gibbs free energy of formation [25,43].

Table 2.1: Characteristics of Fe-Al and Fe-Zn intermetallic phases [44,45]

Phase	Crystal Lattice	ΔH (kJ/mol)	ΔG (450°C) (kJ/mol)
ζ-FeZn$_{13}$	Monoclinic	-11.7	-2.8
δ-FeZn$_{10}$	Hexagonal	-11.5	-3.5
τ1-Fe$_5$Zn$_{25}$	FCC	-11.7	-4.1
τ-Fe$_3$Zn$_{10}$	BCC	-10.9	-4.2
θ-FeAl$_3$	Monoclinic	-35.1	-30
η-Fe$_2$Al$_5$	Orthorombic	-34.6	-32
ζ-FeAl$_2$	Rhombohedral		-31
α-FeAl	BCC		-32

Figure 2.6 depicts the zinc rich corner of Zn-Al-Fe ternary phase diagram [46]. Since Fe is not in equilibrium with the Zn-Al-Fe bath, as soon as the steel strip is immersed into the bath, the bath approaches metastable equilibrium in the vicinity of the steel strip. This results in continuous Fe dissolution from the steel strip. Thus, a local supersaturation of Fe is created adjacent to the steel substrate, as shown in Figure 2.7 [47]. This is followed by the nucleation and lateral growth of the η-Fe$_2$Al$_5$Zn$_X$ or ζ-FeZn$_{13}$ on the steel surface depending on the amount of dissolved aluminium of the zinc bath, since the global equilibrium configuration of the zinc bath has to be obeyed in the longer term.
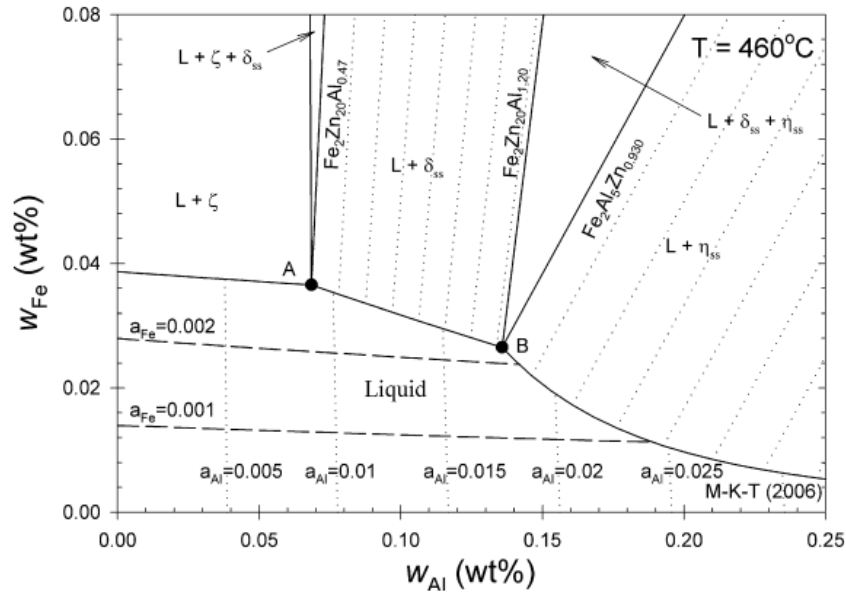
Figure 2.6: Zinc rich corner of the Zn-Al-Fe phase diagram; L: liquid, δ: FeZn$_{10}$, ζ: FeZn$_{13}$ and η-Fe$_2$Al$_5$Zn$_X$. Isoactivity lines of Al and Fe in the liquid phase (with respect to their solid state) are shown on the diagram [46].
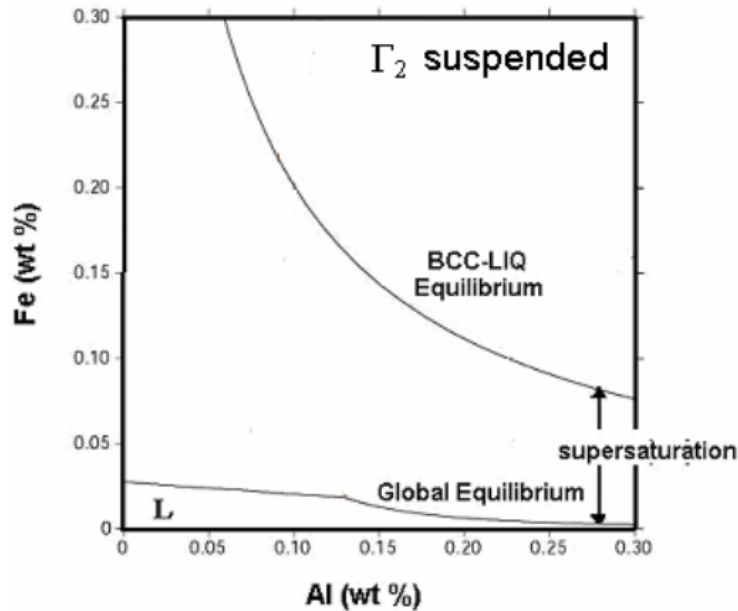
Figure 2.7: Supersaturation of Fe in the Zn (Al, Fe) bath at 450°C [47].

According to Figure 2.6, for the 0.2 wt.% dissolved aluminium bath to be used in this study, η-Fe$_2$Al$_5$Zn$_X$ is the stable phase, which is also in equilibrium with α-Fe [46] and forms at the coating/substrate interface during immersion in the Zn-Al-Fe bath. There is general agreement that upon dissolution of Fe from the steel strip into the Zn-Al bath, a thin (100-200 nm) layer of η-Fe$_2$Al$_5$Zn$_X$ intermetallics nucleates on the substrate from the supersaturated solution and rapidly grows by diffusional transport of Fe through the intermetallic layer. However, in a series of experiments with carefully controlled reaction times, Chen et al. [48] have advocated that the initial intermetallic to form was FeAl$_3$, resulting in a compact layer of fine crystals on the surface of the steel. Although this layer prevented Fe from further dissolution, diffusion of Fe towards the zinc bath and diffusion of Al and Zn towards the substrate transformed the FeAl$_3$ to the η-Fe$_2$Al$_5$Zn$_X$ intermetallic via the following reaction:

$$FeAl_3 + 2Al_{(bath)} + Fe_{(substrate)} + xZn_{(bath)} \rightarrow Fe_2Al_5Zn_x \qquad (2.23)$$
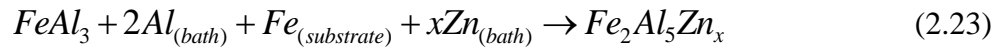
Further growth of this layer is accomplished via diffusion of Fe and Al species. This process is essential for the reactive wetting of the steel substrate by the liquid zinc alloy bath in order to obtain a highly formable, defect free metallic zinc coating.

According to Figure 2.6, at 733 K (460 °C), additions of above 0.136 wt.% aluminium to the zinc bath should result in the formation of η-Fe$_2$Al$_5$Zn$_X$ as the equilibrium phase [46]. However, for full inhibition to occur, the dissolved aluminium content usually needs to exceed 0.15 wt.% [49]. It has been reported by Tang [49] that, in the case of adding 0.135-0.15 wt.% Al to the continuous galvanizing bath, η-Fe$_2$Al$_5$Zn$_X$ and ζ-FeZn$_{13}$ coexist at the steel-coating interface. This is thought to be a result of an increase in Fe content adjacent to the steel strip due to Fe dissolution into the bath pushing the local bath composition into the L+δ-FeZn$_{10}$ region. This

reaction/diffusion path is shown as path 3 in Figure 2.8 [43]. The existence of ζ-FeZn$_{13}$ is likely due to its lower Gibbs free energy of formation versus that of δ-FeZn$_{10}$ as well as the well-known epitaxial relationship between ζ-FeZn$_{13}$ and α-Fe [25].
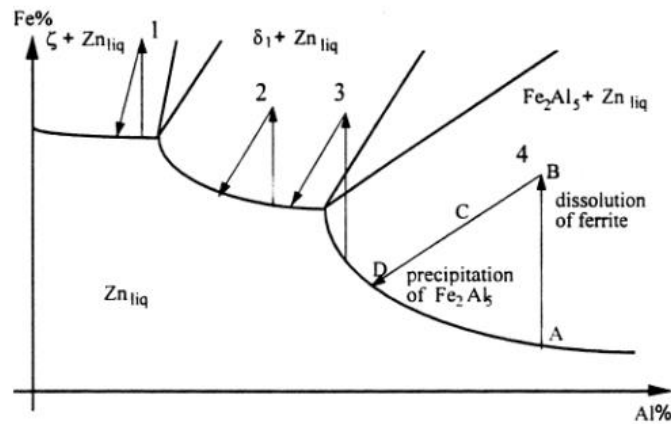
Figure 2.8: Schematic of the zinc corner of Zn-Al-Fe phase diagram showing the effect of Fe dissolution on changing the local composition of the bath adjacent to the steel strip [43].

2.6 The realationship between selective oxidation and reactive wetting in DP and TRIP steels

As mentioned above, the selective oxidation of alloying elements such as Mn and Si during annealing prior to continuous galvanizing can be challenging with regard to reactive wetting by the continuous galvanizing bath. Although the commonly used N$_2$-H$_2$ protective atmosphere is thermodynamically reducing with respect to any iron oxides which may be present on the steel surface, the atmosphere pO$_2$ is sufficient for Si and Mn to oxidize (Figure 2.4). Two main factors control the final coating quality of the substrate by the continuous galvanizing bath.

2.6.1 Oxide Chemistry

It has been well established that the presence of external MnO on AHSS surfaces causes less severe reactive wetting problems [50-52]. This is while the presence of SiO$_2$ and Mn-Si mixed

28

oxides can lead to poor reactive wetting of the steel substrate during continuous galvanizing [53-57].

One of the main mechanisms suggested for the formation of a well-developed interfacial layer despite the existence of external MnO is aluminothermic reduction by the dissolved Al in the Zn (Al, Fe) bath, based on the following reaction:

$$3MnO_{(solid)} + 2Al_{(solution)} \rightarrow Al_2O_{3(solid)} + 3Mn_{(solution)} \tag{2.24}$$
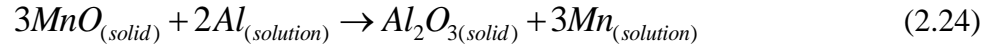
This was first suggested by Khondker et al. [51] as a mechanism which gives rise to a direct contact between the steel substrate and the molten Zn (Al, Fe) bath and consequently the occurrence of the reactive wetting as exemplified by the formation of a well-developed η-$Fe_2Al_5Zn_x$ interfacial layer. Liu et al. [58] cited the formation of Fe-Zn intermetallics (specifically ζ-$FeZn_{13}$) on the interfacial layer as implicit proof for the occurrence of aluminothermic reduction during continuous hot- dip galvanizing of a 0.11C-1.72Mn-0.38Si-0.05Al (wt.%) and 0.12C-1.62Mn-0.3Si-0.04Al-0.39Cr (wt.%) DP steels in a 0.2 wt.% dissolved Al bath. They proposed that the consumption of dissolved aluminium by the reduction of MnO and its local depletion was responsible for the precipitation of Fe-Zn intermetallics. Bellhouse and McDermid [22] also observed ζ-$FeZn_{13}$ at the steel/coating interface after continuous hot dip galvanizing of a 0.2C-1.5Mn-0.5Si-1.0Al (wt.%) TRIP-assisted steel in a 0.2 wt.% dissolved Al bath for which full inhibition was expected.

Aluminothermic reduction reaction of MnO in the continuous galvanizing bath was later validated by Kavitha and McDermid [52], who investigated the in-situ aluminothermic reduction of a MnO film formed at the surface of a 5.1 wt.% Mn steel by dissolved Al in the continuous galvanizing bath. The authors observed a significant reduction in MnO thickness during immersing in the bath. The presence of a thin layer of Al_2O_3 at the MnO-Zn interface with Mn

dissolving into the Zn-alloy bath was consistent with reaction (2.24) and further confirmed the previously proposed mechanism. It is noteworthy that no Fe-Al interfacial layer was observed at the steel-zinc interface in their study, indicating that the consumption of dissolved Al via the formation of η-$Fe_2Al_5Zn_X$ was prevented.

However, it must be cautioned that the kinetics of aluminothermic reduction determine its effectiveness in aiding reactive wetting. For example, Alibeigi et al. [26,59,60] studied the effect of external MnO thickness on reactive wetting by monitoring wetting force versus time for a series of Mn-containing steels. They showed that the wetting force was directly related to the thickness of the MnO film formed at the surface of the steel. The relatively thin MnO oxide layer present on the steels containing lower amounts of manganese could be reduced aluminothermically. The excess Al could further contribute to the formation of the η-$Fe_2Al_5Zn_X$ interfacial layer. This is while additional dissolved Al was needed to reduce thicker MnO oxides observed on steels with higher contents of manganese. This resulted in the local depletion of dissolved Al, thereby giving rise to the formation of Fe-Zn intermetallics. The thicker the MnO films, the higher the population of Fe-Zn intermetallics, as shown in Figure 2.9.

In addition, Gong et al. [61] and Liu et al. [62], respectively, proposed reduction of Mn-Si mixed oxides and Cr oxides by dissolved Al during continuous galvanizing. It should be pointed out that the occurrence of these processes , athough thermodynamically favourable, have not been proven experimentally, nor have any kinetic data for the reduction reactions been published.

2.6.2   *Oxide morphology*

The morphology and distribution of the surface oxides as influenced by the annealing atmosphere have also been reported to significantly affect the reactive wetting of the steel by the

molten Zn (Al, Fe) bath [22,23,50,55,58,63-70]. Bellhouse and McDermid [22] studied the effect of the atmosphere oxygen partial pressure on the reactive wetting of a 0.2C-1.5Mn-0.5Si-1.0Al (wt.%) TRIP-assisted steel. They reported good reactive wetting for a steel annealed under the lowest pO_2 process atmospheres of 220 K (–53 °C) dp and 243 K (–30 °C) dp as a result of the formation of the presence of a mixture of thin film-like and nodule-like surface oxides easing the desired reaction of dissolved Fe, Zn and Al to form the η-$Fe_2Al_5Zn_X$ interfacial layer. This is while increasing the atmosphere pO_2 using 278 K (+5 °C) dp resulted in the formation of relatively thick, localized film-like oxides, which acted as a barrier and prevented the complete dissolution of the MnO layer by aluminothermic reduction reaction and consequently deteriorated the coating quality. Cho et al. [64] related the presence of a discontinuous η-$Fe_2Al_5Zn_X$ interfacial layer with Fe-Zn intermetallics in between, as is indicative of poor reactive wetting, to the formation of thick, film-like oxides on the surface during annealing the 2.2Mn-1.4Si (wt.%) TRIP steel under the lower pO_2 process atmosphere of 213 K (–60 °C) dp. They showed that raising the annealing atmosphere pO_2 via increasing the atmosphere dew point to 263 K (–10 °C) and 278 K (+5 °C) improved the reactive wetting due to the formation of a thinner oxide layer on the steel surface.

Recently, Sagl et al. [67] have argued that the amount of Mn-oxides which could be reduced by aluminothermic reaction is restricted by the just-formed Al oxide which surrounds the partially reduced oxides and suppresses further dissolved Al diffusion to the Mn-oxides. It is noteworthy that this is in contradiction with what was reported by Kavitha and McDermid [52], who determined that the MnO layer thickness decreased continuously with reaction time in the presence of Al_2O_3 at the MnO/Zn alloy interface as a product of the aluminothermic reduction by the dissolved Al present in the continuous hot dip galvanizing bath.

Sagl et al. [67] have also suggested the flaking of Mn-oxides by the growth of Fe-Al intermetallic phases and the trapping of nodular Mn-Si oxides by Fe-Al crystals as two supplementary mechanisms contributing to the improved galvanizability of a series of steels including DP, mild and low-alloyed steels with varying amounts of Si and Mn. These two mechanisms are shown in Figure 2.10. This is in agreement with Bellhouse and McDermid [22,23] and Bellhouse [68], who had previously reported flaking of the oxides as a mechanism for enhancing reactive wetting of oxidized surfaces. For example, it was observed that cracking of Al_2O_3 films and removal of MnO nodules on MnAl TRIP steels had occurred and promoted good reactive wetting by allowing the dissolved Al in the bath to reach the substrate and form the η-$Fe_2Al_5Zn_X$ interfacial layer.
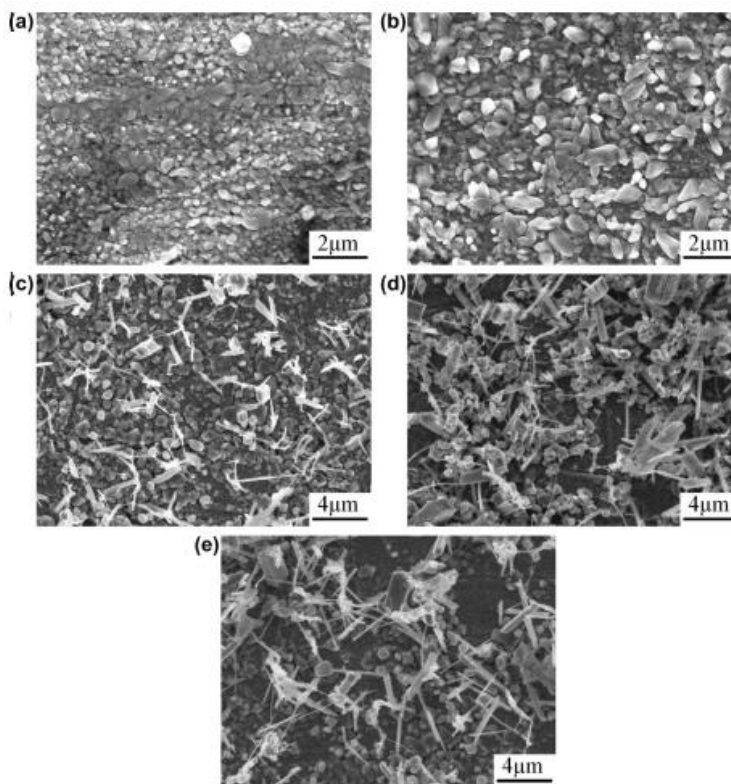
Figure 2.9: SEM images of interfacial layer microstructure formed during continuous galvanizing of steels annealed in a N_2-5 vol.%H_2 annealing atmosphere at a dp=223 K (–30 °C): (a) 0.14 wt.% Mn, (b) 1.4 wt.% Mn, (c) 2.5 wt.% Mn, (d) 3.5 wt.% Mn and (e) 5.1 wt.% Mn [60].
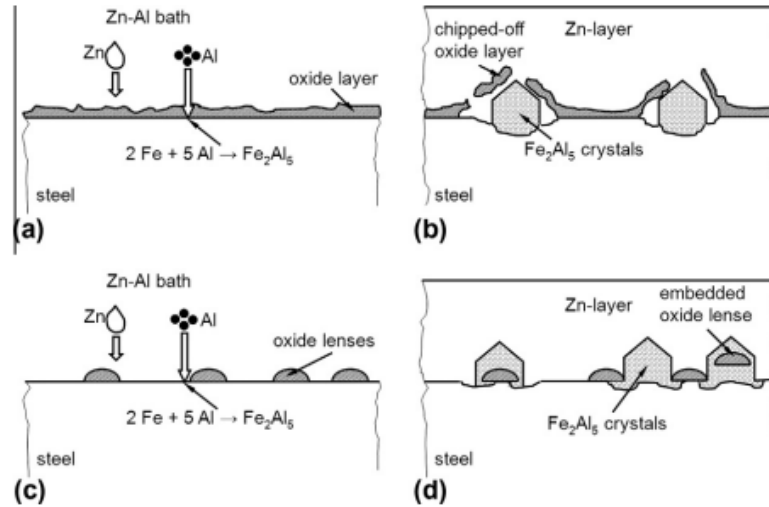
Figure 2.10: Schematic drawing showing: (a and b) flaking of the oxides and (c and d) trapping of the oxides by Fe-Al intermetallic phase [67].

It has also been established that external oxides can affect the formation kinetics of the

η-$Fe_2Al_5Zn_X$ interfacial layer [65,71]. Alibeigi [26,59] studied the kinetics of the interfacial layer formation by measuring Al uptake as a function of time, whose results are shown in Figure 2.11. It is worthwhile to note that, by definition, Al uptake is the weight of Al present in the interfacial layer per unit surface area in mg/m^2, which is an analogue of the interfacial layer thickness [42]. Her observations indicated that growth of the Fe-Al layer is affected by the balance between available dissolved Al and the ability of Fe and dissolved Al to diffuse toward the reaction front. The former is limited by the aluminothermic reduction and the latter is limited by the existing Fe-Al crystals formed at the steel surface.
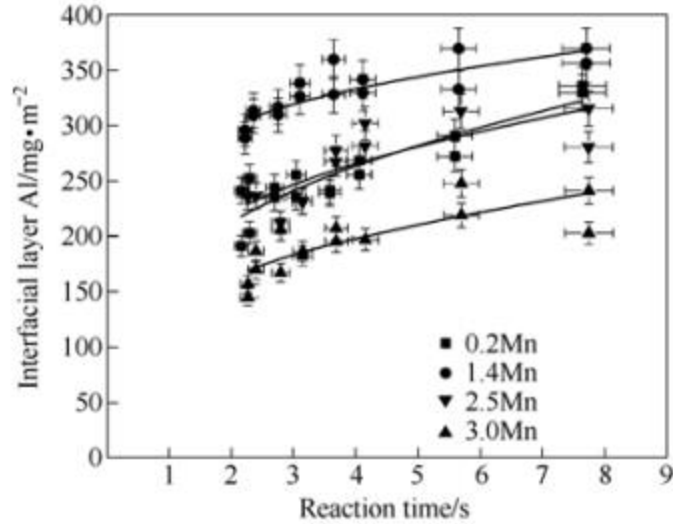
Figure 2.11: Interfacial layer Al uptake as a function of reaction time and Mn content for 0.2 wt.% dissolved Al bath [59].

2.7   Methods of improving reactive wetting by the continuous galvanizing bath

Figure 2.12 schematically shows four process modifications which have been suggested to improve the reactive wetting of AHSSs, which will be discussed in detail in this section:
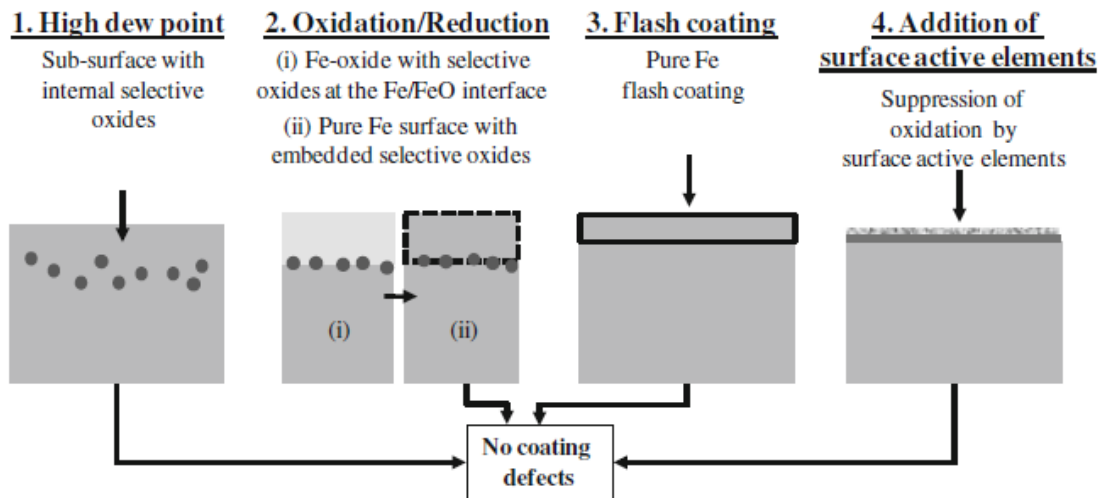
Figure 2.12: Schematic showing four methods proposed for mitigating the adverse effects of surface oxides on the reactive wetting of AHSSs [72].

2.7.1   Oxidation-Reduction

One of the potential ways to improve reactive wetting of AHSS substrates is by a two-step procedure known as the oxidation-reduction process. The first step includes heating the steel in air [73], an oxygen-rich gas fired furnace [74] or in a N_2-O_2 atmosphere [75] for a short time. This step results in the simultaneous selective oxidation of alloying elements such as Mn, Si and Cr and the formation of iron oxides. The steel is then annealed in a conventional CGL atmosphere which is reducing with respect to Fe e.g. N_2- (5-10 vol.%) H_2 with a controlled dew point. The final microstructure of the surface layer usually consists of pure iron, which can be reactively wetted by the Zn bath, with a significant volume fraction of pores and isolated oxide particles embedded within the Fe layer. However, due to the fact that the final pure Fe layer is porous [75], a relatively weak interfacial layer can form during continuous galvanizing.

2.7.2   Flash coating

In the flash coating method [76,77], it is suggested that the deposition of a thin layer of pure Ni, Fe or Cu prior to the annealing stage can prevent the formation of externl oxides on the surface of a Fe-Mn-Si alloy during heat treatment, thereby improving the reactive wetting by the zinc bath during continuous galvanizing. However, the use of this method is limited industrially because of it being relatively expensive.

2.7.3   High dew point

A more promising technique uses higher pO_2 atmospheres or higher atmosphere dew points (at a given annealing temperature) during annealing of the steel in order to encourage the internal selective oxidation of the alloying elements, as generally characterised by the Wagner criterion [29] for the internal to external oxidation transition. According to the Wagner model (equation

36

(2.16)) increasing the process atmosphere oxygen partial pressure leads to an increase in the critical mole fraction of the alloying element required for the transition from internal to external oxidation. Thus, internal oxidation is dominant over external oxidation [35,50,78-85]. As an example, Pourmajidian and McDermid [50] studied the effect of process atmosphere oxygen partial pressure on the spatial distribution and morphology of the oxides formed during annealing of a 0.1C-6Mn-2Si (wt.%) medium-Mn AHSS at an intercritical temperature of 1073 K (800 °C). They showed that, although under the lower pO_2 process atmospheres of 223 K (–50 °C) dp and 243 K (–30 °C) dp the substrate was covered with film-like $MnSiO_3$, SiO_2, MnO and film-like MnO oxides, respectively, increasing the atmosphere pO_2 via using 278 K (+5 °C) dp altered the surface oxide morphology by forming nodule-like MnO particles with thin films in between the particles.

Figure 2.13 shows a schematic drawing indicating how increasing the atmosphere oxygen partial pressure results in a transition from external to internal oxidation and contributes to an improvement in reactive wetting for a 2.2Mn-1.4Si (wt.%) TRIP steel annealed in N_2-10 vol.% H_2 atmosphere [64]. As discussed by the authors, at the lower pO_2 process atmosphere of 213 K (–60°C) dp, the steel surface was covered with both thin and thick oxide layers. For the 278 K (+5 °C) dp process atmosphere; on the other hand, external oxides composed of thin oxide layer and small oxide particles formed internally long grain boundaries. This was in agreement with the predictions made by the Wagner model regarding the occurrence of internal oxidation rather than external due to an increase in the oxygen concentration at the steel surface at higher pO_2 [29].
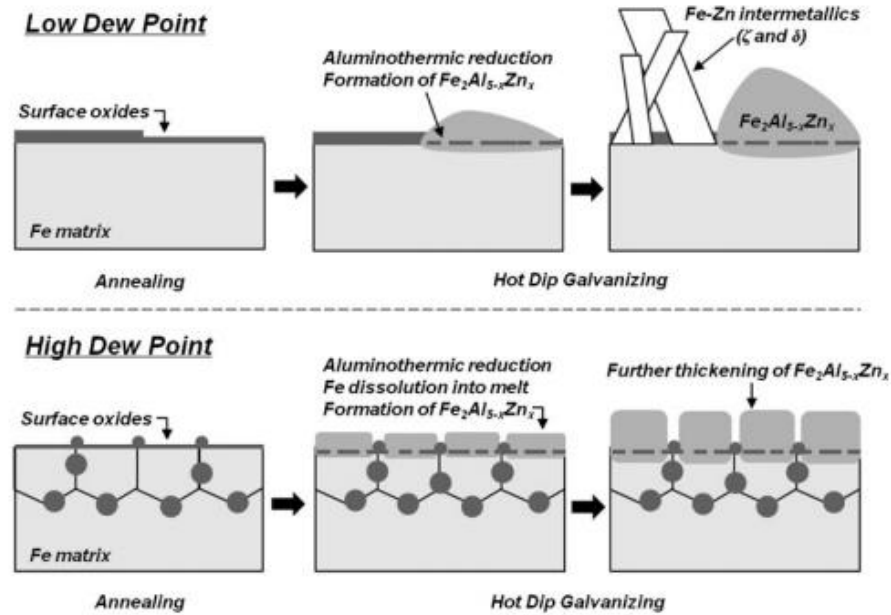
Figure 2.13: Schematic drawing illustrating the reactive wetting behaviour of a CMnSi TRIP steel during continuous galvanizing after being annealed at high and low dew points [64].

However, it should be cautioned that if the transition from external to internal oxidation does not occur, increasing the dew point has an adverse effect. This is due to the fact that higher dew points provide more oxygen for the nucleation and growth of the oxides. As an example, the study done by Bellhouse and McDermid [23] on selective oxidation and reactive wetting of a 0.2C-1.5Mn-1.5Al (wt.%) TRIP steel showed that, while good reactive wetting was obtained after continuous galvanizing of the steel annealed at two lower pO_2 process atmospheres of 220 K ($-53\ ^\circ$C) and 243 K ($-30\ ^\circ$C) dp, the higher pO_2 of 278 K ($+5\ ^\circ$C) dp process atmosphere led to an increase in the thickness of MnO films resulting in poor wettability due to the limited ability of aluminothermic reaction in reducing thick MnO oxides. According to Kavitha and McDermid [52], the successful use of the MnO dissolution reaction to promote reactive wetting depends strongly on reaction time and, for normal continuous galvanizing reaction times, can reduce MnO films with at most 100 nm thickness. As discussed before, this is due to the fact that

aluminothermic reduction reaction is limited by the depletion of dissolved Al occurring during initial reaction which may limit the subsequent reaction kinetics.

2.7.4   Addition of surface active elements

The addition of small amounts of a surface active elements has been suggested to effectively change the composition, morphology and thickness/depth of both external and internal oxides formed during annealing, and are expected to improve reactive wetting during continuous galvanizing [72,82,86-94]. Surface active element have lower affinity to oxygen than the substrate in order for its oxide to be thermodynamically less stable than the substrate oxide. As an example, per Figure 2.14, elements such as Sn can be used as a surface active element in steels.

Seah [95,96] suggested the following equation for calculating the surface enrichment of a solute atom A in a solvent atom B (β_A^S):

$$\ln \beta_A^S = \left[24(T_B^m - T_A^m) + 1.86\Omega + M\,4.64 \times 10^7\, a_B (a_A - a_B)^2 \right] / RT \pm 1.29 \qquad (2.25)$$

where:

T is the temperature

T_B^m and T_A^m are the melting temperatures of pure solids B and A, respectively

Ω is the mixing enthalpy of A and B

a_A and a_B are atomic sizes of A and B, respectively.

M=1 for $a_A > a_B$ and M=0 if $a_A < a_B$
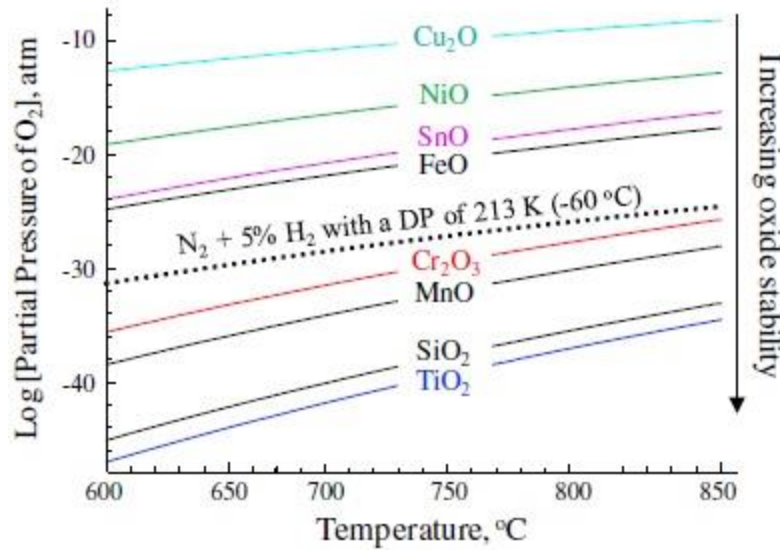
Figure 2.14: Thermodynamic stability of various oxides with respect to temperature and oxygen partial pressure [72].

According to equation (2.25), the difference in the atomic size of the solute and the solvent is considered as one of the main driving forces for the solvent to segregate to the surface. This is due to the fact that the larger atoms experience an elastic strain in the bulk matrix due to lattice mismatch and tend to decrease it through segregating the larger atom to the external surface and grain boundaries. The other driving force for segregation is reducing the surface energy of the substrate by covering its surface and, as the melting temperature of an element is directly related to its surface energy, the difference in the melting temperature of the solute and the solvent is representative of the tendency of the solute to segregate to the surface. Considering these two factors and per Figure 2.15, Sb, Bi and Sn are credible options as surface active elements to be added to steels.

Cho et al. [72] studied the effect of minor additions of Cr, Ni, Ti, Cu and Sn on the selective oxidation and reactive wetting of a 0.1C-1.6Mn-1.5Si (wt.%) TRIP steel and reported Sn as having the most significant influence on improving the reactive wetting, which was achieved by

its effect on modifying the morphology of the surface oxides from film-like to lens-shaped particles. The lens-shaped oxide particles would facilitate the formation of η-$Fe_2Al_5Zn_X$ interfacial layer by allowing Fe and dissolved Al to easily react at the areas in between the oxide particles which were covered with thinner film-like oxide layers through mechanism such as aluminothermic reduction and oxide lift-off. Cho et al. [86] have revealed precise mechanisms through which Sn affects surface oxide characteristics by means of adding various amounts of Sn in the range of 0.05-1 wt.% to a 0.1C-1.6Mn-1.5Si (wt.%) TRIP steel. They reported that the change in the morphology of the surface oxides by the addition of Sn contributed to its ability in changing the oxide/matrix interfacial energy. The change in the chemistry of the surface oxides was also related to its segregation at the surface, which leads to occupying potential adsorption sites for oxygen, thus reducing the oxygen permeability of the surface. As modeled previously by Suzuki et al. [97], dissolved oxygen concentration in the steel which can be manipulated through atmosphere oxygen partial pressure (pO_2) dictates the chemistry of the oxides formed during annealing.

Pourmajidian et al. [87] have recently studied, both themodynamically and kinetically, the combined effects of annealing atmosphere pO_2, annealing time and 0.05 wt.% Sn on the morphology and chemistry of the external and internal oxidation of a 0.1C-6Mn-2Si (wt.%) third generation advanced high strength steel. They reported a refined microstructure for both the external and internal oxides after the addition of Sn under all annealing conditions. This was found to be due to segregation of Sn to the steel surface to approximately 10 times its bulk value, therefore reducing the selective oxidation rates. Later, Pourmajidian and McDermid [98] investigated the reactive wetting of the same steel by a Zn-0.2 wt.% dissolved Al bath and reported a significant improvement, which was attributed to the alteration in the morphology of

external MnO oxides to fine and discrete particles, as a result of the addition of Sn to the steel chemistry.

It is noteworthy that the presence of high amounts of Sn (> 0.1 wt.%) results in hot shortness and deteriorates the steel mechanical properties, hence its addition to practical alloys is suggested to be kept as low as possible [99,100].
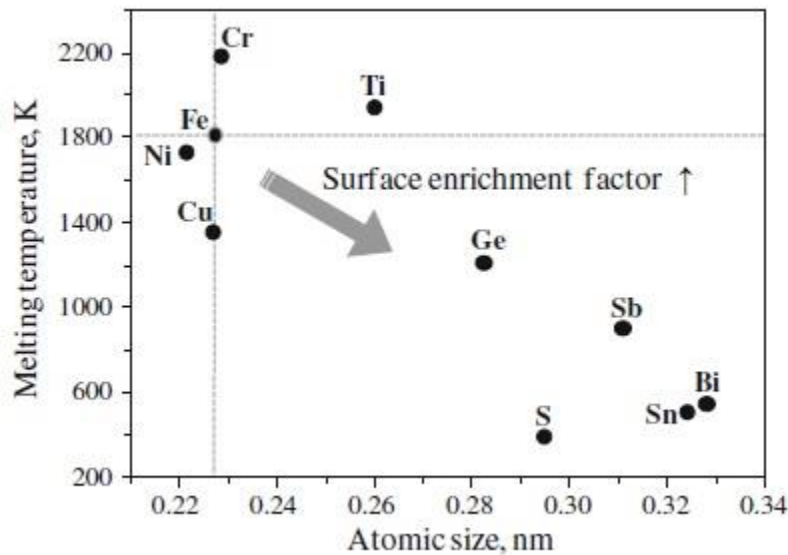
Figure 2.15: Surface enrichment factor of various elements in steel according to their atomic size and melting temperature difference with Fe [72].

2.8   References

[1] C.M. Tamarelli, The evolving use of advanced high-strength steels for automotive applications, Steel Market Development Institute, Michigan (2011).

[2] R. Kuziak, R. Kawalls, S. Waengler, Arch. Civ. Mech. Eng. 8 (2008) 103-117.

[3] J. Galan, L. Samek, P. Verleysen, K. Verbeken, Y. Houbaert, Rev. Met. 48 (2012) 118-131.

[4] http://www.mto.gov.on.ca/english/

[5] http://www.autosteel.org

[6] D.K. Matlock, J.G. Speer, E. De Moor, P.J. Gibbs, JESTECH 15 (2012) 1-12.

[7] E. Billur, T. Atlan, Stamping J. 16-17.

[8] http://www.mercedesclass.net/?page_id=48.

[9] http://www.tatasteelautomotive.com/file_source/Sta.

[10] S. Oliver, T.B. Jones, G. Fourlaris, Mater. Sci. Technol. 23 (2007) 423-431.

[11] W. Bleck, S. papaefthymiou, A. Frehn, Steel Research Int. 75 (2004) 704-710

[12] C.C. Tasan, M. Diehl, D. Yan, M. Bechtold, F. Roters, L. Schemmann, C. Zheng, N. Peranio, D. Ponge, M. Koyama, K. Tsuzaki, D. Raabe, Annu. Rev. Mater. Res. 45 (2014), 391-431.

[13] B.C. De Cooman, Curr. Opin. Solid State Mater. Sci. 8 (2014) 285-303.

[14] M. De Meyer, D. Vanderschuren, B.C. De Cooman, Iron Steel Inst. Japan Int. 39 (1999) 813-822.

[15] M.S. Rashid, Ann. Rev. Mater. Sci. 11 (1981) 245-266.

[16] P. Tsipouridis, "Mechanical properties of dual-phase steels", PhD thesis, Technischen Universitat Munchen (2006).

[17] Y. Granbom, "Structure and mechanical properties of dual phase steels – An experimental and theoretical analysis", PhD thesis, KTH Royal Institute of Technology (2010).

[18] N. Peranio, Y.J. Li, F. Roters, D. Raabe, Mater. Sci. Eng. A 527 (2010) 4161-4168.

[19] V.F. Zackay, E.R. Parker, D. Fahr, R. Busch, ASM Trans. Q.60 (1967) 252-259.

[20] P. Jacques, F. Delannay, X. Cornet, P. Harlet, J. Ladriere, Metall. Mater. Trans. A 29 (1998) 2383-2393.

[21] B.O. Matsumura, Y. Sakuma, H. Takechi, Trans. Iron Steel Inst. Japan Int. 27 (1987) 570-579.

[22] E.M. Bellhouse, J.R. McDermid, Metall. Mater. Trans. A 43A (2012) 2426-2441.

[23] E.M. Bellhouse, J.R. McDermid, Metall. Mater. Trans. A 42A (2011) 2753-2768.

[24] S.M.A. Shibli, B.N. Meena, R. Remya, Surf. Coatings Technol. 262 (2015) 210-215.

[25] M. Guttmann, Mater. Sci. Forum 155-156 (1994) 527-548.

[26] S. Alibeigi, "Short-term formation kinetics of the continuous galvanizing interfacial layer on Mn-containing steels", PhD thesis, McMaster University (2014).

[27] T. Sendzimer (1938) U.S. Patent No. 2,110.893.

[28] H.J. Grabke, V. Leroy, H. Viefhaus, Iron Steel Inst. Japan Int. 35 (1995) 95-113.

[29] C. Wagner, Zh. Elektrochem. 63 (1959) 772-782.

[30] N. Birks, G.H. Meier, F.S. Pettit (2006) "Introduction to the high-temperature oxidation of metals". Cambridge University Press, Cambridge.

[31] S. B. Velez, "Oxidation kinetics and mechanisms in HT-9 ferritic/martensitic stainless steel", Ph.D. thesis, University of Florida (2005).

[32] C. Wagner, Z. Phys. Chem. B21 (1933), 25

[33] S. Mahboubi, "Wet oxidation performance of type 310S stainless steel" Ph.D. thesis, McMaster University (2018).

[34] R.A. Rapp, Corros. 21 (1965) 382-401.

[35] V.A. Lashgari, C. Kwakernaak, W.G. Sloof: Oxid. Met. 81 (2014) 435–451.

[36] D.L. Douglass, Oxid. Met. 44 (1995) 81-111.

[37] J.M. Mataigne, M. Lamberigts, V. Leroy (1992) "Developments in the Annealing of Sheet Steels". In: R. Pradhan, I. Gupta (eds), Minerals, Metals & Materials Society, Warrendale, 511-528.

[38] C.R. Shastry, J.A. Rotole, T.W. Kaiser, in 7th Int. Conf. Zinc Zinc Alloy Coat. Steel Sheet Conf., Osaka (2007) 403–408.

[39] T. Young, Phil. Trans. R. Soc. Lond. 95 (1805) 65-87.

[40] I.A. Aksay, C.E. Hoge, J.A. Pask, J. Phys. Chem. 78 (1974) 1178-1183.

[41] J. Mackowiak, N.R. Short, Int Met Reviews 24 (1979) 1-19.

[42] N.-Y. Tang, Metall. Mater. Trans. A 26A (1995) 1699-1704.

[43] Y. Leprêtre, J.M. Mataigne, M. Guttmann, J. Philibert (1998) "Zinc-Based Steel Coating Systems: Production and Performance". TMS, Warrendale.

[44] J.-Y. Dauphin, P. Perrot, U.G. Tchissambot, Mem. Sci. Rev. Met. 84 (1987) 329-336.

[45] P. Perrot, J.-C. Tissier, J.-Y. Dauphin, Z. Metalkd. 83 (1992) 786-790.

[46] J.R. McDermid, M.H. Kaye, W.T. Thompson, Metall. Mater. Trans. B 38B (2007) 215-230.

[47] J. Nakano, D.V Malakhov, S.Yamaguchi, G.R. Purdy, Comput. Coupling Phase Diagrams Thermochem. 31 (2007) 125-140.

[48] L. Chen, R. Fourmentin, J.R. McDermid, Metall. Mater. Trans. A 39A (2008) 2128-2142.

[49] N.-Y. Tang (1998) "Zinc-Based Steel Coating Systems: Production and Performance". TMS, Warrendale, 3–12.

[50] M. Pourmajidian, J.R. McDermid, Metall. Mater. Trans. A 49A (2018) 1795-1808.

[51] R. Khondker, A. Mertens, J.R. McDermid, Mater. Sci. Eng. A 463 (2007) 157–165.

[52] R. Kavitha, J.R. McDermid, Surf. Coat. Technol. 212 (2012) 152–158.

[53] J. Mahieu, S. Claessens, B.C. De Cooman, Metall. Mater. Trans. A 32A (2001) 2905–2908.

[54] J. Maki, J. Mahieu, B.C. De Cooman, S. Claessens, Mater. Sci. Technol. 19 (2003) 125–131

[55] M.S. Kim, J.H. Kwak, J.S. Kim, Y.H. Liu, N. Gao, N.-Y. Tang, Metall. Mater. Trans. A 40A (2009) 1903–1910.

[56] Y. Kim, J. Lee, J. Park, S.-H. Jeon, Met. Mater. Int. 17 (2011) 607–11.

[57] K.-Ch. Lin, Ch.-S. Lin, Iron Steel Inst. Japan Int. 54 (2014) 2380–2384.

[58] H. Liu, F. Li, W. Shi, R. Liu, L. Li, Surf. Coat. Technol. 205 (2011) 3535-3539.

[59] S. Alibeigi, J.R. Mcdermid, in 9 th Int. Conf. Zinc Zinc Alloy Coat. Steel Sheet Conf., Beijing (2007) 171–176.

[60] S. Alibeigi, R. Kavitha, R.J. Meguerian, J.R. McDermid, Acta Mater. 59 (2011) 3537-3549.

[61] Y.F. Gong, T.J. Song, H.S. Kim, J.H. Kwak, B.C. De Cooman, in Asia-Pacific Galvaniz. Conf., Seoul (2009) B-15.

[62] H. Liu, Y. He, L. Li, Appl. Surf. Sci. 256 (2009) 1399-1403.

[63] M. Pourmajidian, J.R. McDermid, Iron Steel Inst. Japan Int. 58 (2018) 1635-1643.

[64] L. Cho, S.-J. Lee, M.-S. Kim, Y.-H. Kim, B.C. De Cooman, Metall. Mater. Trans. A 44A (2013) 362-371.

[65] S. Prabhudev, S. Swaminathan, M. Rohwerder, Corros. Sci. 53 (2011) 2413-2418.

[66] E.M. Bellhouse, J.R. McDermid, Metall. Mater. Trans. A 41A (2010) 1539-1553.

[67] R. Sagl, A. Jarosik, D. Stifter, G. Angeli, Corros. Sci. 70 (2013) 268-275.

[68] E.M. Bellhouse, "Galvanizing of Al-Si TRIP-assisted steels", Ph.D. thesis, McMaster University (2010).

[69] F. Li, H. Liu, W. Shi, R.Liu, L. Li, Mater. Corros. 63 (2012) 396-400.

[70] Y. Li, S. Jiang, X. Yuan, B. Chen, Q. Zhang, Surf. Interface Anal. 44 (2012) 472-477.

[71] X. Vanden Eynde, J. P. Servais, M. Lamberigts, Surf. Interface Anal. 35 (2003) 1004-1014.

[72] L. Cho, M.-S. Kim, Y.-H. Kim, B.C. De Cooman, Metall. Mater. Trans. A 45A (2014) 4484-4498.

[73] I. Parezanović, M. Spiegel, Surf. Eng. 20 (2004) 285-291.

[74] K. Kahoul, M. Turchetto, in 10th Int. Conf. Zinc Zinc Alloy Coat. Steel Sheet Conf., Toronto (2015) 436–443.

[75] Y.F. Gong, B.C. De Cooman, Iron Steel Inst. Japan Int. 51 (2011) 630-637.

[76] Y.I. Choi, W.J. Beom, C.J. Park, D. Paik, M.H. Hong, Metall. Mater. Trans. A 41A (2010) 3379-3385.

[77] R. Sa-nguanmoo, E. Nisaratanaporn, Y. Boonyongmaneerat, Corros. Sci. 53 (2011) 122-126.

[78] K.-K. Wang, C.W. Hsu, L. Chang, D. Gan, T.-R. Chen, K.-C. Yang, J. Electrochem. Soc. 159 (2012) C561-C570.

[79] V. de Freitas Cunha Lins, L. Madeira, J. Mario Carneiro Vilela, M. Spangler Andrade, V. Tadeu Lopes Buono, J. Porto Guimaraes, E. de Azevedo Alvarenga, Appl. Surf. Sci. 257 (2011) 5871-5878.

[80] X.-S. Li, S.-I. Baek, C.-S. Oh, S.-J. Kim, Y.W. Kim, Scr. Mater. 57 (2007) 113-116.

[81] L. Cho, G.S. Jung, B.C. De Cooman, Metall. Mater. Trans. A 45A (2014) 5158-5172.

[82] Z.T. Zhang, I.R. Sohn, G.H. Meier, S. Sridhar, Metall. Mater. Trans. B 40B (2009) 567-584.

[83] S.-K. Lee, J.-S. Kim, J.-W. Choi, N. Kang, K.-M. Cho, Met. Mater. Int. 17 (2011) 251-257.

[84] S.-K. Lee, J.-S. Kim, N. Kang, K.-M. Cho, Met. Mater. Int. 18 (2012) 951-956.

[85] H. Liu, Y. He, S. Swaminathan, M. Rohwerder, L. Li, Surf. Coat. Technol. 206 (2011) 1237-1243.

[86] L. Cho, E.-J. Seo, G.-S. Jung, D.-W. Suh, B.C. De Cooman, Metall. Mater. Trans. A 47A (2016) 1705-1719.

[87] M. Pourmajidian, B. Langelier, J.R. McDermid, Metall. Mater. Trans. A 49A (2018) 5561-5573.

[88] H. Viefhaus, M. Rusenberg, Surf. Sci. 159 (1985) 1-23.

[89] L. Yin, S. Sridhar, Metall. Mater. Trans. B 41B (2010) 1095-1107.

[90] G. Lyudkovsky, IEEE Trans. Magn. 22 (1986) 508-510.

[91] E. Clauberg, C. Uebing, H.J. Grabke, Appl. Surf. Sci. 143 (1999) 206-214.

[92] Z.T. Zhang, I.R. Sohn, F.S. Pettit, G.H. MeieR, S. Sridhar, Metall. Mater. Trans. B 40B (2009) 550-566.

[93] D.S. Petrovic, M. Jenko, V. Gontarev, H.J. Grabke, Kovine, Zlitine, Tehnologije 32 (1998) 493-496.

[94] J. Oh, L. Cho, M. Kim, K. Kang, B.C. De Cooman, Metall. Mater. Trans. A 47A (2016) 5474-5486.

[95] M. Seah, Acta Metall. 28 (1980) 955–962.

[96] M.P. Seah, J. Catalysts 57 (1979) 450-457.

[97] Y. Suzuki, T. Yamashita, Y. Sugimoto, S. Fujita, S.Yamaguchi, Iron Steel Inst. Japan Int. 49 (2009) 564-573.

[98] M. Pourmajidian, J.R. McDermid, Surf. Coat. Technol. Accepted Manuscript (2018) https://doi.org/10.1016/j.surfcoat.2018.10.028.

[99] D.A. Melford, Proc. R. Soc. Lond. A. 295 (1980) 89-103.

[100] Y. Li, J.P. Han, Z.H. Jiang, P. He, Int. J. Miner. Metall. Mater. 22 (2015) 37-44.

3 SELECTIVE OXIDATION OF A C-2MN-1.3SI (WT.%) ADVANCED HIGH STRENGTH STEEL DURING CONTINUOUS GALVANIZING HEAT TREATMENTS

G. Seyed Mousavi, J.R. McDermid*

Steel Research Centre, McMaster University, Hamilton, Canada ON L8S 4L8

3.1 Abstract

The influence of oxygen partial pressure and annealing time on the selective oxidation of a Fe-0.1C-2Mn-1.3Si (wt.%) advanced high strength steel during intercritical annealing was investigated. The steel was intercritically annealed at 1093 K (820 °C) for annealing times of 60 to 600 s in a N_2-5 vol.% H_2 gas atmosphere with dew points ranging from 223 K (–50 °C) to 278 K (+5 °C). The morphology, thickness, and chemistry of the oxides were determined as a function of process atmosphere oxygen partial pressure and annealing time by means of SEM, XPS and TEM. It was found that for the 223 K (–50 °C) dew point atmosphere, a compact, film-like external oxide comprising $MnSiO_3$, Mn_2SiO_4 and SiO_2 and nodule-like MnO oxides covered the surface. On the other hand, for the 278 K (+5 °C) dew point atmosphere, $MnSiO_3$, Mn_2SiO_4 and MnO nodule/plate-like external oxides were formed while Si was oxidized internally. Longer annealing times resulted in an increase in either the thickness of the external oxide layer or depth of internal oxidation. A comparison between the predictions of the Wagner internal to external transition model found good agreement between the experimental results for Mn and Si in ferrite.

3.2   Introduction

Advanced high strength steels (AHSS) are of great interest to the automotive industry due to legislative requirements for improving fuel efficiency, where reducing vehicle weight is a partial solution to achieving this objective [1]. Dual phase (DP) and Transformation Induced Plasticity (TRIP) steels are amongst the so-called first generation (1G) of AHSSs and possess a unique combination of high strength, good formability and high energy absorption capacity, making it possible to reduce the thickness (and, therefore, the mass) of a part without compromising performance. The promising properties of DP and TRIP steels are brought about by carefully designed heat treatments and through the proper addition of alloying elements such as carbon, manganese and silicon [2]. Carbon is added to stabilize austenite and is a potent solid solution strengthener. Manganese is an austenite stabilizer and a moderate solid solution strengthener. Silicon acts as a solid solution strengthener and also delays carbide formation during isothermal bainitic transformation annealing [3-5] a role critical in the microstructural development of TRIP alloys.

In order to be used in commonly encountered road environments, it is essential to protect the steel from corrosion to ensure its long-term stability, for which the continuous hot-dip galvanizing process is one of the most cost effective techniques to achieve this end [6,7]. However, galvanizing DP and TRIP steels can be challenging. This difficulty arises because, although the commonly used industrial N_2-(5-20 vol.%) H_2-xH_2O annealing atmosphere is reducing for Fe oxides, the oxygen potential is sufficient to selectively oxidize alloying elements such as Si and Mn. Selective oxidation can occur externally, on the surface, or internally, below the surface [8-10]. It has been well established that external oxides can deteriorate the reactive wetting of the steel strip by the molten Zn-Al-Fe bath during the continuous hot dip galvanizing

process [8,11]. Furthermore, it has been advocated by several authors that the shape, thickness, spatial distribution and chemistry of the external oxides also affects the reactive wetting of the steel strip by the molten zinc bath [6,10,1216]. For example, the study of Bellhouse and McDermid [17] on the effect of process atmosphere oxygen partial pressure on the selective oxidation and reactive wetting of a C-1.5Mn-1.5Al (wt.%) TRIP-assisted steels showed that widely spaced external oxide nodules with relatively thin inter-nodular MnO films resulted in a fully developed and homogeneous η-Fe$_2$Al$_5$Zn$_X$ interfacial layer being formed, indicative of reactive wetting, after dipping in a 733 K (460°C) Zn-0.2Al-0.01Fe (wt.%) continuous galvanizing bath. This result was attributed to the ability of the bath to bridge the oxide islands and penetrate the oxide/steel interface due to thermal expansion coefficient mismatch cracking. In addition, it was proposed that aluminothermic reduction of the thin, inter-nodular MnO films [18] may have contributed to the reactive wetting reaction. *In situ* reduction of these thin MnO films by CGL bath dissolved Al was later shown to be kinetically feasible by Kavitha and McDermid [19], confirming this theory. Sagl et al. [20] also observed and advocated for the mechanical damage mechanism whereby the oxide/substrate interface of a 1.8Mn (wt.%) DP steel was cracked and the cracks penetrated by the Zn(Al,Fe) bath to form the η-Fe$_2$Al$_5$Zn$_X$ interfacial layer. In addition, it was suggested by Gong et al. [21] that Mn-Si oxides could be reduced by the bath dissolved Al during continuous galvanizing. However, it should be pointed out that this form of the aluminothermic reduction, while thermodynamically feasible, has not been experimentally verified.

On the contrary, compact, thick, more film-like external oxides have been shown to result in relatively poor reacting wetting by the CGL bath [8,17,22]. For example, Bellhouse and McDermid [17] showed that thicker, compact MnO external oxide films on the surface of a C-

1.5Mn-1.5Al (wt.%) TRIP alloy resulted in poor reactive wetting. Similar findings were reported

by Blumenau et al. [22] for the case of a C-23Mn (wt.%) TWIP steel they examined. Cho et al.

[8] subsequently agreed with these observations for the case of a C-2.2Mn-1.4Si (wt.%) TRIP

steels, where film-like or compact external oxides were found to be detrimental to the formation

of the desired η-$Fe_2Al_5Zn_X$ interfacial phase during reactive wetting.

Thus, it is critical to explicitly understand the morphological and chemical development of

both the external and internal oxides in order to provide predictive tools concerning the

relationship between substrate composition, process atmosphere pO_2, thermal processing

variables and reactive wetting by the Zn(Al,Fe) CGL bath.

Thus, the objectives of the present research are to determine the effect of continuous

galvanizing annealing process parameters, i.e. oxygen partial pressure and annealing time, on the

selective oxidation of a Fe-0.1 C-2Mn-1.3Si (wt.%) AHSS, including the effects of morphology,

composition and thickness of the oxides. A comparison was also made between the present

experimental observations and Wagner model used to predict the selective oxidation mode of

ferrous alloys in continuous galvanizing process atmospheres.

3.3   Experimental procedure

The chemical composition of the model CMnSi AHSS used in the present study is provided in

Table 3.1. The alloy was vacuum melted, cast, hot rolled to a thickness of 4 mm, pickled,

scalped, sandblasted, and cold rolled to a final thickness of 1.2 mm. The hot rolling start and

finish temperatures were, respectively, 1523 K (1250 °C) and 1123 K (850 °C). Experimental

coupons (10 mm × 50 mm) were cut from the cold rolled steel sheet with the longitudinal axis of

the coupon parallel to the rolling direction. Coupons were lightly ground with 1200 grit SiC

paper prior to annealing to avoid substrate roughness effects during surface analysis. Prior to

selective oxidation tests, all samples were cleaned in a 353 K (80 °C) 2 wt.% NaOH solution, rinsed with water, ultrasonically cleaned in isopropanol and dried in a warm air stream. All samples had a type K thermocouple (0.5 mm, ±3 K) spot-welded to the coupon surface prior to insertion in the McMaster Galvanizing Simulator (MGS, Iwatani Surtec) in order to control sample temperature during thermal processing. Immediately before annealing, samples were subjected to a final cleaning step using acetone wipes.

Table 3.1: Experimental Steel Chemical Composition (wt.%)

Steel	C	Mn	Si	Al	Ti	N	S	Fe
Fe-2Mn-1.3Si	0.11	2.03	1.29	0.042	0.011	0.003	0.002	balance

All heat treatments were carried out in a N_2-5 vol.% H_2 process atmosphere with varying dew points in order to determine the effect of oxygen partial pressure on the selective oxidation of the experimental steel. The experimental dew points were 223 K (–50 °C), 243 K (–30 °C), and 278 K (+5 °C). Table 3.2 summarizes the process atmospheres used in the experiments, including the process atmosphere pO_2 at the peak annealing temperature of 1093 K (820 °C) used for all annealing experiments. The reader should note that, for ease of reference, the process atmospheres will be referred to using the process atmosphere name documented in Table 3.2 – i.e. –223 K (–50 °C) dp, 243 K (–30 °C) dp and 278 K (+5 °C) dp – in the below text.

Table 3.2: Experimental Process Atmospheres

Process Atmosphere Name	Process Atmosphere dp [K (°C)]]	N_2 (Vol.%)	H_2 (Vol.%)	pO_2 at 1093 K (820 °C) Atm	pH_2O/pH_2
223 K (–50 °C) dp	223 (–50)	95	5	1.96×10^{-24}	0.0010
243 K (–30 °C) dp	243 (–30)	95	5	1.21×10^{-22}	0.0082
278 K(+5 °C) dp	278 (+5)	95	5	3.45×10^{-20}	0.1380

A schematic of the experimental heat treatment time-temperature profile is shown in

Figure 3.1. Experimental heat treatments consisted of heating the samples to 773 K (500 °C) at a

heating rate of 15 K/s followed by heating to the intercritical annealing temperature (IAT) of

1093 K (820 °C) at a heating rate of 5 K/s, holding at the IAT for t_1 = 60, 120, 240, 360 and 600

s, cooling to 738 K (465 °C) at 20 K/s, holding for t_2 = 20 s to thermally equilibrate the steel with

the galvanizing bath, and cooling at 20 K/s to room temperature (Figure 3.1). Samples were

cooled by N_2 jet cooling. Immediately after removal from the MGS, samples were stored in

anhydrous isopropanol to minimize further surface oxidation. It is noteworthy that the

intercritical temperature of 1093 K (820 °C) was chosen to produce an intercritical

microstructure of 50% α -50% γ (vol.%) as determined using THERMO-CALC software and the

TCFE2 database (Thermo- Calc database for Fe-alloys, version 2.0) using the local equilibrium-

non partitioning (LE-NP) formalism.
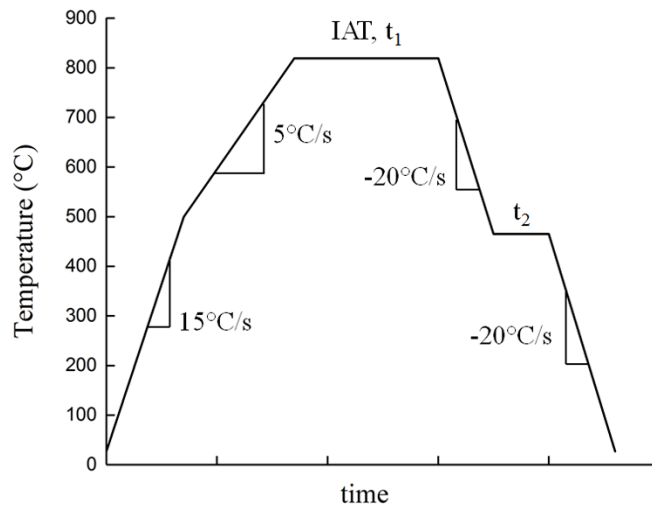
Figure 3.1: Schematic of the experimental thermal cycle.

Microstructural analysis of the steel before and after intercritical annealing was done via

scanning electron microscopy (SEM) using a JEOL 7000F field emission gun SEM (FEG-SEM).

Samples were etched with 4% nitric acid in ethanol (4% nital) where the etching time was approximately 15 seconds. An acceleration voltage of 10 keV and a working distance of 10 mm were used for all samples. All samples were sputter coated with carbon to avoid charging.

The effect of process atmosphere on oxide morphology, thickness, and chemistry was investigated across various length scales using scanning electron microscopy (SEM), X-ray photoelectron spectroscopy (XPS) and transmission electron microscopy (TEM). The morphology, size and distribution of the surface oxides were analyzed using a JEOL 7000F field emission gun SEM (FEG-SEM). An acceleration voltage of 3 keV and a working distance of 6 mm were used for all samples. All sample surfaces were sputter coated with platinum to avoid charging. XPS was used to determine the chemistry and mesoscale thickness of the surface oxides formed during annealing. XPS analysis was performed using a PHI Quantera XPS (Physical Electronics, Chanhassen, MN) with an Al Kα X-ray source (1486.6 eV). XPS data was processed using MultiPak software (Version 6). The spot size of the incident X-ray was 100 μm and the take-off angle was 45°. The metallic iron binding energy of 706.62 eV was used to calibrate all spectra. The accuracy of the obtained binding energy values were within ±0.1 eV. The chemical composition measurements were within ±5% of the measured value in atomic percent. Prior to collecting binding energy data, sample surfaces were sputtered with Ar to a depth of 4 nm to avoid surface contamination arising during sample handling in the ambient atmosphere after removal from the MGS.

TEM was used to analyze the fine scale structure of the surface and subsurface oxides of annealed sample cross-sections. Focused ion beam (FIB) milling via a NVision 40 by Zeiss was used to prepare site-specific TEM samples, during which the sample was milled by 30 keV Ga ions until transparent to the TEM electron beam. In order to protect the steel surface during FIB

sample preparation, carbon was deposited on it. A FEI Titan 80-300 TEM microscope equipped with an electron energy loss spectroscopy (EELS) analytical facility was used for TEM analysis. Both elemental mapping and quantitative point analysis were carried out using EELS, where an acceleration voltage of 300 keV was used and the energy resolution in monochromated mode was tuned to 0.08 eV full width half-maximum (FWHM) at the zero-loss peak. Mn-L, O-K, Si-K and Fe-L edges were collected for all samples. Gatan Digital Micrograph 2.3 was used to process the obtained EELS spectra. The pre-edge background was removed and the spectra for Mn and O were aligned in energy using the highest intensity feature of the Fe-L_3 edge at 708 eV and were normalized for baseline and intensity.

In order to measure either the thickness of the oxides formed on or the depth of the oxides formed below the surface of the experimental steels during annealing prior to galvanizing, at least 30 measurements were done on the TEM cross-sectional micrographs using ImageJ 1.42q software and the average of the values was reported with a 95% confidence interval.

3.4   Results

3.4.1   Selective oxidation prediction

Wagner [23] proposed a model to predict the transition from internal to external bulk selective oxidation for a single crystal binary M-X alloy in which M is the noble matrix and X the selectively oxidized solute element:

$$N_{x,crit}^0 = \left[\frac{\pi g^* V N_O^S D_O}{2n V_{XO_n} D_X} \right]^{1/2} \tag{3.1}$$

where:

$N_{x,crit}^0$ is the critical mole fraction of the alloying element X for the transition from internal to external oxidation;

$g*$ is the critical volume fraction of the oxide in the matrix which blocks the inward flux of oxygen and results in the transition from internal to external oxidation, initially determined to be 0.3 by Rapp [24] for a Ag-In alloy. However, Lashgari et al. [25] experimentally determined this value to be 0.2 for austenitic Fe-Mn alloys;

N_O^S is the oxygen molar concentration at the external surface;

V, V_{XOn} are the molar volumes of the alloy and XO_n oxide, respectively;

and D_O and D_X are the bulk diffusion coefficients for oxygen and the selectively oxidized alloying element X, respectively.

Internal selective oxidation occurs when the outward flux of the alloying element X is greater than the outward flux of oxygen and $N_X^0 < N_{X,crit}^0$. External selective oxidation, on the other hand, occurs when the outward flux of the alloying element is greater than the inward flux of oxygen and $N_X^0 \geq N_{X,crit}^0$.

Mataigne et al. [26], extended the Wagner model by considering that all species diffuse much more rapidly through short circuit diffusion paths such as grain boundaries and dislocation pipes than is the case for the bulk lattice. In their proposed model, grain boundary oxidation was considered by assuming that the activation energy for grain boundary diffusion was half the value of that for bulk diffusion, as given by:

$$N_{X,crit,GB}^O = \left[\frac{\pi g^* V N_O^S D_O' \exp(\frac{-Q_O}{2RT})}{2n V_{XO_n} D_X' \exp(\frac{-Q_X}{2RT})} \right]^{1/2} \tag{3.2}$$

Using the classic Wagner equation [23] and the grain boundary selective oxidation model of Mataigne et al. [26], it is possible to predict the selective oxidation mode of Mn and Si in the

present experimental alloy at 1093 K (820 °C) in a N_2-5 vol.% H_2 process atmosphere as a function of the process atmosphere. It is noteworthy that in predicting the selective oxidation mode for Mn, 0.2 was used for g^* [25].

Figure 3.2 shows an example of the predicted selective oxidation mode of Mn and Si in ferrite at 1093 K (820 °C), in which the transition between external and internal oxidation for Mn and Si is shown for both the bulk and along the grain boundaries using orange and green lines, respectively. The horizontal dashed lines in Figure 3.2(a) and (b) show the mole fraction of Mn and Si (i.e. 0.02 and 0.025, respectively) in the experimental alloy. Table 3.3 summarizes the predicted oxidation mode for Mn and Si in ferrite and austenite, as determined using equations (3.1) and (3.2).
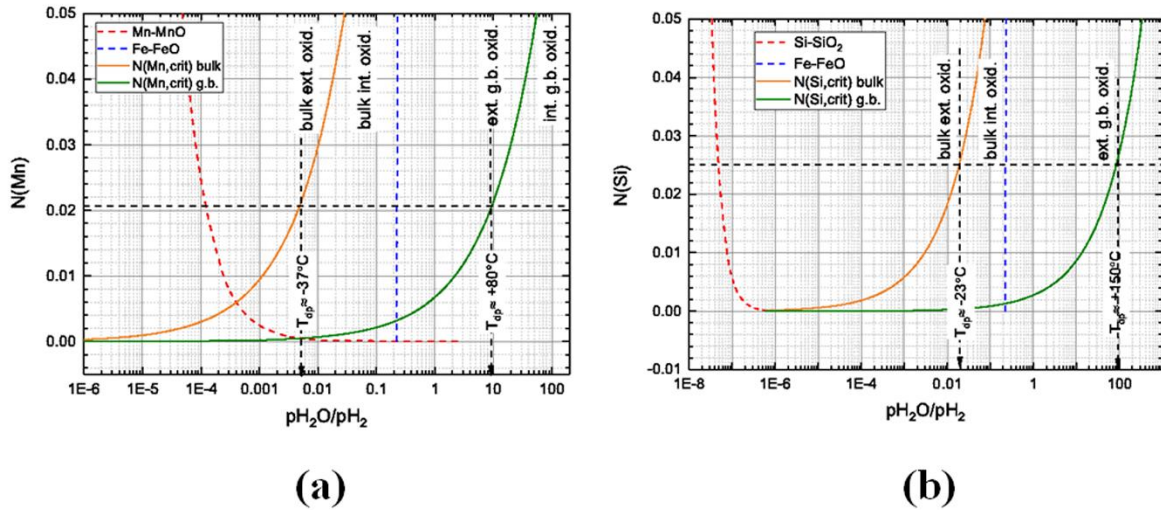
Figure 3.2: Predicted selective oxidation mode of (a) X = Mn and (b) X=Si in a α-Fe-X binary alloy at 1093 K (820 °C) in a N_2-5 vol.% H_2 process atmosphere.

Table 3.3: Predicted Selective Oxidation Mode of Fe-0.1C-2Mn-1.3Si at an Intercritical Annealing Temperature of 1093 K (820 °C) as a Function of Process Atmosphere using the Wagner [23] and Modified Models [26]

Process Atmosphere Name	Alloying Element	GB Diffusion		Bulk Diffusion	
		Ferrite	Austenite	Ferrite	Austenite
223 K (–50 °C) dp	Si	External	External	External	External
	Mn	External	External	External	Internal
243 K (–30 °C) dp	Si	External	External	External	External
	Mn	External	External	Internal	Internal
278 K (+5 °C) dp	Si	External	External	Internal	Internal
	Mn	External	External	Internal	Internal

3.4.2   Microstructure

Figure 3.3 shows the steel cross-sectional microstructure before and after being intercritically annealed for 120 seconds under the three process atmosphere dew points of 223 K (–50 °C), 243 K (–30 °C), and 278 K (+5 °C). The phases found in the microstructures are labeled in each image, where F = ferrite, P = pearlite and M = martensite. The as-received steel microstructure comprised elongated ferrite and pearlite islands, which were homogeneously distributed in the ferrite matrix (Figure 3.3(a)). However, after annealing at all three dew points, non-homogeneities could be observed in the microstructure moving from the center to the surface (Figure 3.3(b-d)). At the center, for example, the microstructure comprised a mixture of ferrite and martensite, whereas at the surface, a layer containing only ferrite, whose thickness increased with increasing process atmosphere pO_2 (i.e. approximately 1 μm, 5 μm and 10 μm under 223 K (–50 °C), 243 K (–30 °C) dp and 278 K (+5 °C) dp process atmospheres, respectively) was observed. The formation of this ferrite layer is known to be the result of either decarburization and/or Mn depletion during selective oxidation. Similar observations have been reported by other authors [9,27,28].
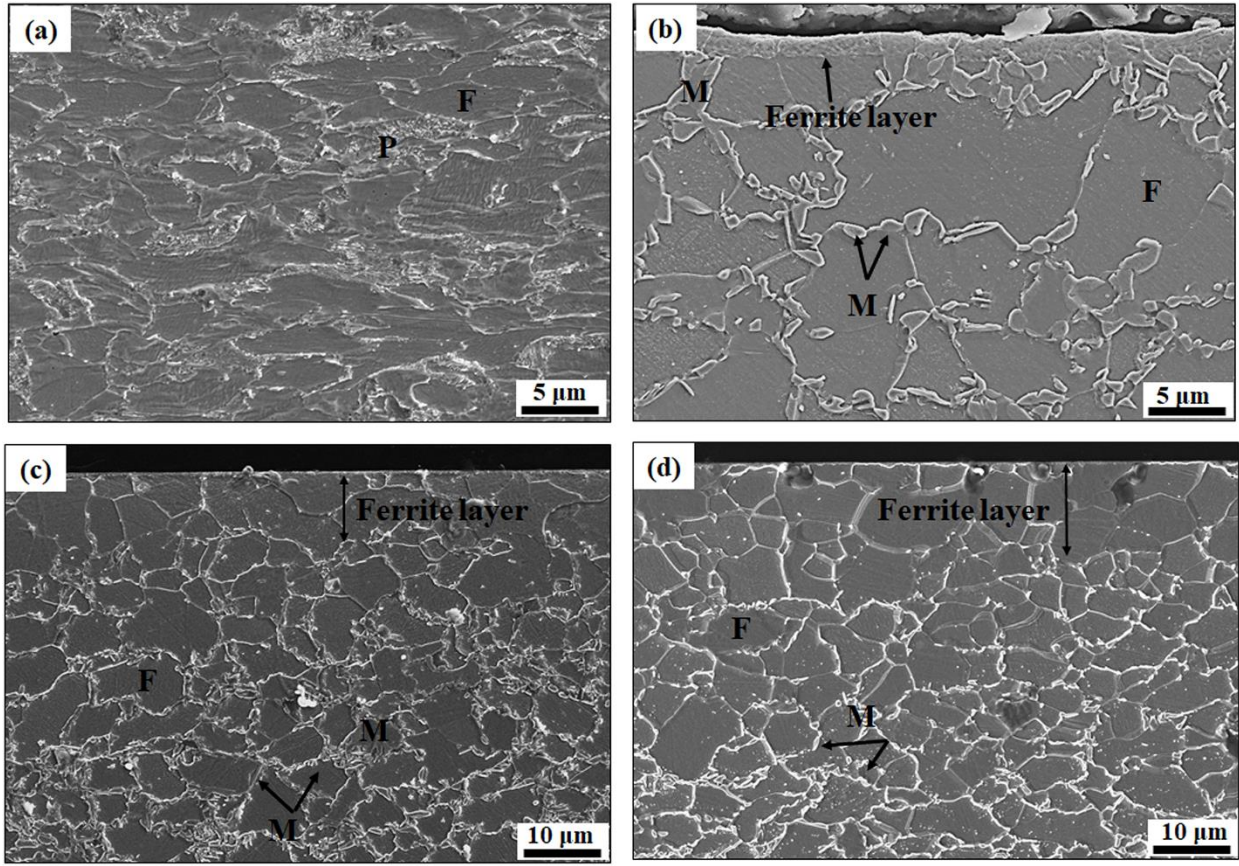
Figure 3.3: SEM images of the steel microstructure before and after annealing for 120 s at 1093 K (820 °C). (a) as-received steel, (b) steel annealed under the 223 K (–50 °C) dp process atmosphere, (c) steel annealed under the 243 K (–30 °C) dp process atmosphere, (d) steel annealed under the 278 K (+5 °C) dp process atmosphere (F = ferrite, P = pearlite and M = martensite).

3.4.3   Selective oxidation

Mn and Si XPS depth profiles are presented in Figure 3.4 to semi-quantitatively determine the surface oxide thickness and the subsurface oxidation mode of the alloying elements during annealing under the three process atmospheres (Table 3.2). For the sake of simplicity, the results are shown for the industrially relevant annealing time of 120 s and the longest annealing time of 600 s used in this research.

For the lowest pO_2 process atmosphere (i.e. 223 K (–50 °C) dp, Table 3.2), both Si and Mn showed considerable surface enrichment relative to their bulk concentrations, which rapidly decreased with increasing depth to values comparable to the nominal bulk concentrations of each element (Figure 3.4(a)). Increasing the annealing time from 120 s to 600 s resulted in an increase in the external oxide thickness and enrichment of the immediate subsurface from approximately 100 nm to approximately 150 nm, respectively. It should be noted that the confinement of the enrichment zone to the outer surface is indicative of an external oxidation mode, consistent with the predictions of the Wagner model for both Mn and Si in ferrite (Table 3.3).

Increasing the process atmosphere pO_2 to the 243 K (–30 °C) dp (Table 3.2) led to enrichment of both Mn and Si above the bulk composition deeper into the subsurface (Figure 3.4(b)), indicative of the transition from external to internal oxidation. This observation is consistent with the Mn oxidation mode predicted by the Wagner [23] and modified Wagner models [26] (Table 3.3) for ferrite and austenite. However, the experimental observation of internal oxidation did not conform to the predictions for Si. Further inspection of Figure 3.4(b) will show that the external oxides for the 243 K (–30 °C) dp process atmosphere samples was significantly thinner (approximately 50 nm) than their 223 K (–50 °C) dp process atmosphere counterparts, also indicative of the transition from external to internal oxidation having occurred. It can also be seen that the depth of internal oxidation increased with increasing annealing time from 120 s to 600 s, as would be expected of a diffusion driven process.

Further increasing the process atmosphere pO_2 to 278 K (+5 °C) dp (Table 3.2) resulted in similar depth profiles as were observed for the 243 K (–30 °C) dp process atmosphere, with the most significant difference being an increased depth of internal oxidation for the 278 K (+5 °C) dp process atmosphere for a given annealing time. As was the case for the 243 K (–30 °C) dp

atmosphere, the depth of internal oxidation increased with increasing the annealing time

(Figure 3.4(c)). Comparison of these results to the predictions of the Wagner model for the 278

K (+5 °C) dp process atmosphere (Table 3.3) will show that these results correlated well for both

Mn and Si for both austenite and ferrite. Overall, for all process atmospheres explored, the

Wagner and modified Wagner model predictions coincided well with the observations of Mn

oxidation mode for ferrite. However, the Wagner model predicted Si external oxidation for the

243 K (–30 °C) dp process atmosphere, which does not agree with the XPS observations.

However, the Wagner model predicted Si internal oxidation for the 278 K (+5 °C) dp process

atmosphere and external oxidation for the 223 K (–50 °C) dp process atmosphere, in agreement

with the XPS observations.

The oxides were identified by comparing the measured XPS binding energies to those taken

from the literature [29,30,31]. Table 3.4 summarizes the major oxide phases identified on the

steel surfaces. For the lower pO_2 223 K (–50 °C) and 243 K (–30 °C), the surface oxides were

identified as either $MnSiO_3$ or Mn_2SiO_4, in addition to MnO and SiO_2. It should be noted that, in

the cases of the 278 K (+5 °C) dp steel, no SiO_2 could be detected. It is also noteworthy that, due

to strong similarities in their Mn $2p_{3/2}$ and O 1s XPS binding energies, $MnSiO_3$ and Mn_2SiO_4

could not be easily distinguished in the present case and this is denoted through the use of

parentheses in Table 3.4. Thus, EELS was also used to identify the surface oxides via the TEM

thin foils, as will be discussed below.

Table 3.4: Identification of Oxides on the Steel Surface Using XPS

Process Atmosphere Name	Major Oxide Phases Present
223 K (–50 °C) dp	($MnSiO_3$, Mn_2SiO_4) [29], MnO [30], SiO_2 [31]
243 K (–30 °C) dp	($MnSiO_3$, Mn_2SiO_4) [29], MnO [30], SiO_2 [31]
278 K(+5 °C) dp	($MnSiO_3$, Mn_2SiO_4) [29], MnO [30]

Figure 3.5 through Figure 3.7 show the morphology and distribution of the external oxides on the surfaces of the experimental steel intercritically annealed at 1093 K (820 °C) for the 223 K (–50 °C) dp, 243 K (–30 °C) dp and 278 K (+5 °C) dp process atmospheres, respectively, as a function of annealing time. As can be seen, regardless of the process atmosphere pO_2, holding for longer times at the IAT led to an increase in surface coverage and coarsening of the oxides. This would be expected as prolonged annealing provided more time for growth of the surface oxides. As an example, per Figure 3.5(a), oxide clusters can be seen after an annealing time of 60 s. Increasing the annealing time to 120 s led to the growth of the oxide clusters and the formation of boundaries between them (Figure 3.5(b)). Further increasing the annealing time resulted in full coverage of the surface by the oxides and no boundaries could be seen for longer annealing times. This observation is in qualitative agreement with the XPS results indicating an increase in oxide thickness by increasing the annealing time from 120 s to 600 s.

Per Figure 3.5, the 223 K (–50 °C) dp process atmosphere steel surfaces were covered with compact oxides. The observed external selective oxidation is in qualitative agreement with both the XPS results (Figure 3.4(a) and the external oxidation mode predicted using the Wagner [23] and modified Wagner models [26] (Table 3.3), which predicted external oxidation for both Mn and Si in bulk ferrite and along grain boundaries. At the higher pO_2 243 K (–30 °C) dp process atmosphere (Figure 3.6), the steel surfaces displayed a thinner external oxide compared to the lower pO_2 223 K (–50 °C) dp process atmosphere, as exemplified by visible rolling and grinding lines "printed through" the external oxide layer, consistent with the XPS observations (Figure 3.4(b)). Further increasing the process atmosphere pO_2 using the 278 K (+5 °C) dp process atmosphere (Figure 3.7) resulted in a reduction in surface coverage, in agreement with the external to internal oxidation transition predicted by the Wagner model [23] and the XPS

data (Figure 3.4(c)), which indicated a significant increase in the depth of internal oxidation and decrease in external Mn and Si external oxidation.

In addition, while for the 223 K (–50 °C) and 243 K (–30 °C) dp process atmosphere samples the surfaces were covered with film-like oxides (Figure 3.5, Figure 3.6), increasing the process atmosphere pO_2 through utilizing the 278 K (+5 °C) dp process atmosphere altered the morphology of the oxides to more widely spaced nodule-like particles (Figure 3.7), which have been shown to be less problematic in the promotion of reactive wetting by the continuous galvanizing bath [6,8].
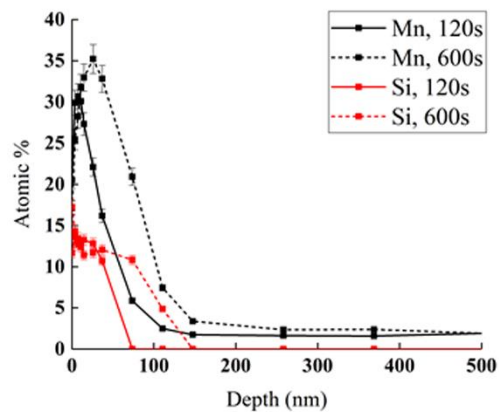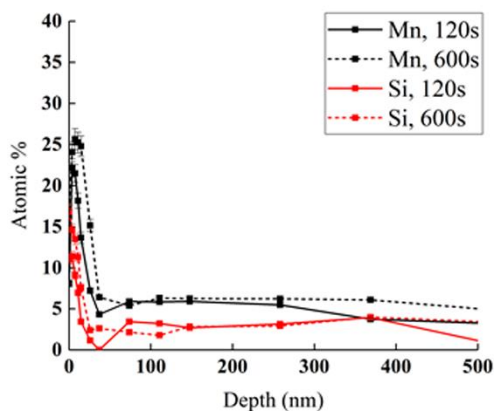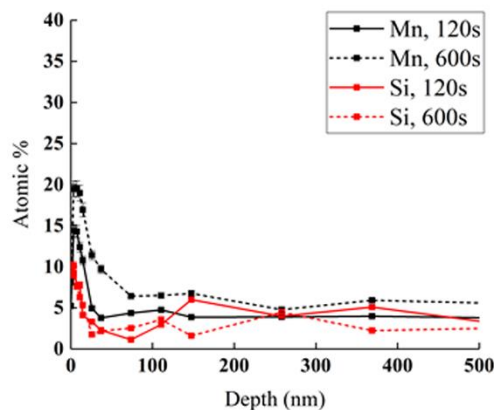
Figure 3.4: Mn and Si XPS elemental depth profiles as a function of 1093 K (820 °C) annealing time and process atmosphere pO$_2$: (a) 223 K (–50 °C) dp for 120 and 600 s, (b) 243 K (–30 °C) dp for 120 and 600 s, (c) 278 K (+5 °C) dp for 120 and 600 s.
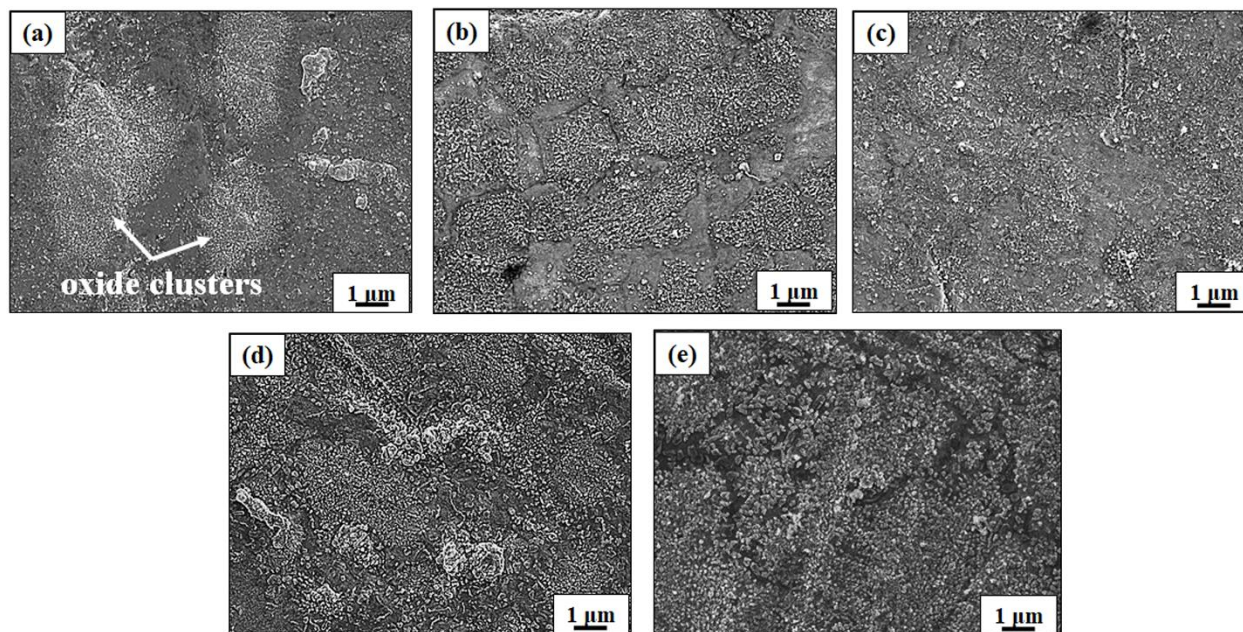
Figure 3.5: SEM images of steel surfaces annealed at 1093 K (820 °C) under the 223 K (–50 °C) dp process atmosphere: (a) 60s, (b) 120s, (c) 240s, (d) 360s and (e) 600s.
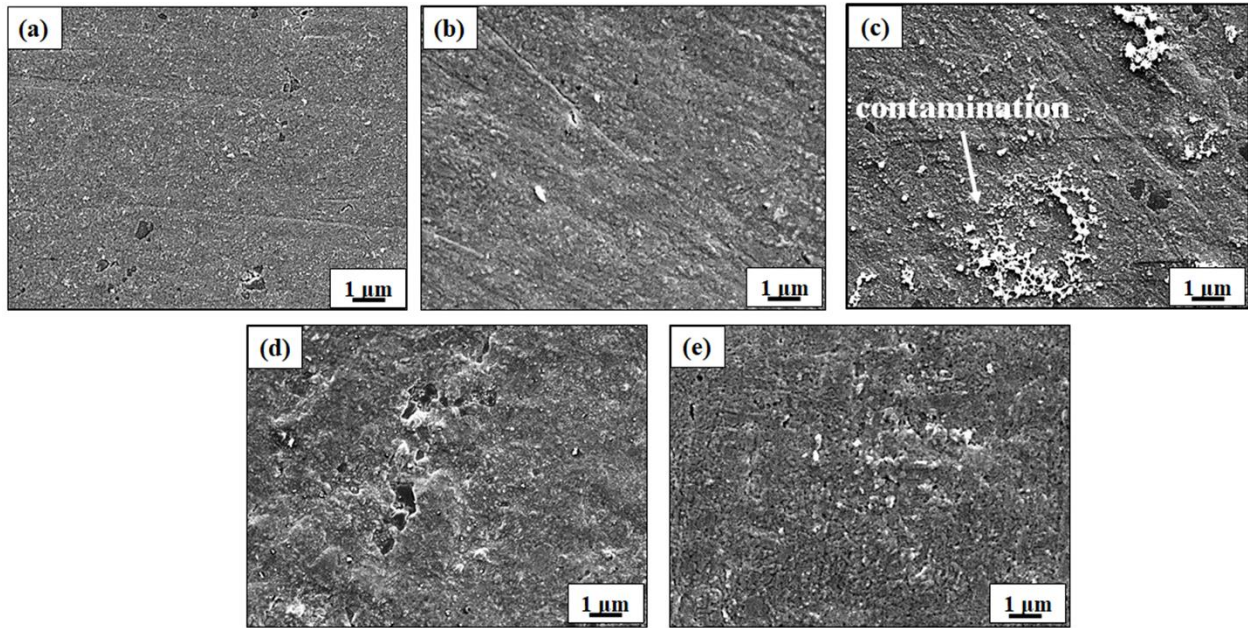
Figure 3.6: SEM images of steel surfaces annealed at 1093 K (820 °C) under the 243 K (–30 °C) dp process atmosphere for: (a) 60s, (b) 120s, (c) 240s, (d) 360s and (e) 600s.
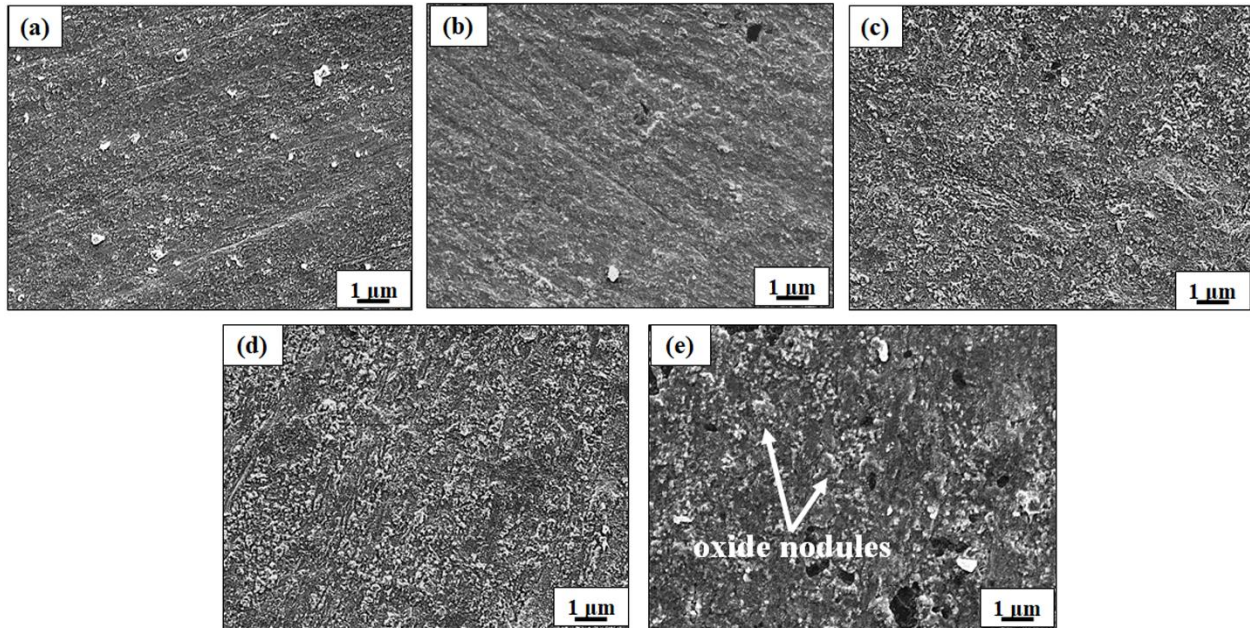
Figure 3.7: SEM images of steel surfaces annealed at 1093 K (820 °C) under the 278 K (+5 °C) dp process atmosphere for: (a) 60s, (b) 120s, (c) 240s, (d) 360s and (e) 600s.

TEM was used to investigate the fine scale external and internal oxide microstructural development. For the sake of clarity, samples which were annealed for 120 s under each of the experimental process atmospheres (see Table 3.2) were chosen to investigate the effect of the process atmosphere on the selective oxidation of the experimental steel.

Figure 3.8 shows a cross-sectional TEM micrograph of the oxide-substrate interface arising from annealing the steel under the 223 K (–50 °C) dp process atmosphere for 120 s. As can be seen from Figure 3.8, two oxide morphologies were observed on the surface as are further detailed in Figure 3.9 and Figure 3.10, respectively. In particular, an area with a multi-layer 32±5 nm-thick oxide, designated area A, and a 38±5 nm-thick compact, film-like oxide, designated as area B, were studied in greater detail. In addition, small particles located in the subsurface to a

depth of 64±15 nm were studied. It can also be seen that oxides formed along the grain boundary (in area A) to a depth of ~200 nm.

Figure 3.9 shows the TEM cross-sectional micrograph of area A (Figure 3.9(a)), indicated in Figure 3.8, along with O, Fe, Mn and Si elemental maps of area A (Figure 3.9(b)) and the Mn-$L_{2,3}$, O-K and Si-K edge energy loss spectra (Figure 3.9(c)) of points 1, 2 and 3 demarcated in Figure 3.9(a). TEM elemental mapping shows that, while the nodule-like upper/external oxides were Mn-rich, the oxides at the steel/oxide interface were rich in Si. The intermediate oxide layer was rich in both Mn and Si. By comparing the features of the Mn-$L_{2,3}$ and O-K edges in the EELS spectra (Figure 3.9(c)) of points 2 and 3 with the standard Mn_2SiO_4, $MnSiO_3$ [29] and MnO [32,33] spectra, it was concluded that the upper and middle oxides correspond to MnO and $MnSiO_3$, respectively. This is while point 1, which showed no Mn peak, corresponds to SiO_2 [34].

Figure 3.10 shows a TEM cross-sectional micrograph of area B (Figure 3.10(a)), indicated in Figure 3.8, along with O, Fe, Si and Mn elemental maps (Figure 3.10(b)). TEM elemental mapping of the grain boundary oxide shows that, while the oxide had a higher concentration of Mn at the surface, the tip of the grain boundary oxide within the subsurface comprised only Si

and O (Figure 3.10(b)). EELS analysis of the surface oxide identified it as $MnSiO_3$ and the oxide at the tip of the grain boundary was identified as SiO_2.
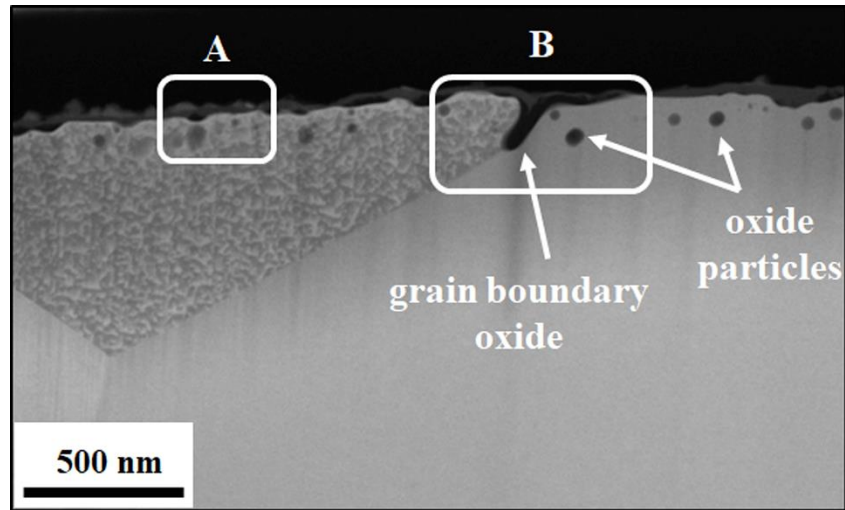
Figure 3.8: TEM cross sectional micrograph of the surface and subsurface of the CMnSi steel annealed at 1093 K (820 °C) under the 223 K (–50 °C) dp process atmosphere for 120 s; A and B correspond to the areas analyzed in greater detail shown in A) Figure 3.9 and B) Figure 3.10 (reprinted with permission from [35]).
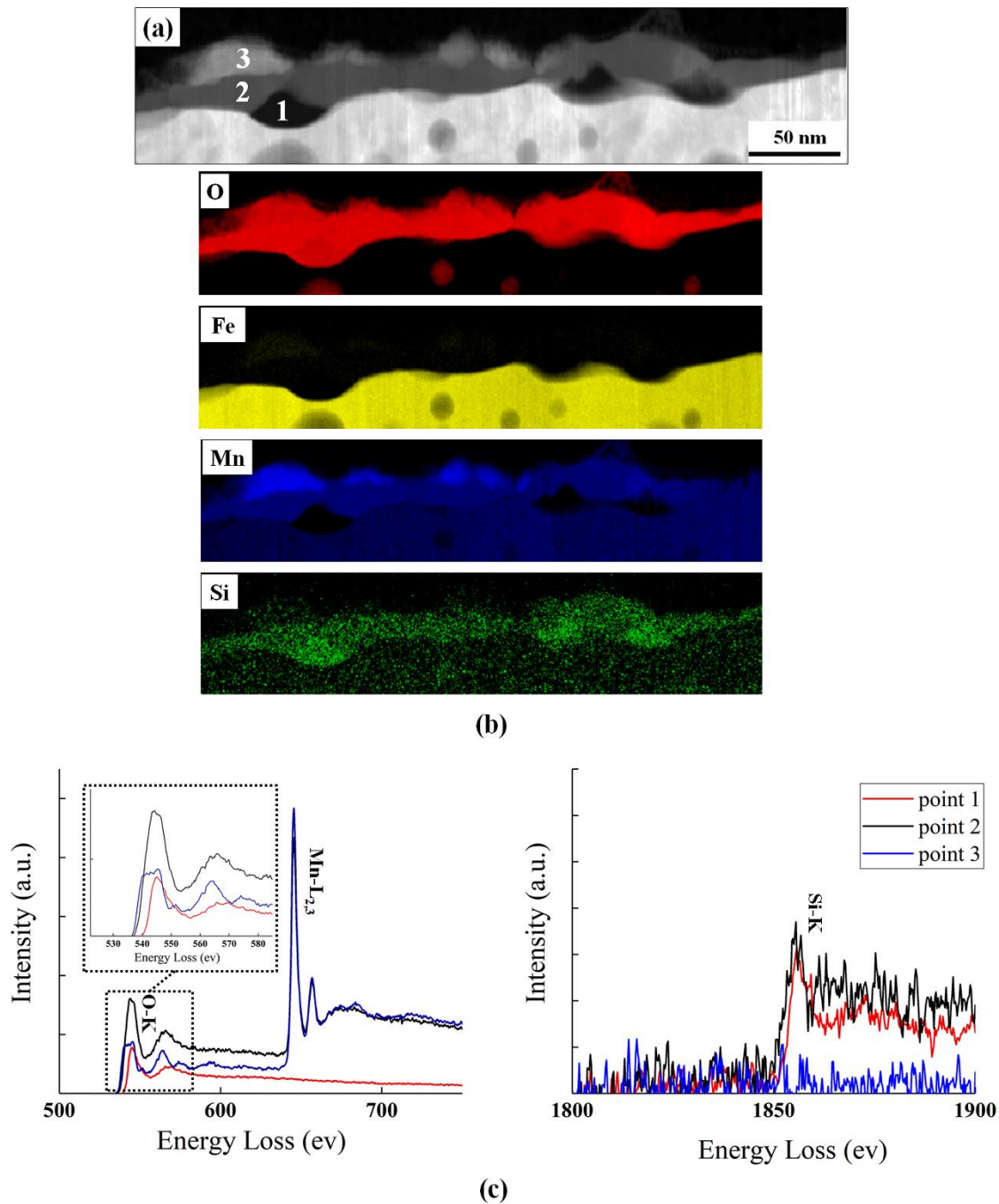
Figure 3.9: (a) TEM cross sectional micrograph of area A, shown in Figure 3.8. (b) TEM elemental maps of (a). (c) Mn-L$_{2,3}$, O-K and Si-K edge energy loss spectra of the points 1 through 3 in (a).
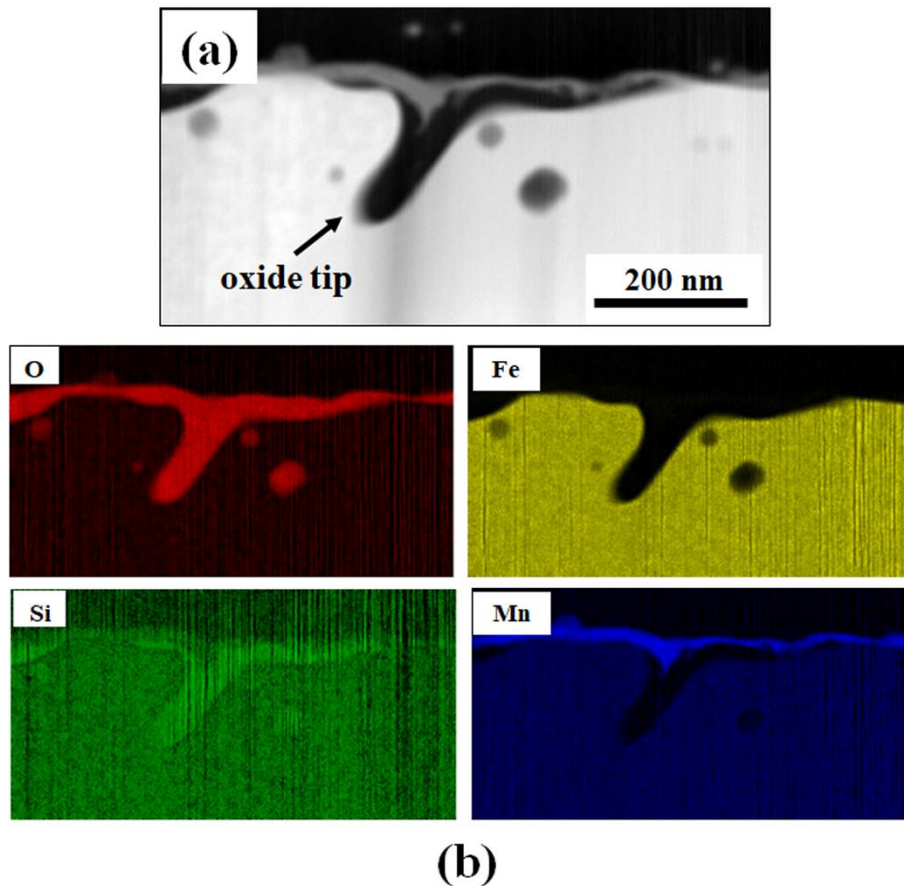
Figure 3.10: (a) TEM cross sectional micrograph of area B, shown in Figure 3.8. (b) TEM elemental maps of (a) (reprinted with permission from [35]).

Figure 3.11 shows a cross sectional TEM view across the oxide-substrate interface after annealing the experimental AHSS under the 243 K (–30 °C) dp process atmosphere for 120 s. As can be seen in Figure 3.11(a), oxides were observed both on the steel surface and in the subsurface. Figure 3.11(b) shows a detailed micrograph of the surface oxides within zone A in Figure 3.11(a). As can be observed, a 15±3 nm thick oxide film was present in this zone. These surface oxides were identified by EELS as a mixture of Mn_2SiO_4 and $MnSiO_3$.

In the internal oxidation zone denoted B in Figure 3.11(a) two distinct oxide morphologies can be easily distinguished and are detailed in Figure 3.11(c). The first zone encompassed the first 351 ± 46 nm below the surface and included oxide particles located both in the bulk microstructure and decorating the grain boundaries. The second zone comprised a network of grain boundary oxides reaching as deep as ~ 1.5 μm below the substrate surface (Figure 3.11(a)). These observations are in agreement with the report of Gong et al. [36] on the oxidation of a C-1.53Mn-1.46Si TRIP steel after intercritical annealing at 1143 K (870 °C) for 220 seconds in a N_2-10 vol.% H_2 process atmosphere with a dew point of 276 K (+3 °C).

The smaller particles located closer to the surface were determined by EELS to be a mixture of $MnSiO_3$ and Mn_2SiO_4. Per Figure 3.11(c), there was a difference in contrast between the center and the shell of the oxide particles located deeper in the subsurface, which suggested a difference in the composition of the oxide from its center to its shell. EELS analysis revealed that, while the center of the oxide was SiO_2, the shell was $MnSiO_3$. The same layered structure was observed for the grain boundary oxide network located further into the subsurface, as can be seen from the elemental maps in Figure 3.12. Using EELS analysis on the grain boundary oxide network shown in Figure 3.12, it was concluded that the upper portion of the oxide comprised a few nanometers of $MnSiO_3$ embracing an SiO_2 core, whereas the lower portion of the grain boundary oxide (i.e. deeper into the subsurface) was SiO_2 only.

Figure 3.13(a-d) exhibit selected area diffraction patterns of the oxides formed during annealing of the experimental steel under the 243 K (–30 °C) dp process atmosphere for 120 s. As the spot patterns of the diffraction pattern are indicative of crystalline phase and a diffuse ring is characteristic of amorphous phase, it can be concluded that the $MnSiO_3$ and Mn_2SiO_4 surface and subsurface oxides were crystalline, while the SiO_2 was amorphous.
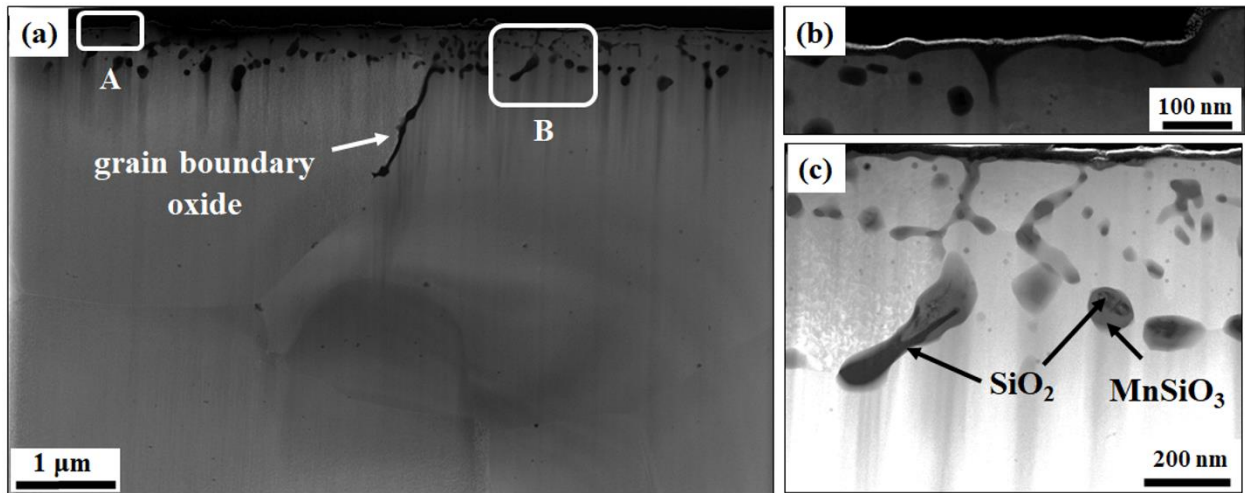
Figure 3.11: TEM cross sectional micrograph of the surface and subsurface of the experimental steel annealed at an intercritical temperature of 1093 K (820 °C) under a 243 K (–30 °C) dp process atmosphere for 120 s. (a) Overview of the surface and subsurface oxides. (b) Detailed micrograph of zone A. (c) Detailed micrograph of zone B.
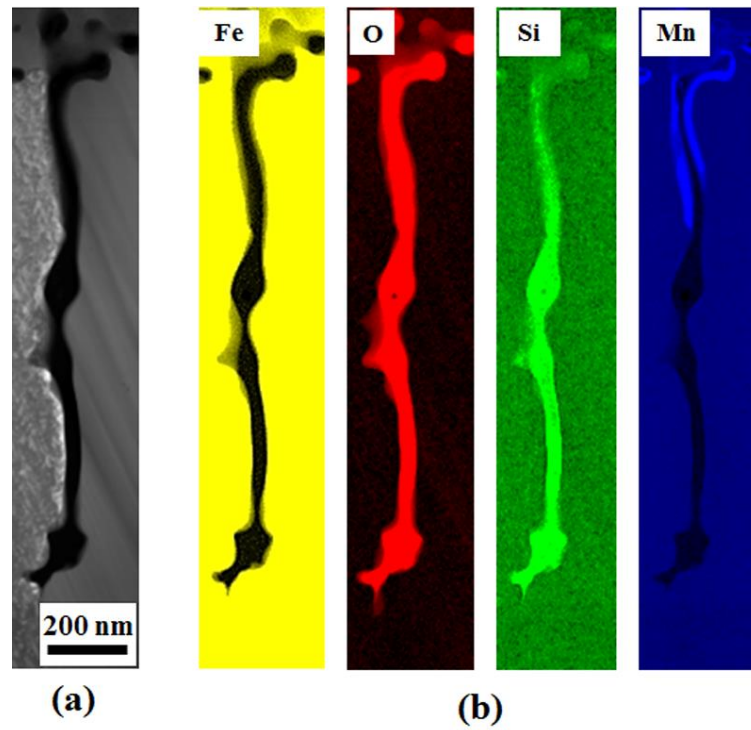
Figure 3.12: (a) Detailed TEM micrograph of the oxide network formed along a grain boundary of the CMnSi steel annealed at an intercritical annealing temperature of 1093 K (820 °C) under the 243 K (–30 °C) dp process atmosphere for 120 s. (b) TEM elemental mapping of the oxide network.
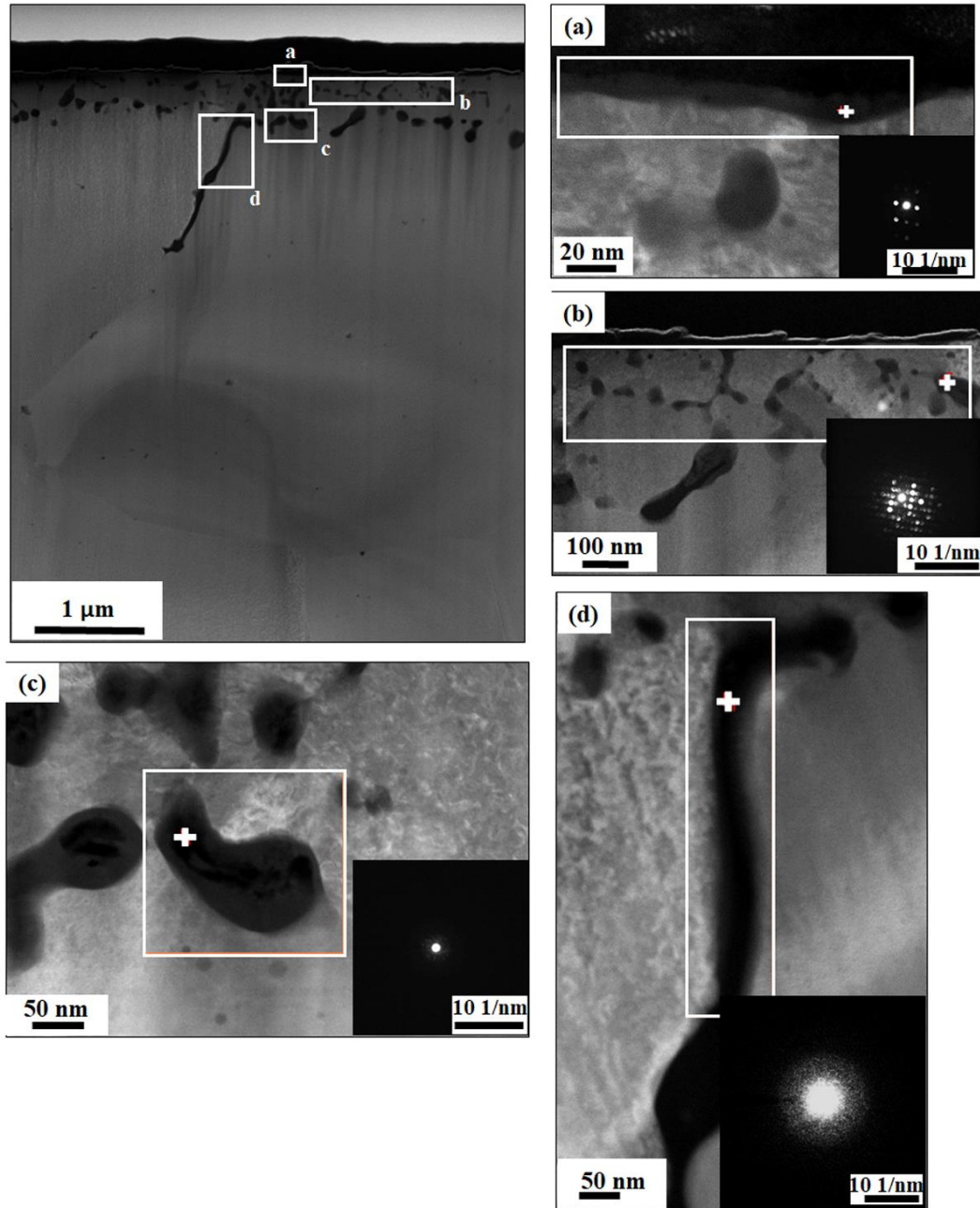
Figure 3.13: (a), (b), (c) and (d) Detailed micrograph of the areas marked as a, b, c and d in the TEM cross sectional micrograph of the surface and subsurface of the CMnSi steel annealed at the intercritical temperature of 1093 K (820 °C) under a 243 K (–30 °C) dp process atmosphere for 120 s, with diffraction patterns corresponding to the points shown.

TEM and EELS analysis of the 278 K (+5 °C) dp steel (not shown here) revealed the existence of a relatively thin, nodule/plate-shaped oxide layer of a mixture of $MnSiO_3$ and

Mn_2SiO_4 on the steel surface along with internal $MnSiO_3$ and Mn_2SiO_4 particles both in the bulk and along the grain boundaries. On the other hand, as for the 243 K (–30 °C) dp process atmosphere samples, a grain boundary oxide network with a layered composition was observed.

Figure 3.14 summarizes the depth of internal oxidation for an annealing time of 120 s at 1093 K (820 °C), according to TEM observations, as a function of atmosphere oxygen partial pressure. As can be seen, increasing the atmosphere pO_2 resulted in an increase in the depth of internal oxidation, in agreement with the XPS results (Figure 3.4) and generally accepted principles on the effect of increasing process atmosphere pO_2 on selective oxidation kinetics.
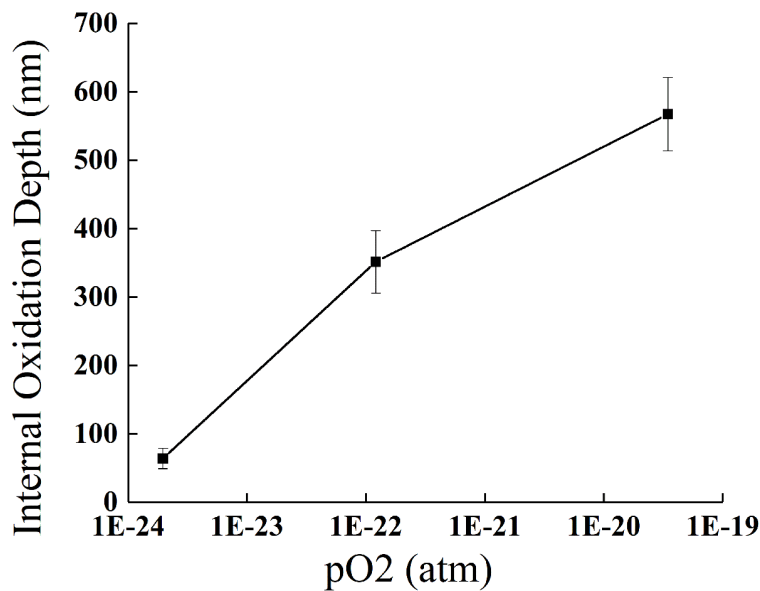
Figure 3.14: Depth of internal oxides formed in the CMnSi steel annealed at 1093 K (820 °C) for 120 s as a function of the process atmosphere pO_2.

3.5 Discussion

The effect of process atmosphere pO_2 on the microstructure of an experimental Fe-0.1C-2Mn-1.3Si (wt.%) AHSS was investigated. It was shown that after annealing the experimental alloy at 1093 K (820 °C) for 120 s under a N_2-5H_2 (vol.%) process atmosphere under three different dew points (i.e. pO_2, Table 3.2) of 223 K (–50 °C), 243 K (–30 °C), and 278 K (+5 °C), the microstructure comprised ferrite and martensite in the bulk and ferrite to a specific depth below the surface, depending on the process atmosphere pO_2. The formation of the ferrite layer is attributed to either decarburization and/or Mn depletion as a consequence of selective oxidation [27]. These observations are consistent with those of multiple authors [9,36,37,38,39] who also observed an austenite to ferrite transformation as a consequence of decarburization and/or Mn depletion during the selective oxidation of alloyed steels. For the lowest pO_2 223 K (–50 °C) dp process atmosphere, the oxygen potential was not sufficient to result in more than a few nanometer-thick ferrite layer below the surface. Moreover, the external film-like oxide covering the surface would impede decarburization. As would be expected, increasing the atmosphere dew point increased the degree of both decarburization and Mn selective oxidation, resulting in an increase in the thickness of the ferrite layer (i.e. approximately 5μm and 10μm under 243 K (–30 °C) dp and 278 K (+5 °C) dp process atmospheres, respectively). Comparison of the thickness of the ferrite layer (Figure 3.3) with the depth of internal oxidation observed at each process atmosphere (Figure 3.14) leads to the conclusion that selective oxidation occurred largely within a ferrite matrix for all the process atmospheres used in this study.

During annealing, oxides initially formed along ferrite grain boundaries as these are faster oxygen diffusion routes. Selective oxidation proceeded more slowly in the bulk ferrite due to the lower diffusivity of oxygen and the alloying elements. SiO_2 was the first oxide to form due to

two reasons: i) it is thermodynamically more stable versus MnO or the Mn-silicate species and ii) it has a negligible solubility product (7.2×10^{-5} $(ppm)^3$) versus MnO (11.22 $(ppm)^2$) in ferrite [40]. With increasing time, Mn atoms diffused to the SiO_2 particles and crystalline $MnSiO_3$ oxide was initially formed around the SiO_2 core as this required fewer Mn and O atoms compared to Mn_2SiO_4. This reaction proceeded from the outer SiO_2 surface to the inner core, resulting in the observed morphology of these structures in the bulk, on the external surfaces (Figure 3.11) and along the grain boundaries (Figure 3.10, Figure 3.12). The only difference observed, in the present case, was that the oxygen potential was higher at the surface versus within the substrate and the oxidation reactions could proceed closer to completion, resulting in the formation of mixed crystalline $MnSiO_3$ and Mn_2SiO_4, as were predicted to be thermodynamically stable [41], while deeper into the subsurface the oxygen flux was lower and the reaction could not reach completion.

As can be seen, the experimental observations are generally in good agreement with the oxidation mode transition predictions for ferrite made by the Wagner (using the $g^* = 0.2$ modification for Mn-MnO [25]) and the modified Wagner model for grain boundary oxidation (Table 3.3). For the lowest pO_2 223 K (–50 °C) dp process atmosphere (see Table 3.2) both Si and Mn were predicted to oxidize externally in the bulk ferrite and along its grain boundaries, which is consistent with the XPS (Figure 3.4(a)), SEM (Figure 3.5) and TEM (Figure 3.8) observations. According to the Wagner model, for the intermediate pO_2 243 K (–30 °C) dp process atmosphere (see Table 3.2), both Mn and Si were predicted to oxidize externally along ferrite grain boundaries. Also, Mn and Si were expected to oxidize internally and externally in the bulk ferrite, respectively. This is while XPS results (Figure 3.4(b)) and TEM results (Figure 3.11) indicated that Si oxidized internally in the bulk ferrite. This disagreement was

likely due to either the limitations of the Si diffusivity data, the proximity of the predicted internal/external transition (i,e. 250 K (–23 °C) dp, Figure 3.2) to the experimental conditions or, more likely, a combinations of both factors. At the highest pO_2 278 K (+5 °C) dp process atmosphere (see Table 3.2), external oxidation of Mn and Si was predicted along the ferrite grain boundaries and internal oxidation was predicted for both elements in the bulk ferrite, in agreement with experimental observations (Figure 3.4(c))

Using a high dew point or high pO_2 atmospheres during AHSS annealing has been reported to be a promising technique to encourage the internal selective oxidation of ignoble alloying elements [8,9,27] and promote reactive wetting of these more highly alloyed steels during continuous galvanizing. For example, surfaces which were relatively free of external oxides or were covered with thinner oxide films can be reactively wetted by the Zn (Al, Fe) bath, as shown by Bellhouse and McDermid [17]. This is due to the fact that external oxides act as barriers for contact between the Zn(Al,Fe) bath and the Fe substrate, preventing the required Fe dissolution reaction required to form the desired η-$Fe_2Al_5Zn_X$ interfacial layer at the substrate/coating interface [42,43].

According to the experimental observations in this study, using process atmosphere pO_2 consistent with promoting internal oxidation – in this case the 243 K (–30 °C) and 278 K (+5 °C) dp process atmospheres (Table 3.2) – are expected to be more advantageous in promoting reactive wetting of the experimental substrate compared to the lower pO_2 223 K (–50 °C) dp process atmosphere (Table 3.2). This advantage arises due to the surface oxide morphology comprised either thin films or widely spaced nodules. In addition, it has been reported that external MnO and Mn-Si mixed oxides cause less reactive wetting problems than SiO_2 [44,45,46] which has been suggested to be partially due to aluminothermic reduction of these

oxides during galvanizing [18,21] and bath infiltration along cracks at the metal/oxide interface, thereby exposing the steel strip to the bath and providing the conditions for the formation of the Fe-Al interfacial layer. However, it must be cautioned that the kinetics of aluminothermic reduction determine its effectiveness in aiding reactive wetting as, for a given set of annealing conditions, the aluminothermic reduction of MnO by dissolved Al in CGL bath is limited by the oxide thickness. Thus, increasing the alloy Mn content can have adverse effects on reactive wetting during continuous galvanizing [22,47,48].

It is also worth mentioning that the use of internal oxidation to promote reactive wetting during continuous galvanizing can have downstream effects with respect to fabrication processes such as forming and resistance spot welding [49]. The latter hypothesis – that internal oxidation will affect the resistance spot welding process – is the subject of a current investigation by the present authors and will be reported in a subsequent publication. In addition, the present authors will be reporting on the effect of the oxide morphology and oxidation mode of the present alloy surfaces on reactive wetting by the continuous galvanizing bath in a future contribution.

3.6   Conclusions

The selective oxidation of a Fe-0.1C-2Mn-1.3Si (wt.%) prototype advanced high strength steel during intercritical annealing at 1093 K (820 °C) in a N_2-5 (vol.%) H_2 atmosphere was investigated as a function of process atmosphere oxygen partial pressure and annealing time. From the above results, the following can be concluded:

1. For the 223 K (–50 °C) dp process atmosphere, a compact, thick, film-like oxide comprising crystalline $MnSiO_3$ and Mn_2SiO_4 and amorphous SiO_2, as well as nodules of MnO oxides, covered the surface while internal oxidation was insignificant.

81

2. Increasing the process atmosphere pO_2 by using the 243 K (–30 °C) dp resulted in a transition from external to internal selective oxidation and led the formation of oxides both on the surface and in the subsurface. The film-like external oxides were identified to be a mixture of crystalline $MnSiO_3$ and Mn_2SiO_4, MnO and amorphous SiO_2. The internal oxides were composed of both bulk spherical oxides and film-like grain boundary networks comprising outer Mn_2SiO_4 and $MnSiO_3$ shells embracing a SiO_2 core.

3. Further increasing the atmosphere pO_2 by employing the 278 K (+5 °C) dp process atmosphere altered the morphology of the external oxides from film-like for the 223 K (–50 °C) and 243 K (–30°C) dp process atmospheres to plate- and nodule-like particles. The external oxides were identified as MnO and mixture of Mn_2SiO_4 and $MnSiO_3$. The internal oxides had the same morphologies and chemistries as those observed for the 243 K (–30 °C) dp process atmosphere, with the most significant difference being an increased depth of internal oxidation.

4. Holding the experimental steel at the intercritical annealing temperature for longer times led to an increase in either the thickness of the external oxides or depth of internal oxidation.

5. A comparison between the experimental observations and the predictions of the Wagner and modified Wagner models for the transition from external to internal oxidation modes for both bulk and grain boundary selective oxidization determined that the oxidation mode predictions were generally in good agreement with the experimental observations.

3.7   Acknowledgments

Thomson and Ray Fullerton from the McMaster Steel Research Centre for assistance with the galvanizing simulations, Travis Casagrande and Andreas Korinek from the Canadian Centre for Electron Microscopy for aid with sample analysis and Li Sun (ArcelorMittal Dofasco) for assistance with XPS.

3.8   References

[1] C.M. Tamarelli, The Evolving Use of Advanced High-Strength Steels for Automotive Applications, Steel Market Development Institute, Michigan (2011).

[2] H. Liu, F. Li, W. Shi, S. Swaminathan, Y. He, M. Rohwerder, L. Li, Surf. Coatings Technol. 206 (2012) 3428–3436.

[3] S.-K. Lee, J.-S. Kim, N. Kang, K.-M. Cho, Met. Mater. Int. 18 (2012) 951–956.

[4] S.-K. Lee, J.-S. Kim, J.-W. Choi, N. Kang, K.-M. Cho, Met. Mater. Int. 17 (2011) 251–257.

[5] X. Vanden Eynde, J.P. Servais, M. Lamberigts, Surf. Interface Anal. 35 (2003) 1004–1014.

[6] E.M. Bellhouse, J.R. McDermid, Metall. Mater. Trans. A 41A (2010) 1539–1553.

[7] S. Alibeigi, "Short-term Formation Kinetics of the Continuous Galvanizing Interfacial Layer on Mn-containing Steels", PhD thesis, McMaster University (2014).

[8] L. Cho, S.J. Lee, M.S. Kim, Y.H. Kim, B.C. De Cooman, Metall. Mater. Trans. A 44A (2013) 362–371.

[9] L. Cho, G.S. Jung, B.C. De Cooman, Metall. Mater. Trans. A 45A (2014) 5158–5172.

[10] E.M. Bellhouse, "Galvanizing of Al-Si TRIP-assisted steels", Ph.D. thesis, McMaster University (2010).

[11] J. Mahieu, S. Claessens, B.C. De Cooman, Metall. Mater. Trans. A 32A (2001) 2905–2908.

[12] I. Parezanović, "Selective oxidation and segregation in commercial steels and model alloys (tools for improving the surface wettability by liquid Zn during hot dip galvanizing", Ph.D. thesis, Rheinisch-Westfälische Technische Hochschule Aachen (2005).

[13] E.M. Bellhouse, J.R. McDermid, Metall. Mater. Trans. A 43A (2012) 2426–2441.

[14] M. Norden, M. Blumenau, T. Wuttke, K.-J. Peters, Appl. Surf. Sci. 271 (2013) 19–31.

[15] E.M. Bellhouse, J.R. McDermid, Metall. Mater. Trans. A 41A (2010) 1460–1473.

[16] G.M. Song, T. Vystavel, N. van der Pers, J.T.M De Hosson, W.G. Sloof, Acta Mater. 60 (2012) 2973–2981.

[17] E.M. Bellhouse, J.R. McDermid, Metall. Mater. Trans. A 42A (2011) 2753–2768.

[18] R. Khondker, A. Mertens, J.R. McDermid, Mater. Sci. Eng. A 463 (2007) 157–165.

[19] R. Kavitha, J.R. McDermid, Surf. Coatings Technol. 212 (2012) 152–158.

[20] R. Sagl, A. Jarosik, D. Stifter, G. Angeli, Corros. Sci. 70 (2013) 268–275.

[21] Y.F. Gong, T.J. Song, H.S. Kim, J.H. Kwak, B.C. De Cooman, in Asia-Pacific Galvaniz. Conf., Seoul (2009) B-15.

[22] M. Blumenau, M. Norden, F. Friedel, K. Peters, Surf. Coat. Technol. 205 (2011) 3319–3327.

[23] C. Wagner, Zh. Elektrochem. 63 (1959) 772–782.

[24] R.A. Rapp, Corros. 21 (1965) 382–401.

[25] V.A. Lashgari, C. Kwakernaak, W.G. Sloof, Oxid. Met. 81 (2014) 435–451.

[26] J.M. Mataigne, M. Lamberigts, V. Leroy (1992) "Developments in the Annealing of Sheet Steels". In: R. Pradhan, I. Gupta (eds), Minerals, Metals & Materials Society, Warrendale, 511–528.

[27] H. Liu, Y. He, S. Swaminathan, M. Rohwerder, L. Li, Surf. Coatings Technol. 2.6 (2011) 1237–1243.

[28] T.L. Baum, R.J. Fruehan, S. Sridhar, Metall. Mater. Trans. B Process Metall. Mater. Process. Sci. 38 (2007) 287–297.

[29] A.P. Grosvenor, E.M. Bellhouse, A. Korinek, M. Bugnet, J.R. McDermid, Appl. Surf. Sci. 379 (2016) 242–248.

[30] B.R. Strohmeier, D.M. Hercules, J. Phys. Chem. 88 (1984) 4929–4992.

[31] J. Finster, Surf. Interface Anal. 12 (1988) 309–314.

[32] L. Laffont, P. Gibot, Mater. Charact. 61 (2010) 1268–1273.

[33] H.K. Schmid, W. Mader, Micron 37 (2006) 426–432.

[34] C.C. Ahnn, O.L. Krivanek with contributions by R.P Burgner, M.M. Disko, P.R. Swann (1983) "EELS Atlas, A reference guide of electron energy loss spectra covering all stable elements", Gatan Inc., Warrendale.

[35] G. Seyed Mousavi, J.R. McDermid, in Int. Conf. Zinc Zinc Alloy Coat. Steel Sheet, Tokyo (2017) 485–92.

[36] Y.F. Gong, H.S. Kim, B.C. De Cooman, ISIJ Int. 49 (2009) 557–563.

[37] M. Blumenau, M. Norden, F. Friedel, K. Peters, Surf. Coatings Technol. 206 (2011) 559–567.

[38] V.A. Lashgari, G. Zimbitas, C. Kwakernaak, W.G. Sloof, Oxid. Met. 82 (2014) 249–269.

[39] Y.F. Gong, H.S. Kim, B.C. De Cooman, ISIJ Int. 48 (2008) 1745–1751.

[40] D. Huin, P. Flauder, J.B. Leblond, Oxid. Met. 64 (2005) 131–167.

[41] Y. Suzuki, T. Yamashita, Y. Sugimoto, S. Fujita, S. Yamaguchi, ISIJ Int. 49 (2009) 564–573.

[42] A.R. Marder, Prog. Mater. Sci. 45 (2000) 191–271.

[43] M. Guttmann, Mater. Sci. Forum 155-156 (1994) 527–548.

[44] J. Maki, J. Mahieu, B.C. De Cooman, S. Claessens, Mater. Sci. Technol. 19 (2003) 125–131.

[45] Y. Takada, S. Shimada, J. Lee, M. Kurosaki, T. Tanaka, ISIJ Int. 49 (2009) 100–104.

[46] Y. Kim, M. Shin, C. Tang, J. Lee, Metall. Mater. Trans. B 41B (2010) 872–875.

[47] S. Alibeigi, R. Kavitha, R.J. Meguerian, J.R. McDermid, Acta Mater. 59 (2011) 3537–3549.

[48] M. Pourmajidian, J.R. Mcdermid, Metall. Mater. Trans. A 49A (2018) 1795–1808.

[49] C. Horvath, C. Matthew Enloe, J. Coryell, J.P. Singh, General Motors Co., in Proc. Int. Symp. New Dev. Adv. High-Strength Sheet Steels, Warrendale (2017) 1–10.

4   EFFECT OF DEW POINT ON THE REACTIVE WETTING OF A C-2MN-1.3SI (WT.%) ADVANCED HIGH STRENGTH STEEL DURING CONTINUOUS GALVANIZING

G. Seyed Mousavi, J.R. McDermid*

Steel Research Centre, McMaster University, Hamilton, Canada ON L8S 4L8

4.1   Abstract

The effect of oxygen partial pressure on the reactive wetting of a Fe-0.1C-2Mn-1.3Si (wt.%) advanced high strength steel during continuous galvanizing was determined. The steel was intercritically annealed at 1093 K (820 °C) for 120 s in a N_2-5 vol.% H_2 process atmosphere, where the oxygen potential was controlled by varying the process atmosphere dew points at 223 K (–50 °C), 243 K (–30 °C) and 278 K (+5 °C). All samples were immersed in a 0.2 wt.% dissolved Al continuous galvanizing bath at 733 K (460 °C) for 4 s. For the 243 K (–30 °C) and 278 K (+5 °C) dew point atmospheres, a well-developed Fe-Al intermetallic layer, indicative of a good reactive wetting, was observed due to the presence of either thin or plate/nodule-like oxides on the steel surface after annealing. This external oxide morphology facilitated contact between the Zn-alloy bath and the substrate via a variety of mechanisms, including interfacial infiltration through cracks due to thermal coefficient of expansion mismatch between the external oxide and substrate and aluminothermic reduction, which resulted in Fe dissolution from the substrate and consequent formation of the observed Fe-Al intermetallics. On the other hand, the poor reactive wetting observed for the samples annealed under the 223 K (–50 °C) dew point atmosphere was due to the formation of a thick, compact oxide layer on the steel surface, which provided an

effective barrier between the substrate and Zn bath, preventing contact between the two phases and the required Fe dissolution from the substrate surface.

Keywords: Reactive wetting; Oxygen partial pressure; Selective oxidation; Continuous galvanizing

4.2   Introduction

In the automotive industry, there is an increasing demand for using thinner cross sections of steel while providing a desirable combination of mechanical properties e.g. high specific strength, good formability and high energy absorption capacity. Dual Phase (DP) and Transformation Induced Plasticity (TRIP) steels are known as first generation (1G) advanced high strength steels (AHSS) which are extensively used in automotive structures due to their ability to satisfy these demands [1]. In order to protect the steel from corrosion by the ambient environment to ensure long-term structural stability during routine vehicle operation, continuous galvanizing is one of the most cost effective industrial processes [2,3]. However, a significant difficulty encountered during galvanizing DP and TRIP steels is that, in the commonly used industrial N_2-(5-20 vol.%) H_2-xH_2O annealing atmosphere, the process atmosphere oxygen partial pressure (i.e. pO_2) is sufficient to selectively oxidize Mn and Si during continuous annealing prior to galvanizing while maintaining reducing conditions with respect to Fe. It has been well established that external oxides, depending on their morphology, thickness, spatial distribution and chemistry, can adversely affect the reactive wetting of the steel strip by the molten zinc bath [4-,,7]. In particular, it has been advocated by several authors that film-like, continuous oxides are the most detrimental types for the promotion of reactive wetting by the continuous galvanizing bath [8-10] and that, in particular, external SiO_2 films should be avoided [11-13].

It has been suggested by Suzuki et al. [14] that the promotion of reactive wetting by the continuous galvanizing zinc bath requires controlling the alloy Si/Mn ratio at 0.5 or less to prevent the formation of external SiO_2. Mahieu et al. [11] reported that the existence of a Si-oxide on the surface of a C-1.57Mn-1.46Si (wt.%) TRIP steel prevented the formation of the desired η-$Fe_2Al_5Zn_X$ interfacial layer and resulted in poor reactive wetting during continuous galvanizing. Kim et al. [15] also related the coating quality of a series of dual phase steels containing 0 to 1.0 wt.% Si to the composition of external oxides formed during annealing. They showed that the reactive wetting of the steel worsened due to the change in the chemistry of external oxides from MnO to Mn_2SiO_4 to $MnSiO_3$ and then SiO_2 as the Si content of the alloy increased.

It has been established by several authors that the process atmosphere pO_2 can affect the morphology, thickness and chemistry of external oxides and, hence, reactive wetting of the steel substrate during continuous galvanizing [5,6,8,11,14,16]. For example, Bellhouse and McDermid [16] determined the effect of oxygen partial pressure on the selective oxidation and reactive wetting of 0.2C-1.5Mn-1.0Si-0.5Al (wt.%) and a 0.2C-1.5Mn-1.5Si (wt.%) TRIP-assisted steels by an Fe saturated Zn-0.2Al (dissolved, wt.%) continuous galvanizing bath. Good reactive wetting was obtained for both steels at lower oxygen partial pressure atmospheres, which was attributed to the presence of larger, relatively widely spaced external oxide nodules. This is while poor reactive wetting was reported to be the result of smaller, more closely spaced external oxide nodules which impeded the formation of the η-$Fe_2Al_5Zn_X$ interfacial layer for the higher oxygen partial pressure process atmosphere. Similarly, as discussed by Cho et al. [8], the reactive wetting of a C-2.2Mn-1.4Si (wt.%) TRIP steel during continuous galvanizing by a Zn-0.22Al (wt.%) bath was affected by the atmosphere pO_2, where a discontinuous, coarse

η-Fe$_2$Al$_5$Zn$_X$ interfacial layer with Fe-Zn intermetallics, indicative of relatively poor reactive wetting, was observed when annealing under a low pO$_2$ process atmosphere. This result was attributed to the presence of thick, film-like external oxides. However, for higher pO$_2$ process atmospheres, a thinner external oxide layer resulted in the formation of a well-developed Fe-Al interfacial layer and good reactive wetting.

Reactive wetting can occur despite the existence of external oxides, for which various mechanisms have been suggested [9,17-21]. One of the proposed mechanisms is the *in situ* aluminothermic reduction of the external oxides by the dissolved Al in the Zn (Al, Fe) bath. This mechanism was first suggested by Khondker et al. [17] for MnO on the surface of a DP steel. Using the Zn(Al, Fe) Al activity data derived from the phase diagram of McDermid et al. [22], the authors determined that there was a strong thermodynamic driving force for the reduction of surface Mn oxides by the dissolved Al in the Zn bath, based on the following reaction:

$$3MnO_{(solid)} + 2Al_{(solution)} \rightarrow Al_2O_{3(solid)} + 3Mn_{(solution)} \tag{4.1}$$
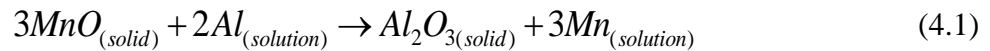
Later, Kavitha and McDermid [18] confirmed the aluminothermic reduction reaction of MnO by dissolved Al in the continuous galvanizing bath by showing that the thickness of the MnO layer grown on the surface of a 5.1 wt.% Mn steel was significantly reduced during immersion in a 0.2 wt.% Al (dissolved) simulated galvanizing bath, where the MnO reduction kinetics were expressed in terms of changes in the MnO layer thickness. In addition, they showed the presence of a thin layer of Al$_2$O$_3$ at the MnO-Zn interface and confirmed the dissolution of Mn into the Zn-alloy bath, consistent with reaction (4.1). Alibeigi et al. [23] also argued that the kinetics of aluminothermic reduction were likely a determining effect in aiding reactive wetting. In addition, the studies of Gong et al. [19] and Liu et al. [20], respectively, revealed the possibility of reducing Mn-Si mixed oxides and Cr oxides by the bath dissolved Al during continuous

galvanizing based on a favourable thermodynamic driving force for the reduction reactions, although it should be pointed out that no physical proof of the occurrence of the reduction reactions was provided.

Bridging of oxides by η-$Fe_2Al_5Zn_X$ intermetallics and liquid infiltration of bath metal through cracks at the oxide-substrate interface was suggested by Bellhouse and McDermid [5,21] as one of the reactive wetting mechanisms during continuous hot-dip galvanizing of the above cited 0.2C-1.5Mn-0.5Si-1Al (wt.%) and 0.2C-1.5Mn-1.5Al (wt.%) TRIP-assisted steels [16]. Similarly, Sagl et al. [24] suggested flaking of Mn-oxides by the growth of Fe-Al intermetallic phases and the trapping of nodular Mn-Si oxides by Fe-Al crystals as two supplementary mechanisms contributing to the improved reactive wetting of a series of DP steels with varying amounts of Si and Mn. This was in agreement with Bellhouse and McDermid [5,21] and Bellhouse [25], who had previously reported oxide flaking as a mechanism for enhancing the reactive wetting of a series of externally oxidized low-alloy Si-Al TRIP steels.

The aim of the present research is to determine the effect of steel surface chemistry, external oxide morphology and annealing process atmosphere oxygen partial pressure on the reactive wetting of a Fe-0.1C-2Mn-1.3Si (wt.%) AHSS. Within this context, it should be noted that the Si/Mn ratio of this alloy (Si/Mn = 0.65) is above the range advocated by Suzuki et al [14] for the promotion of reactive wetting and, thus, a secondary objective of this paper is to assess this thermodynamics-based recommendation relative to the impact of any morphological effects of the process atmospheres.

4.3   Experimental procedure

The chemical composition of the experimental steel is specified in Table 4.1. Experimental selective oxidation and reactive wetting/galvanizing CMnSi AHSS samples were used in this

investigation. The former comprised coupons with dimensions of 10 mm $\times$ 50 mm and the latter comprised 120 mm $\times$ 200 mm panels, and were cut from the as-received, 1.2 mm thick cold rolled steel sheet such that the longitudinal axis of the samples was parallel the rolling direction. Oil and other contaminants were removed from the galvanizing samples by brushing them with a nylon brush in a 353 K (80 °C) 2 wt.% NaOH solution. Samples were then rinsed with water, ultrasonically cleaned in isopropanol and dried in a warm air stream. Selective oxidation samples were lightly ground with 1200 grit SiC paper prior to annealing to avoid substrate roughness effects during surface analysis.

Table 4.1: Experimental Steel Chemical Composition (wt.%)

Steel	C	Mn	Si	Al	Ti	N	S	Fe	Si/Mn
Fe-2Mn-1.3Si	0.11	2.03	1.29	0.042	0.011	0.003	0.002	balance	0.65

During the annealing and galvanizing experiments, all of which were performed in the McMaster Galvanizing Simulator (MGS, Iwatani Surtec), the sample temperature were controlled by a K-type thermocouple (0.5 mm, ±3 K) spot welded to the sample surface coupled with a resident temperature process controller.

Selective oxidation experiments comprised heating to 773 K (500 °C) at 15 K/s, followed by heating to the intercritical annealing temperature (IAT) of 1093 K (820 °C) at 5 K/s, holding at the IAT for 120 s, cooling to 738 K (465 °C) at −20 K/s and holding at 738 K (465 °C) for 20 s to establish thermal equilibrium throughout the sample thickness. Samples were finally cooled to room temperature by N_2 jet cooling. In galvanizing experiments, another step was added before the final cooling, which comprised dipping the samples for 4 s in an Fe saturated 0.2 wt.% dissolved Al zinc bath at 733 K (460 °C). All heat treatments were carried out in a N_2-5 vol.% H_2 atmosphere with dew points (dp) of 223 K (–50 °C), 243 K (–30 °C) and 278 K (+5 °C).

Specifications for the process atmospheres, including the oxygen partial pressure (pO_2) at the IAT and the process atmosphere pH_2O/pH_2 ratio, can be found in Table 4.2. All oxidation samples were subsequently stored in anhydrous isopropanol in order to minimize additional oxidation of the surfaces prior to surface analysis. Full details of the analysis techniques and results from the selective oxidation samples can be found in reference [26].

Table 4.2: Experimental Process Atmospheres

Process Atmosphere Dew Point	N_2 (vol.%)	H_2 (vol.%)	pO_2 at 1093 K (820 °C) (atm.)	pH_2O/pH_2
223 K (–50 °C)	95	5	1.96×10^{-24}	0.0010
243 K (–30 °C)	95	5	1.21×10^{-22}	0.0082
278 K (+5 °C)	95	5	3.45×10^{-20}	0.1380

Coating property analysis was done for the 90 mm × 90 mm uniform temperature and coating area centered in the lower portion of the as-galvanized panels. In order to quantify the reactive wetting behaviour of the as-annealed steel surfaces by the liquid Zn(Al,Fe) bath as a function of process atmosphere, bare spots were counted and their areas were measured with an accuracy of ±0.01 mm^2 using ImageJ 1.42q software .

Coating adhesion was tested by 180° bend tests per ASTM A653/A 653M-05 [27] from 90 mm×10 mm coupons excised from the as-galvanized panels. A 4.8 mm diameter pin was used based on the galvanized specimen dimensions (90 mm×10 mm) and its thickness (1.2 mm). Coating adhesion was determined by inspection of the outer bend surface using a Keyence VHX-5000 digital optical microscope.

The morphology and distribution of the external oxides formed during annealing prior to galvanizing and any reaction products at the Fe-Zn interface after galvanizing were analyzed using a JEOL 7000F field emission gun scanning electron microscope (FEG-SEM). All

oxidation sample surfaces were sputter coated with platinum to avoid charging during examination. In order to remove the zinc overlay and analyze the interfacial layer on the galvanized panels, samples were stripped using both aqueous 10 vol.% H_2SO_4 and fuming HNO_3, which leaves any Fe-Al/Fe-Zn intermetallics and Fe-Al intermetallics present at the coating/substrate interface, respectively.

The fine-scale cross-sectional microstructure and chemistry of the oxides formed on the surface and in the subsurface of the experimental steel prior to galvanizing as well as any reaction products formed at the Fe-Zn interface after galvanizing were determined using a FEI Titan 80-300 transmission electron microscope (TEM) and the resident electron energy loss spectroscopy (EELS) system. Both EELS elemental maps and quantitative point analyses were performed. TEM samples were prepared by focused ion beam (FIB) milling using a NVision 40 by Zeiss. Carbon was deposited on the sample surface to protect it from damage during FIB sample preparation. The TEM was operated at 300 keV, where the energy resolution in monochromated mode was tuned to 0.08 eV full width half-maximum (FWHM) at the zero-loss peak. Mn-L, O-K, Si-K, Al-L, Zn-L and Fe-L EELS edges were collected for all samples and were processed using Gatan Digital Micrograph 2.3. The pre-edge background was removed and the spectra for Mn and O were energy aligned using the highest intensity feature of the Fe-L_3 edge at 708 eV and were normalized for baseline and intensity.

The reported thickness of the external oxides and the depth of the internal oxides formed prior to galvanizing comprised the average of at least 30 measurements on the TEM cross-sectional micrographs using ImageJ 1.42q. The error limits reported herein comprise the 95% confidence interval of the average oxide thickness.

4.4   Results

Figure 4.1 shows the morphology and distribution of the external oxides formed on the experimental steel during annealing at 1093 K (820 ℃) for 120 s under the various process atmosphere pO_2 employed prior to galvanizing. As can be seen in Figure 4.1(a), annealing under the 223 K (–50 ℃) dp process atmosphere resulted in the steel surface being covered with compact, film-like granular oxides. Increasing the process atmosphere pO_2 using the 243 K (–30 ℃) dp process atmosphere (Table 4.2) led to the formation of less compact, film-like external oxides (Figure 4.1(b)). Further increasing the process atmosphere pO_2 through utilizing the 278 K (+5 ℃) dp process atmosphere (Table 4.2) resulted in an alteration of the surface oxide morphology to more widely spaced nodular particles (Figure 4.1(c)). Figure 4.2 shows cross sectional TEM micrographs of the as-annealed oxides formed prior to galvanizing the experimental steel as a function of process atmosphere pO_2. Per Figure 4.2(a), under the lowest pO_2 223 K (–50 ℃) dp process atmosphere, external oxides formed in either a thick, compact film-like oxides comprising $MnSiO_3$ oxide (area I) or multi-layer oxide comprising MnO, $MnSiO_3$ and SiO_2 oxides (area II). Subsurface or internal oxidation was found to be insignificant under this annealing condition. By increasing the process atmosphere pO_2 by employing the 243 K (–30 ℃) dp (Table 4.2), the transition from external to internal oxidation occurred, as exemplified by the significant increase in the depth of internal oxidation versus the 223 K (–50 ℃) dp process atmosphere, as can be seen by comparing Figure 4.2(a) and (b). In addition, a higher magnification image of the external oxides, designated as area III, shows that, although the morphology of the Mn-Si surface oxide remained as film-like, its thickness decreased considerably. Further increasing the atmosphere oxygen partial pressure led to an increase in the depth of internal oxidation as well as a change in the morphology of the external Mn-Si oxides

from film-like under the 223 K (–50 °C) dp and 243 K (–30 °C) dp process atmospheres

(Figure 4.2(a,b)) to discrete nodule-like particles under the 278 K (+5 °C) dp process atmosphere

(Figure 4.2(c)), which is in agreement with the observations shown in Figure 4.1. A complete

characterization of the external and internal oxides formed during intercritical annealing of the

experimental steel as a function of annealing times ranging from 60 to 600 s and process

atmosphere pO_2 was disseminated in a recent study by the present authors [26]. A summary of

the findings concerning the morphology, thickness and chemistry of the external oxides and the

depth of internal oxidation for the present intercritical annealing parameters and process

atmospheres can be found in Table 4.3.
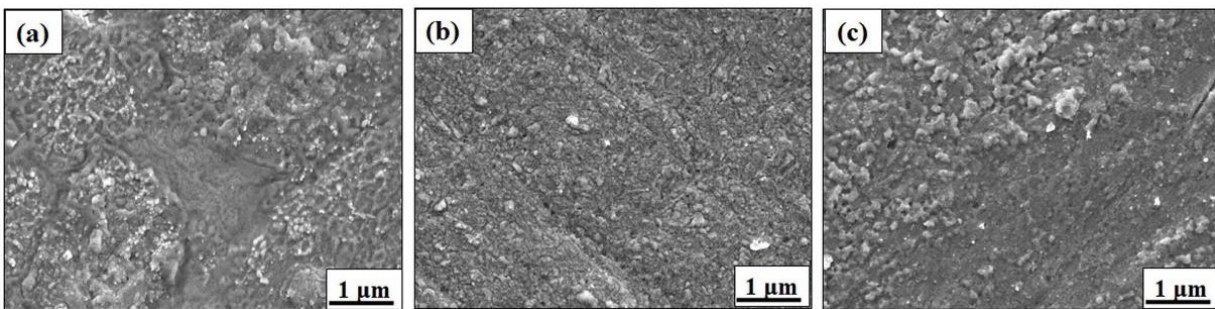
Figure 4.1: SEM images of the as-annealed external oxides using the (a) 223 K (–50 °C) dp, (b)
243 K (–30 °C) dp and (c) 278 K (+5 °C) dp process atmospheres.
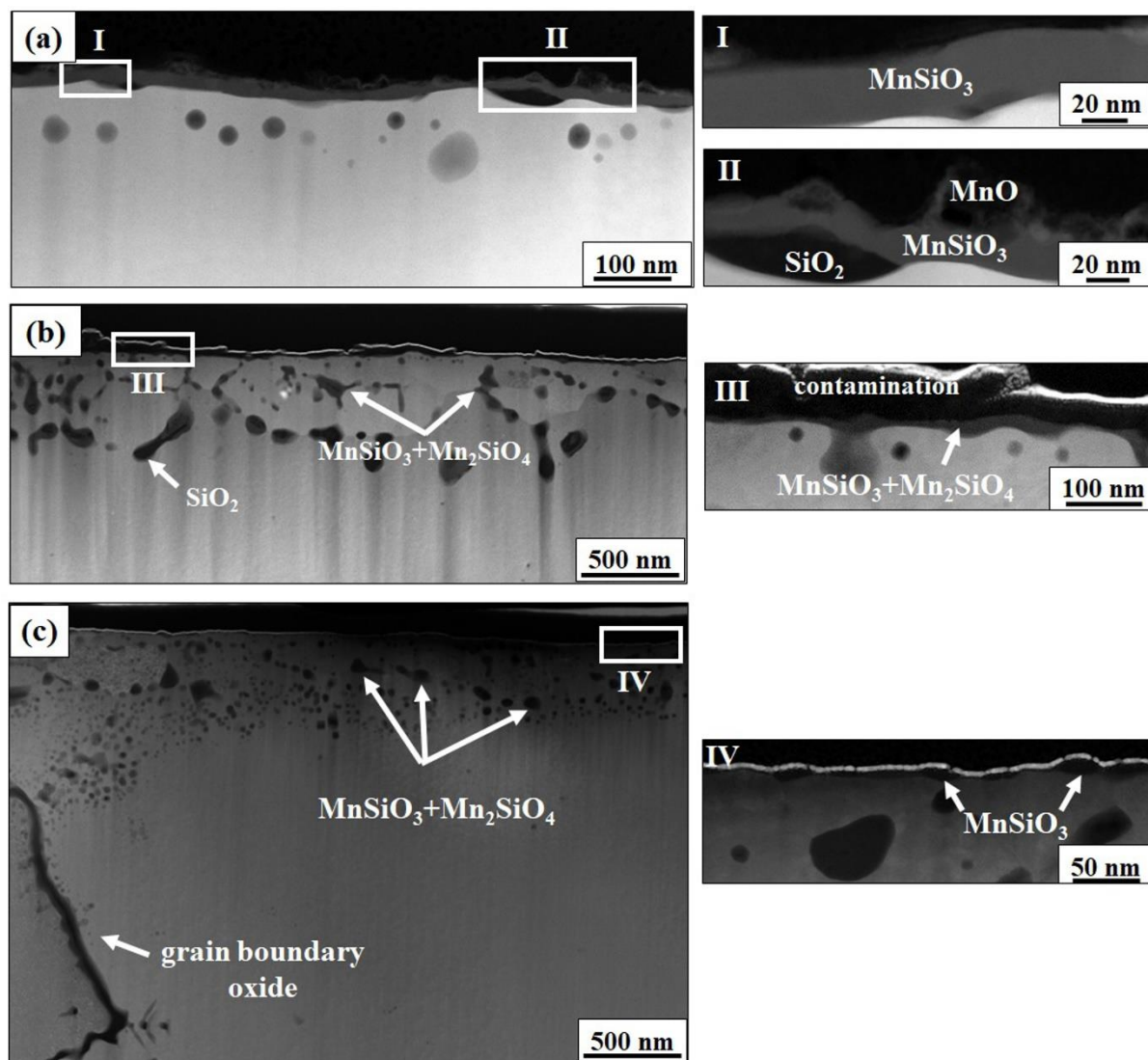
Figure 4.2: TEM cross sectional micrographs of the as-annealed external and internal oxides as a function of process atmosphere pO_2: (a) 223 K (–50 °C) dp, (b) 243 K (–30 °C) dp and (c) 278 K (+5 °C) dp.

Table 4.3: Morphology, Thickness and Chemistry of the External and Internal Oxides Formed on the Experimental Steel as a Function of Process Atmosphere [26]

Process Atmosphere Dew Point	Annealing Time (s)	Internal Oxidation Depth (nm)	External Oxide(s) Morphology	External Oxide(s) Thickness (nm)	External Oxide Chemistry
223 K (–50 °C)	120	64±15	film-like	46±6	$MnSiO_3$, Mn_2SiO_4, MnO, SiO_2

243 K (−30 °C)	120	351±46	film-like	15±3	MnSiO$_3$, Mn$_2$SiO$_4$, MnO, SiO$_2$
278 K (+5 °C)	120	567±53	plate- and nodule-like particles	18±4	MnSiO$_3$, Mn$_2$SiO$_4$, MnO

Figure 4.3 shows an overview of the uniform temperature and coating area of the CMnSi galvanized panels intercritically annealed under the 223 K (−50 °C), 243 K (−30 °C) and 278 K (+5 °C) dp process atmospheres. The number and area of the bare spots from the uniform coating and temperature area of the as-coated panels are summarized in Table 4.4.

After being annealed under the lowest pO$_2$ 223 K (−50 °C) dp process atmosphere, the steel was not coated and only solidified zinc droplets were observed on the substrate (Figure 4.3(a)). Under the higher pO$_2$ 243 K (−30 °C) dp process atmosphere, although a few bare spots were observed (Figure 4.3(b)), the substrate was almost completely coated and only a small fraction of bare area was present (less than 1%, Table 4.4). No bare spots were observed on the sample annealed under the highest pO$_2$ 278 K (+5 °C) dp process atmosphere, which is indicative of a significant improvement in the coating quality and reactive wetting (Figure 4.3(c) and Table 4.4).
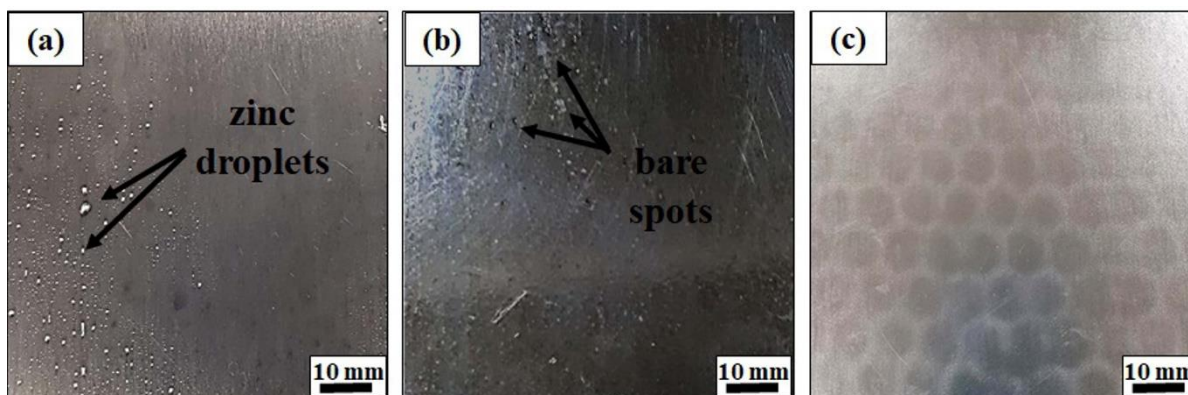
Figure 4.3: Macrographs of the uniform temperature and coating area of the galvanized steel as a function of process atmosphere pO$_2$: (a) 223 K (−50 °C) dp, (b) 243 K (−30 °C) dp and (c) 278 K (+5 °C) dp.

Table 4.4: Bare Spot Analysis of the Galvanized Panels pictured in Figure 4.3

Process Atmosphere Dew Point	Number of bare spots	Total Bare Area (mm^2)	Pct Bare Area
223 K (–50 °C)	--	≥ 8000	≥ 95%
243 K (–30 °C)	9	27.4	0.34
278 K (+5 °C)	0	0.00	0.00

Figure 4.4 shows the outer radius of the as-coated 243 K (–30 °C) dp and 278 K (+5 °C) dp samples subjected to the ASTM 180° bend test. From Figure 4.4, it can be seen that the coating remained intact along the outer surface of all samples for both process atmospheres and no cracking or flaking of the coating was observed, even at the edges. These results indicate that the adhesion of the coatings produced under the higher pO_2 process atmospheres was good and is indicative of reasonably good reactive wetting of the as-annealed surfaces by the galvanizing bath.
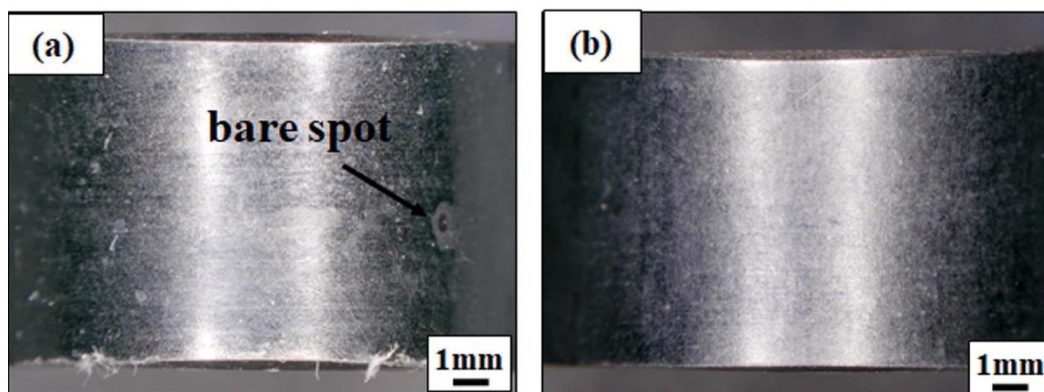
Figure 4.4: ASTM A653/A 653M-05 180° bend test results of the galvanized steel as a function of process atmosphere pO_2: (a) 243 K (–30 °C) dp, and (b) 278 K (+5 °C) dp.

Figure 4.5 shows the results of the SEM analysis of the substrate/coating interface of the galvanized samples after stripping the zinc layer using fuming HNO_3. Equiaxed crystals were observed at the Fe/Zn interface of all samples. As can be seen, these crystals were formed locally

on the sample annealed under the 223 K (–50 °C) dp process atmosphere (Figure 4.5(a)), indicating some degree of localized reactive wetting under these processing conditions. By increasing the process atmosphere pO_2 using the 243 K (–30 °C) dp process atmosphere, a more compact interfacial layer comprising smaller crystals was observed (Figure 4.5(b)). Further increasing the process atmosphere pO_2 using the 278 K (+5 °C) dp process atmosphere resulted in the interfacial layer comprising a fine-grained, closely packed morphology (Figure 4.5(c)). Further comparison of Figure 4.5(b) and (c) will show that the crystals formed at the Fe/Zn interface of the steel annealed under the 278 K (+5 °C) dp process atmosphere were smaller and more compact compared to those of the steel annealed under the 243 K (–30 °C) dp process atmosphere. It is worth noting that stripping the samples using aqueous 10 vol.% H_2SO_4 did not reveal any significant population of Fe-Zn intermetallics at the coating/substrate interface. This is in contrast with Cho et al. [8] who observed Fe-Zn intermetallics in areas where the η-$Fe_2Al_5Zn_X$ interfacial layer was not formed, which was thought to be due to localized depletion of Al during aluminothermic reduction of thick oxide layers formed under low oxygen partial pressures.
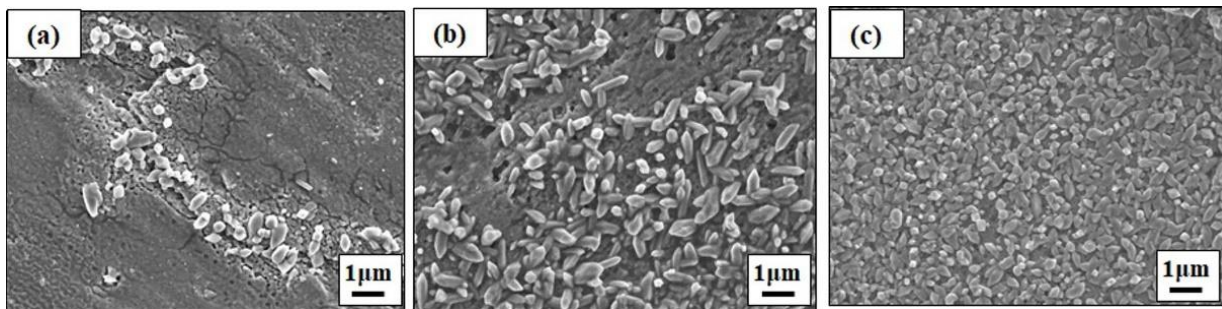
Figure 4.5: SEM analysis of the Fe/Zn interface of the galvanized steel as a function of process atmosphere pO_2: (a) 223 K (–50 °C) dp, (b) 243 K (–30 °C) dp and (c) 278 K (+5 °C) dp.

TEM was used to investigate the fine scale structure of any reaction products formed at the Fe/Zn interface during galvanizing as well as to document any changes to the as-annealed oxides

after contact with the galvanizing bath. Figure 4.6 shows a cross sectional TEM micrograph of the galvanized steel annealed under the lowest pO_2 223 K (–50 °C) dp process atmosphere. Poor reactive wetting of the substrate by the galvanizing bath, in this micrograph, was characterized by the contained voids with high contact angles at the Fe/Zn interface. An area which was not covered with a zinc droplet, as specified with the white box in Figure 4.6, was chosen to analyze the fine scale microstructure of the surface oxides to determine if the morphology, thickness and chemistry of the oxides had changed during contact with the Zn(Al, Fe) bath. Figure 4.7(a) shows a TEM cross-sectional micrograph of this area, along with O, Fe, Si, Mn and C EELS elemental maps (Figure 4.7(b)) and the Mn-$L_{2,3}$, O-K and Si-K edge energy loss spectra (Figure 4.7(c)) of points 1 through 3 demarcated in Figure 4.7(a). It should be noted that the dark area above the oxides in Figure 4.7(a) corresponds to the C film deposited on the sample prior to FIB milling.

Per the Figure 4.7 elemental maps, the external oxide had three distinct layers. The topmost oxide was rich in Mn, the middle oxide was rich in Mn and Si and the bottom oxide was rich in Si. A comparison between the features of the Mn-$L_{2,3}$ and O-K edges with the standard $MnSiO_3$, Mn_2SiO_4, MnO and SiO_2 EELS spectra [28-31] determined that the top, middle and bottom oxides corresponded to MnO, $MnSiO_3$ and SiO_2, respectively. It is worth mentioning that the layer present on top of the oxides rich in C and O, according to the elemental maps, is believed to be contamination remaining on the surface during sample handling. It is worth noting that the identification of the oxides via EELS is because of its high spatial resolution and accuracy in comparison with the techniques [32] used in previous studies [8,19,34,35].
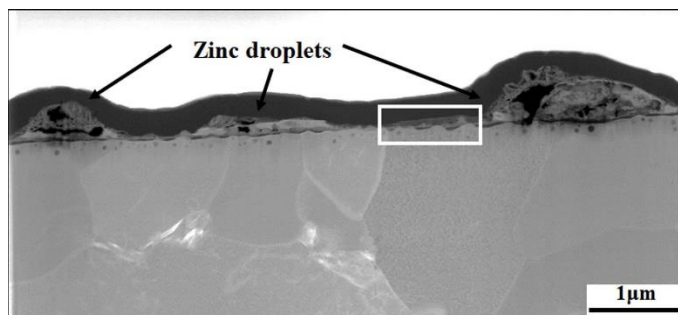
Figure 4.6: TEM cross sectional micrograph of the coating/substrate interface and subsurface of the galvanized steel intercritically annealed under the 223 K (–50 °C) dp process atmosphere; the area specified with the white box corresponds to the area analyzed in greater detail in Figure 4.7.

Figure 4.8 shows a TEM cross-sectional view and EELS elemental maps across the coating/substrate interface taken from the galvanized steel annealed under the 243 K (–30 °C) dp process atmosphere. Per the EELS elemental map in Figure 4.8(b), the Fe/Zn interface was covered with lens-shaped oxides rich in Mn and Si as well as crystals rich in Fe and Al. The Fe-Al crystals were located between, below and above the oxides. Furthermore, a lens-shaped oxide can be seen which was trapped within the Fe-Al intermetallic layer. Using high resolution EELS spectra, it was determined that the external oxide corresponded to $MnSiO_3$ [28]. EELS quantitative point analysis was also performed on the points labelled A through E on Figure 4.8(b) in order to identify the interfacial reaction products, the results of which are presented in Table 4.5, where it can be seen that the Fe-Al atomic ratios were consistent with the η-$Fe_2Al_5Zn_X$ intermetallic. In this case, the presence of η-$Fe_2Al_5Zn_X$ intermetallics is indicative of the desired reactive wetting reaction having taken place between the Zn-alloy bath and the substrate and is consistent with the good coating adherence determined by the 180° bend tests (Figure 4.4(a)).
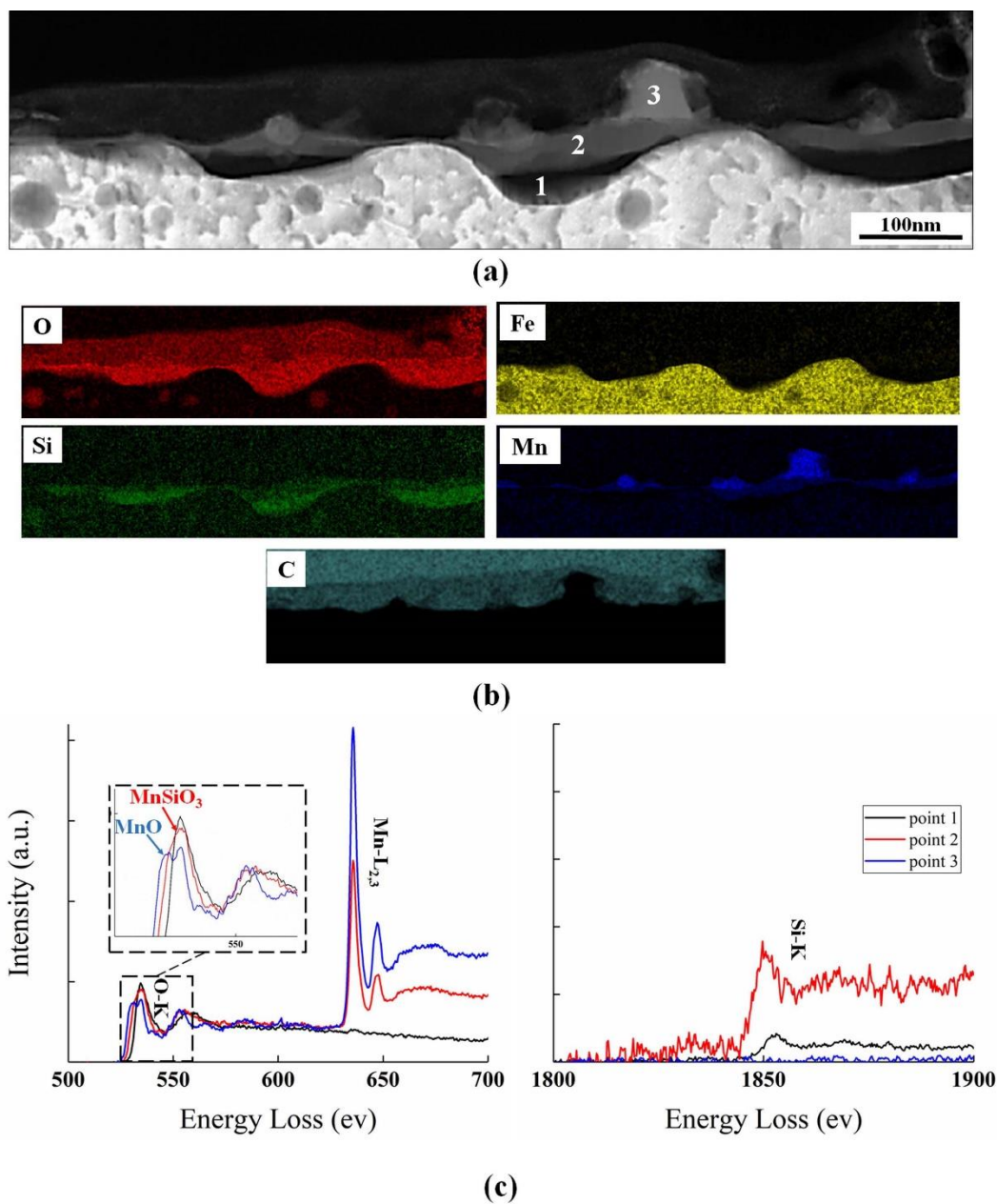
Figure 4.7: (a) TEM cross sectional micrograph of the area specified with a white box in Figure 4.6. (b) TEM elemental maps of (a). (c) Mn-L$_{2,3}$, O-K and Si-K edge energy loss spectra of points 1 through 3 in (a).

Figure 4.9 shows a TEM cross-sectional micrograph of an area at the Fe/Zn interface of the galvanized steel annealed under the 278 K (+5 °C) dp process atmosphere along with EELS elemental maps of this area. Per the EELS elemental maps (Figure 4.9(b)), the surface was

103

covered with a thin, discontinuous (Mn,Si)-O layer sandwiched by Fe-Al crystals. The surface

oxides were identified as $MnSiO_3$ using high resolution EELS spectra [28]. Comparing

Figure 4.8 and Figure 4.9, it can be seen that Fe-Al crystals formed under the higher pO_2 278 K

(+5 °C) dp process atmosphere (Figure 4.9) were more compact and finer than those of the lower

pO_2 243 K (–30 °C) dp process atmosphere (Figure 4.8), in agreement with the SEM analysis

shown in Figure 4.5(b,c).
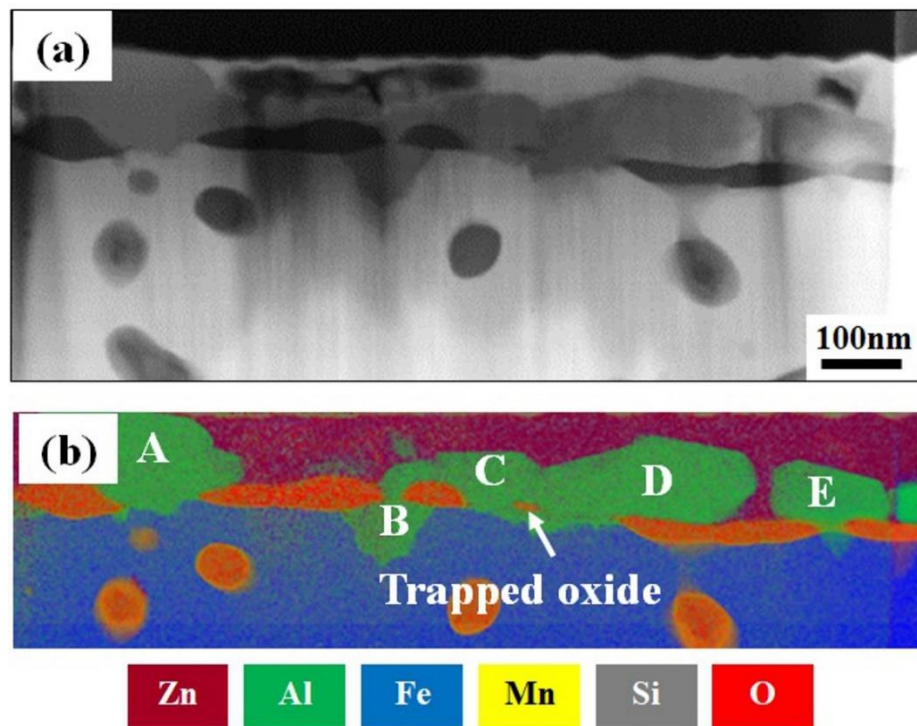
Figure 4.8: (a) TEM cross-sectional micrograph of the coating/substrate interface and subsurface of the galvanized steel intercritically annealed under the 243 K (–30 °C) dp process atmosphere. (b) Color over-lay EELS elemental map of the area shown on (a) (reproduced with permission of the Iron and Steel Institute of Japan [33]).
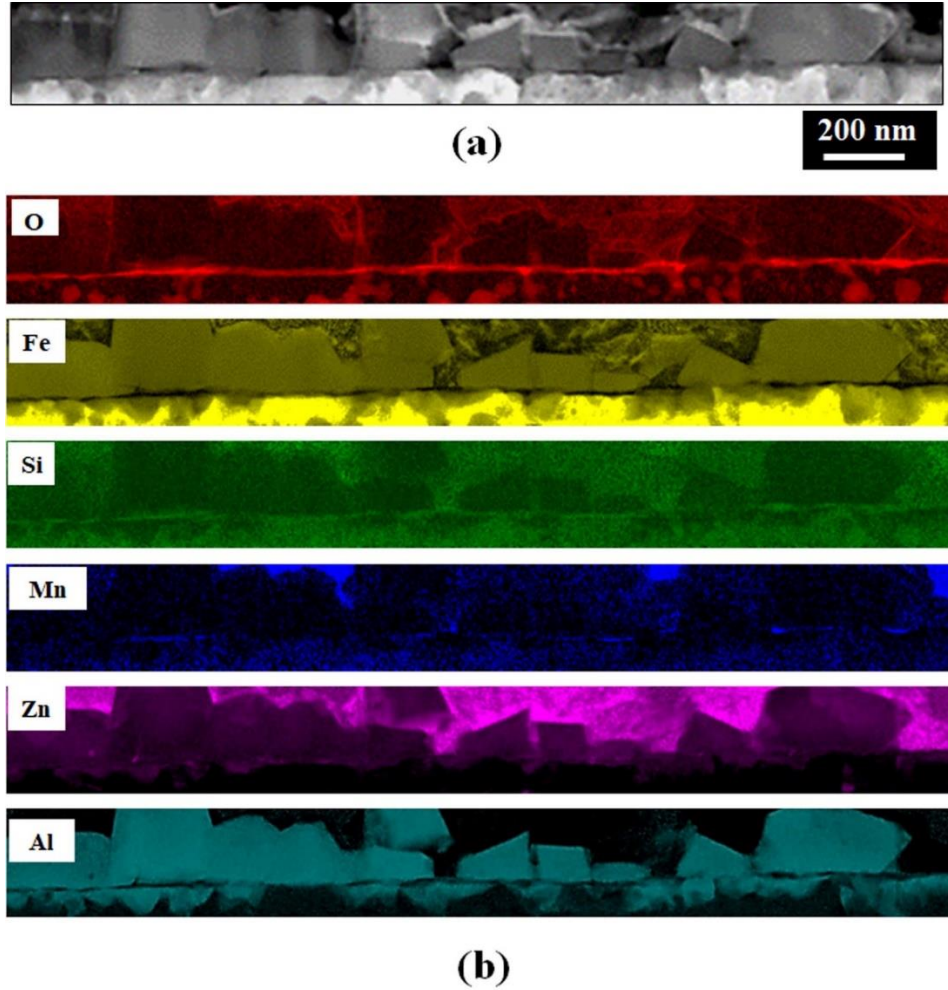
Figure 4.9: (a) TEM cross-sectional micrograph of the coating/substrate interface and subsurface of the galvanized steel intercritically annealed under the 278 K (+5 °C) dp process atmosphere. (b) TEM elemental maps of the area shown on (a).

Table 4.5: TEM EELS Analysis of Points A through E shown in Figure 4.8(b) (at.%)

Point	O	Mn	Si	Fe	Al	Zn	Intermetallic Present
A	5.4	6.1	3.5	20.6	57.9	6.5	η-Fe$_2$Al$_5$Zn$_X$
B	7.1	6.6	0.0	22.5	55.0	8.9	η-Fe$_2$Al$_5$Zn$_x$
C	9.9	1.3	3.8	27.1	51.2	6.7	η-Fe$_2$Al$_5$Zn$_X$
D	8.5	5.9	5.1	19.6	54.4	6.5	η-Fe$_2$Al$_5$Zn$_x$
E	6.8	1.7	2.2	27.1	51.4	10.8	η-Fe$_2$Al$_5$Zn$_X$

4.5   Discussion

As shown in Figure 4.1 and Figure 4.2 and according to the results determined in a recent report by the present authors [26], summarized in Table 4.3, it was determined that annealing parameters such as oxygen partial pressure significantly affected the morphology, distribution, thickness and chemistry of the surface oxides formed during 1093 K (820 °C) intercritical annealing of the present C-2Mn-1.3Si (wt.%) experimental steel.

The experimental steel annealed under the lowest pO_2 223 K (–50 °C) dp process atmosphere exhibited poor reactive wetting, as can be clearly seen in Figure 4.3 and Figure 4.6. As a consequence, no well-developed, integral Fe-Al interfacial layer was observed at the Fe/Zn interface, as shown in Figure 4.5(a). This can be attributed to the thickness and morphology of the external oxides formed on the surface during annealing prior to galvanizing, as shown in Figure 4.1, Figure 4.2 and Table 4.3. It was established that under the 223 K (–50 °C) dp process atmosphere, a compact, 46 ± 6 nm-thick film-like oxide comprising crystalline $MnSiO_3$, Mn_2SiO_4, MnO and amorphous SiO_2 formed on the external surface prior to galvanizing. These external oxides acted as a barrier to the dissolution of Fe from the substrate surface and the prevented the desired reaction of dissolved Fe, Zn and dissolved Al to form the η-$Fe_2Al_5Zn_X$ interfacial layer at the substrate/coating interface.

Using a higher dew point – i.e. higher pO_2 – process atmospheres during substrate annealing has been established as a promising technique to improve reactive wetting by encouraging internal selective oxidation of the alloying elements [8,34,35], as generally characterized by the Wagner criterion for the internal to external oxidation transition [36]. Promotion of internal oxidation often results in surfaces comprised of either relatively thin oxide films or widely-

spaced, discrete nodule-like external oxides with thin oxide inter-nodular oxides, where these surfaces have been shown to aid in promoting reactive wetting by the Zn(Al, Fe) bath [8,16].

Good reactive wetting was obtained for the steels annealed under the two higher pO_2 process atmospheres (i.e. 243 K (–30 °C) dp and 278 K (+5 °C) dp), as exemplified by the low number and small total area of bare spots in the Zn overlay (Table 4.4 and Figure 4.3), no cracking or flaking of the coating during bend testing (Figure 4.4) and the consequent formation of the desired Fe-Al interfacial layer at the Fe/Zn interface, as shown in Figure 4.5, Figure 4.8 and Figure 4.9. This is due to the formation of relatively thin oxide layers and plate/nodule-like particles on the surface of the steel arising from the transition from external to internal oxidation when annealing under the 243 K (–30 °C) dp and 278 K (+5 °C) dp process atmospheres, respectively (Figure 4.1, Figure 4.2 and Table 4.3). A variety of reactive wetting mechanisms were identified as the reason for good reactive wetting, despite the external selective oxidation observed on the steel surface after annealing under these process atmosphere pO_2.

Prior to galvanizing the experimental CMnSi steel, external MnO as well as a layer of $MnSiO_3$ and Mn_2SiO_4 formed during annealing under the 243 K (–30 °C) dp process atmosphere (Figure 4.1, Figure 4.2 and Table 4.3). However, after contact with the Zn(Al,Fe) bath and reactive wetting, as shown by comparing Figure 4.2 and Figure 4.8, the $MnSiO_3$ took on a lens-like shape, indicating that the as-annealed morphology had been significantly altered during the reaction with the galvanizing bath. In addition, as can be seen in Figure 4.8, η-$Fe_2Al_5Zn_X$ crystals formed above, between and below the interfacial oxides. As suggested by Bellhouse and McDermid [21], upon cooling from the IAT, spalling and cracking of the oxide can occur as the result of the difference in coefficient of thermal expansion (CTE) between the substrate and the

oxide. The CTE mismatch stress imposed in the oxide upon cooling can be calculated using

equation (4.2) [37], where the oxide is considerably thinner than the substrate:

$$\sigma_{oxide} = \frac{-E_{oxide}(\alpha_{oxide} - \alpha_{Fe})\Delta T}{(1 - \nu_{oxide})}$$ (4.2)

where σ_{oxide} is the CTE mismatch stress imposed in the oxide, E_{oxide} is the Young's modulus

of the oxide, ν_{oxide} is the Poisson's ratio of the oxide, α_{oxide} is the linear coefficient of thermal

expansion of the oxide, α_{Fe} is the linear coefficient of thermal expansion of iron and ΔT is the

temperature difference. The stress in MnO and SiO_2 when cooling from the IAT of 1093 K (820

°C) to the thermal equilibration temperature of 738 K (465 °C) prior to galvanizing were

calculated to be –750 MPa and –470 MPa, respectively using equation 1 and the relevant

material properties shown in Table 4.4. Since the imposed stresses in MnO and SiO_2 are large,

cracks could have formed in the oxides during cooling prior to immersing in the continuous

galvanizing bath.

Table 4.6: Material Properties Required for Computation of the Thermal Stresses Imposed in
Surface Oxides upon Cooling using equation (4.2)

Variable	Value	Reference
α_{Fe}	15.3×10^{-6} K^{-1}	[37]
E_{MnO}	175 GPa	[38]
ν_{MnO}	0.31	[38]
α_{MnO}	7.0×10^{-6} K^{-1}	[39]
E_{SiO2}	73 GPa	[40]
ν_{SiO2}	0.17	[40]
α_{SiO2}	0.4×10^{-6} K^{-1}	[40]

These interfacial cracks and voids consequently allowed liquid bath

infiltration and promoted direct contact with the substrate, resulting in Fe dissolution from the

substrate and the precipitation of η-$Fe_2Al_5Zn_X$ crystals between and below the oxides. The other

path through which this infiltration can occur would be along the boundaries between the oxide

and substrate. As suggested by Sagl et al. [24], adjacent to the surface areas covered with thinner oxide layers and nodule-like oxide particles, where Fe dissolution in the zinc bath and formation of the η-$Fe_2Al_5Zn_X$ crystals is possible, oxides can lose their adherence to the substrate and lift off into the zinc bath or become trapped within η-$Fe_2Al_5Zn_X$ crystals as they grow, as was seen in Figure 4.8.

The complete reactive wetting observed for the steel annealed under the 278 K (+5 °C) dp process atmosphere can also be explained by the morphology of the surface oxides formed during annealing. As shown in Figure 4.1, Figure 4.2 and Table 4.3, increasing the process atmosphere pO_2 to 278 K (+5 °C) dp altered the morphology of the surface oxides from film-like under the 223 K (–50 °C) and 243 K (–30 °C) dp process atmospheres to a more widely distributed plate- and nodule-like $MnSiO_3$, Mn_2SiO_4 + MnO with relatively thin oxide films between the oxide plates or nodules. The aforementioned oxide morphology would facilitate aluminothermic reduction of the thinner oxides and dissolution of Fe into the galvanizing bath, an essential step in the formation of the observed Fe-Al interfacial layer and, consequently, resulted in the formation of a more continuous and compact interfacial layer (Figure 4.5 and Figure 4.9) and fewer bare spots (Figure 4.3 and Table 4.4) compared to the lower pO_2 243 K (–30 °C) dp process atmosphere.

This general mechanism is in agreement with Bellhouse and McDermid [16] who related the formation of a full and homogeneous η-$Fe_2Al_5Zn_X$ layer after hot-dip galvanizing a CMnSiAl TRIP steel to widely spaced oxide nodules with relatively thin inter-nodular MnO films arising from the higher pO_2 of the annealing atmosphere used. Furthermore, the formation of a finer and more compact Fe-Al layer under the higher pO_2 278 K (+5 °C) dp process atmosphere (Figure 4.5(c), Figure 4.9) compared to those of the lower pO_2 243 K (–30 °C) dp process

atmosphere (Figure 4.5(b), Figure 4.8), is known to be the result of surface oxide thickness and morphology as thinner film-like and nodule-like oxides provide more nucleation sites for the Fe-Al crystals. This is in agreement with observations reported by Alibeigi and McDermid [41] who determined that the external MnO thickness strongly affected the interfacial η-$Fe_2Al_5Zn_X$ morphology for a series of Mn-containing steels, where the η-$Fe_2Al_5Zn_X$ crystals coarsened significantly with increasing external MnO thickness. It should be noted that no Al oxides were observed in the TEM elemental maps shown in Figure 4.9 to directly support the occurrence of aluminothermic reduction. However, it is worth noting that the Al_2O_3 reaction products observed by Kavitha and McDermid [18] as direct evidence for the occurrence of aluminothermic reduction reaction were very thin (less than 2 nm) for the reduction of a much thicker MnO film. Thus, this mechanism is cited as a probable contributing mechanism for the observed reactive wetting in the present case. In addition, the significant population of η-$Fe_2Al_5Zn_X$ in the present case versus the samples annealed under the 243 K (–30 °C) dp process atmosphere is indicative of large scale contact between the bath and substrate, for which aluminothermic reduction is a likely mesoscopic-scale candidate.

As was mentioned earlier and highlighted in Table 4.1, the Si/Mn ratio of the model alloy under investigation was 0.65, slightly in excess of the recommended maximum Si/Mn = 0.5 ratio of Suzuki et al. [14] to ensure good reactive wetting. In summary, Suzuki et al. proposed a thermodynamic model where the alloy Si/Mn ratio and process atmosphere pO_2 were used to predict the chemical composition of the oxides that will form on Mn-Si steels as well as predict the relative probability of the reactive wetting occurring based primarily on the presence or absence of SiO_2. This has proven to be a useful guideline for preliminary process design, but, as supported by the reactive wetting results reported by Suzuki et al. [14] and in the present case,

the recommended Si/Mn $\leq$ 0.5 ratio is not universally applicable under all processing conditions. This is due to the fact that the thermodynamic-based model did not take into account transient, kinetically driven phenomena which can significantly affect the chemistry and morphology of the external oxides. Per the present investigation and those of other workers [5,8,16], these latter factors have been shown to play a significant, if not dominant, role in reactive wetting processes in the present alloy system and in those of other authors.

Specifically, it has been shown in the present instance and in reference [26] that the oxide precipitation sequence is controlled by a combination of thermodynamic driving forces – meaning that the most thermodynamically stable oxide is the most likely to precipitate first, in this case SiO_2 – combined with the relative diffusion rates of the oxide-forming species [42] and the relative solubilities of the oxides in either ferrite or austenite. With respect to this latter, MnO is relatively soluble in ferrite (with a solubility product of 11.22 $(ppm)^2$ [43]) whereas SiO_2 and Mn_2SiO_4 are relatively insoluble (with solubility products of 7.2×10^{-5} $(ppm)^3$ [43] and 4.8×10^{-5} $(ppm)^7$ [44,45], respectively). Thus, the oxide species present will be driven not only by thermodynamic factors, but by the relative diffusivities and other kinetic factors, with the resulting configurations not necessarily conforming to the thermodynamic predictions. In the present case, these factors manifested themselves in the multi-layer external oxide morphologies highlighted in Figure 4.2 and Figure 4.7 through Figure 4.9.

However, it should be pointed out that some significant work has been performed in the direction of kinetically-based modelling of both external and internal oxidation, starting with the work of Huin et al. [44] and continuing with Brunac et al., Lashgari et al. and Leblond et al. [46-48]. These models have shown better agreement with the present experimental results compared to the solely thermodynamic-based models. However, since, as has been shown here, external

oxide morphology plays a dominant role in determining the interactions between the as-annealed substrate surfaces and the continuous galvanizing bath and the resultant reactive wetting, it is imperative that progress be made in the modelling of selective oxidation to include the development of external and internal oxide morphology in addition to thermodynamic and kinetics considerations, for which phase-field or similar approaches show some promise. These efforts will present a significant challenge to the continuous galvanizing research community moving forward.

4.6   Conclusions

The reactive wetting of a Fe-0.1C-2Mn-1.3Si (wt.%) advanced high strength steel by a Zn(0.2Al (dissolved),Fe) (wt.%) continuous galvanizing bath was investigated as a function of process atmosphere oxygen partial pressure (pO$_2$) and its effect on external oxide morphology during 1093 K (820 °C) intercritical annealing for 120 s. Increasing the annealing process atmosphere pO$_2$ was shown to be an effective way to improve the reactive wetting of the experimental steel during continuous galvanizing. This was determined to be attributed to the transition from external to internal oxidation occurred by increasing the atmosphere dew point from 223 K (–50 °C) to 243 K (–30 °C) and 278 K (+5 °C). The consequence of this transition was a decrease in the thickness of the film-like surface oxides under the 243 K (–30 °C) dp process atmosphere and a change in their morphology from film-like to widely distributed plate- and nodule-like particles under the 278 K (+5 °C) dp process atmosphere. The modified surface oxide structure could ease aluminothermic reduction and facilitate interfacial infiltration, Fe dissolution from the substrate and the consequent precipitation of the Fe-Al interfacial layer. Oxide lift-off and oxide trapping were also observed during growth of the Fe-Al crystals, which resulted in further improvement of the coating quality.

It is recommended that future modelling efforts be focussed on incorporating the kinetic aspects of oxide growth, such as relative diffusion kinetics and oxide solubilities, as well as the morphological factors in order to successfully predict reactive wetting by the continuous galvanizing bath.

4.7   Acknowledgments

4.8   References

[1] C.M. Tamarelli, The Evolving Use of Advanced High-Strength Steels for Automotive Applications, Steel Market Development Institute, Michigan (2011).

[2] S.M.A. Shibli, B.N. Meena, R. Remya, Surf. Coatings Technol. 262 (2015) 210-215.

[3] M. Guttmann, Mater. Sci. Forum 155-156 (1994) 527-548.

[4] M. Norden, M. Blumenau, T. Wuttke, K.-J. Peters, Appl. Surf. Sci. 271 (2013) 19-31.

[5] E.M. Bellhouse, J.R. McDermid, Metall. Mater. Trans. A 43A (2012) 2426-2441.

[6] E.M. Bellhouse, J.R. McDermid, Metall. Mater. Trans. A 41A (2010) 1460-1473.

[7] G.M. Song, T. Vystavel, N. van der Pers, J.Th.M. De Hosson, W.G. Sloof, Acta Mater. 60 (2012) 2973-2981.

[8] L. Cho, S. J. Lee, M. S. Kim, Y. H. Kim, B. C. De Cooman, Metall. Mater. Trans. A 44A (2013) 362-371.

[9] E.M. Bellhouse, J.R. McDermid, Metall. Mater. Trans. A 42A (2011) 2753-2768.

[10] M. Blumenau, M. Norden, F. Friedel, K. Peters, Surf. Coat. Technol. 205 (2011) 3319-3327.

[11] J. Mahieu, S. Claessens, B.C. De Cooman, Metall. Mater. Trans. A 32A (2001) 2905-2908.

[12] J. Maki, J. Mahieu, B.C. De Cooman, S. Claessens, Mater. Sci. Technol. 19 (2003) 125–131.

[13] M.S. Kim, J.H. Kwak, J.S. Kim, Y.H. Liu, N. Gao, N.Y. Tang, Metall. Mater. Trans. A 40A (2009), 1903–1910.

[14] Y. Suzuki, T. Yamashita, Y. Sugimoto, S. Fujita, S. Yamaguchi, Iron Steel Inst. Japan Int. 49 (2009) 564-573.

[15] Y. Kim, J. Lee, J. Park, S-H. Jeon, Met. Mater. Int. 17 (2011) 607-611.

[16] E.M. Bellhouse, J.R. McDermid, Metall. Mater. Trans. A 41A (2010) 1539-1553.

[17] R. Khondker, A. Mertens, J.R. McDermid, Mater. Sci. Eng. A 463 (2007) 157-165.

[18] R. Kavitha, J. R. McDermid, Surf. Coat. Technol. 212 (2012) 152-158.

[19] Y.F. Gong, T.J. Song, H.S. Kim, J.H. Kwak, B.C. De Cooman, in Proc. of Asia-Pacific Galvaniz. Conf., Seoul (2009) B-15.

[20] H. Liu, Y. He, L. Li, Appl. Surf. Sci. 256 (2009) 1399-1403.

[21] E.M. Bellhouse, J.R. McDermid, Metall. Mater. Trans. A 42A (2011) 2753-2768.

[22] J.R. McDermid, M.H. Kaye, W.T. Thompson, Metall. Mater. Trans. B 38B (2007) 215-230.

[23] S. Alibeigi, R. Kavitha, R.J. Meguerian, J.R. McDermid, Acta Mater. 59 (2011) 3537-3549.

[24] R. Sagl, A. Jarosik, D. Stifter, G. Angeli, Corros. Sci. 70 (2013) 268-275.

[25] E.M. Bellhouse, "Galvanizing of Al-Si TRIP-assisted steels", Ph.D. thesis, McMaster University (2010).

[26] G. Seyed Mousavi, J.R. McDermid, Metall. Mater. Trans. A 49 A (2018) 5546-5560.

[27] ASTM A 653/A 653M – 05, (2005) Standard specification for steel sheet, zinc-coated (galvanized) or zinc-iron alloy-coated (galvannealed) by the hot-dip process.

[28] A.P. Grosvenor, E.M. Bellhouse, A. Korinek, M. Bugnet, J.R. McDermid, Appl. Surf. Sci. 379 (2016) 242-248.

[29] H.K. Schmid, W. Mader, Micron 37 (2006) 426-432.

[30] L. Laffont, P. Gibot, Mater. Charact. 61 (2010) 1268-1273.

[31] C.C. Ahnn, O.L. Krivanek, with contributions by: R.P Burgner, M.M. Disko, P.R. Swann, EELS Atlas, A reference guide of electron energy loss spectra covering all stable elements, Gatan Inc., Warrendale, 1983.

[32] C.R. Brundle, C.A. Evans, Jr., S. Wilson, Encyclopedia of Materials Characterization, Manning Publications Co., United States of America, 1992.

[33] G. Seyed Mousavi, J.R. McDermid, in Proc. of 11th Int. Conf. Zinc Zinc Alloy Coat. Steel Sheet, Tokyo (2017) 485-492.

[34] L. Cho, G.S. Jung, B.C. De Cooman, Metall. Mater. Trans. A 45A (2014) 5158-5172.

[35] H. Liu, Y. He, S. Swaminathan, M. Rohwerder, L. Li, Surf. Coatings Technol., 206 (2011) 1237-1243.

[36] C. Wagner, Zh. Elektrochem., 63 (1959) 772-782.

[37] N. Birks, G.H. Meier, F.S. Pettit, Introduction to the High-Temperature Oxidation of Metals, Cambridge University Press, Cambridge, 2006.

[38] G. Simmons, H. Wang, Single Crystal Elastic Constants and Calculated Aggregate Properties: A Handbook, second ed., The M.I.T. Press, Cambridge, 1971.

[39] R. Wanke, Schweissen Schneiden 25 (1973) 252–254.

[40] W.D. Callister, Materials Science and Engineering: An Introduction, seventh ed., John Wiley & Sons, New York, 2007.

[41] S. Alibeigi, J. R. McDermid, in Proc. of 9th Int. Conf. Zinc Zinc Alloy Coat. Steel Sheet, Beijing (2013) 171-176.

[42] H. Oikawa, Lattice diffusion of substitutional elements in iron and iron-base solid solutions. A critical review, Technology Reports, Tohoku University 48 (1983) 7-77.

[43] Thermodata. Electronic data bank for thermodynamic quantities. http://thermodata.online.fr, 2005.

[44] D. Huin, P. Flauder, J-B. Leblond, Oxid. Met., 64 (2005) 131-167.

[45] G. Eriksson, P. Wu, M. Blander, A.D. Pelton, Can. Metall. Q. 33 (1994) 13-21.

[46] J-B. Brunac, D. Huin, J-B. Leblond, Oxid. Met., 73 (2010) 565-589.

[47] V.A. Lashgari, G. Zimbitas, C. Kwakernaak, W.G. Sloof, Oxid. Met., 82 (2014) 249-269.

[48] J-B. Leblond, J-M. Bergheau, R. Lacroix, D. Huin, Finite Elem. Anal. Des., 132 (2017) 8-26.

5 EFFECT OF SN ADDITION, PROCESS ATMOSPHERE PO₂ AND ANNEALING TIME ON THE SELECTIVE OXIDATION OF A C-2MN-1.7SI (WT.%) ADVANCED HIGH STRENGTH STEEL DURING CONTINUOUS GALVANIZING

G. Seyed Mousavi[1], B. Langelier[2], J.R. McDermid*[1]

[1]Steel Research Centre, McMaster University, Hamilton, Canada ON L8S 4L8

[2]Department of Materials Science and Engineering, McMaster University, Hamilton, Canada ON L8S 4L8

5.1 Abstract

The effects of process atmosphere pO_2, annealing time and a minor Sn addition on the selective oxidation of a Fe-0.1C-2Mn-1.7Si (wt.%) advanced high strength steel during continuous galvanizing heat treatments were determined. The reference and 0.05 wt.% Sn-added steels were intercritically annealed at 1113 K (840 °C) for annealing times between 60 to 600 s in a N₂-5 vol.% H₂ gas atmosphere, where the process atmosphere pO_2 was controlled by varying the dew points at 223 K (–50 °C), 243 K (–30 °C) and 278 K (+5 °C). It was found that both the internal and external oxidation kinetics followed a parabolic rate law and were significantly reduced by the Sn addition to the alloy. For the lowest pO_2 223 K (–50 °C) dew point atmosphere, the external oxides comprised compact, film-like $MnSiO_3$, SiO_2 and granular MnO. The addition of Sn to the alloy reduced the compactness of the granular oxides. Increasing the atmosphere dew point to 243 K (–30 °C) and 278 K (+5 °C) reduced the thickness of the external oxides and increased the depth of internal oxidation. Under the highest pO_2 278 K (+5 °C) dew point atmosphere, although the reference steel surface was covered with small, closely-packed $MnSiO_3$

nodule-like particles, the addition of Sn altered their morphology to larger and widely-spaced nodules and decreased the depth of internal oxidation. The effect of Sn was found to be the result of its segregation at the surface oxide/substrate interface, as shown by 3D atom probe tomography. The alterations in oxide morphology resulting from the Sn addition are expected to enhance the reactive wetting of the substrate surfaces by the continuous galvanizing bath.

5.2 Introduction

One of the most intense fields of study by the steel industry since the mid-1990s has been the galvanizing of advanced high strength steels (AHSS), which can be challenging due to the selective oxidation of the alloying elements required to achieve the desired microstructures and properties during annealing prior to galvanizing in the commonly employed process atmosphere of N_2-(5-20 vol.%) H_2-xH_2O [1-5]. Morphology, spatial distribution and chemistry of these oxides on the substrate surface indicate whether the desired η-$Fe_2Al_5Zn_x$ interfacial layer can form and whether the finished coating is acceptable [1-4]. For example, it has been established by several authors [4-12] that the presence of film-like external oxides can block the reaction between the substrate Fe and bath dissolved Al to form the required η-$Fe_2Al_5Zn_X$ interfacial layer, characteristic of reactive wetting having occurred. However, the presence of either thin film-like or widely-distributed nodule-like external oxides can promote contact between the substrate Fe and bath Al to facilitate the formation of the η-$Fe_2Al_5Zn_X$ interfacial layer through mechanisms such as aluminothermic reduction, oxide lift-off and bath infiltration between the oxide and substrate, thereby leading to high-quality Zn coatings during continuous galvanizing.

Several authors have proposed processing methods to alter the external oxide chemistry and morphology to facilitate reactive wetting of AHSS surfaces by the continuous galvanizing bath. For example, annealing under higher process atmosphere oxygen partial pressures (pO$_2$) (i.e.

higher dew points) [13-16] and applying the oxidation-reduction process [17,18] have been reported to favorably modify surface oxide characteristics and, consequently, improve the reactive wetting of AHSSs. Another recently advocated approach to modifying the external oxide morphology is the addition of surface-active elements such as Bi, Sn and Sb to the steel composition. These elements have a strong tendency to segregate to the steel surface and grain boundaries in order to decrease the local elastic lattice strain energy, attributed to their larger atomic radius compared to the substrate [19,20]. This segregation can also decrease the substrate surface energy, as shown by Seah and Hondros [21] in the case of adding Sn to pure iron.

Several studies have examined the effect of Sn [22-25] and Sb [2630] on the surface and subsurface oxide characteristics arising from annealing. Lyudkovsky [26] added up to 0.08 wt% Sb to a 0.02C-4Mn-1Si-2Al (wt.%) steel and showed that the most significant drop in the depth of internal oxidation could be achieved when the concentration of Sb was between 0.015 and 0.055 wt.%. Below and above this range, Sb had very little effect on oxidation. Cho et al. [24] showed that, in the case of the addition of Sn to a 0.1C-1.6Mn-1.5Si (wt.%) TRIP steel, the external oxide morphology was altered from film-like to lens-shaped particles, thereby improving the reactive wetting of the substrate by a Zn-0.22Al (wt.%) continuous galvanizing bath considerably. Cho et al. [25] also reported that changes in the oxide morphology were attributed to changes in the oxide-substrate interfacial energy arising from the addition of Sn to the steel chemistry. In addition, the authors observed a reduction in the external oxide Si/Mn ratio, which was attributed to the occupation of potential oxygen adsorption sites and a consequent reduction in the oxygen permeability of the surface. It is noteworthy that although Cho et al. [25] have performed the aforementioned study by adding Sn to their base TRIP composition in the range of 0.05-1 wt.%, in order to maintain the mechanical properties of the

steel, it is generally accepted that the Sn addition to steels be a maximum of 0.1 wt.% in order to avoid hot shortness [31,32].

More recently, Pourmajidian and McDermid [33] considered the combined effect of 0.05 wt.% Sn addition and annealing parameters – i.e. annealing time and annealing atmosphere pO_2 – on the selective oxidation of a 0.1C-6Mn-2Si (wt.%) medium-Mn third generation AHSS. They reported a reduction in the kinetics of both external and internal oxidation after the addition of Sn to the steel chemistry as a result of Sn segregation to the steel surface and its consequent effect on reducing the oxygen flux into the substrate. The interfacial Sn enrichment was determined to be a 10-fold increase compared to its bulk value, using 3D atom probe tomography.

It should be pointed out that, except for the research of Pourmajidian and McDermid [33], the vast majority of studies to date on the effect of Sn on the selective oxidation and reactive wetting of AHSSs are restricted to a specific set of experimental annealing parameters with a fixed process atmosphere pO_2. Thus, the objective of the present study is to determine the effects of annealing atmosphere pO_2, annealing time and the addition of 0.05 wt.% Sn on the external and internal selective oxidation of an intercritically annealed Fe-0.1C-2Mn-1.7Si (wt.%) AHSS within the context of application to the continuous galvanizing process.

5.3   Experimental procedure

Two series of CMnSi steels, referred to as Reference and Sn-added in the subsequent text, were fabricated with the chemical composition shown in Table 5.1 for use in the present study.

Table 5.1: Chemical Composition of Experimental Steels (wt.%)

Steel	C	Mn	Si	Al	Ti	N	S	Sn	Fe
Reference	0.10	2.03	1.76	0.04	0.01	0.004	0.002	0.005	balance
Sn-added	0.11	2.04	1.75	0.04	0.01	0.003	0.002	0.05	balance

1.2 mm-thick cold-rolled steel sheets were cut into 10 mm×50 mm coupons with their longitudinal axis parallel to the sheets' rolling direction. All coupons were ground with 1200 grit SiC paper to mitigate the effect of surface roughness on subsequent surface analysis. Experimental heat treatments were executed in the McMaster Galvanizing Simulator (MGS, Iwatani Surtec) at an intercritical temperature of 1113 K (840 °C), in a N_2-5 vol.% H_2 process atmosphere and under three different dew points (dp) of 223 K (–50 °C), 243 K (–30 °C) and 278 K (+5 °C). A detailed summary of the experimental process atmospheres, including their pO_2 at the intercritical annealing temperature, is presented in Table 5.2.

Experimental samples were initially heated to 773 K (500 °C) at a heating rate of 15 K/s and to the intercritical annealing temperature (IAT) of 1113 K (840 °C) at a heating rate of 5 K/s. In order to investigate the effect of annealing time on the selective oxidation of the samples, they were held at the IAT for 60, 120, 240, 360 and 600 seconds. Samples were then cooled to 738 K (465 °C) at 20 K/s, held for 20 seconds to promote thermal equilibrium within the thickness of the sample and were eventually cooled at 20 K/s to room temperature by N_2 jet cooling. In all cases, the sample thermal profile was controlled by a 0.5 mm type K thermocouple welded to a coupon. All heat treatments employed triplicate samples. Immediately upon removal from the MGS, samples were stored in anhydrous isopropanol in order to mitigate further oxidation.

Table 5.2: Experimental Process Atmospheres

Process Atmosphere dp [K (°C)]	N_2 Content (Vol.%)	H_2 Content (Vol.%)	pH_2O/pH_2	pO_2 at 1113 K (840 °C) atm
223 (–50)	95	5	0.0010	5.52×10^{-24}
243 (–30)	95	5	0.0082	3.41×10^{-22}
278 (+5)	95	5	0.1380	9.68×10^{-20}

Several analytical techniques across a variety of length scales were used to investigate various aspects of the experimental steels' selective oxidation and to cross-correlate the results.

In order to determine the thickness of oxides as well as the mode of oxidation of Mn and Si, as a function of annealing parameters and the Sn addition, on a mesoscopic scale, elemental depth profiling was carried out using X-ray photoelectron spectroscopy (XPS) (PHI Quantera, Physical Electronics, Chanhassen, MN) with an Al Kα X-ray source (1486.6 eV). A 100 μm×100 μm area was analysed on each sample. The elemental depth profiled are considered accurate to ±5% of the measured value in atomic percent. Oxide speciation was determined via binding energy analysis and comparison to the appropriate standards. It should be noted that depth profiles were started after sputtering such that no significant C peak, arising from sample contamination during exposure to the ambient atmosphere, was present. All XPS data was processed using the MultiPak software (Version 6). The metallic Fe2$p_{2/3}$ binding energy was used to calibrate all spectra.

The morphology, size and spatial distribution of the external oxides during the annealing heat treatments were analyzed using a JEOL 7000F field emission gun scanning electron microscope (FEG-SEM). Prior to imaging, samples were coated with 5 nm-thick layer of Pt to avoid charging.

In order to measure the thickness of the external oxides and the depth of the internal oxides formed on the surface and in the subsurface of the experimental steels as a function of annealing time – i.e. determine the external and internal oxidation kinetics – focussed ion beam (FIB, NVision 40 by Zeiss) milling and image analysis was employed. In this case, at least two 15 μm-wide trenches were cut randomly on the cross section of each oxidized sample. Using a grid system, approximately 100 measurements of the external oxide thickness and internal oxidation

depth were carried out on each sample using ImageJ 1.42q software. The data were then averaged for the purposes of the kinetic study. It should be noted that the error bars presented in the kinetic study represent the 95% confidence interval of the mean in all cases. A more detailed explanation of this methodology is available elsewhere [33].

In order to determine the fine scale structure of the external and internal oxides, transmission electron microscope (TEM) integrated with a Gatan 865 electron energy loss spectroscopy (EELS) spectrometer was applied. TEM samples were fabricated via FIB lift-outs and standard preparation techniques across the external oxide-substrate interface, where the oxide was protected during FIB milling via C and W deposits. The resultant samples were then analysed using a FEI Titan 80 300 TEM using an acceleration voltage of 300 keV, where the energy resolution in monochromated mode was tuned to 0.08 eV full width half-maximum (FWHM) at the zero-loss peak. The obtained EELS spectra were processed using Gatan Digital Micrograph 2.3.

3D atom probe tomography (3D APT) across the external oxide-substrate interface was carried out using a Cameca LEAP 4000X HR atom probe. APT samples were prepared by sputter coating the sample surface with a 400 nm-thick Cr or Ni layer followed by APT needle preparation using established FIB lift-out procedures [34] and a 30 keV Ga ion beam, with final cleaning performed at 10 keV. The sharped tips were analyzed using laser pulse mode ($\lambda = 355$ nm) with pulse energy of 60 or 90 pJ/pulse at a base temperature of approximately 60 or 76 K for the as-received Sn-added and annealed Sn-added samples, respectively. The target detection rate was set at 0.003 ions/pulse (0.3%) which was maintained by an applied DC voltage. The laser pulsing rate was 125 kHz and 200 kHz for the as-received Sn-added and annealed Sn-added

samples, respectively. The data obtained were subsequently processed using IVAS v3.8 software.

5.4 Results

XPS elemental depth profiles of the Reference and Sn-added steels annealed under the three process atmospheres (Table 5.2) are shown in Figure 5.1. It should be noted that, for the sake of simplicity, the XPS results presented here were confined to annealing times of 120 s and 600 s.

In the case of the Reference steel, for the lowest pO_2 process atmosphere (i.e. 223 K (–50 °C) dp, Table 5.2) and annealing time of 120 s, enrichment of Si and Mn could be observed both on the surface and in the subsurface (Figure 5.1(a)) to a depth of approximately 350 nm, where their concentrations reduced to their bulk concentrations (3.4 and 2.0 at.%, respectively). This is while for the Sn-added steel annealed for 120 s at the same pO_2, Si showed only surface enrichment, indicative of the occurrence of external oxidation only (Figure 5.1(a)). Holding the experimental steel at the intercritical annealing temperature for the time of 600 s led to an increase in the external oxide thickness as well as the internal oxidation depth (Figure 5.1(b)) for both steels. However, for the 600 s annealing time, the Sn-added steel continued to show minimal internal oxidation (Figure 5.1(b)).

Raising the process atmosphere pO_2 to the 243 K (–30 °C) dp (Table 5.2) resulted in a decrease in the thickness of the external oxides and an increase in the depth of the internal oxidation of the Reference steel (Figure 5.1(c)) for the 120 s annealing time compared to the same steel annealed under the 223 K (–50 °C) dp process atmosphere. Addition of Sn to the steel did not significantly affect the thickness of the external oxides after the 120 s anneal (Figure 5.1(c)), but did appear to have resulted in a slight decrease in the thickness of external oxides after annealing 600 s (Figure 5.1(d)).

At the highest pO_2 process atmosphere (278 K (+5 °C) dp, Table 5.2), after annealing for 120 s, further reduction in the thickness of the external oxides and increase in the depth of internal oxidation were observed for both Reference and Sn-added steels (Figure 5.1(e)) compared to the lower pO_2 process atmospheres for the same annealing time. It can also be seen that, for both experimental steels, the thickness of the external oxides increased slightly with increasing annealing time from 120 to 600 s, due to providing more time for oxygen and alloying element diffusion to occur (Figure 5.1(f)). In addition, for both annealing times of 120 and 600 s, no significant change could be observed in the thickness of the external oxides between the Sn-added and the Reference steel (Figure 5.1(e,f)).

It should be noted that no significant Sn segregation could be observed in the XPS elemental profiles of the Sn-added steels for all annealing times and process atmosphere pO_2. This was due the inability of XPS to detect elements in the low concentrations associated with the Sn levels in the experimental steel, in this case 0.02 at.% [35].
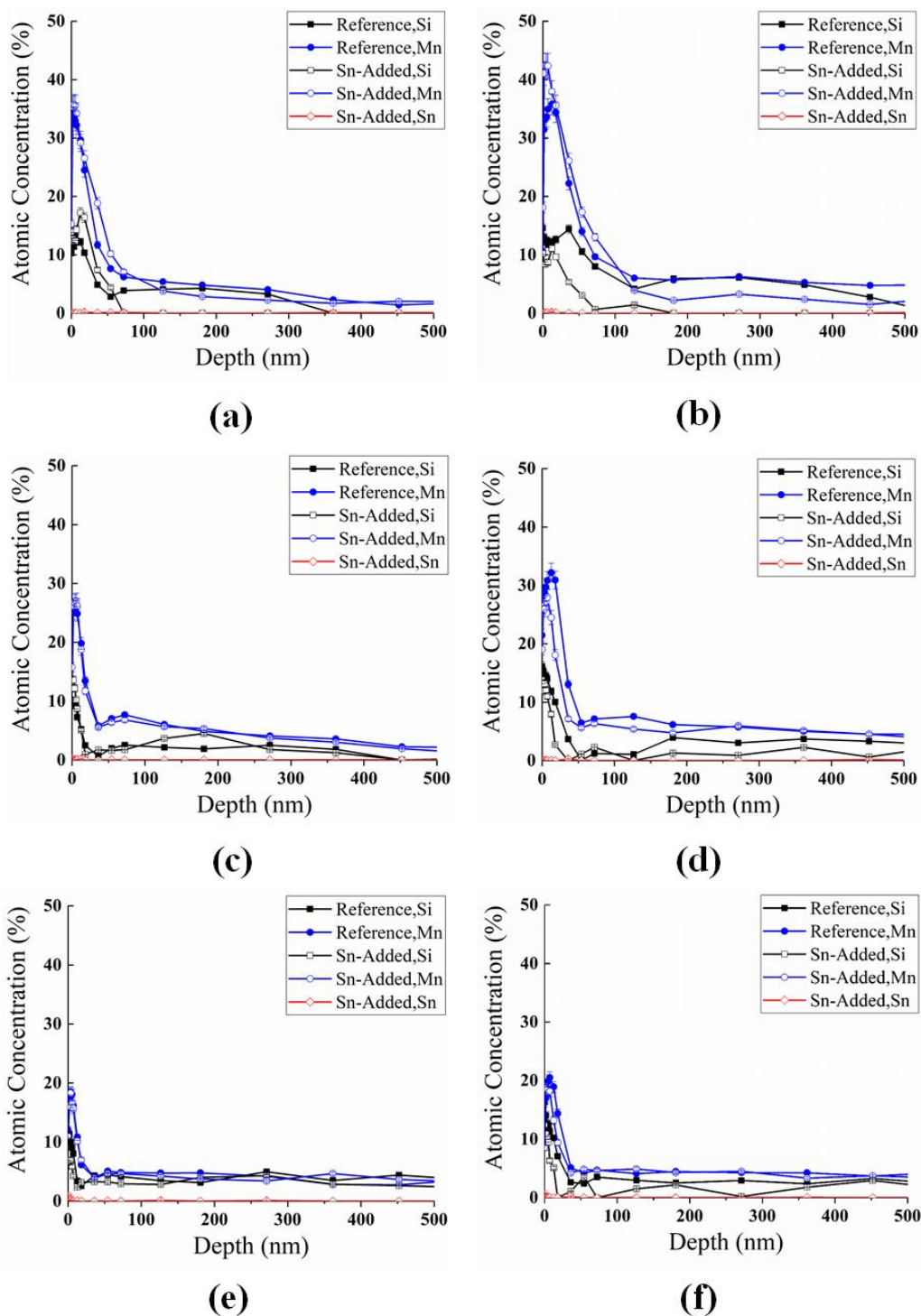
Figure 5.1: XPS elemental depth profiles of the Reference and Sn-added steels as a function of annealing time and process atmosphere pO$_2$: (a) 223 K (–50 °C) dp for 120 s, (b) 223 K (–50 °C) dp for 600 s, (c) 243 K (–30 °C) dp for 120 s, (d) 243 K (–30 °C) dp for 600 s,(e) 278 K (+5 °C) dp for 120 s, and (f) 278 K (+5 °C) dp for 600 s.

Figure 5.2(a) and (b) show the growth kinetics of the external and internal oxides, respectively, as a function of process atmosphere pO_2 and Sn addition, which were achieved by measuring the thickness of the external oxides and the depth of internal oxidation formed during annealing of the experimental steels on the FIB trench cut micrographs. As can be seen, for both the Reference and Sn-added steels under all of the process atmosphere pO_2 explored, the external oxide thickness and internal oxidation depth kinetics obeyed a parabolic rate law, indicative of solid-state diffusion controlled oxidation [36]. It is noteworthy that the coefficient of determination (i.e. R^2 value) of the regression lines was greater than 0.79 for all of the data presented in Figure 5.2. Moreover, increasing the annealing atmosphere pO_2 via increasing the process atmosphere dew point resulted in a decrease in the thickness of the external oxides (Figure 5.2(a)) and an increase in the depth of internal oxidation (Figure 5.2(b)), as would be expected according to the Wagner criterion for the internal to external oxidation transition [37]. In addition, it can be seen that, for all process atmosphere pO_2, the rates of both external and internal oxidation were decreased significantly by the addition of Sn to the substrate for a given process atmosphere pO_2. This result is further highlighted in Figure 5.3, which shows the variation in the parabolic rate constant (k_P) with process atmosphere and substrate composition for external (Figure 5.3(a)) and internal oxidation (Figure 5.3(b)), respectively. From this, it can be seen that the rate constants for external oxidation (Figure 5.3(a)) decreased significantly for both the Reference and Sn-added substrates with increasing the process atmosphere pO_2 from the 223 K (–50 °C) dp to the 243 K (–30 °C) dp, after which the value of k_P did not change significantly for the highest pO_2 278 K (+5 °C) dp process atmosphere. These trends are consistent with the transition from external to internal oxidation and the internal oxidation kinetic data in Figure 5.2(b) and Figure 5.3(b), which show the reverse trend to that of the

external oxidation – i.e. significantly increasing depth of internal oxidation and increasing k_P values with increasing process atmosphere pO_2. However, in all cases, the external and internal oxidation kinetics and k_P values for the Sn-added steel were significantly lower than those observed for the Reference alloy, indicating that the 0.05 wt.% Sn addition significantly lowered the transport of O into the steel and Mn/Si to the oxidation front, as previously suggested by Cho et al. [25]. Similar results were reported by Pourmajidian and McDermid [33] as the effect of the addition of 0.05 wt.% Sn to a 0.1C-6Mn-2Si (wt.%) medium-Mn AHSS on the oxide growth kinetics.
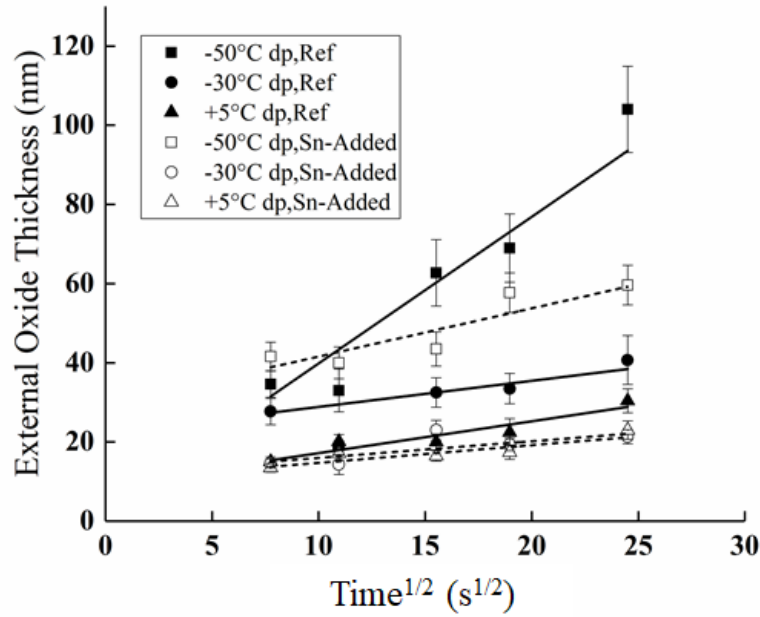
(a)
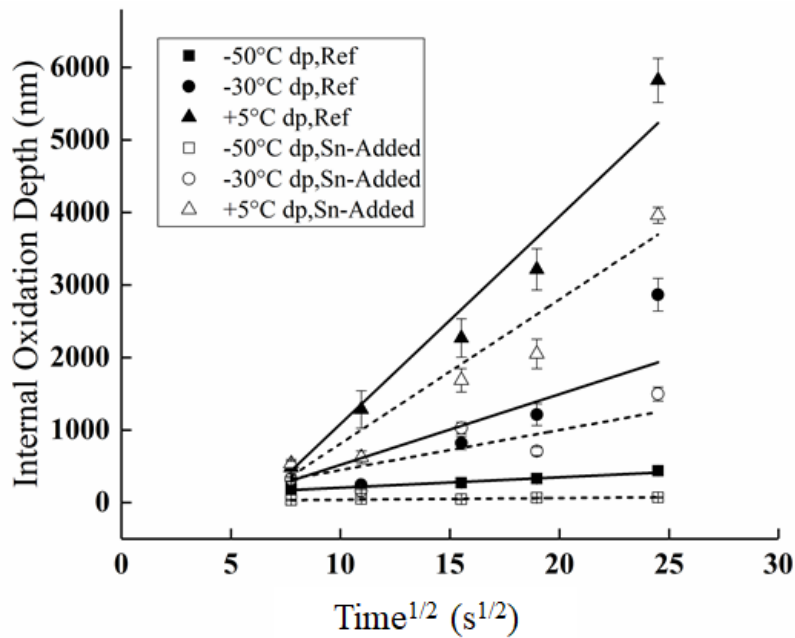
(b)

Figure 5.2: Growth kinetics of (a) external oxides and (b) internal oxides formed during annealing the Reference and Sn-added steels as a function of process atmosphere.
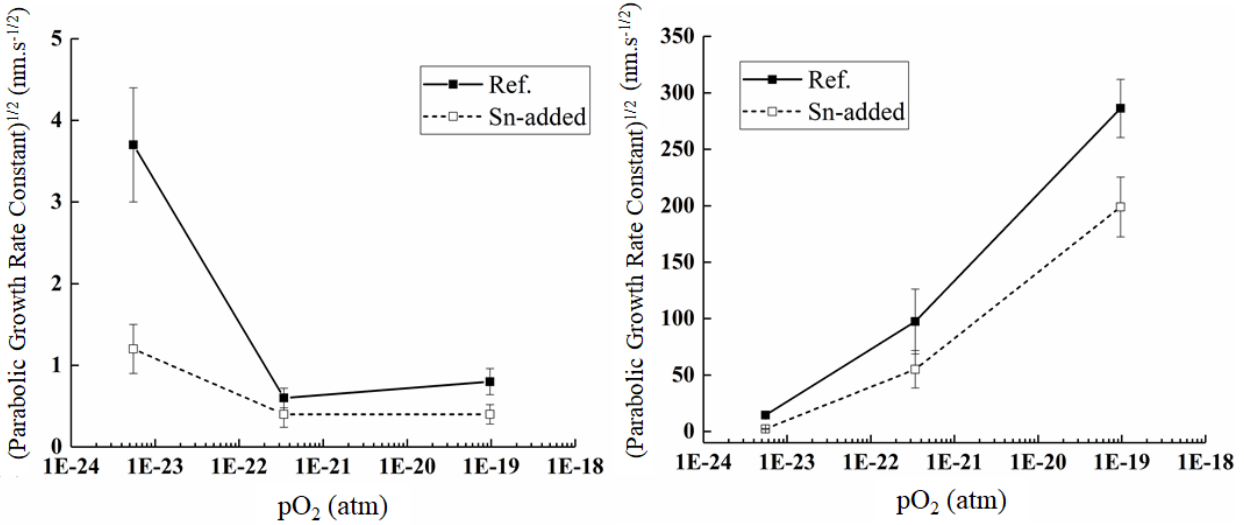
Figure 5.3: Parabolic growth rate constants for the Reference and Sn-added steel selective oxidation (a) external oxidation; (b) internal oxidation.

Figure 5.4 through Figure 5.6 show the morphology and distribution of the oxides formed on the surface of the Reference and Sn-added steels after being intercritically annealed under the 223 K (–50 °C) dp, 243 K (–30 °C) dp and 278 K (+5 °C) dp process atmospheres, respectively, for annealing times of 120 and 600 s.

Per Figure 5.4, annealing the Reference steel under the lowest pO_2 process atmosphere (i.e. 223 K (–50 °C) dp, Table 5.2) for 120 s resulted in the formation of closely-packed patches of compact granular oxides with areas in between these oxide patches consisting of compact, film-like oxides (Figure 5.4(a)). However, in the case of the Sn-added steel, although the same oxide morphology was observed, the patches of granular oxides were relatively widely spaced and the steel surface comprised larger area fractions of film-like oxides compared to the Reference steel (Figure 5.4(b)). Annealing the steel for 600 s led to the formation of compact, film-like oxide on the Reference steel (Figure 5.4(c)) and an increase in surface coverage and coarsening of the oxides on the Sn-added steel (Figure 5.4(d)), as would be expected due to the growth of the

oxides during prolonged annealing. These results are generally consistent with the XPS results provided in Figure 5.1(a,b) and the external oxidation kinetic data presented in Figure 5.2.

As can be seen in Figure 5.5, increasing the process atmosphere pO_2 to the 243 K (–30 °C) dp (Table 5.2) led to the formation of compact, film-like external oxides on the surface of the Reference steel after 120 s of intercritical annealing (Figure 5.5(a)). Increasing the annealing time to 600 s resulted in an increase in the compactness of the external oxides (Figure 5.5(b,d)). However, although these external oxides formed in a film-like morphology on the Reference steel (Figure 5.5(a,b)), the addition of Sn to the steel altered their morphology to nodular particles (Figure 5.5(c,d)).

From Figure 5.6, it can be seen that annealing the Reference steel under the highest pO_2 process atmosphere of 278 K (+5 °C) dp (Table 5.2) for 120 s modified the external oxide morphology from the relatively compact, granular oxides with small fractions of interspersed films observed for the lowest pO_2 process atmosphere of 223 K (–50 °C) dp (Figure 5.4(a)) and compact, film-like oxides observed for the intermediate pO_2 process atmosphere of 243 K (–30 °C) dp (Figure 5.5(a)) to a combination of film-like and fine, closely spaced nodule-like particles (Figure 5.6(a)). Adding Sn to the steel, however, significantly changed the morphology of the oxides to large, widely spaced nodule-like particles (Figure 5.4(b)). As reported by Bellhouse and McDermid [38], the existence of large, widely-spaced oxide nodules on the surface of the steel can have benefits in promoting good reactive wetting, which the authors attributed to the formation of Fe-Al intermetallics between the oxide nodules. Significant coarsening of the external oxides for the Sn-added alloy was observed for the longer annealing time of 600 s (Figure 5.6(c,d)), as would be expected given the diffusional nature of external oxide growth.
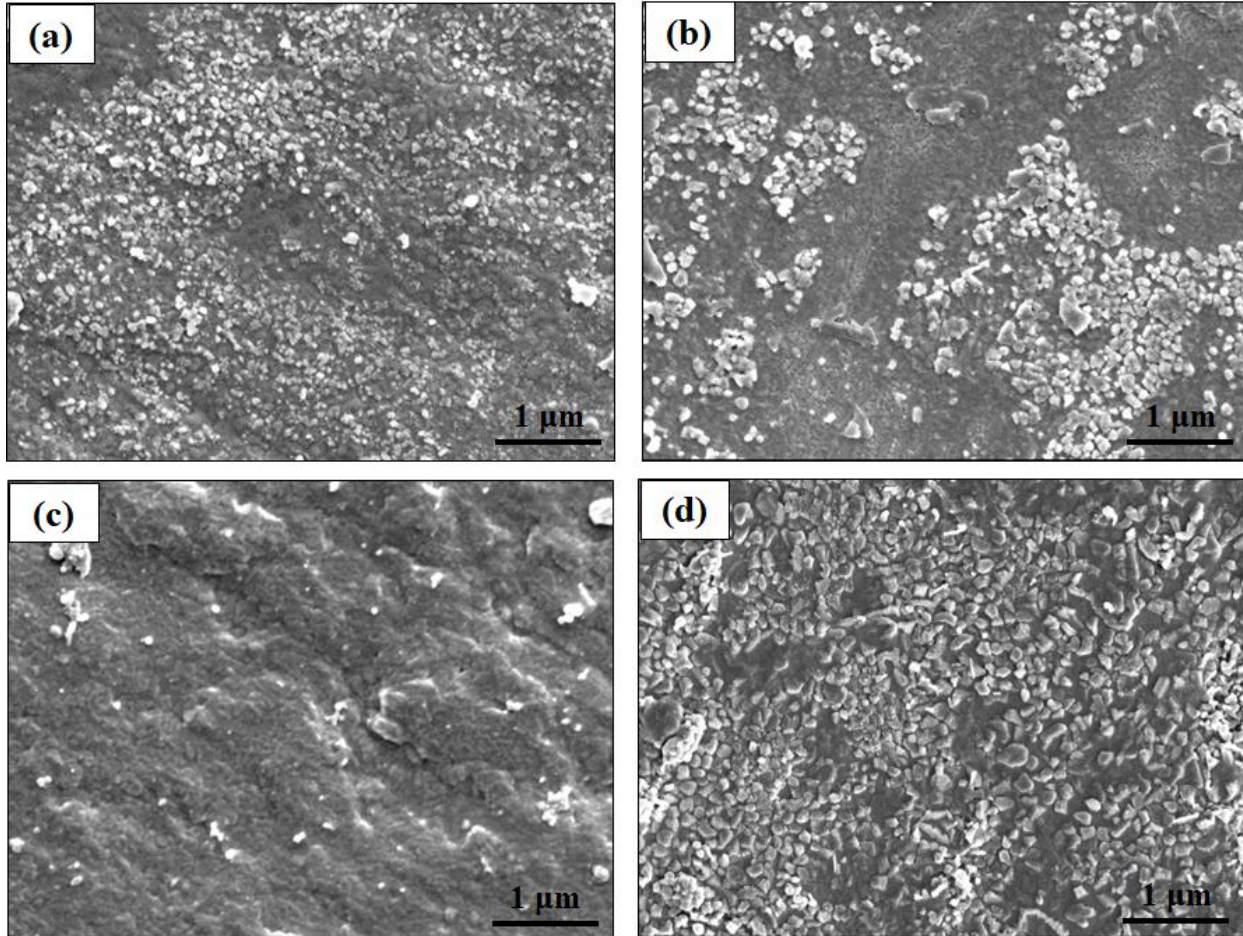
Figure 5.4: SEM images of the Reference and Sn-added steel surfaces annealed under the 223 K (–50 °C) dp process atmosphere as a function of annealing time: (a) Reference steel, 120 s, (b) Sn-added steel, 120 s, (c) Reference steel, 600 s, and (d) Sn-added steel, 600 s.
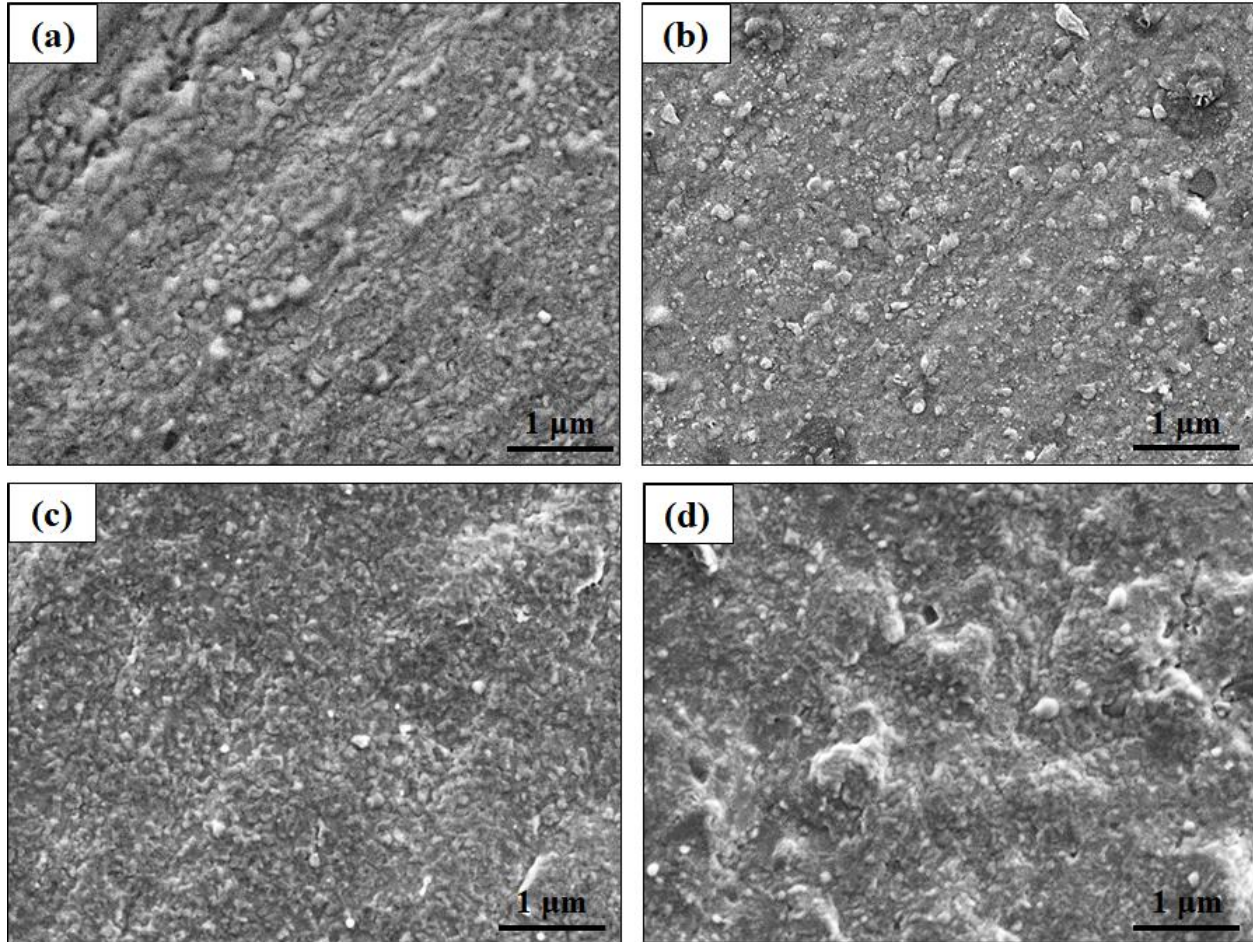
Figure 5.5: SEM images of the Reference and Sn-added steel surfaces annealed under the 243 K (–30 °C) dp process atmosphere as a function of annealing time: (a) Reference steel, 120 s, (b) Sn-added steel, 120 s, (c) Reference steel, 600 s, and (d) Sn-added steel, 600 s.
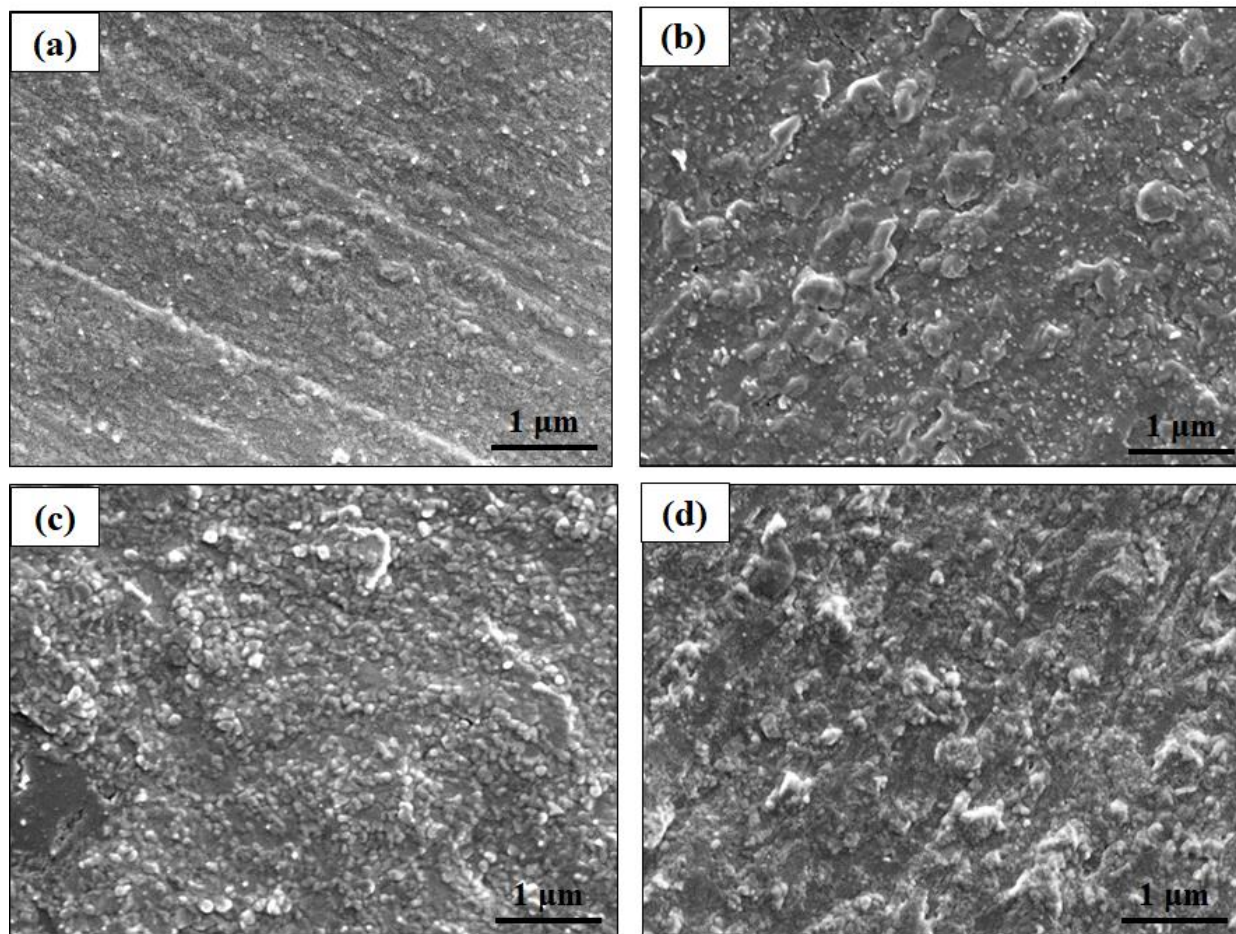
Figure 5.6: SEM images of the Reference and Sn-added steel surfaces annealed under the 278 K (+5 °C) dp process atmosphere as a function of annealing time: (a) Reference steel, 120 s, (b) Sn-added steel, 120 s, (c) Reference steel, 600 s, and (d) Sn-added steel, 600 s.

TEM was used to characterize the fine scale microstructural details of the external and internal oxides. Due to the importance of the of the 120 s annealing time to the industrial continuous galvanizing process, the TEM results presented herein have been confined to this annealing time as a function of process atmosphere pO_2. Figure 5.7(a) and (b) show TEM cross-sectional micrograph of the Reference and Sn-added steels annealed under the lowest pO_2 223 K (–50 °C) dp process atmosphere (Table 5.2), respectively, along with the Mn-$L_{2,3}$, O-K and Si-K edge EELS spectra (Figure 5.7(c)) of the points labeled as 1, 2 and 3 in Figure 5.7(a). It should

be noted that the dark area above the oxides in Figure 5.7(a,b) correspond to the C film deposited on the sample prior to FIB milling. Per Figure 5.7(a), a two-layer 33±5 nm-thick external oxide can be seen on the surface of the Reference steel. A comparison between the features of the Mn-$L_{2,3}$, O-K and Si-K edges with the standard $MnSiO_3$, Mn_2SiO_4 [39], MnO [40] and SiO_2 [41] EELS spectra revealed that the compact granular external oxides corresponded to MnO and the oxides at the steel/oxide interface corresponded to $MnSiO_3$. The darkest oxide, demarcated as point 3 in Figure 5.7(a), was determined to be SiO_2. On the other hand, per Figure 5.7(b), a 40±4 nm-thick multi-layer external oxide formed on the Sn-added steel, with granular particles located farther apart compared to the Reference steel (Figure 5.7(a)). The top, middle and bottom oxides corresponded to MnO, $MnSiO_3$ and SiO_2, respectively. The formation of less compact granular oxides on the surface of the Sn-added steel compared to the Reference steel is consistant with the SEM observations in Figure 5.4(a,b). Comparing Figure 5.7(a) and (b), it can be seen that the internal oxides formed in the Reference steel (Figure 5.7(a)) were larger and were located deeper into the subsurface compared to those of the Sn-added steel (Figure 5.7(b)), as was observed the XPS elemental profiles (Figure 5.1(a)). The internal oxides were identified as $MnSiO_3$ closer to the surface and a mixture of $MnSiO_3$ and SiO_2 deeper in the subsurface in both steels.

Figure 5.8 shows TEM views across the external oxide interface and subsurface of the Reference and Sn-added steels after annealing under the 243 K (–30 °C) and 278 K (+5 °C) dp process atmospheres for 120 s. As previously observed with the XPS data (Figure 5.1) and internal oxidation kinetics study (Figure 5.2(b), Figure 5.3 and Table 5.2), increasing the annealing atmosphere pO_2 resulted in a significant increase in the depth of internal oxidation from 206±25 nm under the 223 K (–50 °C) dp process atmosphere to 247±35 nm to 1285±259 nm under the 243 K (–30 °C) and 278 K (+5 °C) dp process atmospheres, respectively, for the

Reference steel. Similarly, in the case of the Sn-added steel, the depth of internal oxidation increased from 51 ± 18 nm under the 223 K (–50 °C) dp process atmosphere to 165 ± 36 nm and 627 ± 87 nm under the 243 K (–30 °C) and 278 K (+5 °C) dp process atmospheres, respectively.

Under the 243 K (–30 °C) dp process atmosphere, the external oxide morphology was changed from large, thick and compact plate-like and film-like particles to smaller and thinner ones after the addition of Sn, the composition of which was determined to be SiO_2 and $MnSiO_3$ via EELS (Figure 5.8(a,b)) in both cases. Under the 278 K (+5 °C) dp process atmosphere, internal oxides formed in two distinct morphologies in the Reference and Sn-added steels. For the Reference steel, zone I included $MnSiO_3$ and Mn_2SiO_4 oxide particles sited both in the bulk and along the grain boundaries, to a depth of approximately 500 nm. Zone II, on the other hand, defined as the area in which a network of grain boundary oxides were observed, encompassed the region approximately ~2 μm below the surface (Figure 5.8(c)). Adding Sn to the steel composition resulted in a similar oxidation pattern and oxide composition in the steel subsurface, with the most significant difference being the overlap between zone I and zone II (Figure 5.8(d)). This result would indicate that Sn plays a significant role in slowing mass transport of O and the oxidizing species along the grain boundary network. In addition, comparing the higher magnification cross sectional views of the external oxides of the Reference and Sn-added steels, shown in Figure 5.8(c) and (d), respectively, revealed that, although the oxides formed in small, compact nodule-like particles on the surface of the Reference steel (Figure 5.8(c)), the addition of Sn to the steel resulted in the modification of the oxide morphology to distinct, larger and more widely spaced nodules (Figure 5.8(d)), which are known to provide fewer obstacles for reactive wetting during continuous galvanizing [4,6]. The external oxides were identified as $MnSiO_3$ for both Reference and Sn-added steels via EELS analysis.
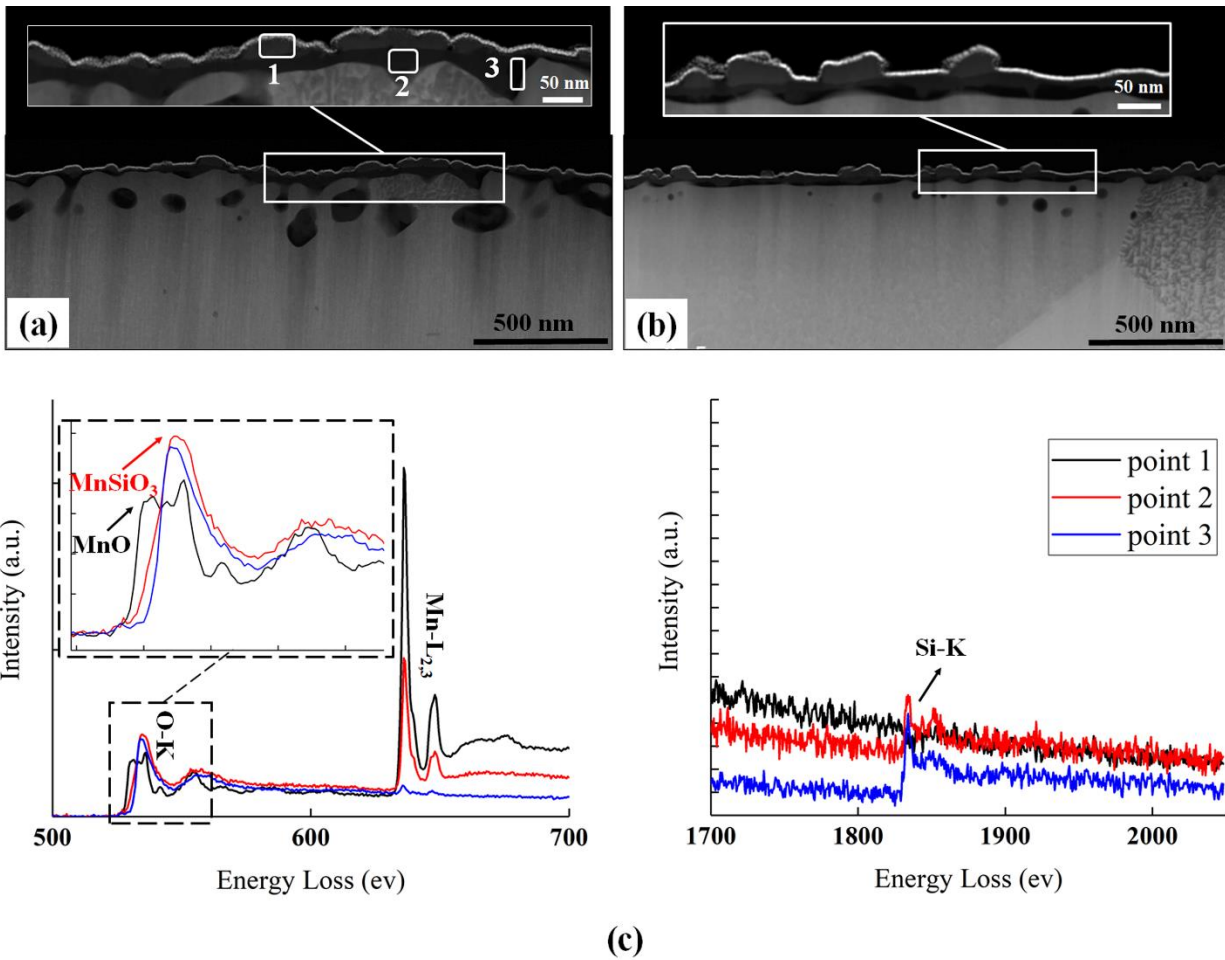
Figure 5.7: TEM cross sectional micrograph of the (a) reference steel and (b) Sn-added steel annealed under the 223 K (–50 °C) dp process atmosphere. (c) Mn-$L_{2,3}$, O-K and Si-K edge electron energy loss spectra of points 1 through 3 in (b).
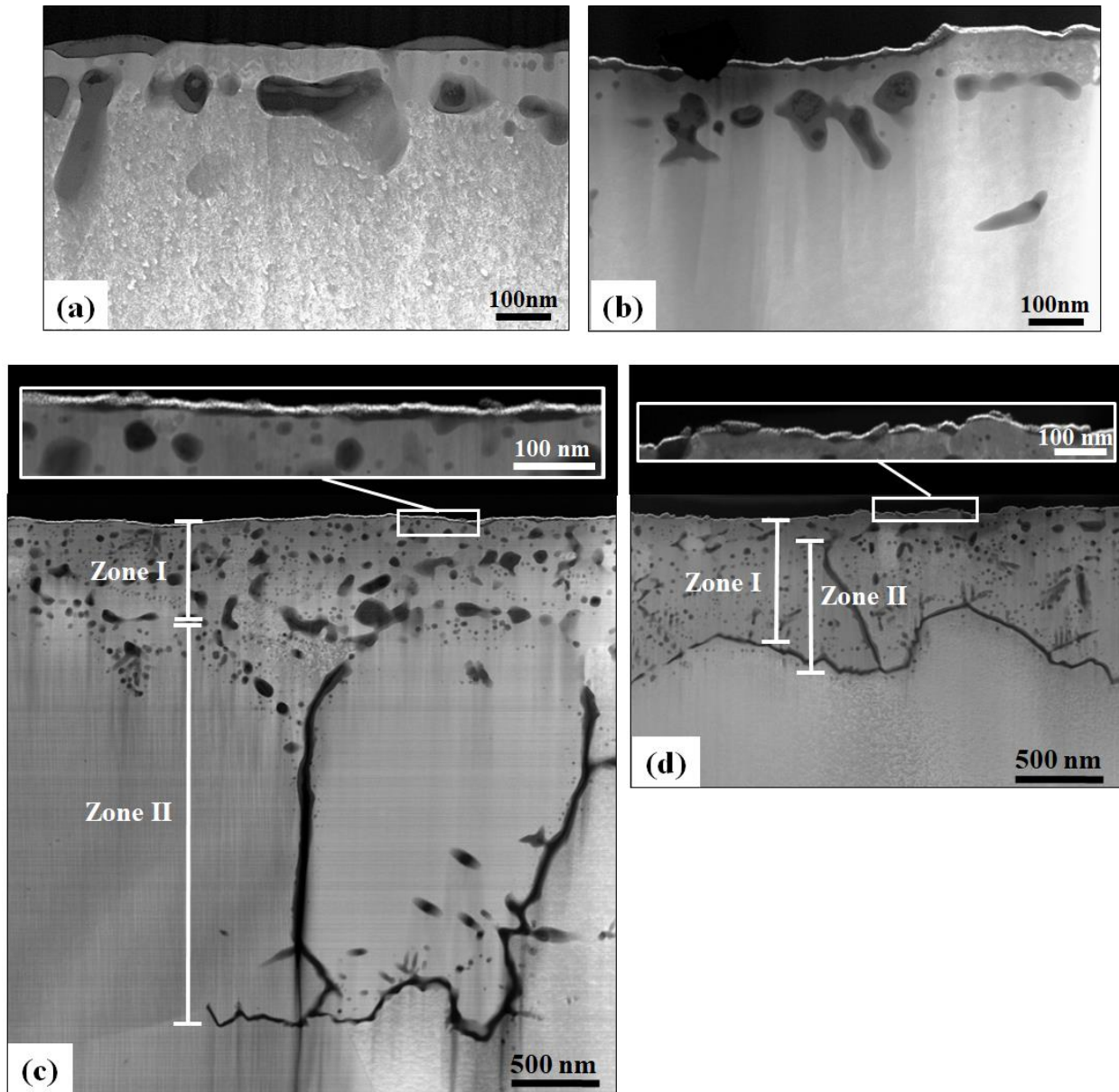
Figure 5.8: TEM cross sectional micrograph of the surface and subsurface of the (a and b) Reference and Sn-added steels, respectively annealed under the 243 K (–30 °C) dp process atmosphere and (c and d) Reference and Sn-added steels, respectively, annealed under the 278 K (+5 °C) dp process atmosphere.

Figure 5.9 shows a TEM micrograph and EELS elemental maps of the oxide network formed along a grain boundary of the Sn-added steel shown in Figure 5.8(d). Two different oxide compositions were expected to be identified in the oxide network as there was a difference in

contrast between the core and the shell of the oxide (Figure 5.9(a)). The corresponding TEM elemental maps shown in Figure 5.9(b) indicated that, although the center of the grain boundary oxide was rich in Si, the outer shell was rich in both Si and Mn. Using EELS analysis, the outer shell and the core of the oxide network were identified as $MnSiO_3$ and SiO_2, respectively.
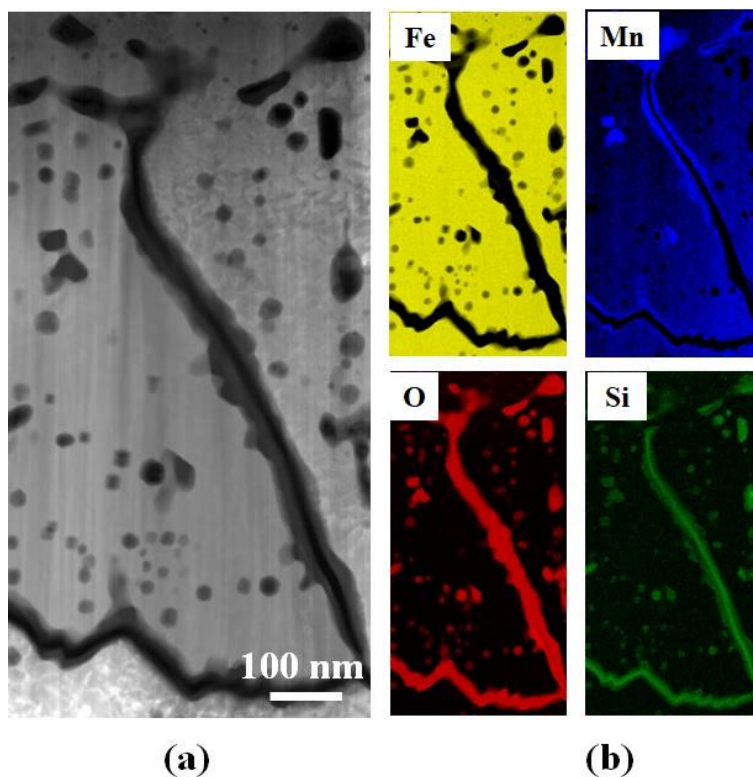
Figure 5.9: (a) Detailed TEM micrograph of the oxide network formed along a grain boundary of the Sn-added steel annealed under the 278 K (+5 °C) dp process atmosphere. (b) TEM elemental maps of the oxide network.

Figure 5.10 shows the APT results obtained to identify the elemental distribution at the steel/external oxide interface of the Sn-added steel annealed under the lowest pO_2 223 K (–50 °C) dp process atmosphere for 600 s. Figure 5.10(a) provides the 3D atom map of Fe, Mn, Si and Sn. Figure 5.10(b) shows a one-dimensional (1D) concentration profile generated via a proximity histogram (proxigram) from the 95 at.% Fe isosurface. As can be seen, there was a Si-rich oxide

transition region between the Mn-rich oxide and the Fe-rich substrate. Sn was concentrated in this interface region to a maximum of approximately 3 at.%, which is roughly $150\times$ its bulk concentration of 0.02 at.%. It can also be seen from Figure 5.10(b) that there was some segregation of Sn, albeit very slight, into the external oxide, which the Mn:O ratio from the elemental profiles suggests was MnO, consistent with the previous EELS (Figure 5.7) and XPS (Figure 5.1) analyses. The existence of Fe, Si and O enrichment simultaneously at the interface beneath the oxide is likely an artefact in the APT results, due either to the known issue of O retention with analysis depth [42], or because of the relatively rough interface from which the results are obtained.

To confirm that Sn segregation to the external surface occurred during intercritical annealing and was not present on the as-received surfaces, the as-received steel/external oxide interface was also analyzed by APT, the results of which are shown in Figure 5.11. Figure 5.11(a) shows the 3D atom map of Fe, FeO and Ni (Ni comes from the cap deposited prior to FIB milling and is present at the base of the APT volume, with the Fe metal on the top), with elemental compositional profiles shown in Figure 5.11(b). As can be seen in Figure 5.11(b), there was a transition from the substrate to the Ni coating over a distance of approximately 6 nm. The O content increased significantly in this region, suggesting the presence of an Fe-O layer on the steel surface, as would be expected due to the exposure of the substrate to ambient O_2. This O enrichment extended slightly into the Ni layer, which is a typical artefact of APT due to preferential retention of O [42]. Some Si enrichment can be seen just below the Fe oxide. No evidence of Sn segregation could be found at the steel/oxide interface. In order to ensure that Sn was detectable by APT and no artefact was present in the results, a concentration measurement was taken from a region of steel below the surface. The result of this analysis is shown in

Table 5.3. As can be seen, the Sn concentration was consistent with the bulk values reported in Table 5.1. Thus, it can be concluded that there was no significant, pre-annealing Sn segregation to the oxide/substrate. This implies that any Sn enrichment arising from the hot rolling operation was removed from the interface during the pickling, scraping or sandblasting operations prior to cold rolling and annealing at that the observed Sn segregation to the external oxide/substrate interface occurred during intercritical annealing.
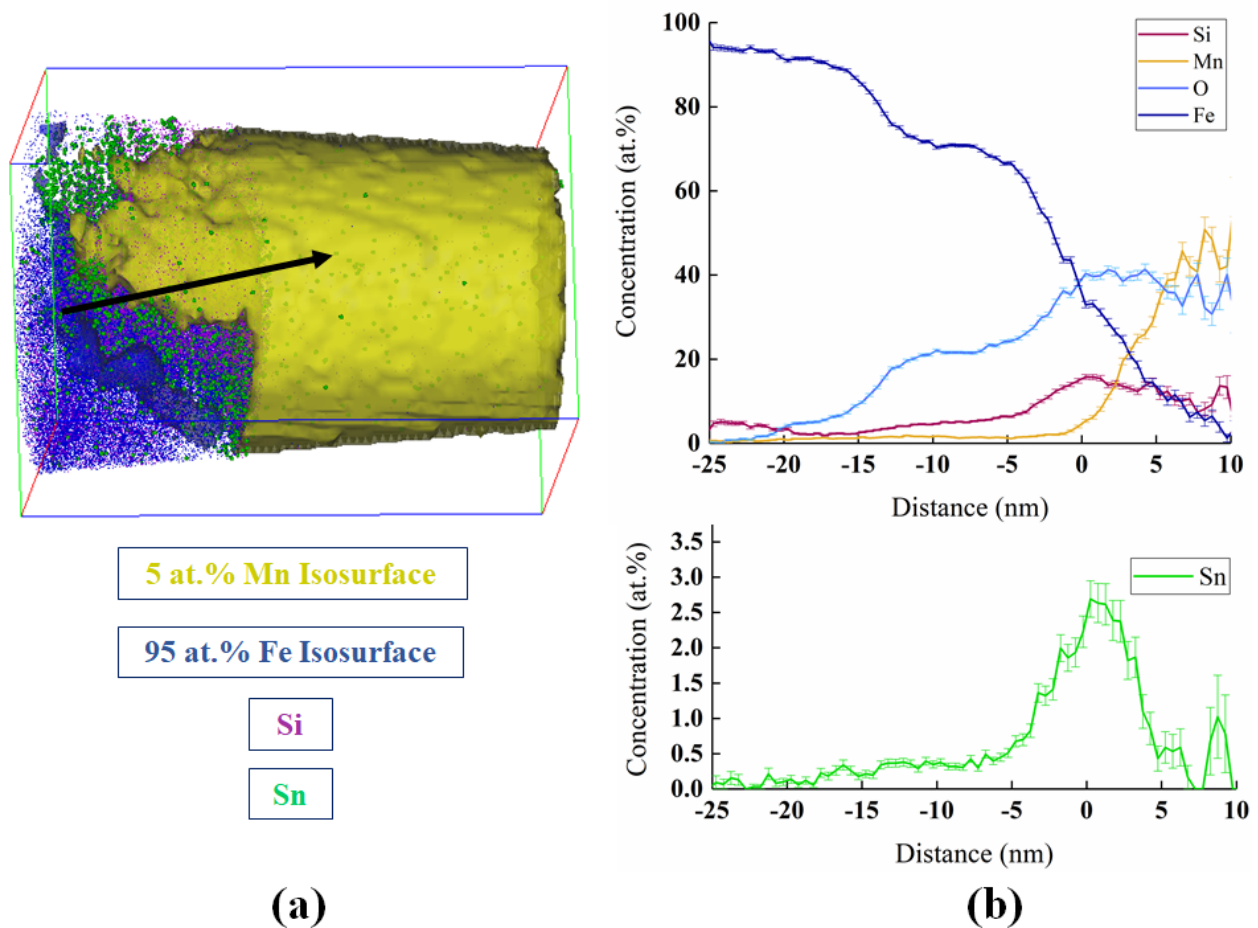
Figure 5.10: (a) 3D APT atom map of the surface oxide/substrate interface of the Sn-added steel annealed under the 223 K (–50 °C) dp process atmosphere for 600 s. (b) 1D concentration profiles of Fe, O, Mn, Si and Sn along the arrow in (a).
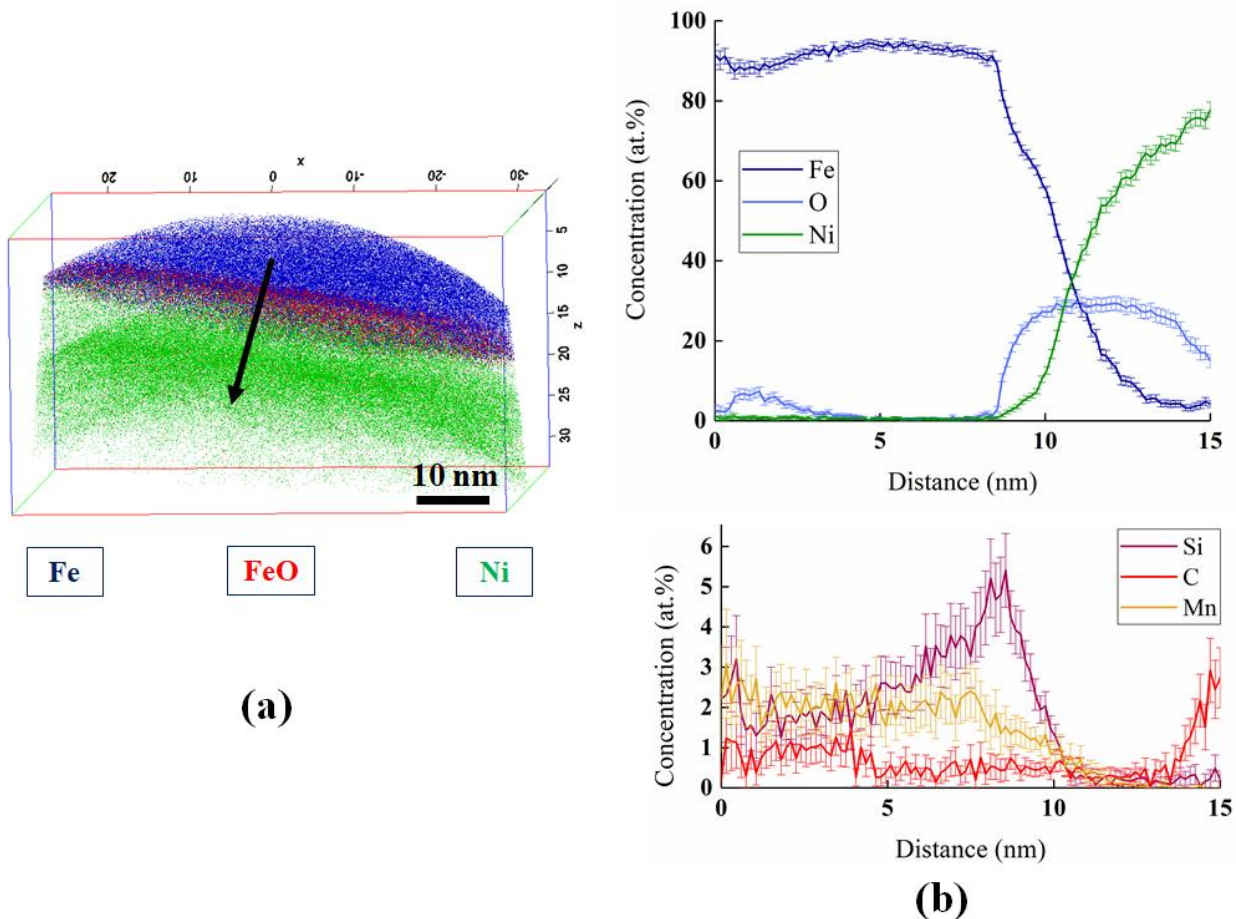
Figure 5.11: (a) 3D APT atom map of the surface oxide/substrate interface of the as-received Sn-added steel. (b) 1D concentration profiles of Fe, O, Ni, Si, C and Mn along the direction shown by the arrow in (a).

Table 5.3: Elemental Concentration obtained from the As-Received Sn-added steel using APT

Element	Concentration (at.%)	Concentration (wt.%)
Fe	93.68	95.69
Si	4.168	2.14
Mn	2.052	2.06
Sn	0.0169	0.04

5.5   Discussion

The effects of process atmosphere oxygen partial pressure (pO_2), addition of 0.05 wt.% Sn to the steel chemistry, and annealing time on the morphology, chemistry, and growth kinetics of both external and internal oxides formed during annealing heat treatments prior to galvanizing of a Fe-0.1C-2Mn-1.7Si (wt.%) advanced high strength steel in a simulated continuous galvanizing process were determined.

For both the Reference and Sn-added steels, as was anticipated according to the Wagner criterion [37], increasing the process atmosphere pO_2 via increasing the process atmosphere dew point was shown to encourage internal oxidation and reduce external oxidation of the alloying elements. This is exemplified by the observed decrease in the surface enrichment of Si and Mn and increase in the depth of internal oxidation per the XPS elemental depth profiles (Figure 5.1), as well as the lower coverage of the experimental steels' surfaces by the oxides shown in the SEM surface images (Figure 5.4 through Figure 5.6) for the higher pO_2 process atmospheres. This finding is further supported by the greater depth at which oxides formed in the subsurface, as shown in the TEM cross-sectional micrographs (Figure 5.7 and Figure 5.8) under the higher pO_2 243 K (–30 °C) and 278 K (+5 °C) dp process atmospheres compared to the lowest pO_2 223 K (–50 °C) dp process atmosphere (Table 5.2).

That the transition from external to internal oxidation occurred by increasing the process atmosphere pO_2 from the 223 K (–50 °C) dp to 278 K (+5 °C) dp was also confirmed by the decrease in the external oxide thickness and increase in internal oxidation depth exhibited in Figure 5.2(a) and (b) respectively, as well as the decrease established in the growth rate constant of the external oxides shown in Figure 5.3(a) and (b), respectively. The decrease in the thickness of the film-like surface oxides obtained by increasing the atmosphere dew point from 223 K (–50

°C) to 243 K (–30 °C) and the modifications which occurred in the morphology of the surface oxides from film-like to nodule-like particles by further increasing the process atmosphere pO_2 using the 278 K (+5 °C) dp is expected to promote reactive wetting of the alloys during continuous galvanizing through providing conditions for the formation of the η-$Fe_2Al_5Zn_X$ interfacial layer via mechanisms such as aluminothermic reduction and interfacial infiltration of the Zn(Al,Fe) continuous galvanizing bath, as has been reported by several authors [4,6,13,24,43].

Adding 0.05 wt.% Sn to the steel chemistry was shown to affect both external and internal oxide morphology and their growth kinetics. As was shown by comparing the 3D APT data from Figure 5.10 and Figure 5.11, Sn segregation to the steel surface occurred during intercritical annealing and was not present on the as-received surface. As shown in Figure 5.10(b), the enrichment of Sn to the oxide/substrate interface on the Sn-added steel annealed for 600 s under the 223 K (–50 °C) dp process atmosphere was approximately 150× times the nominal bulk concentration value, indicating a strong driving force for surface segregation. Per the oxide growth kinetics shown in Figure 5.2, for all process atmosphere pO_2 and annealing times, the Sn addition to the steel chemistry reduced the thickness of the external oxides and the depth of internal oxidation, in agreement with the results reported using XPS elemental depth profiles (Figure 5.1) and TEM cross-sectional micrographs (Figure 5.7 and Figure 5.8). Moreover, as shown in Figure 5.3, in all cases, the parabolic growth constants (i.e. k_P values) were lowered by the addition of Sn to the substrate. As the thickness of external oxides and depth of internal oxidation were found to have a parabolic relationship with square root of annealing time, characteristic of a solid-state diffusion controlled oxidation, it can undoubtedly be concluded that the diffusion barrier function of Sn segregation reduced the inward diffusion of oxygen and

outward diffusion of the alloying elements, thus reduced the oxide growth kinetics in the alloy under a given process atmosphere pO_2 and annealing time (Figure 5.2 and Figure 5.3) [25,33]. This hypothesis is further supported by the change in internal oxide morphology shown in Figure 5.8 between the Reference and Sn-added alloy, where the grain boundary oxidation depth was significantly greater for the Reference vs. Sn-added steel.

The reduction in the compactness of granular MnO oxides under the 223 K (–50 °C) dp process atmosphere (Figure 5.4 and Figure 5.7), as well as the alteration observed in the external oxide morphology from compact, large and thick $MnSiO_3$ and SiO_2 particles to smaller, thinner and less compact nodule-like ones under the 243 K (–30 °C) dp (Figure 5.5 and Figure 5.8(a,b)), and from film-like and fine, closely spaced nodule-like $MnSiO_3$ particles to larger, more widely spaced ones under the 278 K (+5 °C) dp process atmosphere (Figure 5.6 and Figure 5.8(c,d)) arising from the addition of Sn to the steel can be attributed to the Sn effect on reducing the substrate surface energy [21]. This result arises from the Sn segregation overcoming the sum of surface energy of the oxide film and the interfacial energy of the substrate and the oxide over the substrate surface energy, as suggested by Cho et al. [25]. As mentioned before, the external oxide morphologies observed for the Sn-added alloy are expected to improve reactive wetting during continuous galvanizing, which is subject of current investigation by the present authors and will be reported as a complement to the current research.

It should also be noted that, in the present case, the Reference and Sn-added external oxides were identified as MnO, SiO_2 and $MnSiO_3$, with no significant change in the composition of the external oxides as a result of the addition of Sn. However, it should be noted that Cho et al. [25], reported a decrease in their external oxides' Mn to Si ratio with the addition of Sn to their low alloy TRIP-assisted steel. This was probably due to the higher amounts of Sn added to their

experimental steel compared to the current experimental steel. As mentioned previously, the amount of Sn was deliberately selected as 0.05 wt.% in this research in order to minimize or mitigate any detrimental effects on the mechanical properties of the steel [31,32].

It is worth mentioning that, per Figure 5.3 it seems that Sn suppresses the kinetics of both external and internal oxidation, it should be considered that holding the steel for longer annealing times simultaneously increased the thickness of the external oxides and the depth of the internal oxides, the presence of which will deteriorate the steel coating quality during continuous galvanizing and may have detrimental impact on the fabrication operations such as resistance spot welding, which is the subject of an investigation by the present authors.

5.6   Conclusions

The combined effects of annealing time, atmosphere oxygen partial pressure and a 0.05 wt.% Sn on the morphology, thickness and chemistry of the oxides formed during annealing an experimental Fe-0.1C-2Mn-1.7Si (wt.%) alloy under 223 K (–50 °C), 243 K (–30 °C) and 278 K (+5°C) dp process atmospheres were investigated. The following was determined:

1. Increasing the annealing atmosphere pO_2 via increasing the process atmosphere dew point from 223 K (–50 °C) to 243 K (–30 °C) and 278 K (+5 °C) was found to encourage internal oxidation rather than external oxidation, thus decreased the thickness of the external oxides and increased the depth of internal oxidation.

2. Significant surface Sn enrichment at the surface/oxide interface occurred during intercritical annealing relative to its bulk concentration.

3. It was determined that, in the case of the Sn-added steel, the external and internal oxidation kinetics were significantly reduced, likely as a result of the observed segregation of Sn to the

146

surface of the steel and its effect on the inward diffusion of O and the outward diffusion of the alloying elements. This reduction in kinetics manifested itself via a significant effect on the parabolic rate constants for the Sn-added alloy for the growth of both the external and internal oxides.

4. The Sn addition changed the morphology of the external oxides for all annealing conditions explored. Under the 223 K (–50 °C) process atmosphere, Sn reduced the surface coverage of closely-packed areas of compact granular MnO oxides. Under the 243 K (–30 °C), the addition of Sn altered the morphology of the surface oxides from film-like $MnSiO_3$ and SiO_2 layers comprised of large and thick particles to smaller, thinner and less compact nodule-like oxides. Under the highest pO_2 278 K (+5 °C) dp process atmosphere, Sn modified the surface oxides from film-like and fine, closely spaced nodule-like $MnSiO_3$ particles to larger, more widely spaced nodules. The observed changes are very likely a consequence of the Sn segregation to the external oxide/substrate interface, locally altering the surface tension of the substrate.

5. It is expected that the changes in the external oxide morphology observed for the Sn-added alloy will have positive benefits with respect to the reactive wetting of the experimental alloy by the continuous galvanizing Zn(Al,Fe) bath.

5.7   Acknowledgments

with the galvanizing simulations, Mr. Travis Casagrande and Dr. Andreas Korinek from the

Canadian Centre for Electron Microscopy for aid with the sample analysis and Ms. Li Sun

(ArcelorMittal Dofasco) for assistance with XPS.

5.8   References

[1] P. Drillet, Z. Zermout, D. Bouleau, J. Mataigne, S. Claessens, Revue De Métallurgie, 101(2004) 831-837.

[2] J. Mahieu, S. Claessens, B.C. De Cooman, Metall. Mater. Trans. A 32A (2001) 2905-2908.

[3] J. Mahieu, S. Claessens, B.C. De Cooman, F. Goodwin, in 6th Int. Conf. Zinc Zinc Alloy Coat. Steel Sheet Conf., Chicago (2004) 529-538.

[4] E.M. Bellhouse, "Galvanizing of Al-Si TRIP-assisted steels", Ph.D. thesis, McMaster University (2010).

5 I. Parezanović, "Selective oxidation and segregation in commercial steels and model alloys (tools for improving the surface wettability by liquid Zn during hot dip galvanizing)", Ph.D. thesis, Rheinisch-Westfälische Technische Hochschule Aachen (2005).

[6] E.M. Bellhouse, J.R. McDermid, Metall. Mater. Trans. A 41A (2010) 1539-1553.

[7] E.M. Bellhouse, J.R. McDermid, Metall. Mater. Trans. A 43A (2012) 2426-2441.

[8] M. Norden, M. Blumenau, T. Wuttke, K.J. Peters, Appl. Surf. Sci. 271 (2013) 19–31.

[9] E.M. Bellhouse, J.R. McDermid, Metall. Mater. Trans. A 42A (2011) 2753–2768.

[10] S. Alibeigi, R. Kavitha, R.J. Meguerian, J.R. McDermid, Acta Mater. 59 (2011) 3537-3549.

[11] S. Prabhudev, S. Swaminathan, M. Rohwerder, Corros. Sci. 53 (2011) 2413-2418.

[12] R. Sagl, A. Jarosik, D. Stifter, G. Angeli, Corros. Sci. 70 (2013) 268-275

[13] L. Cho, S.J. Lee, M.S. Kim, Y.H. Kim, B.C. De Cooman, Metall. Mater. Trans. A 44A (2013) 362-371.

[14] H. Liu, Y. He, S. Swaminathan, M. Rohwerder, L. Li, Surf. Coatings Technol. 206 (2011) 1237-1243.

[15] V.F.C. Lins, L. Madeira, J.M.C. Vilela, M.S. Andrade, V.T.L. Buono, J.P. Guimarães, E.A. Alvarenga, Appl. Surf. Sci. 257 (2011) 5871-5878.

[16] M.S. Kim, J.H. Kwak, J.S. Kim, Y.H. Liu, N. Gao, N.Y. Tang, Metall. Mater. Trans. A 40A (2009) 1903-1910.

[17] K. Kahoul, M. Turchetto, in 10th Int. Conf. Zinc Zinc Alloy Coat. Steel Sheet Conf., Toronto (2015) 436–443.

[18] Y.F. Gong, B.C. De Cooman, Iron Steel Inst. Japan Int. 51 (2011) 630-637.

[19] M. Seah, Acta Metall. 28 (1980) 955–962.

[20] M.P. Seah, J. Catalysts 57 (1979) 450-457.

[21] M.P. Seah, E.D. Hondros, Proc. R. Soc. Lond. A. 335 (1973) 191-212.

[22] H. Viefhaus, M. Rusenberg, Surf. Sci. 159 (1985) 1-23.

[23] L. Yin, S. Sridhar, Metall. Mater. Trans. B 41B (2010) 1095-1107.

[24] L. Cho, M.S. Kim, Y.H. Kim, B.C. De Cooman, Metall. Mater. Trans. A 45A (2014) 4484-4498.

[25] L. Cho, E.J. Seo, G.S. Jung, D.W. Suh, B.C. De Cooman, Metall. Mater. Trans. A 47A (2016) 1705-1719.

[26] G. Lyudkovsky, IEEE Trans. Magn. 22 (1986) 508-510.

[27] E. Clauberg, C. Uebing, H.J. Grabke, Appl. Surf. Sci. 143 (1999) 206-214.

[28] Z.T. Zhang, I.R. Sohn, F.S. Pettit, G.H. Meier, S. Sridhar, Metall. Mater. Trans. B 40B (2009) 550-566.

[29] Z.T. Zhang, I.R. Sohn, F.S. Pettit, G.H. Meier, S. Sridhar, Metall. Mater. Trans. B 40B (2009) 567-584.

[30] D.S. Petrovic, M. Jenko, V. Gontarev, H.J. Grabke, Kovine, Zlitine, Tehnologije 32 (1998) 493-496.

[31] D.A. Melford, Proc. R. Soc. Lond. A. 295 (1980) 89-103.

[32] Y. Li, J.P. Han, Z.H. Jiang, P. He, Int. J. Miner. Metall. Mater. 22 (2015) 37-44.

[33] M. Pourmajidian, J.R. McDermid, Metall. Mat. Trans. A 49A (2018) 5561-5573.

[34] K. Thompson, D. Lawrence, D.J. Larson, J.D. Olson, T.F. Kelly, B. Gorman, Ultramicroscopy 107 (2007) 131-139.

[35] C.R. Brundle, C.A. Evans, Jr., S. Wilson, Encyclopedia of Materials Characterization. United States of America, Butterworth-Heinemann, 1992.

[36] N. Birks, G.H. Meier, F.S. Pettit, Introduction to the High-Temperature Oxidation of Metals, Cambridge University Press, Cambridge, 2006.

[37] C. Wagner, Zh. Elektrochem., 63 (1959) 772-782.

[38] E.M. Bellhouse, J.R. McDermid, Metall. Mater. Trans. A 41A (2010) 1539-1553.

[39] A.P. Grosvenor, E.M. Bellhouse, A. Korinek, M. Bugnet, J.R. McDermid, Appl. Surf. Sci. 379 (2016) 242–248.

[40] H.K. Schmid, W. Mader, Micron 37 (2006) 426-432.

[41] C.C. Ahnn and O.L. Krivanek, with contributions by: R.P Burgner, M.M. Disko, P.R. Swann, EELS Atlas, A reference guide of electron energy loss spectra covering all stable elements, Gatan Inc., Warrendale, 1983.

[42] E.A. Marquis, B.P. Geiser, T.J. Prosa, D.J. LarsonJ. Microscopy 241 (2011) 225-233.

[43] G. Seyed Mousavi, J.R. McDermid, Surf. Coat. Technol. 351 (2018) 11-20.

6 EFFECT OF ANNEALING ATMOSPHERE PO₂ AND SN ON THE REACTIVE WETTING OF A C-2MN-1.7SI (WT.%) ADVANCED HIGH STRENGTH STEEL DURING CONTINUOUS GALVANIZING

G. Seyed Mousavi, J.R. McDermid*

Steel Research Centre, McMaster University, Hamilton, Canada ON L8S 4L8

6.1 Abstract

The effects of morphology and chemistry of surface oxides on the reactive wetting of a Fe-0.1C-2Mn-1.7Si (wt.%) advanced high strength steel during continuous galvanizing were investigated as a function of annealing atmosphere oxygen partial pressure and Sn addition. Both reference and 0.05 wt.% Sn-added steels were annealed intercritically at 1113 K (840 °C) for 120 s in a N₂-5 vol.% H₂ process atmosphere under the three dew points of 223 K (–50 °C), 243 K (–30 °C) and 278 K (+5 °C). Galvanizing process was done by immersing the samples in a 733 K (460 °C) 0.2 wt.% dissolved Al bath for 4 s. For both steels, the best reactive wetting was attained under the 278 K (+5 °C) dew point atmosphere, as exemplified by the most compact Fe-Al intermetallic layer formed at the substrate/coating interface. This was found to be attributed to the presence of nodule-like MnSiO₃ external oxides compared to the film-like MnSiO₃, MnO and SiO₂ oxides formed on the surface of the steel under the 223 K (–50 °C) and 243 K (–30 °C) dew point atmospheres. Addition of Sn was found to reduce the compactness of the film-like surface oxides under the 223 K (–50 °C) and 243 K (–30 °C) and increase the size and space between surface oxide nodules under the 278 K (+5 °C) dew point atmosphere. This modified oxide morphology along with mechanisms such as liquid bath interfacial infiltration enhanced the reactive wetting of the steel remarkably.

Keywords: Sn addition; oxygen partial pressure; reactive wetting; continuous galvanizing

6.2   Introduction

Transformation Induced Plasticity (TRIP) steels are amongst the so-called first generation (1G) of advanced high strength steels (AHSS), which have attracted growing interest in the automotive industry due to having a unique combination of high strength, good formability and high energy absorption capacity [1,2]. Addition of alloying elements such as C, Mn and Si to these steels is essential in order to obtain the promising properties [3-6]. However, Mn and Si can deteriorate the wettability of the intercritically annealed strip by the molten Zn-Al-Fe bath during the continuous hot dip galvanizing as they selectively oxidize during annealing in the commonly used industrial N_2-(5-20 vol.%) H_2-xH_2O annealing atmosphere prior to galvanizing [7,8]. Reactive wetting of the steel is reported to be influenced by the morphology, thickness, chemistry and spatial distribution of the surface oxides, as they control contact between the Zn-alloy bath and the substrate. It has been well established by several authors that compact, thick, film-type oxides as well as closely-packed nodule-like oxide particles have the most adverse effect on the reactive wetting [9-12].

As addition of alloying elements to the steel chemistry is inevitable, a few in-line processes have been suggested for improving the steel reactive wetting by the Zn (Al, Fe) bath via modifying the chemistry and morphology of the surface oxides formed prior to galvanizing. These methods include increasing the annealing atmosphere dew point at a given annealing temperature [13-19], a two-step procedure known as oxidation-reduction process [20-22], and addition of surface active elements to the steel chemistry [23-32] to the steel chemistry.

Increasing the annealing atmosphere pO_2 encourages the oxides to form in the subsurface rather than on the surface, as typified by the Wagner model [33] for the internal to external

oxidation transition, therefore leaves a surface which is covered with thinner oxides. Seyed Mousavi and McDermid [19] reported improved reactive wetting as a result of an increase in the annealing process atmosphere pO_2, due to either a decrease in the thickness of the film-like surface oxides or an alteration in the surface oxide morphology from film-like to nodule-like particles. It was observed by the authors that the modified surface oxide structure eased the Fe dissolution from the substrate and led to the formation of the Fe-Al intermetallics. The authors reported aluminothermic reduction and interfacial infiltration of the galvanizing bath through cracks formed due to the thermal coefficient of expansion mismatch between the external oxide and the substrate, as the main mechanisms responsible for the good reactive wetting at higher atmosphere pO_2.

During oxidation-reduction process the steel is annealed in air [20], an oxygen-rich gas fired furnace [21], or in a N_2-O_2 atmosphere [22], followed by annealing in in a conventional continuous galvanizing line (CGL) atmosphere reducing with respect to Fe e.g. N_2- (5-10 vol.%) H_2 with a controlled dew point.

Addition of trace amounts of surface active elements, such as Sn [23-27], Sb [28-31] and Bi [32] to the steel chemistry, on the other hand, has recently brought many researchers' attention to itself as a potentially promising method to improve the reactive wetting during continuous galvanizing. The most crucial characteristic of these surface active elements is that their oxides are thermodynamically less stable compared to Fe-oxides so that their oxides do not form in the N_2-(5-20 vol.%) H_2-xH_2O annealing atmosphere. In addition, they have larger atomic size than Fe, therefore they tend to segregate to the steel surface as well as the grain boundaries in order to reduce the elastic strain they are being exposed to in the bulk [34,35]. They are also required to have lower melting temperature than Fe, as the melting temperature of an element is directly

related to its surface energy i.e. the lower their melting temperature, the more tendency they would have to segregate to the surface in order to reduce the surface energy [*36*]. Pourmajidian et al. [27] studied the combined effect of 0.05 wt.% Sn and annealing atmosphere pO_2 on the thermodynamics and kinetics of oxide formation in a 0.1C-6Mn-2Si (wt.%) medium-Mn AHSS. They observed a significant refinement of the internal oxide network and a decrease in the thickness of external oxides, which was reported to be due to the reduced rate of both external and internal oxidation after the addition of Sn to the steel composition. Pourmajidian and McDermid [*37*] also related the observed modification in the oxide characteristics to the steel reactive wetting by the Zn (Al, Fe) continuous galvanizing bath. It was shown that the beneficial effect of Sn on the oxide morphology assisted with less bare spots to remain on the Zn coating as well as the formation of well-developed η-$Fe_2Al_5Zn_X$ layer at the steel/coating interface, indicative of higher quality coating compared to the reference steel.

The aim of the present research is to determine the combined effects of the addition of Sn and annealing atmosphere oxygen partial pressure on the selective oxidation and reactive wetting of a Fe-0.1C-2Mn-1.7Si (wt.%) AHSS. It should be pointed out that a more comprehensive investigation on the selective oxidation of the present experimental alloy during intercritical annealing at 1113 K (840 °C) as a function of Sn addition, annealing time and process atmosphere pO_2 has been recently reported by the present authors [*38*] and the oxidation section of the present article will contain a summary of their observations and mainly focus on the effect of morphology, thickness and chemistry of the surface oxides on the reactive wetting of the experimental steel during continuous hot-dip galvanizing.

6.3 Experimental procedure

Two series of AHSSs with the compositions shown in Table 6.1, referred to as Reference and a Sn-added, were used in the present research. For oxidation and galvanizing tests, respectively, 10 mm × 50 mm coupons and 120 mm × 200 mm panels were cut from the as-received cold rolled steel sheets, brushed in 2 wt.% NaOH solution at 353 K (80 °C), rinsed with water, cleaned with isopropanol in an ultrasonic bath and finally dried with warm air. Right before the tests, a K-type thermocouple (0.5 mm, ±3 K) was spot welded to each sample to control the sample temperature on line. Figure 6.1 shows a schematic of the experimental thermal cycle performed in the McMaster Galvanizing Simulator (MGS, Iwatani Surtec). Samples were heated to the intercritical annealing temperature (IAT) of 1143 K (870 °C), according to the pattern shown in Figure 6.1, held at the IAT for annealing times of t_1= 120 s, cooled to 738 K (465 °C) and held at this temperature for 20 s in order to allow the sample to reach thermal equilibrium throughout its thickness. As the final step, while oxidation samples were cooled to room temperature using N_2 jet cooling, galvanizing samples were dipped for 4 s in a 733 K (460 °C)-zinc bath which was Fe saturated and contained 0.2 wt.% dissolved Al before final cooling to room temperature.

Three dew points (dp) of 223 K (–50 °C), 243 K (–30 °C) and 278 K (+5 °C) were used in an atmosphere of N_2-5 vol.% H_2 to manipulate the pO_2 at the IAT, corresponding pO_2 and pH_2O/pH_2 of which is provided in Table 6.2.

Table 6.1: Chemical Composition of Experimental Steels (wt.%)

Steel	C	Mn	Si	Al	Ti	N	S	Sn	Fe
Reference	0.10	2.03	1.76	0.04	0.01	0.004	0.002	0.005	balance
Sn-added	0.11	2.04	1.75	0.04	0.01	0.003	0.002	0.05	balance

Table 6.2. Experimental Process Atmospheres

Process Atmosphere dp [K (°C)]]	N₂ (Vol.%)	H₂ (Vol.%)	pO₂ at 1113 K (840°C) Atm	pH₂O/pH₂ at 1113 K (840 °C)
223 (–50)	95	5	5.52×10^{-24}	0.0010
243 (–30)	95	5	3.41×10^{-22}	0.0082
278 (+5)	95	5	9.68×10^{-20}	0.1382

Figure 6.2 shows a schematic of the galvanized panel, from which 90 mm × 90 mm uniform temperature and coating area, centered in the lower portion of the panel, was cut. It is noteworthy that only material from this area was used for the subsequent analysis.
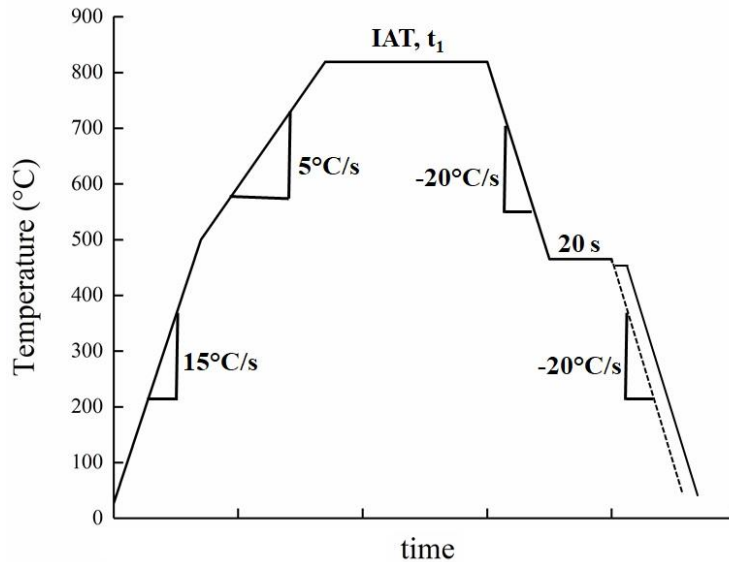
Figure 6.1: Schematic of the thermal cycle used for the experiments.

In order to quality check the coatings in macro scale, bare spots were counted and their areas were measured on the 90 mm × 90 mm areas cut from the galvanized panels using ImageJ 1.42q software. In addition, 10 mm × 90 mm coupons were slit from this area and were subjected to 180° bend tests by considering ASTM A653/A 653M-05 [39] to examine the coating adhesion of different samples. It is noteworthy that as the experimental steel is not an industrial grade, no specific parameter was found in the standard. Thus, the test parameters such as load and depth

were chosen by performing trial tests on the as-received sample up to the point that the sample cracked. The bent area was imaged at 20x magnification using a Keyence VHX-5000 digital optical microscope and inspected for any flaking or cracking of the coating occurred during the test.
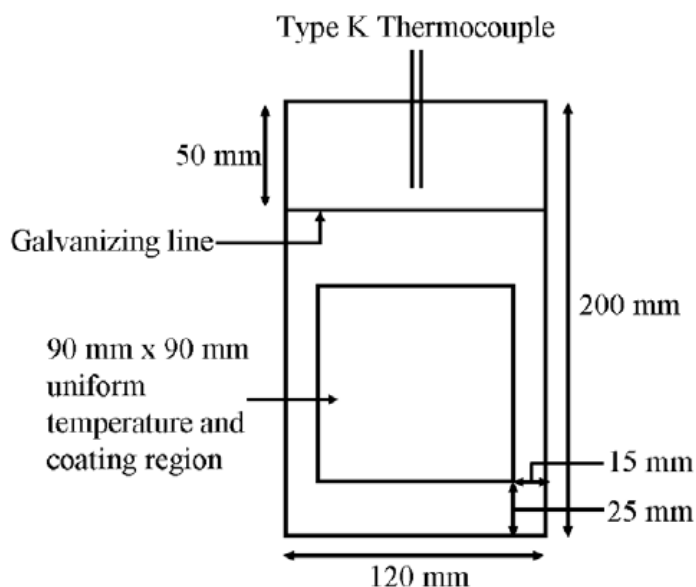
Figure 6.2: Schematic of the uniform temperature and coating area on galvanized panels [7].

In order to image the surface oxides formed under different annealing conditions prior to galvanizing, as well as the reaction products formed at the Fe/Zn interface after galvanizing, a JEOL 7000F field emission gun scanning electron microscope (FEG-SEM) was applied after coating each sample with a 5 nm-thick Pt layer. In order to expose the reaction products, galvanized panels was etched using 10 vol.% H_2SO_4 in water which corrodes the zinc overlay and leaves both Fe-Al and Fe-Zn intermetallics.

In order to compare the oxides' morphology as well as the thickness of the external oxides and the depth of internal oxides, as a function of annealing atmosphere pO_2 and Sn addition,

trenches were cut and imaged on the cross section of each oxidized samples using focussed ion beam (FIB, NVision 40 by Zeiss) milling.

Identification of the chemical composition of the external and internal oxides formed during annealing heat treatment, as well as the reaction products formed at the Fe-Zn interface after galvanizing, transmission electron microscope (TEM) lift-outs were done using FIB. Lift-out were then transferred to a FEI Titan 80-300 equipped with an electron energy loss spectroscopy (EELS) analytical facility by which elemental maps and point analyses were obtained. Mn-L, O-K, Si-K, Al-L, Zn-L and Fe-L edges were collected for all samples at 300 keV and were processed using Gatan Digital Micrograph 2.3. The pre-edge background was removed and all the elements spectra were energy aligned using the highest intensity feature of the Fe-L_3 edge at 708 eV and were normalized for baseline and intensity.

6.4 Results

Figure 6.3 shows the surface SEM micrographs of Reference and Sn-added experimental steels annealed for 120 s at the 1113 K (840 °C) under the 223 K (–50 °C), 243 K (–30 °C) and 278 K (+5 °C) dp process atmospheres. As can be seen, for Reference steel, although the surface was covered with compact, film-like and granular oxides under the 223 K (–50 °C) dp process atmosphere and compact, film-like layer under the 243 K (–30 °C) dp process atmosphere, increasing the atmosphere pO_2 utilizing the 278 K (+5 °C) dp process atmosphere (Table 6.2) resulted in the formation of nodule-like oxides on the steel surface. The granular and film-like oxides were identified as MnO and SiO_2/ $MnSiO_3$, respectively and the nodule-like particles were determined to be $MnSiO_3$. Comparing Figure 6.3(a) and (d) reveals that addition of Sn to the steel increased the size of the granular oxides and reduced their compactness under the 223 K (–50 °C) dp process atmosphere. Per Figure 6.3(b) and (e), under the intermediate pO_2 process

atmosphere of 243 K (–30 °C) dp (Table 6.2), addition of Sn refined the morphology of the surface oxides from compact, film-like on Reference steel to nodule-like particles on Sn-Added steel. Under the highest pO_2 process atmosphere of 278 K (+5 °C) dp (Table 6.2), oxides formed in larger and more widely-spaced nodules after the addition of Sn (Figure 6.3(c) and (f)). Detailed explanation of how the oxides compositions were identified is presented in an article by the present authors [38].

Figure 6.4 illustrates the FIB-derived cross-sectional micrographs of the experimental steels, showing the oxides formed prior to galvanizing on the surface and in the subsurface of Reference and Sn-added steels. As can be seen, increasing the process atmosphere dew point, i.e. pO_2, influenced both the morphology and thickness of the external oxides and depth of the internal oxides. In other words, proceeding from 223 K (–50 °C) to 243 K (–30 °C) process atmosphere reduced the thickness of the film-like oxides and increased the depth of internal oxidation, as would be expected based on the Wagner transition from external to internal oxidation model [33]. The same trend was observed by further increasing the atmosphere dew point to 278 K (+5 °C). Also, the morphology of the surface oxides altered to nodule-like particles, which is in agreement with observations exhibited in Figure 6.3. In addition, Sn was found to remarkably decrease the thickness of the external oxides and depth of the internal oxides (Figure 6.4(d-f)), which is known to be the result of the reduction occurred in the growth kinetic rate of the oxides in the presence of segregated Sn at the steel surface [27,38]. Also, granular MnO and nodule-like $MnSiO_3$ oxides formed on the surface of the 223 K (–50 °C) and 278 K (+5 °C) steels, respectively, grew larger and spaced farther apart, comparable to the surface SEM micrographs shown in Figure 6.3(d,f).
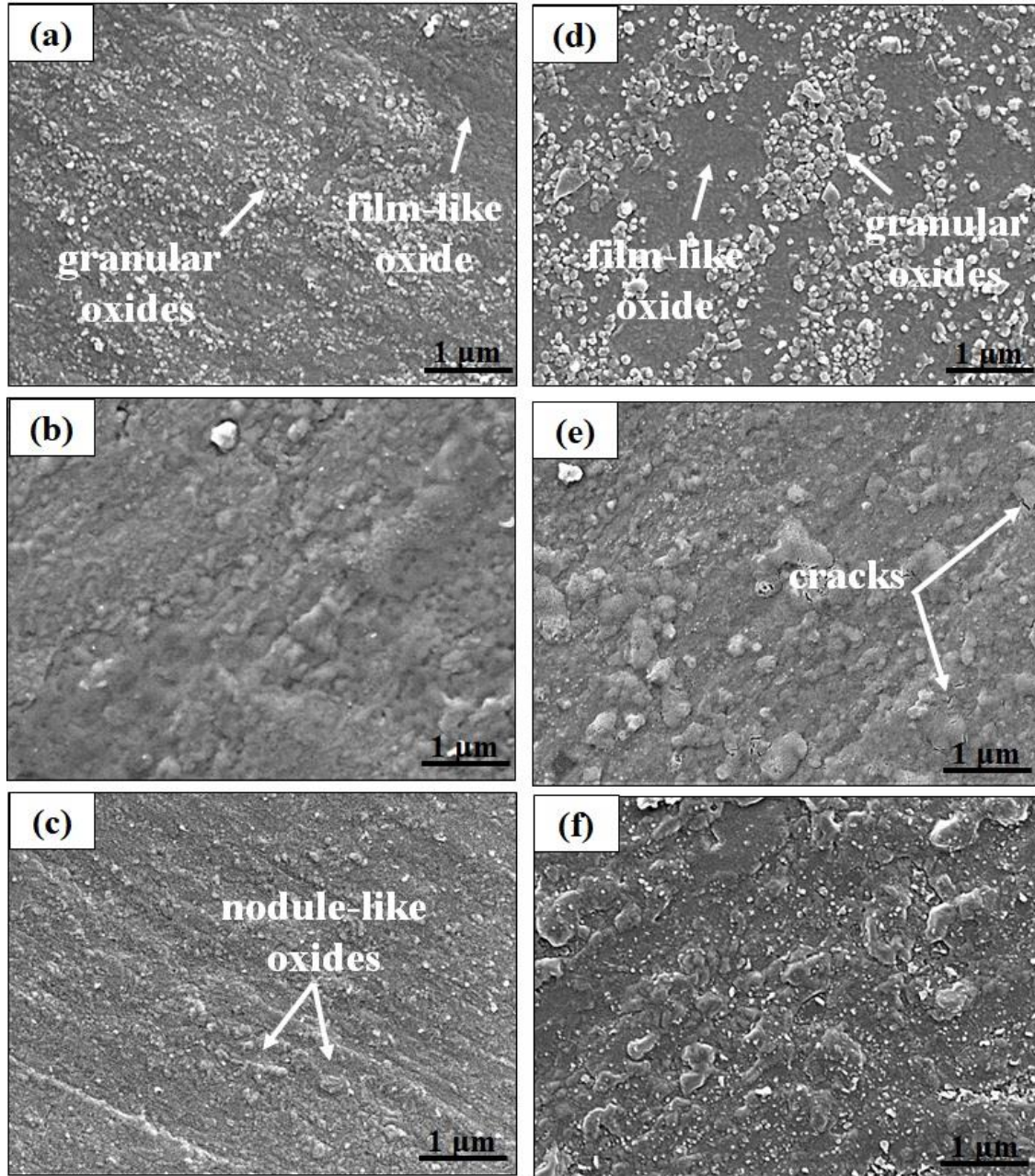
Figure 6.3: Surface SEM micrographs of the Reference steel (a,b,c) and Sn-added steel (d,e,f) as a function of process atmosphere pO_2: (a,d) 223 K (–50 °C) dp, (b,e) 243 K (–30 °C) dp and (c,f) 278 K (+5 °C) dp.
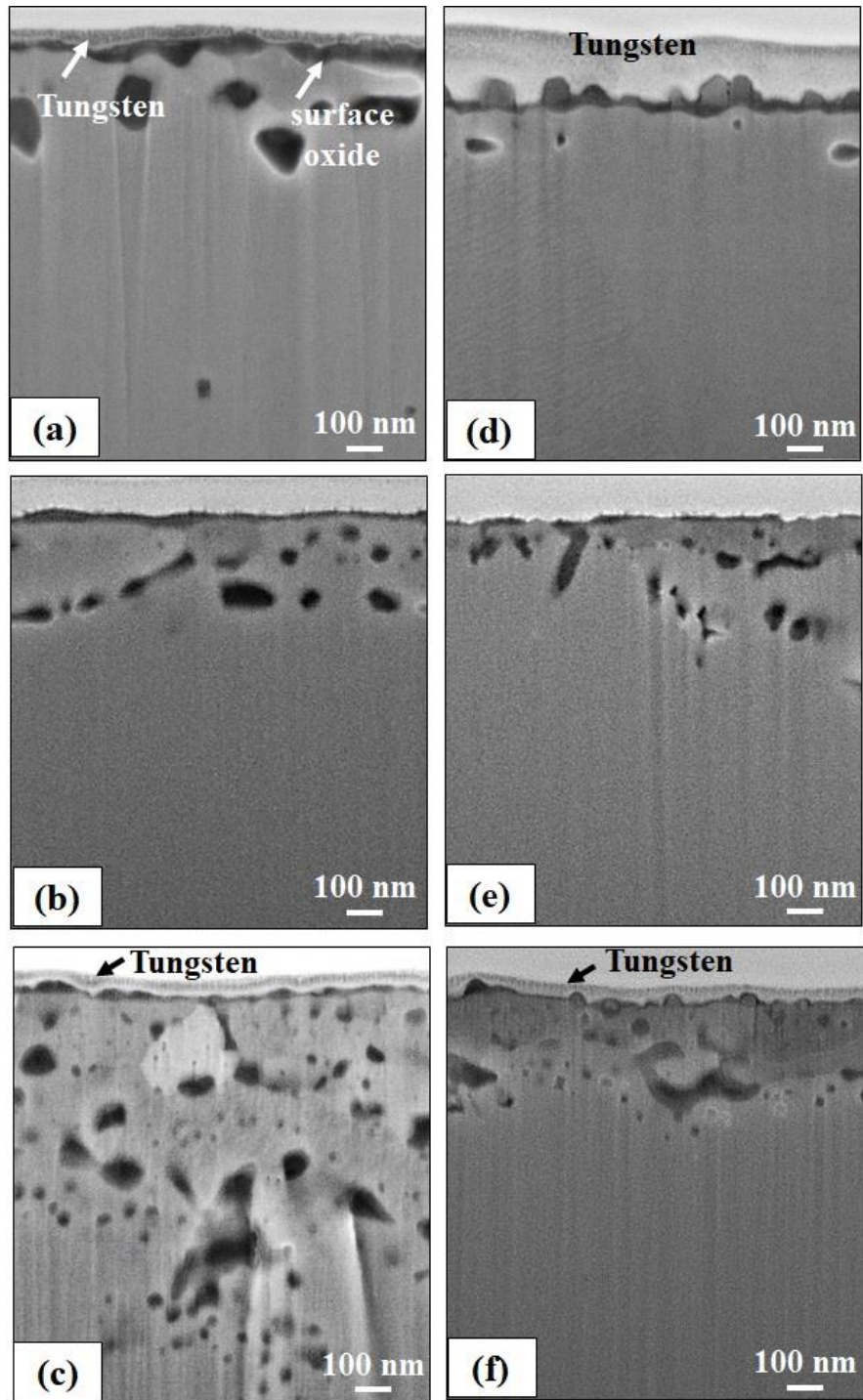
Figure 6.4: Cross-sectional micrographs of Reference steel (a,b,c) and Sn-added steel (d,e,f) as a function of process atmosphere pO_2: (a,d) 223 K (–50 °C) dp, (b,e) 243 K (–30 °C) dp and (c,f) 278 K (+5 °C) dp.

Overview of the 90 mm × 90 mm uniform temperature and coating areas of Reference and Sn-added steels annealed under the three atmosphere pO_2 (Table 6.2) and continuously galvanized in the Zn (Al, Fe) bath is shown in Figure 6.5. The corresponding coating quantification carried out on the samples by counting the bare spots and measuring their areas, the result of which is provided in Table 6.3. Comparing Figure 6.5(a) with Figure 6.5(b) and (c) and considering Table 6.3, it can be seen that even though Reference steel was not coated after being annealed under the lowest pO_2 223 K (–50 °C) dp process atmosphere (Table 6.2), increasing the atmosphere pO_2 utilizing 243 K (–30 °C) and 278 K (+5 °C) dp process atmospheres (Table 6.3) significantly improved the coating quality. On the other hand, the addition of 0.05 wt.% Sn considerably enhanced the coating quality, which is exemplified by the lower percentage of the bare areas measured on Sn-added steel compared to Reference steel, under all experimental process atmosphere pO_2 (Figure 6.5 and Table 6.3). A complete coating with zero percentage of bare spot area was achieved on the Sn-added steel annealed under the highest pO_2 278 K (+5 °C) dp process atmosphere (Table 6.2, Figure 6.5(e),Table 6.3).
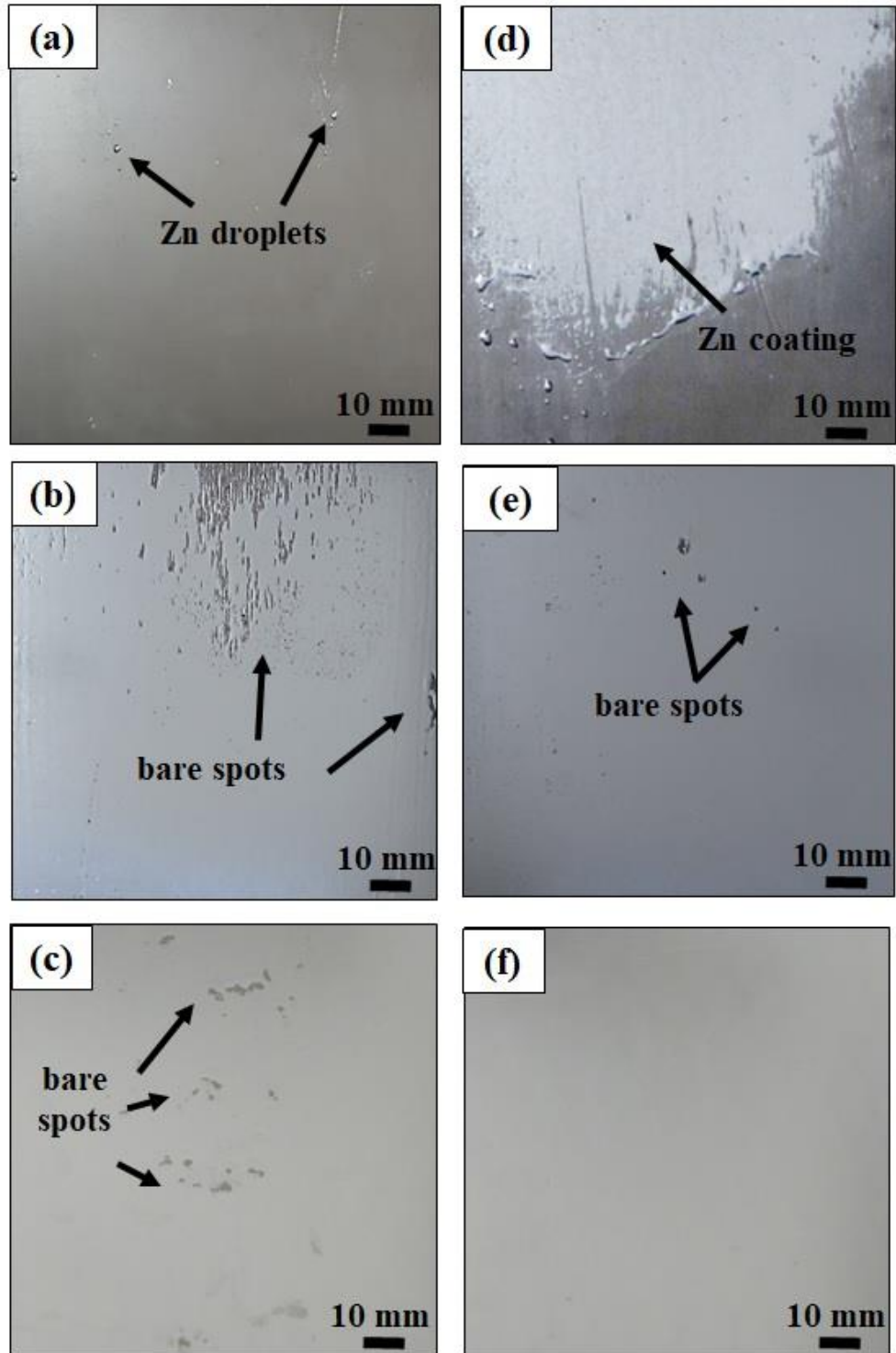
Figure 6.5: Overview of the uniform temperature and coating area of the galvanized Reference steel (a,b,c) and Sn-added steel (d,e,f) as a function of process atmosphere pO_2: (a,d) 223 K (–50 °C) dp, (b,e) 243 K (–30 °C) dp and (c,f) 278 K (+5 °C) dp.

Table 6.3: Bare Spot Analysis of the Uniform Temperature and Coating Areas of Reference and Sn-added Galvanized Panels Illustrated in Figure 6.5

Process Atmosphere Dew Point	Number of bare spots	Total Bare Area (mm^2)	Bare Area (%)
Ref., 223 K (–50 °C)	–	~8020	~99
Ref., 243 K (–30 °C)	66	358.85	4.43
Ref., 278 K (+5 °C)	48	66.55	0.82
Sn-Added, 223 K (–50 °C)	–	~4050	~50
Sn-Added, 243 K (–30 °C)	24	24.20	0.30
Sn-Added, 278 K (+5 °C)	0	0.00	0.00

Figure 6.6 illustrates high magnification micrographs of the outer radius of the galvanized Reference and Sn-added steels after being subjected to 180° bend test. No flaking or cracking could be observed on the bent area, which is indicative of an acceptable adherence of the Zn (Al,Fe) coating to the substrate. It is worth to mention that as Reference steel was not coated by the continuous galvanizing bath after being annealed under the 223 K (–50 °C) dp process atmosphere, it will not be considered in any of the further characterizations mentioned in this text.

Figure 6.7 shows the SEM images of the Fe/Zn interfaces of the continuously-galvanized Reference and Sn-added steels after being annealed under the three atmosphere pO$_2$ (Table 6.2). As was mentioned before, aqueous 10 vol.% H$_2$SO$_4$ was applied which strips the zinc layer and leaves Fe-Zn and Fe-Al intermetallics unattacked. Equiaxed crystals formed at the substrate-coating interface of all samples. For the Sn-added sample annealed under the lowest pO$_2$ 223 K (–50 °C) dp process atmosphere (Table 6.2), needle-like intermetallics can be observed in addition to the equiaxed crystals (Figure 6.7(c)). It can be seen that for both Reference (Figure 6.7(a,b)) and Sn-added (Figure 6.6(c,d,e)) steels, increasing the annealing atmosphere pO$_2$ using higher dew points (Table 6.2), led to the formation of smaller and more compact crystals at the interface, in agreement with the results reported by Seyed Mousavi and McDermid

[19]. Besides, a comparison between Figure 6.7(a,b) with Figure 6.7(c,d,e) shows that the

intermetallics formed at the Fe/Zn interface of Sn-Added samples were more closely-packed and

smaller in size than those of Reference samples.
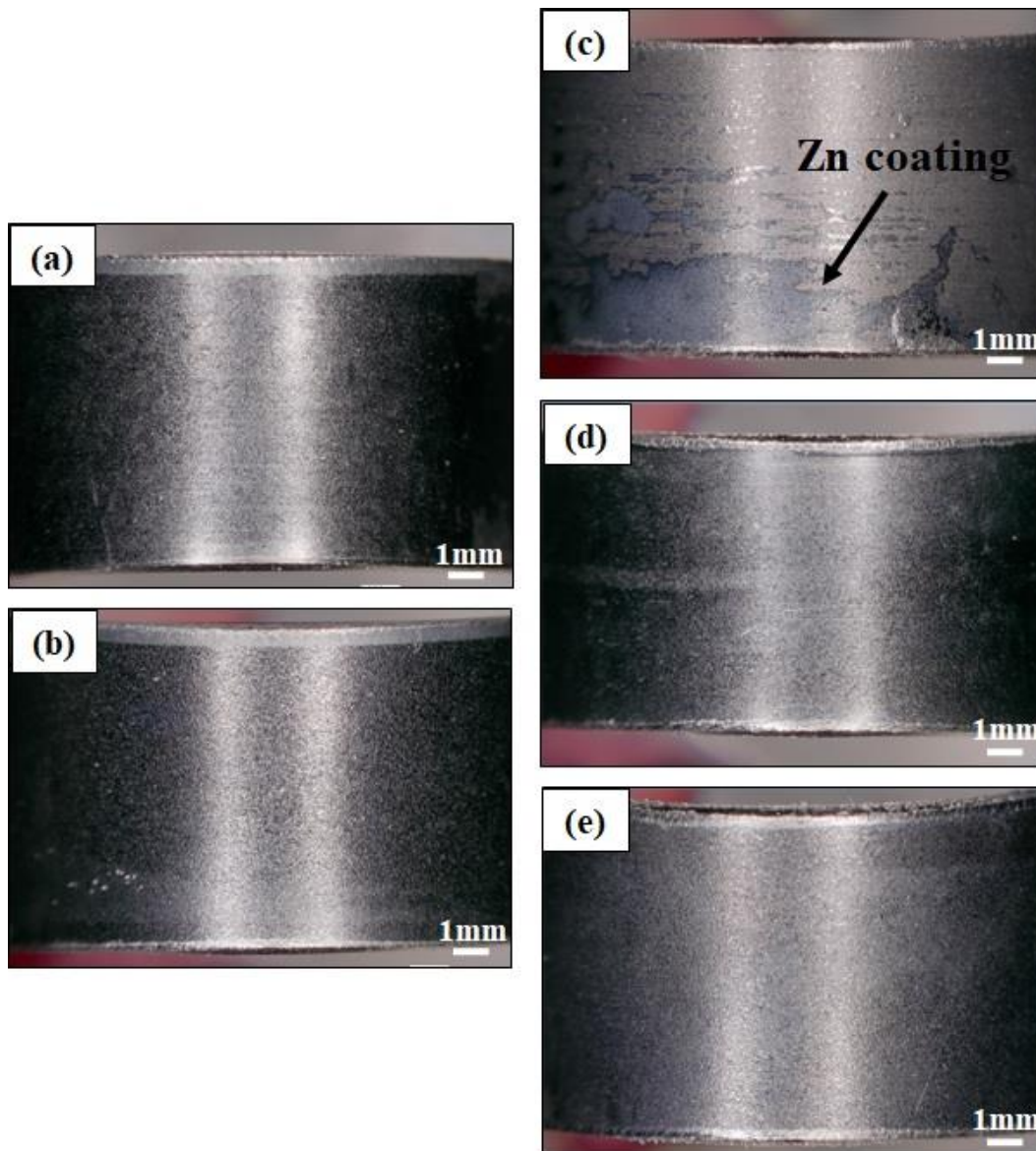
Figure 6.6: 20X magnification view of the bent are of the galvanized Reference steel (a,b) and Sn-added steel (c,d,e) as a function of process atmosphere pO_2: (c) 223 K (–50 °C) dp, (a,d) 243 K (–30 °C) dp and (b,e) 278 K (+5 °C) dp.
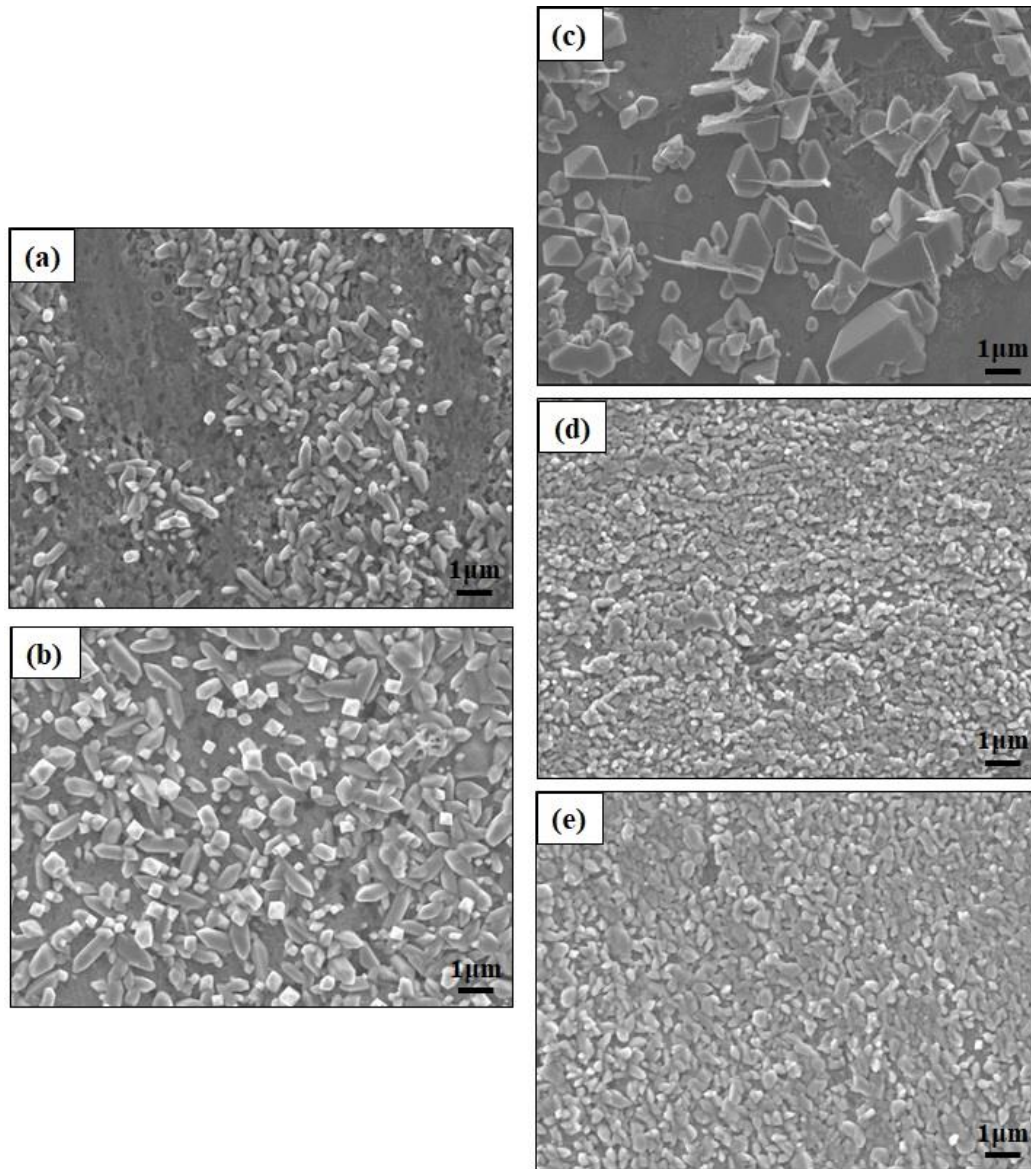
Figure 6.7: Fe/Zn interface SEM images of the galvanized Reference steel (a,b) and Sn-added steel (c,d,e) as a function of process atmosphere pO_2: (c) 223 K (–50 °C) dp, (a,d) 243 K (–30 °C) dp and (b,e) 278 K (+5 °C) dp.

As the best-quality coating-sample of each Reference and Sn-added series of steels, the one annealed under the highest pO_2 278 K (+5 °C) dp process atmosphere (Table 6.2) was chosen for

TEM characterizations in order to determine the mechanisms contributed to the desired reactive wetting despite the presence of oxides on the surface of the steels.

Figure 6.8(a) shows the TEM cross-sectional view of the Fe/Zn interface and subsurface of the Reference steel along with the corresponding EELS elemental map. As can be seen, the intermetallics rich in Fe and Al formed above, below or in between the surface oxides. In addition, Zn had penetrated into the subsurface along a grain boundary. The interfacial infiltration of the galvanizing bath through oxide cracks and along grain boundaries and the consequent nucleation and growth of the Fe-Al crystals below the oxides were reported previously by Bellhouse and McDermid [12] and Pourmajidian and McDermid [*40*]. Using high resolution EELS spectra shown in Figure 6.8(b) as an example, the surface oxides were identified as $MnSiO_3$ by comparing the detailed features of the $Mn-L_{2,3}$ and O-K edges with the those of the standard $MnSiO_3$, Mn_2SiO_4 EELS spectra [41]. A hole can also be observed in a surface oxide particle as pointed out in Figure 6.8(a) which is likely to be formed due to spalling of a part of the oxide, as previously suggested by Bellhouse [7].

Figure 6.9 illustrates TEM cross-sectional micrograph and EELS elemental map of an area at the Fe/Zn interface and subsurface of the continuously galvanized Sn-added sample after being annealed under the 278 K (+5 °C) dp process atmosphere. Similar to the observations on Reference steel, Fe-Al intermetallics formed above, below or in between the surface oxides. A small area rich in Zn can also be seen below the surface oxide, which is indicative of the galvanizing bath penetration through the oxide layer. The surface oxides were identified as $MnSiO_3$. It is noteworthy that the holes formed in the Zn overlay during FIB milling the TEM lift-out due to the higher milling rate of Zn compared to that of Fe.

Table 6.4 shows the results of the EELS point analysis performed on points A through E on the Fe-Al intermetallics formed at the Fe/Zn interface of Reference and Sn-added steels, as labeled in Figure 6.8(a) and Figure 6.9.As can be seen, the Fe, Al and Zn ratios are comparable with the η-$Fe_2Al_5Zn_X$ intermetallic, the formation of which indicates the occurrence of the reactive wetting reaction between the Zn (Al,Fe) galvanizing bath and the substrate.
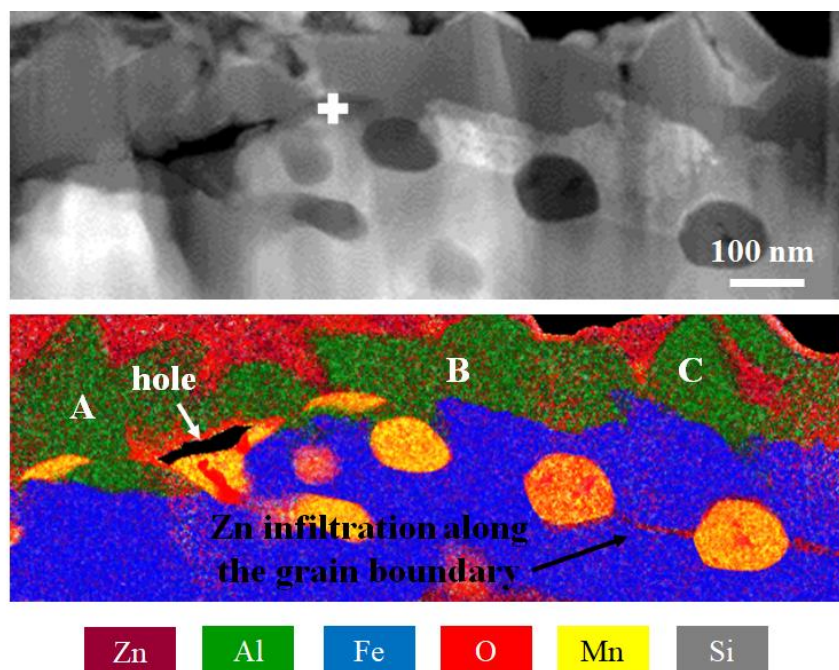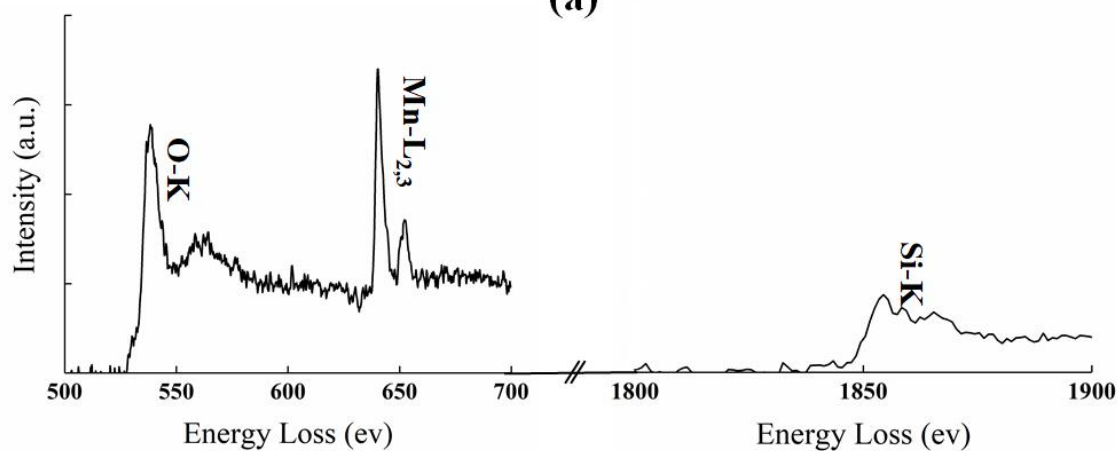
Figure 6.8: (a) Dark field TEM cross-sectional micrograph of the galvanized Reference steel annealed under the 278 K (+5 °C) dp process atmosphere along with its corresponding color over-lay EELS elemental map, (b) Mn-$L_{2,3}$, O-K and Si-K edge EELS spectra of the oxide marked with a white cross in the dark field TEM image in (a).
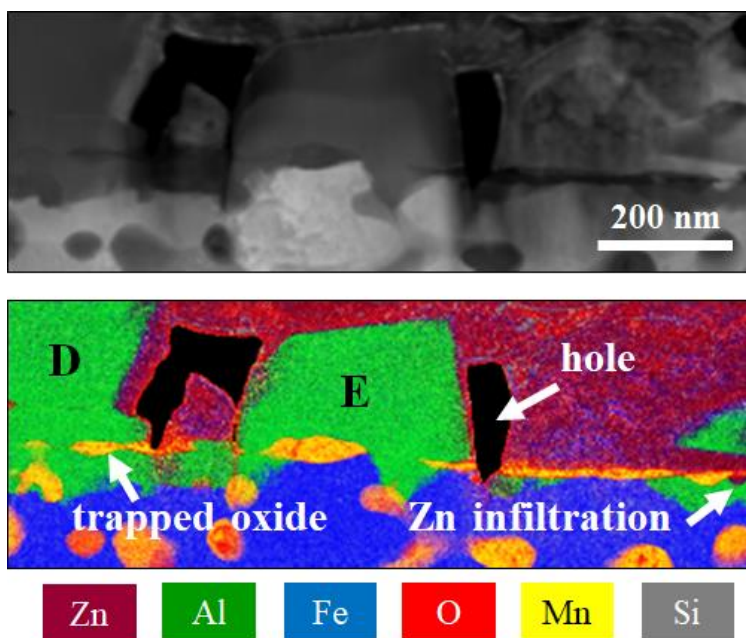
Figure 6.9: Dark field TEM cross-sectional micrograph of the galvanized Sn-added steel annealed under the 278 K (+5 °C) dp process atmosphere along with its corresponding color over-lay EELS elemental map.

Table 6.4. TEM EELS Analysis of Points A through E shown in Figure 6.8(a) and Figure 6.9

Point	O	Mn	Si	Fe	Al	Zn	Intermetallic Present
A	14.3	0.0	0.0	21.9	60.2	3.7	η-Fe$_2$Al$_5$Zn$_X$
B	17.5	0.0	0.0	23.2	55.0	4.3	η-Fe$_2$Al$_5$Zn$_X$
C	16.8	0.0	0.0	22.3	58.0	2.9	η-Fe$_2$Al$_5$Zn$_X$
D	17.9	0.4	0.0	17.8	59.8	4.1	η-Fe$_2$Al$_5$Zn$_X$
E	7.9	0.0	0.0	23.2	63.6	5.3	η-Fe$_2$Al$_5$Zn$_X$

6.5   Discussion

According to the results reported by the present authors [38], which have been summarized in

Figure 6.3 and Figure 6.4, under the lowest pO$_2$ 223 K (–50 °C) dp process atmosphere

(Table 6.2), Reference steel was covered with thick, compact film-like MnO, MnSiO$_3$ and SiO$_2$

oxides, the presence of which blocked the steel surface and suppressed the Fe dissolution from

the substrate and its consequent chemical reaction with the dissolved Al while the sample was immersed into the Zn (Al,Fe) galvanizing bath. Therefore, the sample was not coated and only a few zinc droplets remained solidified on the surface, as shown in Figure 6.5(a) and Table 6.3. This is while the addition of Sn to the steel resulted in approximately half coverage of the steel surface with the galvanizing bath (Figure 6.5(d) and Table 6.3). Also, Fe-Al intermetallics were identified at the Fe/Zn interface after stripping the Zn layer using 10 vol.% H_2SO_4 in water (Figure 6.7(c)), which indicates the occurrence of the chemical reaction between the substrate and the bath. This was attributed to the alteration observed on the morphology of the surface oxides after the addition of Sn to the steel composition. Per Figure 6.3(a,d) and Figure 6.4(a,d), Sn resulted in the formation of thinner and less compact film-like SiO_2 and $MnSiO_3$ as well as larger and widely-spaced granular MnO oxides on the surface of the steel. However, as the external oxidation were dominant over the internal oxidation at this low pO_2 annealing atmosphere (Table 6.2, Figure 6.4(a,d)), the reactive wetting could not occur completely and η-$Fe_2Al_5Zn_X$ crystals formed along with needle-like intermetallics (Figure 6.7(c)). Although applying characterization techniques such as X-ray diffraction were not capable of detecting these needle-like intermetallics due to their low volume fraction (<1%), they have been reported to be Fe-Zn intermetallics and are known to form as a result of the presence of thick surface oxides is in agreement with studies done by several authors [12,16,17]. The formation of the Fe-Zn intermetallics is attributed to the localized depletion of Al, where it was consumed to reduce surface oxides such as MnO through aluminothermic reduction reaction [42,43], as well as to form η-$Fe_2Al_5Zn_X$ crystals.

Increasing the annealing atmosphere pO_2 using the 243 K (–30 °C) and 278 K (+5 °C) dew points (Table 6.2) led to the transition from external to internal oxidation, per Figure 6.4, which

is known to be a beneficial method for improving the reactive wetting during continuous galvanizing [14,16,19,44]. The formation of thinner film-like SiO_2 and $MnSiO_3$ oxides under the 243 K (–30 °C) dp and nodule-like $MnSiO_3$ oxides under the 278 K (+5 °C) dp process atmosphere on the surface of Reference steel could facilitate the occurrence of the reaction between Fe and Al. This is exemplified by the formation of an acceptable coating quality (Figure 6.5(b,c), Figure 6.6(a,b)) with less than 5% and 1% bare area under the 243 K (–30 °C) and 278 K (+5 °C) dp process atmospheres, respectively (Table 6.3), and developed η-$Fe_2Al_5Zn_X$ interfacial layer at the substrate/coating interface (Figure 6.7(a,b), Figure 6.8 and Table 6.4), indicative of relatively good reactive wetting compared to the lower pO_2 223 K (–50 °C) dp process atmosphere (Table 6.2).

Combined effects of Sn and higher annealing atmosphere pO_2 further improved the coating quality of the experimental steel, as can be observed in the overview of the galvanized panels illustrated in Figure 6.5(e,f) which had <0.3% and 0.0% bare area after being annealed under the 243 K (–30 °C) and 278 K (+5 °C) dp process atmospheres, respectively (Table 6.3). Well-developed interfacial layer comprised of small, compact equiaxed η-$Fe_2Al_5Zn_X$ crystals were also formed at the substrate/coating interface of Sn-added steel, which is representative of a complete reactive wetting (Figure 6.5(d,e), Figure 6.7 and Table 6.4). As was shown in Figure 6.3 and Figure 6.4, Sn altered the morphology of the surface oxides, which according to the results reported in reference 38, is the result of Sn segregation to the external oxide/substrate interface, as verified by 150X increase in its concentration at the oxide/substrate interface compared to its bulk value using atom probe tomography (APT). Presence of Sn at the steel surface could affect the inward diffusion of oxygen and outward diffusion of the alloying elements, thus, reduce the kinetics of the selective oxidation. These results are in agreement with

the studies done by Pourmajidian and McDermid [27] and Cho et al. [26] on the effect of Sn on

the selective oxidation of a 0.1C-6Mn-2Si (wt.%) medium-Mn AHSS and 0.1C-1.6Mn-1.5Si

(wt.%) TRIP steel, respectively.

Reference and Sn-added steels continuously galvanized after being annealed under the highest

pO_2 278 K (+5 °C) dp process atmosphere (Table 6.2) were examined in order to determine the

mechanism through which the reactive wetting occurred despite the presence of surface oxides.

Comparing the oxides formed on surface of the Reference and Sn-added samples prior to

galvanizing (Figure 6.3(c) and (f), respectively) with the ones observed after dipping them into

the Zn (Al,Fe) bath (Figure 6.8 and Figure 6.9, respectively) reveals that although the former

comprised of compact nodule-like and thin film-like $MnSiO_3$ oxides, the latter included mainly

lens-shaped oxides being trapped in the Fe-Al intermetallics. As can be seen in Figure 6.8 even

most of the surface was free of any visible oxides. The grain boundary which is rich in Zn and

the observed in the overlay-color EELS elemental maps of the Reference and Sn-added samples,

respectively indicate the infiltration of the Zn (Al, Fe) bath into the subsurface via either grain

boundaries or the cracks formed in the oxides as a result of the difference in thermal expansion

coefficient of the surface oxide and the substrate, as suggested by Bellhouse and McDermid [12].

This provides conditions for nucleation of the η-$Fe_2Al_5Zn_X$ crystals between and below the

oxides, during growth of which, oxides having weaker interface with the substrate would lose

their adhesion and spall off or be trapped in the Fe-Al crystals [**45**]. The hole shown in

Figure 6.8(a) is the result of this oxide lift-off. The same observations were reported previously

by other authors [7,9,12,44] as one of the main contributions responsible for a good reactive

wetting during continuous hot-dip galvanizing of AHSSs. Cracks although were not visible in the

surface SEM micrographs of the as-oxidized sample annealed under the 278 K (+5 °C) dp

process atmosphere, can be clearly seen in the Sn-added steel annealed under the 243 K (–30 °C) dp process atmosphere, as shown and labelled in Figure 6.3(e).

6.6 Conclusions

The combined effects of annealing atmosphere partial pressure (pO_2) and addition of 0.05 wt.% Sn to the steel chemistry on the reactive wetting of a Fe-0.1C-2Mn-1.7Si (wt.%) AHSS by a Zn (0.2 dissolved Al , Fe) (wt.%) continuous galvanizing bath were examined by focusing on their influence on the morphology of oxides selectively formed during intercritical annealing heat treatments. The following conclusions were made:

1. Although poor reactive wetting was observed under the 223 K (–50 °C) dp process atmosphere, increasing annealing atmosphere pO_2 via rising the dew point to 243 K (–30 °C) and 278 K (+5 °C) led to the formation of well-developed η-$Fe_2Al_5Zn_X$ interfacial layer, thus complete reactive wetting in both Reference and Sn-added steels. This was due to the fact that under the 223 K (–50 °C) dp process atmosphere, thick, compact film-like MnO, SiO_2 and $MnSiO_3$ oxides covered the steel surface, thus suppressed the chemical reaction between the Fe from the substrate with Al in the galvanizing bath. This is while the improved reactive wetting obtained using higher process atmosphere pO_2 of 243 K (–30 °C) and 278 K (+5 °C) reaped the benefit from the altered surface oxide morphology, due to the occurrence of the transition from external to internal oxidation.

2. The addition of Sn was found to substantially boost the coating quality of the Reference steel as a result of its beneficial effect on reducing the kinetics of the external oxidation. The modified surface oxide morphology could ease the Fe dissolution from the substrate and provide more nucleation sites for η-$Fe_2Al_5Zn_X$ crystals.

3. Infiltration of the liquid bath through the grain boundaries as well as the cracks formed due to the difference between the thermal expansion coefficient of the oxides and the substrate was found as the main mechanism for the good reactive wetting despite the presence of surface oxides on both Reference and Sn-Added steels.

4. The Sn-added steel intercritically under the 278 K (+5 °C) dp process atmosphere for 120 seconds reaped the benefits of both Sn and high annealing atmosphere pO_2.

6.7   Acknowledgments

6.8   References

[1] V.F. Zackay, E.R. Parker, D. Fahr, R. Busch, ASM Trans. Q.60 (1967) 252-259.

[2] B.C. De Cooman, Curr. Opin. Solid State Mater. Sci. 8 (2014) 285-303.

[3] H. Liu, F. Li, W. Shi, S. Swaminathan. Y. He, M. Rohwerder, L. Li, Surf. Coat. Technol. 206 (2012) 3428–3436.

[4] S.-K. Lee, J.-S. Kim, N. Kang, K.-M. Cho, Met. Mater. Int. 18 (2012) 951–956.

[5] S.-K. Lee, J.-S. Kim, J.-W. Choi, N. Kang, K.-M. Cho, Met. Mater. Int. 17 (2011) 251-257.

[6] X. Vanden Eynde, J. P. Servais, M. Lamberigts, Surf. Interface Anal. 35 (2003) 1004-1014.

[7] E.M. Bellhouse, "Galvanizing of Al-Si TRIP-assisted steels", Ph.D. thesis, McMaster University (2010).

[8] I. Parezanović, "Selective oxidation and segregation in commercial steels and model alloys (tools for improving the surface wettability by liquid Zn during hot dip galvanizing)", Ph.D. thesis, Rheinisch-Westfälische Technische Hochschule Aachen (2005).

[9] E.M. Bellhouse, J.R. McDermid, Metall. Mater. Trans. A 43A (2012) 2426-2441.

[10] M. Norden, M. Blumenau, T. Wuttke, K.J. Peters, Appl. Surf. Sci. 271 (2013) 19–31.

[11] E.M. Bellhouse, J.R. McDermid, Metall. Mater. Trans. A 41A (2010) 1460–1473.

[12] E.M. Bellhouse, J.R. McDermid, Metall. Mater. Trans. A 42A (2011) 2753–2768.

[13] V.A. Lashgari, C. Kwakernaak, W.G. Sloof, Oxid. Met. 81 (2014) 435–451.

[14] M. Pourmajidian, J.R. McDermid, Metall. Mater. Trans. A 49A (2018) 1795-1808.

[15] H. Liu, Y. He, S. Swaminathan, M. Rohwerder, L. Li, Surf. Coat. Technol. 206 (2011) 1237-1243.

[16] L. Cho, S. J. Lee, M. S. Kim, Y. H. Kim, B. C. De Cooman, Metall. Mater. Trans. A 44A (2013) 362-371.

[17] E.M. Bellhouse, J.R. McDermid, Metall. Mater. Trans. A 43A (2012) 2426-2441.

[18] E.M. Bellhouse, J.R. McDermid, Metall. Mater. Trans. A 41A (2010) 1539-1553.

[19] G. Seyed Mousavi, J.R. McDermid, Surf. Coat. Technol. 351 (2018) 11-20.

[20] I. Parezanović, M. Spiegel, Surf. Eng. 20 (2004) 285-291.

[21] K. Kahoul, M. Turchetto, in 10th Int. Conf. Zinc Zinc Alloy Coat. Steel Sheet Conf., Toronto (2015) 436–443.

[22] Y.F. Gong, B.C. De Cooman, Iron Steel Inst. Japan Int. 51 (2011) 630-637.

[23] H. Viefhaus, M. Rusenberg, Surf. Sci. 159 (1985) 1-23.

[24] L. Yin, S. Sridhar, Metall. Mater. Trans. B 41B (2010) 1095-1107.

[25] L. Cho, M.S. Kim, Y.H. Kim, B.C. De Cooman, Metall. Mater. Trans. A 45A (2014) 4484-4498.

[26] L. Cho, E.J. Seo, G.S. Jung, D.W. Suh, B.C. De Cooman, Metall. Mater. Trans. A 47A (2016) 1705-1719.

[27] M. Pourmajidian, B. Langelier, J.R. McDermid, Metall. Mater. Trans. A 49A (2018) 5561-5573.

[28] G. Lyudkovsky, IEEE Trans. Magn. 22 (1986) 508-510.

[29] E. Clauberg, C. Uebing, H.J. Grabke, Appl. Surf. Sci. 143 (1999) 206-214.

[30] Z.T. Zhang, I.R. Sohn, F.S. Pettit, G.H. Meier, S. Sridhar, Metall. Mater. Trans. B 40B (2009) 550-566.

[31] Z.T. Zhang, I.R. Sohn, F.S. Pettit, G.H. Meier, S. Sridhar, Metall. Mater. Trans. B 40B (2009) 567-584.

[32] J. Oh, L. Cho, M. Kim, K. Kang, B.C. De Cooman, Metall. Mater. Trans. A 47A (2016) 5474-5486.

[33] C. Wagner, Zh. Elektrochem., 63 (1959) 772-782.

[34] M. Seah, Acta Metall. 28 (1980) 955–962.

[35] M.P. Seah, J. Catalysts 57 (1979) 450-457.

[36] M.P. Seah, E.D. Hondros, Proc. R. Soc. Lond. A. 335 (1973) 191-212.

[37] M. Pourmajidian, J.R. McDermid, Surf. Coat. Technol. Accepted Manuscript (2018) https://doi.org/10.1016/j.surfcoat.2018.10.028.

[38] G. Seyed Mousavi, B. Langelier, J.R. McDermid, Submitted Manuscript to Metall. Mater. Trans. A (2018) (Ref. No.: E-TP-18-1790A).

[39] ASTM A 653/A 653M – 05, (2005) Standard specification for steel sheet, zinc-coated (galvanized) or zinc-iron alloy-coated (galvannealed) by the hot-dip process.

[40] M. Pourmajidian, J.R. McDermid, Iron Steel Inst. Japan Int. 58 (2018) 1635-1643

[41] A.P. Grosvenor, E.M. Bellhouse, A. Korinek, M. Bugnet, J.R. McDermid, Appl. Surf. Sci. 379 (2016) 242-248.

[42] R. Khondker, A. Mertens, J.R. McDermid, Mater. Sci. Eng. A 463 (2007) 157-165.

[43] R. Kavitha, J. R. McDermid, Surf. Coat. Technol. 212 (2012) 152-158.

[44] R. Sagl, A. Jarosik, D. Stifter, G. Angeli, Corros. Sci. 70 (2013) 268-275.

[45] H.E. Evans, R.C. Lobb, Corros. Sci. 24 (1984) 209-222.

7   DISCUSSION AND FUTURE DIRECTIONS

The general results observed on the effects of annealing atmosphere oxygen partial pressure (pO_2), annealing time and a minor Sn addition to the steel chemistry on the selective oxidation and reactive wetting of the experimental advanced high strength steels during continuous hot-dip galvanizing have been discussed briefly in this chapter. For the sake of simplicity, the effect of each parameter on the selective oxidation and reactive wetting of the experimental steels have been analysed in a separate section. In the last section, the experimental results have been compared to a thermodynamic-based model and the observations have been discussed briefly.

7.1   Annealing atmosphere oxygen partial pressure

Increasing annealing atmosphere pO_2 via raising the process atmosphere dew point was shown to be an effective way to modify the external oxide morphology and consequently improve the reactive wetting of both the 0.1C-2Mn-1.3Si and 0.1C-2Mn-1.7Si (wt.%) advanced high strength steels by the Zn (0.2 wt.% dissolved Al, Fe) continuous galvanizing bath, in agreement with the observations reported by several authors [1-5].

For the 0.1C-2Mn-1.3Si steel, poor reactive wetting was observed after continuous galvanizing of the steel annealed under the lowest pO_2 223 K (–50 °C) dp process atmosphere (Table 3.2 and Table 4.2). Visual inspection of the galvanized panels revealed > 95% bare area (Table 4.4 and Figure 4.3). In addition, no well-developed interfacial layer was found at the Fe/Zn interface after stripping the zinc layer (Figure 4.5(a)). This poor reactive wetting was attributed to the selective oxidation of Mn and Si. The selective oxidation mode was determined as external under this condition using XPS (Figure 3.4(a)) and the TEM observations in Figure 3.8, which was in agreement with the predictions made using Wagner model [6] and its modified

model suggested for grain boundary oxidation [7] (Figure 3.2 and Table 3.3). Using the SEM surface images (Figure 3.5) and the TEM cross-sectional micrographs (Figures 3.8, 3.9 and 3.10), two external oxide morphologies were identified. A multi-layer, 32 ± 5 nm-thick oxide comprising crystalline $MnSiO_3$ with granular MnO oxides above and amorphous SiO_2 oxide beneath, and a 38 ± 5 nm-thick compact, film-like $MnSiO_3$ and SiO_2 oxide, as shown in Figures 3.5, 3.8, 3.9 and 3.10. The presence of this relatively thick external oxide layer could block contact between the Fe on the substrate surface and impede the occurrence of the desired chemical reaction between the substrate Fe and Al from the galvanizing bath.

Increasing the annealing atmosphere pO_2 via raising the process atmosphere dew point to 243 K ($-30\,°C$) (Table 3.2 and Table 4.2) considerably improved the coating quality, as exemplified by a more uniform coating of the continuously galvanized panels with less than 1% bare area (Figure 4.3 and Table 4.3). Furthermore, no cracking or flaking of the coating was observed during the 180° bend test (Figure 4.4). Further investigation revealed the formation of an interfacial layer comprising η-$Fe_2Al_5Zn_X$ crystals at the Fe/Zn interface (Figures 4.5 and 4.8, Table 4.5). The formation of a well-developed η-$Fe_2Al_5Zn_X$ interfacial layer was the result of the transition from external to internal oxidation, and thus the alteration of the external oxides' morphologies occurred by increasing the annealing atmosphere pO_2 (Table 3.2 and Table 4.2), as shown by the XPS elemental depth profile (Figures 3.4(b)), TEM cross-sectional micrographs (Figures 3.6, 3.11 and 4.2), and the thickness of the external oxides and depth of internal oxidation, graphed in Figure 3.14 and summarized in Table 4.3. The external to internal oxidation transition led to a decrease in the compactness of the SiO_2, MnO, $MnSiO_3$ and Mn_2SiO_4 surface oxides, (Figures 3.6 and 4.1(b)), as well as their thickness (Figures 3.4(b), 3.11, 4.1(b), 4.2(b), and Table 4.3), compared to the thick, compact, film-like and granular

oxides observed under the lower process atmosphere dew point of 223 K (–50 °C) (Figures 3.5, 3.4(a), 3.5, 3.8, 3.9, 3.10, 4.1(a), 4.2(a) and Table 4.3 Figure 3.11). It is worth to mention that this transition in oxidation mode was predicted for Mn using the the Wagner model [6], but was not successfully predicted for Si in the bulk ferrite (Figure 3.2 and Table 3.3). This failure was purported to be due to (1) inadequate Si diffusivity data and, (2) the proximity of the predicted Si internal/external transition (i,e. 250 K (–23°C) dp, Figure 3.2) to the experimental conditions.

Two main mechanisms are known to be responsible for the improved reactive wetting observed by increasing the atmosphere pO_2. Aluminothermic reduction reaction and interfacial infiltration of the bath alloy. As mentioned in Chapter 2, per Alibeigi et al. [8] studies, aluminothermic reduction can occur in the case of the presence of thinner external oxides and the excess Al can contribute to the formation of the η-$Fe_2Al_5Zn_X$ interfacial layer. Reduction of the external oxides then provides condition for a direct contact between the steel substrate and the molten Zn (Al, Fe) bath, the occurrence of the reactive wetting, and thus the formation of a well-developed η-$Fe_2Al_5Zn_x$ interfacial layer. In addition, as explained in detail in Chapter 3, due to the fact that the thermal expansion coefficient of the MnO and SiO_2 oxides were significantly different from that of the substrate, the oxides could either crack or flake off of the substrate surface, as a consequence of the large stress imposed to them during cooling the sample from the intercritical temperature to the thermal equilibration temperature of the 738 K (465 °C) before immersing into the galvanizing bath. These cracks and holes, along with the grain boundaries, could provide paths for the infiltration of the Zn bath and facilitate the occurrence of the reactive wetting by mitigating the contact between the bath alloy and the substrate.

Further increasing the annealing atmosphere pO_2 by using 278 K (+5 °C) dew point process atmosphere (Table 3.2 and Table 4.2), ameliorated the coating quality to the level that no bare

spot could be found on the galvanized panel (Figure 4.3, Table 4.3). This was found to be due to the alteration observed in the morphology of the surface oxides from film-like under the 223 K (–50 °C) dp and 243 K (–30 °C) dp process atmospheres to nodule-like $MnSiO_3$ and MnO particles, as shown in Figures 3.7, 4.1(c) and 4.2(c). The smaller and more compact η-$Fe_2Al_5Zn_X$ crystals formed at the Fe/Zn interface of the sample annealed under the 278 K (+5 °C) (Figure 4.5(c)) dp process atmosphere compared to those of the 223 K (–50 °C) dp and 243 K (–30 °C) dp process atmospheres indicated that the presence of oxides in the form of nodule-like particles with thin films-like oxides in between could provide easier access for the Al in the bath to the substrate Fe to promote the reactive wetting reaction. Aluminothermic reduction reaction and infiltration of the zinc bath are again known to contribute to the formation of the η-$Fe_2Al_5Zn_X$ crystals (Figures 4.5, 4.9 and Table 4.5).

For the 0.1C-2Mn-1.7Si (wt.%) steel, on the other hand, it was found that, similar to the observations on the 0.1C-2Mn-1.3Si (wt.%) steel, increasing the annealing atmosphere pO_2 by using the 243 K (–30 °C) dp versus 223 K (–50 °C) dp (Table 5.2 and Table 6.2) process atmosphere decreased the thickness of the external oxides and increased the depth to which the internal oxides penetrated into the subsurface, as a result of the transition from external to internal oxidation (Figures 5.1, 5.2, 5.7, 5.8(a) and 6.4). Again, this facilitated reactive wetting between the substrate and the zinc bath and, consequently, improved the coating quality of the steel (Figures 6.5, 6.6, 6.7 and Table 6.3).

Further raising the atmosphere dew point to 278 K (+5 °C) led to the formation of fine, closely-spaced nodule-like external oxide particles (Figures 5.4, 5.6, 5.8(c)and 6.3) which, consistent with the results observed for the 0.1C-2Mn-1.3Si (wt.%) steel, promoted the formation of the desired Fe-Al interfacial layer, indicative of the reactive wetting reaction between the

substrate and the galvanizing bath (Figures 6.7 and 6.8). It is noteworthy that, as expected, although the 0.1C-2Mn-1.3Si (wt.%)×278 K (+5 °C) dp steel was coated completely (0% bare area (Figure 4.3, Table 4.4), a few bare spots were found on the coated 0.1C-2Mn-1.7Si (wt.%)×278 K (+5 °C) dp steel (Figure 6.5, Table 6.3), which was attributed to the formation of more detrimental-structured external oxides due to having higher Si/Mn ratio (5.6, 6.3(c), 6.4(c).

7.2   Sn addition

As suggested by Suzuki et al. [4], increasing the Si/Mn ratio would increase the possibility of forming Si-containing oxides, in particular SiO_2, which has been shown to be problematic during continuous galvanizing [9-13]. As an example, it was reported by Mahieu et al. [9] that formation of Si oxides on the surface of a 0.19C-1.57Mn-1.46Si (wt.%) TRIP steel during annealing at 1073 K (800 °C) under the dew point of 243 K (–30 °C) in a N_2-5 vol.% H_2 atmosphere deteriorated the wettability during continuous galvanizing using a Zn bath containing 0.2 wt.% Al. They showed that although the coating quality was improved using higher process atmosphere pO_2, it was not possible to fully eliminate the bare areas.

Thus, it became the next objective of the current Ph.D. research to determine the beneficial effects, if any, of adding a surface active element to the 0.1C-2Mn-1.7Si (wt.%) steel composition and increasing the atmosphere pO_2 on external oxide formation and growth as well as their consequent effect on the reactive wetting during continuous galvanizing. Sn has a high tendency for segregation to the surface and grain boundaries in the substrate [14,15] and, therefore has the potential to reduce the the dissolved oxygen concentration both on the surface and in the subsurface and decrease the external and internal oxidation kinetic rate [16-18].

Adding 0.05 wt.% Sn to the steel chemistry was found to lead to well-developed reactive wetting during continuous galvanizing. As illustrated in Figure 6.5 and Table 6.3, the addition of

Sn reduced the bare area percentage of the Reference steel annealed for 120 s under the 223 K (–50 °C), 243 K (–30 °C) and 278 K (+5 °C) dp process atmospheres, by 50%, 93% and 100%, respectively. Under the lowest pO_2 223 K (–50 °C) dp process atmosphere, the addition of Sn increased the size and spacing between the granular external MnO (Figures 5.2, 5.5, 6.3(a,d), 6.4(a,d)). Under the intermediate pO_2 243 K (–30 °C) dp process atmosphere, the addition of Sn altered the morphology of the surface oxides from a film-like $MnSiO_3$ and SiO_2 layer comprised of large and thick particles to smaller, thinner and less compact nodule-like ones (Figures 5.3, 5.6(a,b), 6.3(b,e), 6.4(b,e)). Under the highest pO_2 278 K (+5 °C) dp process atmosphere although the $MnSiO_3$ particles formed fine and closely packed structures on the Reference steel, they configured themselves as discrete widely-spaced ones after the addition of Sn to the steel composition (Figures 5.4, 5.6(c,d), 6.3(c,f), 6.4(c,f)).

As verified by atom probe tomography (Figures 5.10 and 5.11), Sn segregated to the external oxide/substrate interface during annealing process, the occurrence of which lowered oxygen diffusion ito the subsurface and the alloying elements' diffusion towards the surface, thus, reduced the parabolic rate constant for both internal and external oxidation and, consequently, decreased the thickness of the external oxides and the depth of internal oxidation under all three annealing atmosphere dew points, as shown in Figures 5.2 and 5.3, in agreement with the XPS results shown in Figure 5.1 and the cross-sectional TEM micrographs shown in Figures 5.7, 5.8 and 6.4.

The Sn-added steel annealed under the highest pO_2 278 K (+5 °C) dp process atmosphere showed the highest-quality coating after being continuously galvanized in the Zn (0.2 wt.% dissolved Al, Fe) bath, compared to the other annealing atmospheres. No bare spots were observed upon inspection of the galvanized panels (Figure 6.5(f) and Table 6.3) and no flaking

or cracking could be found in the coating after a 180° bend test (Figure 6.6(e)). A well-developed η-$Fe_2Al_5Zn_X$ interfacial layer was also detected at the Fe/Zn interface (Figure 6.7(e)). The observed outstanding reactive wetting for the Sn-added steel annealed under the highest pO_2 278 K (+5 °C) dp process atmosphere, despite the relatively high Si/Mn ratio of the steel, can thus be related to the mutual effects of the Sn addition and increased annealing atmosphere pO_2. The main mechanism responsible for the improved reactive wetting was shown to be infiltration of the liquid Zn-alloy bath through the interface via grain boundaries as well as the cracks formed in the oxides during the annealing process (Figure 6.8 and 6.9). This resulted in the precipitation of η-$Fe_2Al_5Zn_X$ intermetallics (Table 6.4) between and below the surface oxides, the growth of which resulted in oxide lift-off into the bath or oxide trapping in the η-$Fe_2Al_5Zn_X$ crystals [19].

As mentioned in Chapter 3, although transition from external to internal oxidation promotes the reactive wetting during continuous galvanizing, it can have detrimental effects with respect to fabrication processes such as forming and resistance spot welding [20]. As there is not sufficient research on this area, it is recommended for the future studies to examine the welding properties of the experimental steels.

7.3   Annealing time

Although in industrial continuous galvanizing lines, annealing times are confined to lower times of 60 and 120 s, extended annealing processes were also used for the examination of oxide formation and growth in order to investigate the kinetics of oxidation, as it provides a better understanding of their effects on the steel reactive wetting. Measurements were done on the thickness of the oxides formed on the 0.1C-2Mn-1.7Si (wt.%) and 0.1C-2Mn-1.7Si-0.05Sn (wt.%) steels' surfaces as well as the depth to which internal oxides formed in the steels' subsurfaces on at least 100 lines on the FIB-derived cross-sectional micrographs, the result of

which has been summarized in Figure 5.2. For both the Reference and Sn-added steels, it was revealed that holding the steel for longer annealing times at the intercritical annealing temperature increased the oxidation rate parabollically. As oxidation growth is a diffusion-based phenomenon, providing more time for both oxygen and the alloying elements can increase the thickness of external oxides and the depth of internal oxides, as shown in Figures 5.2(a) and (b), respectively. These results are in agreement with the increase observed in the oxide size and the steels' surface coverage by the oxides at prolonged annealing time of 600 seconds (Figures 5.4, 5.5 and 5.6 for the 223 K (–50 °C), 243 K (–30 °C) and 278 K (+5 °C) dp process atmospheres, respectively). Surface SEM images of the 0.1C-2Mn-1.3Si (wt.%) steel annealed under the 223 K (–50 °C), 243 K (–30 °C) and 278 K (+5 °C) dp process atmospheres (Figures 3.5, 3.6 and 3.7, respectively) for annealing times of 60 to 600 s, showed the same trend.

7.4   Comparison between the experimental results and a thermodynamic-based model

Suzuki et al. [4] proposed a thermodynamic model, where the alloy Si/Mn ratio and process atmosphere pO_2 were used to predict the chemical composition of the oxides that would form on Mn-Si steels at 1123 K (850 °C) and predict the reactive wetting based on the presence or absence of SiO_2. Figure 7.1 shows the Suzuki et al. model with the reactive wetting results obtained for the experimental 0.1C-2Mn-1.3Si, 0.1C-2Mn-1.7Si and 0.1C-2Mn-1.7Si-0.05Sn (wt.%) steels superimposed on the plot as a function of process atmosphere pO_2 (Table 4.2 and Table 6.2).

As can be seen from Figure 7.1, there are some inconsistencies in the chemistry of the oxides predicted by the Suzuki et al. model [4] compared to those observed in the present research. For the 0.1C-2Mn-1.3Si (wt.%) steel, Suzuki et al. predicted the formation of $MnSiO_3$ for the 223 K (–50 °C) process atmosphere, SiO_2 and $MnSiO_3$ for the 243 K (–30 °C) process atmosphere and

MnSiO$_3$ and Mn$_2$SiO$_4$ for 278 K (+5 °C) dp process atmosphere, whereas the present work determined the external oxides to be MnO, MnSiO$_3$, Mn$_2$SiO$_4$ and SiO$_2$ for 223 K (–50 °C) and 243 K (–30 °C) dp process atmospheres and MnO, MnSiO$_3$, Mn$_2$SiO$_4$ for 278 K (+5 °C) dp process atmospheres. On the other hand, for the 0.1C-2Mn-1.7Si (wt.%) steel, Suzuki et al. predicted the formation of SiO$_2$ and MnSiO$_3$ for both 223 K (–50 °C) and 243 K (–30 °C) process atmospherses and Mn$_2$SiO$_4$ for 278 K (+5 °C) dp process atmosphere and does not anticipate the presence of MnO in any of the annealing conditions, although it was identified on the surface of both Reference and Sn-added steels examined in the current research.
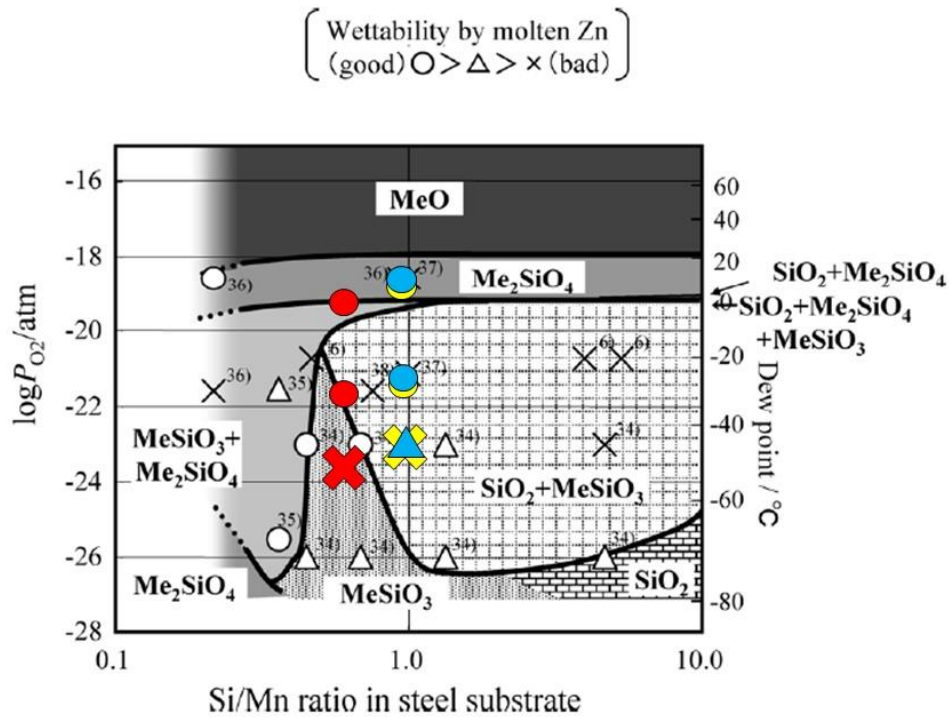

Figure 7.1: Superimposition of the wetting results of the 0.1C-2Mn-1.3Si (wt.%) steel (red symbols), 0.1C-2Mn-1.7Si (wt.%) (yellow symbols) and 0.1C-2Mn-1.7Si-0.05Sn (wt.%) steel (blue symbols) on the thermodynamic model proposed by Suzuki et al. [4] for annealing at 1123 K (850 °C).

The disagreements between the experimental results and the predictions made by the model may be due to the fact that the oxide predominance diagram shown in Figure 7.1 was calculated at 1123 K (850 °C) rather than the present annealing temperatures (1093 K (820 °C) for the 0.1C-2Mn-1.3Si (wt.%) steel and 1113 K (840 °C) for the 0.1C-2Mn-1.7Si (wt.%) steel). But the largest source of disagreement with the model in this case is likely due to the fact that kinetic factors were not taken into account. As was shown in Chapters 4 and 6, external oxide morphology plays a dominant role in determining the interactions between the as-annealed substrate surfaces and the continuous galvanizing bath and the resultant reactive wetting. Thus, although thermodynamic predictions can be used as a starting point for identifying the oxides expected during annealing, it is imperative that future modelling of selective oxidation within the context of the continuous galvanizing process include kinetic and morphological factors in addition to thermodynamic considerations when considering the combined processes of selective oxidation and reactive wetting by the continuous galvanizing bath.

7.5   References

[1] E.M. Bellhouse, J.R. McDermid, Metall. Mater. Trans. A 43A (2012) 2426-2441.

[2] E.M. Bellhouse, J.R. McDermid, Metall. Mater. Trans. A 41A (2010) 1460-1473.

[3] E.M. Bellhouse, J.R. McDermid, Metall. Mater. Trans. A 41A (2010) 1539-1553.

[4] Y. Suzuki, T. Yamashita, Y. Sugimoto, S. Fujita, S. Yamaguchi, Iron Steel Inst. Japan Int. 49 (2009) 564-573.

[5] L. Cho, S. J. Lee, M. S. Kim, Y. H. Kim, B. C. De Cooman, Metall. Mater. Trans. A 44A (2013) 362-371.

[6] C. Wagner, Zh. Elektrochem. 63 (1959) 772–82.

[7] J.M. Mataigne, M. Lamberigts, and V. Leroy: in *Dev. Annealing Sheet Steels*, R. Pradhan and I. Gupta, eds., Minerals, Metals & Materials Society, PA, 1992, pp. 511–28.

[8] S. Alibeigi, R. Kavitha, R. J. Meguerian, and J. R. McDermid, Acta Mater. 59 (2011) 3537-(2011).

[9] J. Mahieu, S. Claessens, B.C. De Cooman, Metall. Mater. Trans. A 32A (2001) 2905–2908.

[10] J. Maki, J. Mahieu, B.C. De Cooman, S. Claessens, Mater. Sci. Technol. 19 (2003) 125–131.

[11] M.S. Kim, J.H. Kwak, J.S. Kim, Y.H. Liu, N. Gao, N.Y. Tang, Metall. Mater. Trans. A 40A (2009) 1903–1910.

[12] Y. Kim, J. Lee, J. Park, S.-H. Jeon, Met. Mater. Int. 17 (2011) 607–611.

[13] K.-Ch. Lin, Ch.-S. Lin, Iron Steel Inst. Japan Int. 54 (2014) 2380–2384.

[14] M. Seah, Acta Metall. 28 (1980) 955–962.

[15] M.P. Seah, J. Catalysts 57 (1979) 450-457.

[16] M. Pourmajidian, B. Langelier, J.R. McDermid, Metall. Mater. Trans. A 49A (2018) 5561-5573.

[17] L. Cho, M.S. Kim, Y.H. Kim, B.C. De Cooman, Metall. Mater. Trans. A 45A (2014) 4484-4498.

[18] L. Cho, E.J. Seo, G.S. Jung, D.W. Suh, B.C. De Cooman, Metall. Mater. Trans. A 47A (2016) 1705-1719.

[19] R. Sagl, A. Jarosik, D. Stifter, G. Angeli, Corros. Sci. 70 (2013) 268-275.

[20] C. Horvath, C. Matthew Enloe, J. Coryell, J.P. Singh, and General Motors Co., in Proc. Int. Symp. New Dev. Adv. High-Strength Sheet Steels, Warrendale (2017), 1–10.

8 CONCLUSIONS

The effects of annealing process parameters – i.e. annealing atmosphere oxygen partial pressure (pO_2) and annealing time – on the selective oxidation and reactive wetting of a series of 0.1C-2Mn-xSi (wt.%) advanced high strength steels (AHSSs) with Si contents of 1.3 and 1.7 wt.% were determined. The process atmosphere pO_2 was manipulated by varying the atmosphere dew point (dp) in the base N_2-5 vol.% H_2-xH_2O system at 223 K (–50 °C), 243 K (–30 °C), and 278 K (+5 °C). In addition, minor amounts of Sn (0.05 wt.%) was added to the 0.1C-2Mn-1.7Si (wt.%) steel composition and its combined effect with annealing atmosphere pO_2 and annealing time was examined. The objective of this research was to develop a comprehensive understanding of the combined effects of the aforementioned parameters on the characteristics of the oxides formed prior to galvanizing and their consequent influence on the reactive wetting of the experimental steels during continuous galvanizing in a Zn (Al, Fe) bath. Various meso- to nano-scale analysis techniques were applied to elucidate the mechanisms reported, with the longer term objective of influencing alloy development and continuous galvanizing practices. The global key findings are summarized as follows:

1. Chemistry, morphology and spatial distribution of the external oxides were found to be affected by the annealing atmosphere pO_2. For both 0.1C-2Mn-1.3Si and 0.1C-2Mn-1.7Si (wt.%) steels, increasing pO_2 by raising the process atmosphere dew point from 223 K (–50 °C) to 243 K (–30 °C) and 278 K (+5 °C) was found to encourage the internal oxidation rather than the external one, thus decreased the thickness of the film-like external oxides under the 243 K (–30 °C) dp process atmosphere and altered their morphology from film-like under the 223 K (–50 °C) and 243 K (–30 °C) dp process atmospheres to plate-/nodule-like particles under the 278 K (+5 °C) dp.

2. Addition of Sn to the 0.1C-2Mn-1.7Si (wt.%) steel chemistry was found to result in a considerable change in the morphology of the surface oxides, as well as a significant reduction in the oxide growth kinetics of both external and internal oxidation. These observations are likely to be due to Sn segregation at the external oxide/substrate interface -to approximately 150 times greater than its nominal bulk concentration- as verified using atom probe tomography (APT), thus, acting as a diffusion barrier for both oxygen and the alloying elements and impeding the selective oxidation process.

3. External oxide morphology modification through either increasing the atmosphere pO_2 or Sn addition was found to promote the reactive wetting of the experimental steels. The best coating quality was observed for the 0.1C-2Mn-1.7Si-0.05Sn (wt.%) steel annealed under the highest pO_2 278 K (+5 °C) dp process atmosphere, which was found to be the result of the presence of large, widely-spaced nodule-like particles on the steel surface, thereby the chemical reaction between Fe from the subsurface with Al from the galvanizing bath was eased. Interfacial infiltration through cracks formed due to the thermal expansion coefficient mismatch between the substrate and the surface oxides, as well as the grain boundaries was found to be the main mechanism responsible for the formation of the η-$Fe_2Al_5Zn_x$ crystals during continuous galvanizing of the experimental steels.

4. For both the 0.1C-2Mn-1.7Si (wt.%) and 0.1C-2Mn-1.7Si-0.05Sn (wt.%) steels, annealing time was found to have a parabolic relationship with both the thickness of external oxides and the depth of internal oxidation.